Energy and Moisture Transport in the Earth Climate System: Mean State and the Perturbation Response

Hansi K. A. Singh

A dissertation submitted in partial fulfillment of
the requirements for the degree of

Doctor of Philosophy

University of Washington

2015

Reading Committee:

Cecilia M. Bitz, Chair

Dennis Hartmann

Christopher Bretherton

Randall J. Leveque

Program Authorized to Offer Degree:
University of Washington Department of Atmospheric Sciences

University of Washington

Abstract

Energy and Moisture Transport in the Earth Climate System: Mean State and the Perturbation Response

Hansi K. A. Singh

Chair of the Supervisory Committee:
Professor Cecilia M. Bitz
Department of Atmospheric Sciences

Four studies are presented which investigate how energy and moisture transport define the mean state of the Earth Climate System and its response to perturbations.

In the first study, we use a global climate model to study the effect of flattening the orography of the Antarctic Ice Sheet on climate. A general result is that the Antarctic continent and the atmosphere aloft warm, while there is modest cooling globally. The large local warming over Antarctica leads to increased outgoing longwave radiation, which drives anomalous southward energy transport towards the continent and cooling elsewhere. Atmosphere and ocean both anomalously transport energy southward in the Southern Hemisphere. Near Antarctica, poleward energy and momentum transport by baroclinic eddies strengthens. Anomalous southward cross-equatorial energy transport is associated with a northward shift of the inter-tropical convergence zone. In the ocean, anomalous southward energy transport arises from a slowdown of the upper cell of the oceanic meridional overturning circulation and a weakening of the horizontal ocean gyres, causing sea ice in the Northern Hemisphere to expand and the Arctic to cool. Comparison with a slab ocean simulation confirms the importance of ocean dynamics in determining the climate system response to Antarctic orography. We conclude this study by briefly discussing the relevance of these results to climates of the past and to future climate scenarios.

The remaining studies consider atmospheric moisture transport. First, we develop a new mathematical framework for analyzing results from climate modeling studies that employ numerical water tracers (WTs). Data made available from WTs, which track the movement of water in the aerial hydrological cycle from evaporation to precipitation, are used to analyze the sources and transport of precipitable water in the climate system. The precipitation over a tagged region is subdivided into contributions from local evaporation and remote evaporation. The contribution from remote evaporation, the moisture convergence, can be further subdivided into zonal, meridional (north-to-south and south-to-north), intrabasin, and interbasin parts to yield additional insight into how the aerial hydrological cycle transports water. This theory is applied to the preindustrial mean state climate as simulated by a global climate model in which evaporated water has been tagged in 10° latitude bands in each of the major ocean basins, and in which each major land mass has been tagged separately. Findings from analysis of the mean state concur with findings from earlier studies of the hydrological cycle: water evaporated at the equator and in the high latitudes tends to precipitate locally, whereas water evaporated in the subtropics and midlatitudes tends to precipitate remotely; water evaporated in the subtropics precipitates either equatorward or poleward of its source region, while water evaporated in the midlatitudes mostly precipitates poleward. New insights from the method reveal fundamental differences between the major ocean basins in locally-sourced precipitation, remotely-sourced precipitation and their relative partitioning. Per unit area, the subtropical Atlantic is the largest global moisture source, providing precipitable water to adjacent land areas and to the eastern Pacific intertropical convergence zone while retaining the least for in situ precipitation. Subtropical moisture is least divergent over the Pacific basin, which is the smallest moisture source (per unit area) for global land areas. Basins also differ in how subtropical moisture sources are partitioned between tropical, midlatitude, and land regions.

Next, we use the same matrix operator framework to study the aerial hydrological cycle

response to quasi-equilibrium CO_2-doubling. The total change in precipitation is separated into contributions from changes in moisture transport and changes in evaporation, and these, in turn, are further separated into changes due to local moisture divergence and remote moisture convergence. While increased surface evaporation increases precipitation everywhere, changes in moisture transport are necessary to create a spatial pattern where precipitation decreases in the subtropics and increases substantially at the equator. This finding agrees broadly with other findings that have emphasized the role of both surface thermodynamics and transport in determining precipitation changes. Overall, changes in the convergence of remotely-evaporated moisture are more important to the overall precipitation change than changes in the amount of locally-evaporated moisture that precipitates in situ. Further decompositions show that CO_2-doubling increases the fraction of locally-evaporated moisture that is exported, enhances moisture exchange between ocean basins, and shifts moisture convergence within a given basin towards greater distances between moisture source (evaporation) and sink (precipitation) regions. These changes can be understood in terms of the increased residence timescale of water in the atmosphere with CO_2-doubling, which correspond to an increase in the advective length scale of moisture transport. As a result, the distance between where moisture evaporates and where it precipitates increases. Analyses of several heuristic models further support this finding. We conclude by discussing implications of our findings, including effects of changing atmospheric moisture transport on ocean circulation and interpretation of water isotope proxy records.

Finally, we investigate the role of atmospheric moisture transport in maintaining the high salinity of surface waters in the tropical Atlantic basin. Two independent observational estimates show a 0.5 Sv freshwater deficit over the Atlantic drainage basin, and moisture flux calculations from the ERA interim observational reanalysis shows that at least half of this deficit is due to moisture export from the subtropical Atlantic basin, over the Panama Isthmus, into the tropical Pacific. Global Climate Model (GCM) experiments with water

tracers show that most moisture exported from the Atlantic to the Pacific originates between the equator and 30N, with a significant maximum in the 10N to 20N latitude band. Analysis of the CMIP5 abrupt CO_2-quadrupling experiment shows striking intermodel agreement between decreased Atlantic drainage basin freshwater input (approximately 0.1 Sv in the multimodel mean) and increased tropical Atlantic sea surface salinity. GCM water tracer experiments reveal that enhanced Atlantic-to-Pacific moisture transport in a quasi-equilibrium CO_2-doubling experiment is responsible for approximately one-quarter of the precipitation increase over the equatorial Pacific, resulting in freshening of the Pacific basin and salinizing of the Atlantic. Most of this increased Atlantic-to-Pacific moisture export originates between the equator and 30N in the Atlantic. This intensification of the interbasin moisture flux is due to altered transport attributable to increased atmospheric specific humidity; this results in increased moisture residence time scales and advective length scales, favoring longer distances between moisture source and sink regions. Implications of these findings are discussed.

TABLE OF CONTENTS

LIST OF FIGURES

LIST OF TABLES

ACKNOWLEDGMENTS

Thanks to my advisor, Cecilia Bitz, for her support and advice throughout my graduate career. Thanks to collaborators and friends Aaron Donahoe, Emily Newsom, Jesse Nusbaumer, David Noone, Phil Rasch, and Dennis Hartmann for all their brainpower. Thanks to Chris Bretherton, for useful perspectives and feedback on this work. Thanks to current and past graduate students Naomi Goldenson, Judy Twedt, Ana Ordonez, Angie Pendergrass, Paul Hezel, Kelly McCusker, and Ed Blanchard-Wrigglesworth for their friendship, kindness, and wisdom. Thanks to Graduates '09 for their comraderie. Thanks to the wonderful Atmospheric Sciences Department at the University of Washington for its support and accommodations. Thanks to Scott Sipes for kindness and cookies. Thanks to Marc Michelson for brilliant computing support. Thanks to Randy LeVeque and the UW Applied Mathematics department for brilliant mathematical teaching. Thanks to both the National Science Foundation and Department of Energy for graduate funding.

And thanks to my partner Aaron and my sister Nansi, for believing in me.

DEDICATION

For Aaron Bee, who never doubted that I could get here. And for Ambrose, Stella Mae, and Zyanya, who are always inspiring me to do more.

VITA

Hansi A. Singh is currently a resident of Seattle, Washington, where she lives with her partner and three children. In her past lives, she has taught mathematics and science, written a book on knitting amigurumi, raced motorcycles, and danced professionally. Her current non-science obsessions are dressmaking and bicycling.

Chapter 1

INTRODUCTION

The Earth's climate arises from interconnected processes, an intricate branching of the atmosphere, ocean, ice, and solid earth that plays out over a range of spatial scales, from molecular to planetary, and a range of time scales, from hourly to the lifetime of the planet. Not surpisingly, our understanding of these connections is a work-in-progress, evolving as modeling, observations, and theory incrementally unveil the breadth of this interconnectedness.

The connections between different components of the Earth system, and how these connections affect climate, has only recently been appreciated. While atmospheric general circulation models have always relied on ocean boundary conditions, dynamic coupling between the atmosphere and ocean has only been studied with vigor over the past two decades. Much of this reliance on atmosphere-only modeling as predictor of the climate system has resulted from pragmatic considerations, namely that running ocean models concomittantly with atmospheric ones requires computing resources well out of range of what was available until relatively recently. These studies of atmosphere-ocean coupling reveal how essential these interactions are for the climate mean state, variability, and the perturbation response. While both the atmosphere and ocean can be understood as separate entities themselves, it is only through their interaction on many different spatial and time scales that the climate system responds to perturbations.

More recently, coupled atmosphere and ocean models have evolved into comprehensive Earth system models, which incorporate sea ice, land, vegetation, ocean biogeochemistry, and ice sheets. As Earth system models become more complex and demand even more computing

resources, the full extent of the connectedness of the climate system, both local and remote, has become more apparent. At the same time, the output of these complex models has become increasingly difficult to interpret. Models have tended towards a black box in which cause and effect, correlation and causation, attribution and association, become hopelessly confounded. To counter this tendency towards greater complexity but less insight, experiments with Earth system models must be devised methodically and specifically. Moreover, their results must be interpreted in the context of mechanisms, particularly how thermodynamics, dynamics, and coupling between system components. Such care in experimental design and scrutiny of mechanisms allows for significant advances in our understanding the workings of the climate system.

Amid this mounting complexity, there are two fundamental principles that can serve as a framework for understanding planetary climate, including coupling between its components and its response to perturbations: energetics and transport. First, energy is the driving force of the climate system, and, in steady-state, solar input is balanced by radiative heat loss to space. Energy is transferred between the atmosphere and ocean through radiative, sensible, and latent heat fluxes. Any changes in the distribution of energy will alter the thermodynamic drivers of the general atmospheric and oceanic circulation, and thereby alter the circulation itself. In other words, both the atmosphere and ocean circulation respond to perturbations in this energy input, which subsequently perturbs energetics itself.

Second, both the atmosphere and ocean act in concert to transport energy, with transport by the atmosphere subdivided into dry and moist components. The transport of moisture and energy, which is made possible by the general circulation, acts to decrease the magnitude of local perturbations while increasing their remote impact. As changes in atmospheric and oceanic transport alter the distribution of energy and moisture, the circulation may also adjust in response. While the total change in energy transport may be determined by energetics, the relative changes in atmospheric and oceanic transport are determined by their coupling, through heat, moisture, and momentum. Thus, energetics and transport, which are crucial and linked, can serve as an effective framework for understanding how the mean

state climate arises and how it responds to perturbations.

In the ensuing chapters of this dissertation, we use the framework of transport and energetics to gain insight on the interconnectedness of the climate system and its many components. This thesis is organized as follows. In Chapter 2, we investigate the impact of the high orography of the AIS on the climate system. Chapter 3 explores atmospheric moisture transport in the preindustrial mean state, while Chapter 4 explores how atmospheric moisture transport changes in a doubled-CO_2 climate. Chapter 5 considers the impact of atmospheric freshwater export on the salinity of the Atlantic basin in the preindustrial mean state and with warming. Finally, we outline some succinct conclusions from our work in Chapter 6, and discuss directions for future research in Chapter 7.

1.1 Orography-Driven Teleconnections from Poles to Tropics

The tropics and midlatitudes undoubtedly impact polar climate, both in the mean state and its variability on many time scales. Moisture transported from the extratropics provide much of the moisture for high latitude precipitation in winter (see, e.g., Johnsen and White, 1989; Ciais et al., 1995). Rossby waves transport energy from the tropical Pacific to the both the Arctic and Antarctic during the warm phase of the El Niño Southern Oscillation (ENSO) (see, e.g., Mysak et al., 1996; Gloersen, 1996; Ding et al., 2011), causing synoptic disturbances that affect local weather, sea ice, and ice sheet mass balance. These connections from extrapolar to polar regions are not surprising, given that the general circulation transports both atmospheric moist static energy and oceanic heat poleward.

Understanding teleconnections from polar to extrapolar regions, however, remains a less established and more elusive enterprise. Nevertheless, it is clear that large-scale features in the polar regions, like Arctic sea ice, the Greenland Ice Sheet, and the Antarctic Ice Sheet (AIS, elevation from satellite observations shown in Figure 1.1), are characteristic of the current climate state. Furthermore, past climate states have seen different configurations of these polar features, with warmer (or cooler) climates of the past characterized by less (or more) extensive polar ice. The fundamental question to be answered is the extent to which

these large-scale polar features create the global climate state in which they are found, and the extent to which positive or negative feedbacks mediated by these features themselves act to destabilize or stabilize polar ice, respectively.

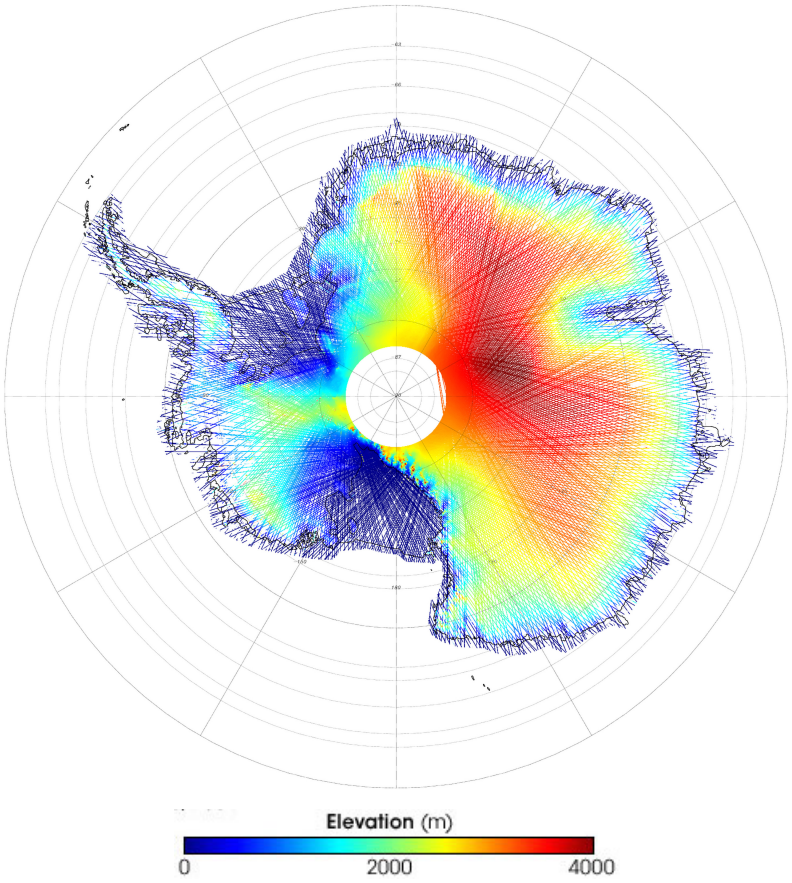

Figure 1.1: Elevation map of the Antarctic Ice Sheet. Data obtained from observations from NASA's Ice, Cloud, and Land Elevation Satellite (ICESat), Goddard Space Flight Center. Data collected between October 3 to November 8, 2004.

In Chapter 2 of this thesis, we consider the extent to which perturbations to the height of the AIS affect the global mean climate, and show that the presence of the AIS creates a climate state that is amenable to its persistence. From the results of a state-of-the-art GCM, we present an analysis of the global climate system response to lowering the AIS to 10% of its preindustrial elevation, while keeping all other parameters, including surface

albedo, identical to that in the preindustrial mean state. We find a range of local and remote responses that accompany the lowering of the ice sheet, including net global cooling. Indeed, we find that the largest response to lowering of the AIS may be found over the Arctic, where sea ice expands and temperatures plummet. From our analysis, we conclude that the polar regions do, in fact, have the ability to affect the global climate state substantially, and that the most remote of these connections are mediated by changes in oceanic energy transport. We find that lowering of the AIS drives global cooling which acts as a modest negative feedback on any processes that would act to lower AIS orography.

1.2 Evaporation, Precipitation, and Moisture Transport

Over 70% of the surface of our planet is covered by water, both liquid and ice. The presence of liquid water on our planet's surface shapes the climate in important ways, altering energy balance through surface albedo and allowing energy to be transported from equator to pole. Furthermore, the substantial concentration of water vapor in the atmosphere, at equilibrium with its surface reservoisr, further affects the climate system, by altering both longwave and shortwave radiative transfer, and transporting energy through latent heating. The latter is the fundamental means by which the hydrological cycle is linked energetically to global climate.

Figure 1.2 shows the precipitation and evaporation, both in the annual mean and seasonally, from CESM1.2 (Hurrell et al., 2013), a state-of-the-art global climate model (GCM). The importance of moisture transport is highlighted by the substantial spatial differences between the two: the evaporation field is diffuse and decreases gradually from equator to pole while the precipitation field displays sharp spatial features. While the source regions of moisture are diffuse and result from the surface energy available for evaporation, the sink regions are sharp and well-defined, and are a result of dynamic processes that converge and diverge moisture heterogeneously. Thus, in the mean state, all precipitation is a result of evaporation, but the distinctive spatial pattern of precipitation is determined by moisture transport.

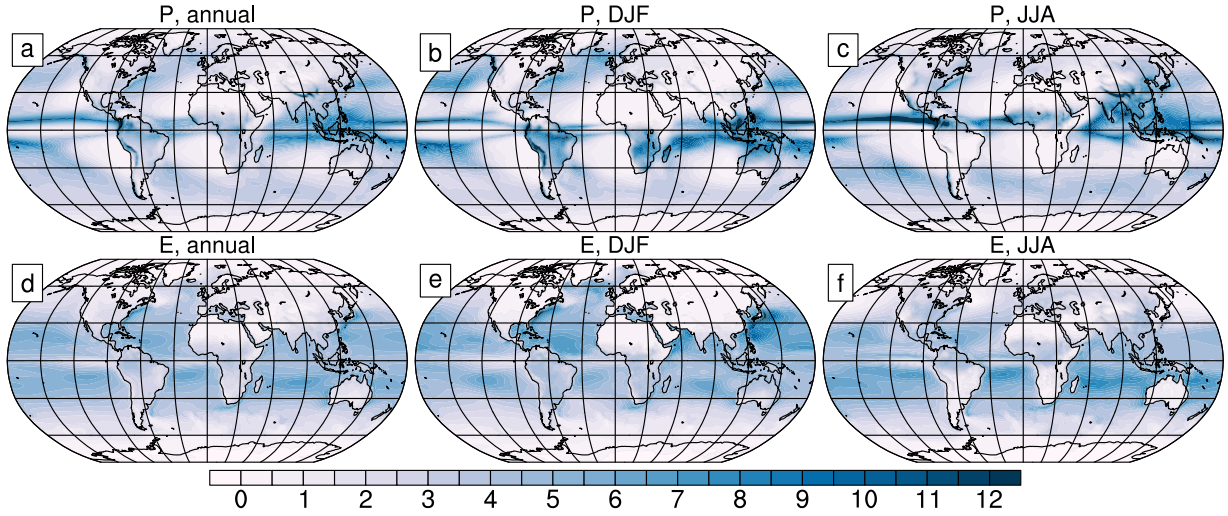

Figure 1.2: Precipitation (a-c) and evaporation (d-f) in the Community Earth System Model version 1.2 (CESM1.2) preindustrial mean state, in mm day^{-1}. Quantities are shown in the annual mean (a, d), DJF (b, e), and JJA (c, f).

In Chapter 3, we analyze how moisture transport acts to shape the diffuse spatial pattern of evaporation into the distinct spatial pattern of precipitation. To do this, we use CESM1.2 in which water tags have been implemented, which allows us to track water as it evaporates from the surface, through transport and phase changes, to its point of precipitation. We develop a novel matrix operator framework for systematically analyzing this moisture transport, from evaporation (or sublimation) to precipitation, and use it to analyze the mean state precipitation, both in the annual mean and seasonally. The matrix operator framework allows us to analyze the local and remote contributions to the precipitation. The remote contribution to the precipitation may be further subdivided into an arbitrary number of subcomponents, including meridional, zonal, intrabasin, and interbasin parts. The tags used in the experiment, which separate evaporative source regions by basin and by 10° latitude bands, allows study of the differences between the major ocean basins as moisture source and sink regions.

In Chapter 4, we investigate how quasi-equilibrium CO_2-induced warming affects precip-

itation by conducting a second GCM experiment with water tags in which CO_2 is doubled from its preindustrial level. Using the matrix operator framework developed in Chapter 3, we subdivide the precipitation change into a part due to increasing evaporation, and a part due to changing transport. Then, to understand how such a large portion of the change in precipitation can be due to changing transport, given that the atmospheric general circulation only responds minimally to CO_2-induced warming, we perform several other decompositions of the precipitation change. With the aid of these experiments, and with the use of a heuristic box model, we arrive at a fundamental understanding of how moisture transport changes shape the hydrological cycle response to CO_2, namely that the advective length scale of moisture transport lengthens as the planet warms. We find that changes in moisture transport are not necessarily attributable to changes in circulation, but may be due to this fundamental change that characterizes the climate response to warming due to greenhouse gases.

1.3 The Atmosphere as Driver of Basin-Wide Salinity

Interactions between the atmosphere and ocean take many different forms. One way by which atmosphere-ocean coupling occurs is through atmospheric freshwater input into the ocean. The aerial component of the hydrological cycle, particularly surface precipitation and evaporation, affect the freshwater balance of the ocean on a basinwide scale, thereby affecting salinity. Changes in seawater salinity, which impact density, have the potential to affect the circulation, through changes in steric height, density gradients, and baroclinicity.

The Atlantic and Indo-Pacific differ drastically in their salinity (Figure 1.3), with the salinity of the Atlantic basin exceeding that of the Indo-Pacific by over 1.0 at most depths above 1000 meters north of the equator. The north Atlantic is the only site of deep water formation in the northern hemisphere, and the high salinity of Atlantic may be a necessary condition for deep water formation. While the aerial hydrological cycle has been implicated in the high salinity of the Atlantic relative to the Indo-Pacific (Broecker, 1991; Zaucker and Broecker, 1992), the details of this salinization mechanism have not been thoroughly investigated.

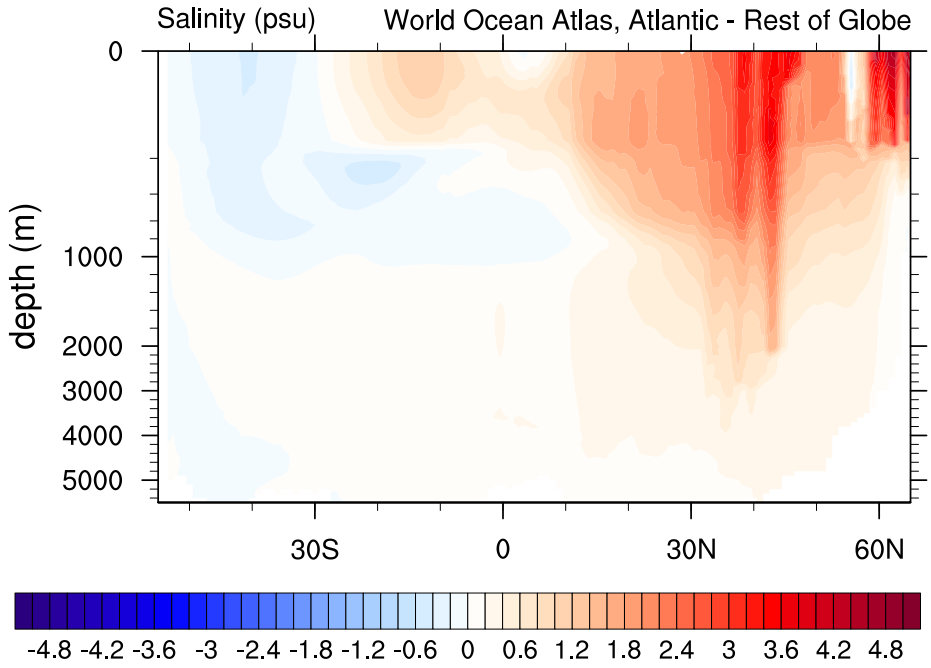

Figure 1.3: Salinity difference (in psu) between the Atlantic basin and the Indo-Pacific, as seen in the observational record. Data from the World Ocean Database, Boyer et al. (2013).

In Chapter 5, we use GCM experiments with water tags to describe the mechanism by which atmospheric freshwater export from the Atlantic to the Indo-Pacific engenders the mean-state salinity difference between these basins. We further consider how this atmospheric freshwater export changes in a high-CO_2 scenario, and show that the changes in interbasin moisture exchange may be explained by fundamental changes in the hydrological cycle with warming. We find that the robust intensification of the Atlantic to Indo-Pacific interbasin salinity contrast in high-CO_2 experiments conducted for the fifth phase of the Climate Model Intercomparison Project (CMIP5) supports our finding that fundamental changes in the hydrological cycle accompany CO_2-induced warming, and that some of the consequences of this shift are evident in the CMIP5 model experiments.

Chapter 2

THE GLOBAL CLIMATE RESPONSE TO LOWERING SURFACE OROGRAPHY OF ANTARCTICA AND THE IMPORTANCE OF ATMOSPHERE-OCEAN COUPLING

2.1 Introduction

Antarctica is among the largest plateaus on Earth, and its ice cover (and, consequently, surface orography) has fluctuated dramatically even while it has occupied its polar position. In this study, we investigate how the orography of the Antarctic Ice Sheet (AIS) influences the Earth's climate system. We use a coupled atmosphere, ocean, land, and sea ice model (i.e., fully-coupled) to study how local and remote responses to orography removal are facilitated through energy balance requirements and global teleconnections.

Orography can affect the local angular momentum balance of the atmosphere, altering the winds at the surface and aloft, the jet and mid-latitude storm track, and climate variability. Steering by orography affects the position of major atmospheric features, including arid zones and monsoonal circulations. Many studies have investigated midlatitude orographic influences on climate, focusing on that of the Andes, Himalayas, and Rockies (see, e.g., Manabe and Terpstra, 1974; Hahn and Manabe, 1975; Manabe and Broccoli, 1990; Seager et al., 2002; Takahashi and Battisti, 2007). The climate impact of the orography from the Laurentide and Fennoscandian Ice Sheets at the Last Glacial Maximum has also been studied extensively, starting with Manabe and Broccoli (1985).

While the Antarctic continent assumed its polar position nearly 100 million years before present (mya), the initial glaciation of Antarctica occurred over the Eocene-Oligocene boundary (33 mya). This glaciation was concurrent with the isolation of the continent as the Drake passage opened and circumpolar ocean flow commenced (Kennett, 1977), suggest-

ing a strong association between ocean circulation and the AIS from the start. A decrease in atmospheric CO_2 levels and changes in orbital parameters that favored cooler Southern Hemisphere (SH) summers are other factors that may have contributed to this initial glaciation (DeConto and Pollard, 2003). Over the past 5 million years, proxy evidence (Scherer, 1991; Lisiecki and Raymo, 2005) and modeling studies (Pollard and DeConto, 2009) suggest that the West Antarctic Ice Sheet has been particularly sensitive to changes in orbital parameters and fluctuations in atmospheric greenhouse gas concentrations (see the review by de Q. Robin, 1988, and references therein).

Indeed, many modeling studies have simulated past (and future) climates in which the orography of the AIS has been (or is projected to be) substantially lower than at present. Goldner et al. (2014) used a GCM with an Oligocene-Eocene configuration of continents, sea level, and solar insolation to study the initial glaciation of Antarctica 34 mya. They found that a modest decline of CO_2 that, in turn, initiated the expansion of land ice over Antarctica, was sufficient to invigorate the ocean circulation and cause the dramatic changes in ocean hydrography, surface winds, and deep water formation as seen in paleo-proxy data. Opening of the Drake Passage or Tasman Gateway, on the other hand, did not produce such a similar rapid reorganization of the ocean circulation and hydrography. Knorr and Lohmann (2014) used GCM time-slice experiments to study the Middle Miocene transition 13 mya, which was characterized by global cooling and expansion of the AIS to nearly its present-day volume. They found that on 100,000-year timescales, the response of their model's winds, surface temperature, sea ice, and ocean circulation due to AIS expansion alone was consistent with paleo-proxy data. Only on million-year timescales and longer was atmospheric CO_2 drawdown necessary in their model to cause the global cooling seen in paleo-proxy data.

These and other paleoclimate modeling studies provide interesting insights on the impact of AIS orography on the Earth climate system, and suggest that AIS orography may affect the ocean circulation. Nevertheless, these studies do not isolate the effect of lowered orography on the climate system from other competing factors, including changes in continental

configurations, orbital parameters, greenhouse gas concentrations, and meltwater fluxes.

On the other hand, a few studies have considered the impact of AIS orography on global climate in atmosphere-only GCMs (AGCMs) without such confounding factors. Several of these found enhanced poleward energy transport with lowered AIS orography (Mechoso, 1981; Parish et al., 1994; Walsh et al., 2000; Ogura and Abe-Ouchi, 2001), enhanced poleward momentum transport (Mechoso, 1980, 1981; Parish et al., 1994; Simmonds and Law, 1995; Walsh et al., 2000), decreased cyclogenesis over the Southern Ocean (Mechoso, 1980, 1981; Simmonds and Law, 1995; Walsh et al., 2000), and a weakening and poleward shift of the region of maximum baroclinicity (Mechoso, 1980, 1981; Parish et al., 1994; Simmonds and Law, 1995; Quintanar and Mechoso, 1995; Walsh et al., 2000). While most of these studies used prescribed SSTs, Ogura and Abe-Ouchi (2001) showed that the local atmospheric circulation response to removing Antarctic orography tends to be similar but weaker when an AGCM is coupled to a mixed-layer ocean rather the same AGCM with prescribed SSTs. Further, the significant surface wind response found in all of these experiments, given the sensitivity of Southern Ocean circulation and Antarctic sea ice to surface wind forcing, motivates further study of this problem using models that can capture dynamical coupling with the ocean.

As far as we know, the only study that has isolated the climate impact of AIS orography in a fully-coupled GCM is Justino et al. (2014). However, the results of Justino et al. (2014) are surprising. Unlike many previous studies that have linked increased poleward energy transport with flattening of the AIS (e.g. Mechoso, 1981; Parish et al., 1994; Walsh et al., 2000; Ogura and Abe-Ouchi, 2001), Justino et al. (2014) found that the poleward energy transport in the SH decreased when the AIS was lowered by 25%. It is unclear whether this major discrepancy can be attributed to the use of a fully-coupled GCM by Justino et al. (2014), or if the amount the AIS was lowered was a factor.

In this study, we isolate the climate impact of lowering AIS orography in both a fully-coupled GCM and a companion model with a mixed-layer only (slab) ocean. Our strategy allows us to investigate the important role of ocean dynamics on the climate response to

lowering the AIS.

As expected, we find that lowering the AIS (while leaving the surface albedo unchanged) results in local surface warming of Antarctica. In addition, we find a range of remote effects on winds at the surface and aloft, equatorial precipitation, the ocean's meridional overturning and surface gyre circulations, and sea ice in both hemispheres. We find that the scope of these global changes can be understood in terms of energy balances maintained by oceanic and atmospheric energy transports.

2.2 Experimental Setup

To explore the climate impact of lowering AIS orography, we performed a fully-coupled simulation using the Community Climate System Model 4.0, CCSM4 (Gent et al., 2011). The atmosphere component has a finite-volume dynamical core, a horizontal resolution of 1.9°× 2.5°, and 26 vertical levels. The horizontal grid of the land component is the same as that of the atmosphere. The ocean and sea ice lie on a nominally 1° resolution displaced-pole grid, with the north pole singularity centered within Greenland. The ocean eddy parameterization is a Gent and McWilliams (GM) form (Gent and McWilliams, 1992), with the GM coefficient varying in space and time (Danabasoglu et al., 2012). The sea ice is fully thermodynamic and dynamic (Hunke and Lipscomb, 2008).

As a baseline for comparison, we use a pre-industrial control simulation with the CCSM4 run at the same resolution, hereafter referred to as C, in which ozone, carbon dioxide and other greenhouse gases, volcanic constituents, and solar insolation are all held fixed at pre-industrial levels (see Table 2.1). The experimental Flat Antarctic run (hereafter referred to as FA) branched from C at year 700 and had all parameters set as in C, but with the orography of Antarctica replaced by one in which the elevation is 10% of the original (present-day) value (see Figure 2.1 for the elevation anomaly). We ran FA for 230 years, to quasi-equilibrium. Results are presented as climatologies of the final 30 years of the simulations (years 900–929 for C and 200–229 for FA). The net annual top-of-atmosphere flux imbalance in the climatologies is 0.13 W/m^2 for FA and 0.05 W/m^2 for C.

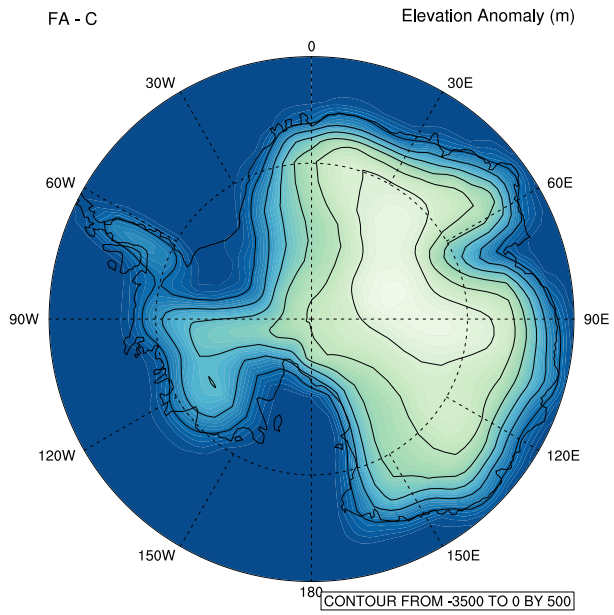

Figure 2.1: Elevation anomaly, in meters, imposed over Antarctica in the FA and FASOM experiments, expressed as the difference FA - C. Contours are drawn from 500 m to 3000 m at intervals of 500 m.

Table 2.1: Summary of preindustrial settings (solar insolation, greenhouse gas concentrations, and aerosol forcing) used in all simulations.

Constituent	Concentration or Value	Notes
Total Solar Irradiance	1360.9 W/m^2	mean of 1844 to 1856 irradiance
CO_2	284.7 ppm	
N_2O	275.7 ppb	
CH_4	791.6 ppb	
Aerosol Forcing	-0.033 W/m^2	equivalent aerosol forcing

We isolate the the role of ocean dynamics in the climate response to lowering the AIS by comparing results from fully-coupled C and FA simulations to results from a pair of runs where we replace the ocean GCM with a slab ocean model (known hereafter as SOM). All other model components are otherwise identical. The control and flat Antarctic experiments with the SOM (known hereafter CSOM and FASOM) differ from one another only in their AIS surface orography, with the same surface orography anomaly in FASOM as in FA. In both SOM runs, the ocean energy transport flux convergence field (often called q-flux) was prescribed to be annually periodic but spatially heterogeneous from a monthly climatology derived from C (Bitz et al., 2012). Results are presented as climatologies of the final 30 years of 60-year runs, which can be considered to be at equilibrium.

We present the response to lowering AIS as the anomaly FA minus C in §3a through §3e. The role of ocean dynamics is investigated by comparing FA minus C with FASOM minus CSOM in §3f.

2.3 Results

2.3.1 Temperature Response and Energy Balance

The local response to lowering AIS orography is a strong surface warming over most of East Antarctica and a mixed pattern of warming and cooling over West Antarctica. Remote surface cooling away from the AIS dominates the global mean surface temperature,

however, which decreases by 0.3 °C (see Figures 2.2a and 2.2b). In the zonal mean, the atmosphere above the AIS warms from the troposphere to the stratosphere, while cooling over the Southern Ocean and in the Northern Hemisphere (NH) high latitudes remains confined to the surface and mid-troposphere (Figure 2.2c).

At top-of-atmosphere (TOA), the outgoing longwave radiation (OLR) increases substantially over the AIS (Figure 2.3a), driven by a temperature increase at the effective radiating level; this result is similar to that described by Ogura and Abe-Ouchi (2001). Although the AIS surface albedo is prescribed as that for a glaciated surface irrespective of elevation, the TOA absorbed shortwave (ASW) increases over the AIS because the warmer and deeper (by way of greatly increased surface pressure) atmosphere has much more precipitable water (not shown). Overall, the OLR increase wins out, and a larger amount of energy is lost to space over the AIS in FA. Partitioning the energetic fluxes between clear-sky and all-sky conditions shows that the TOA radiation anomalies over the AIS are predominantly clear-sky. While an increase in low clouds plays a minor role in enhancing the OLR anomaly and diminishing the ASW anomaly, the TOA net radiative response due to clouds is modest (< 10 % of the total anomaly in the zonal mean). The enhanced energy loss to space over the continent implies that there must be anomalous southward energy transport (as shown in Figure 2.4a).

The increased greenhouse effect of the warmer and deeper atmosphere increases the downwelling longwave (LW) radiation over the AIS. The warming at the surface is unable to offset this effect and the net upward LW radiation decreases sharply (Figure 2.3b). The surface ASW decreases, though by a smaller amount, due to increased atmospheric absorption. An increase in the (upward) sensible heat flux balances these surface radiative changes.

Enhanced cooling to space over the AIS in FA drives anomalous southward energy transport in both atmosphere and ocean in the SH (Figure 2.4a). This increase in southward energy transport near 60° S is a source of dynamical warming that augments the simple adiabatic warming due to lowering the AIS. The positive slope of the total energy transport anomaly from 60° S to 40° N (Figure 2.4a) implies dynamical cooling throughout these latitudes.

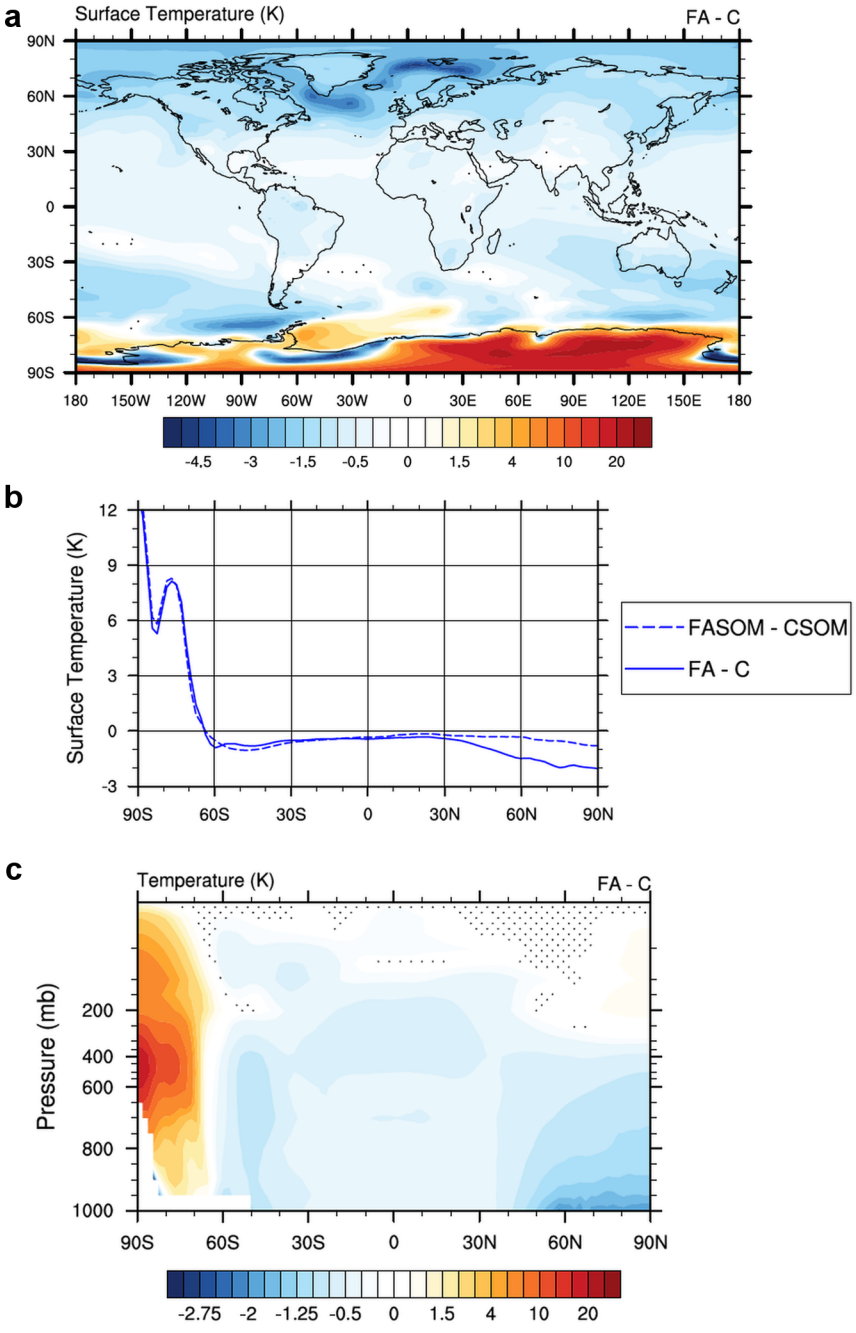

Figure 2.2: Temperature response to lowering the AIS: **(a)** surface temperature in FA - C; **(b)** zonally-averaged surface temperature in FA - C and FASOM - CSOM; **(c)** zonally-averaged atmospheric temperature in FA - C. Stippled areas in the top and bottom panels indicate regions where the temperature anomaly is not statistically significant at $p < 0.05$. Note that positive and negative anomalies have been scaled asymmetrically to make negative anomalies more discernible.

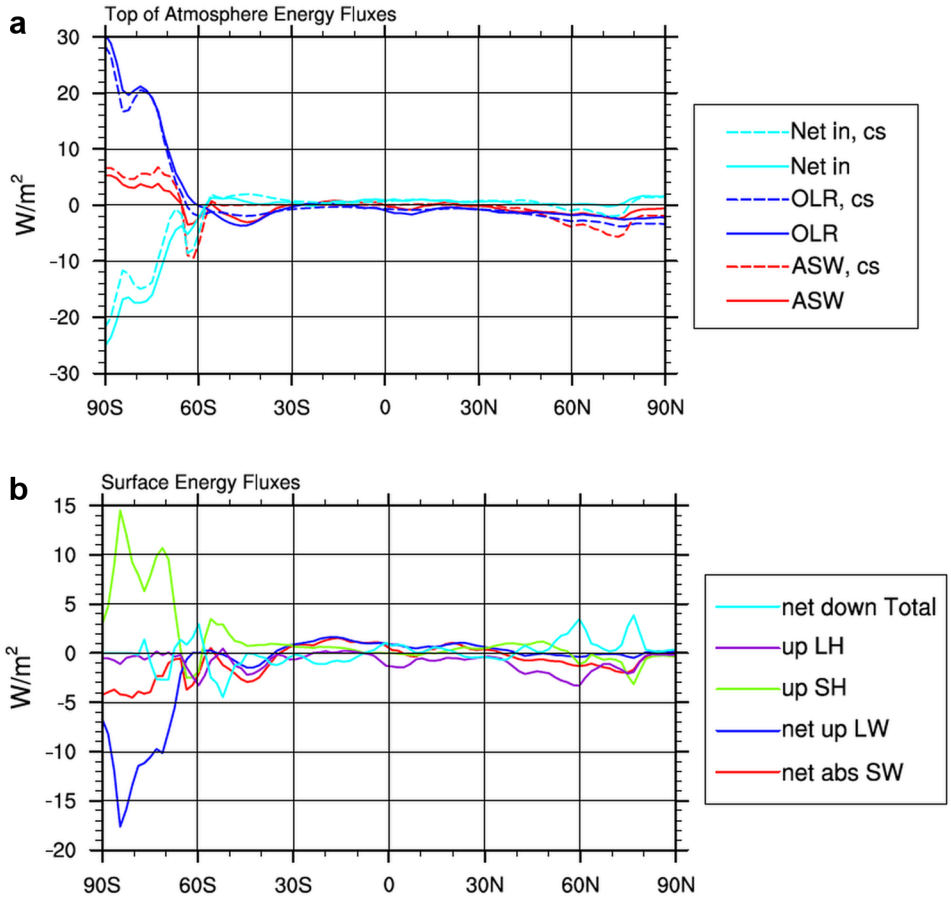

Figure 2.3: Energetic response to lowering the AIS, expressed as the anomaly FA - C: **(a)** clear-sky (cs) and all-sky outgoing longwave radiation (OLR), absorbed shortwave radiation (ASW), and net incoming radiation at top-of-atmosphere; and **(b)** net upward longwave radiation (net up LW), net absorbed shortwave radiation (net abs SW), upward sensible heat flux (up SH), upward latent heat flux (up LH), and net downward energy flux at the surface. Note that all fluxes are reckoned positive upward except the SW and net anomalies.

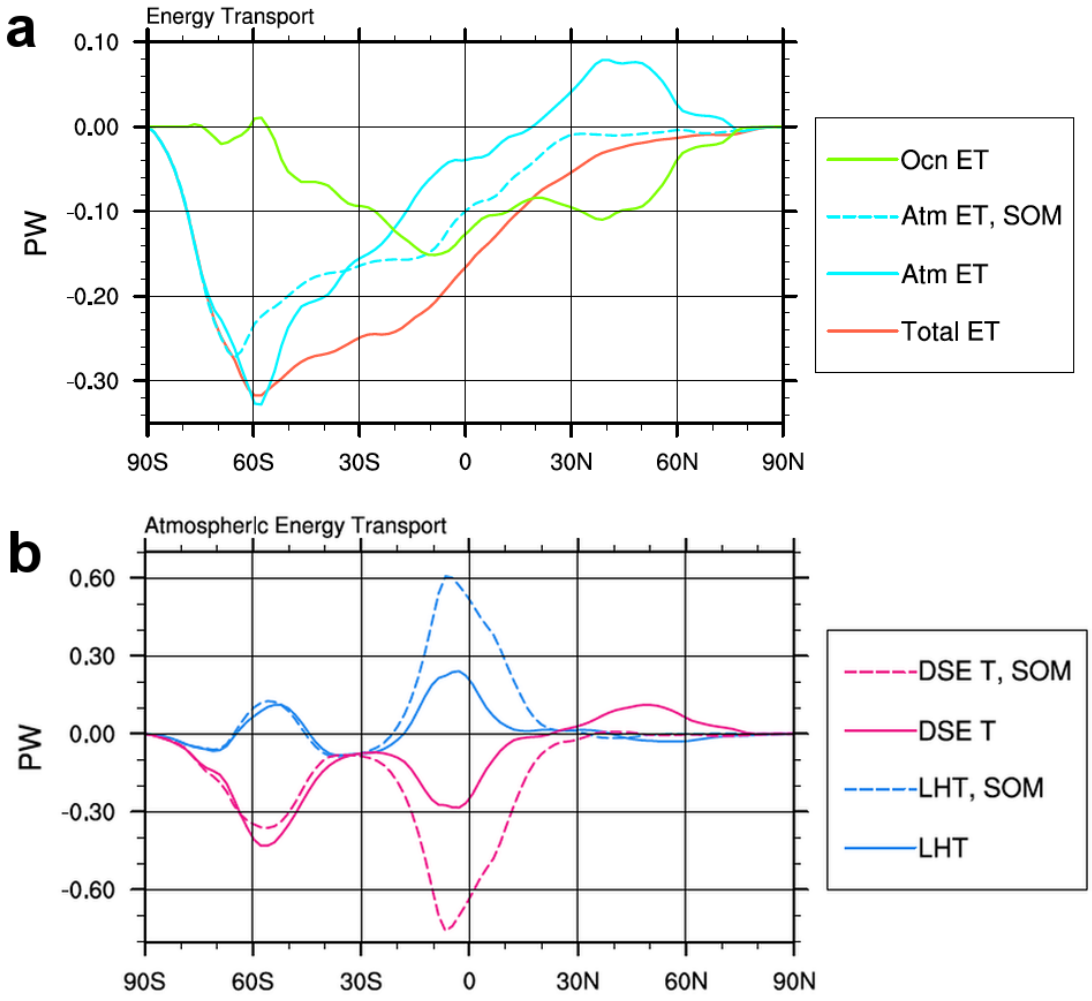

Figure 2.4: Energy transport response to lowering the AIS (in PW), expressed as the anomaly FA - C or FASOM - CSOM: **(a)** total, atmospheric, and oceanic northward energy transport response; and **(b)** breakdown of atmospheric northward energy transport response into dry static energy transport (DSE T) and latent heat transport (LHT).

The partitioning of the total energy transport anomaly between the ocean and atmosphere varies with latitude. In the SH high and middle latitudes, the atmosphere dominates, while the ocean transports most of the energy northward of 20° S. The direction of the atmospheric energy transport anomaly reverses around 20° N. Note that atmospheric and total energy transports are calculated implicitly, with total energy transport computed from integrating (in latitude) the net TOA energy fluxes, and atmospheric energy transport computed by integrating the difference between the TOA and surface energy fluxes. The oceanic energy transport is computed directly as a global integral of $V\theta$, where V is the meridional ocean velocity and θ is the potential temperature.

Southward atmospheric energy transport increases primarily due to increasing southward dry static energy (DSE) transport at all latitudes south of 20° N, with latent heat (LH) transport weakly opposing the atmospheric energy transport anomaly at most latitudes (Figure 2.4b). LH transport is northward from 65° S to 45° S, and from 20° S to 10° N; the former suggests both a northward shift in the midlatitude storm track and a decrease in poleward eddy moisture transport (due to decreased specific humidity with cooler temperatures), while the latter suggests a northward shift in the rising branch of the Hadley circulation. Indeed, the response of the SH storm track and Hadley circulation is also evident in the atmospheric sensible heat transport anomaly (Figure 2.7d) and the global precipitation response (Figure 2.10), which we address further in §3b and §3e.

2.3.2 Atmospheric Circulation Response

Lowering the AIS alters the SH atmospheric circulation, which is evident in the zonal wind field (Figure 2.5a). In FA, both the polar vortex and eddy-driven jet weaken on their poleward sides, the low-level easterly winds south of 65° S de-accelerate, and the surface and mid-tropospheric westerlies from 60° to 65° S accelerate slightly. At the surface, westerly winds decrease to the north and increase to the south of 60° S (Figure 2.5b), decreasing the wind stress curl over the Southern Ocean.

Eddy-driving of zonal wind changes are assessed using the transformed Eulerian mean

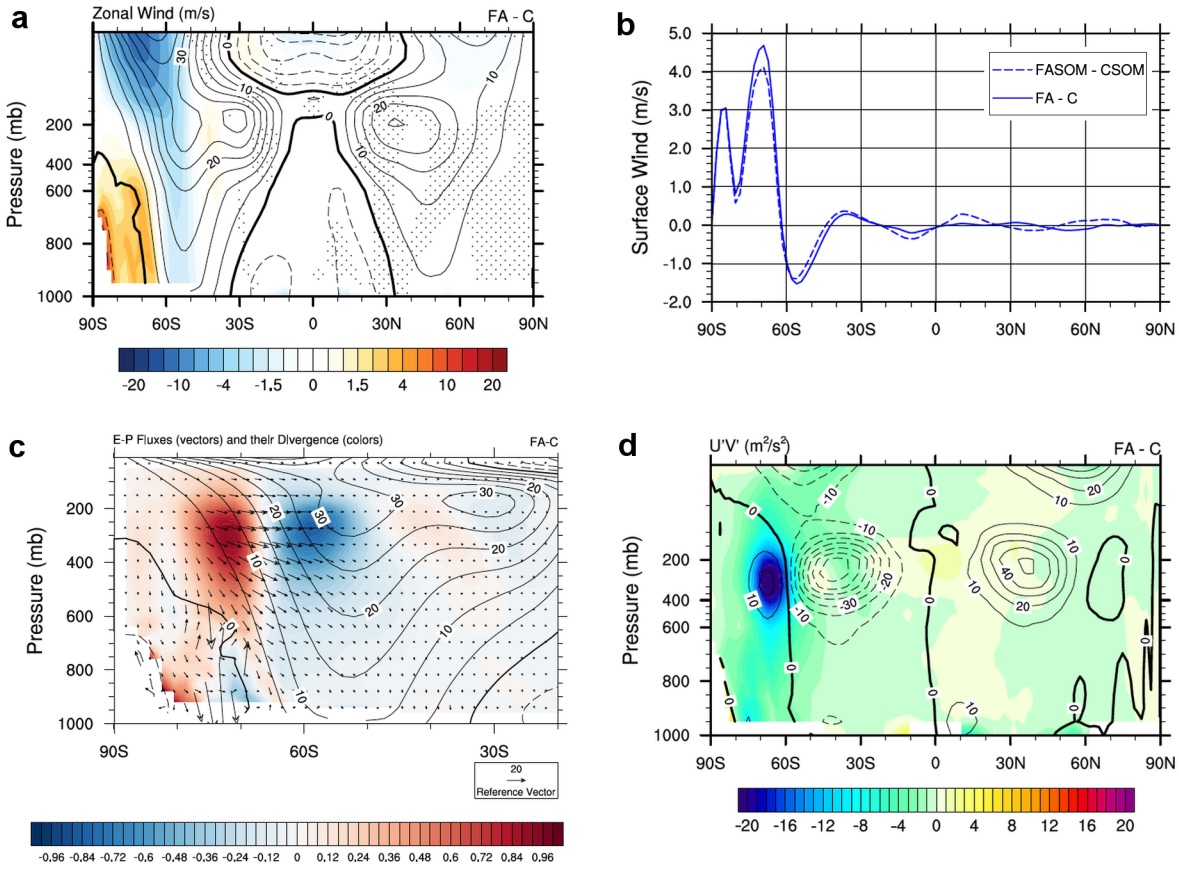

Figure 2.5: Annually- and zonally-averaged momentum and zonal wind response to lowering the AIS: **(a)** zonal wind (in m/s); **(b)** surface winds in FA - C and FASOM - CSOM; **(c)** E-P fluxes (in $m^2\ s^{-2}$, arrows) and their divergence (in $m\ s^{-2}$, colors) in FA - C, with zonal winds (contours) in C; and **(d)** eddy momentum flux $\overline{U'V'}$ (in $m^2 s^{-2}$); . In panels (a) and (d), the contours depict the mean state C (with the zero contour thickened and negative contours dashed) and colors depict the anomaly FA - C. In panel (a), stippled areas indicate regions where the anomaly is not statistically significant at $p < 0.05$.

framework, where the effect of eddies on the mean flow is analyzed using the Eliassen-Palm (E-P) flux vectors $\vec{F}$ (see Holton, 1992) given by

$$\vec{F} = \left(-\overline{u'v'},\ \frac{f_0 R}{N^2 H} \overline{v'T'} \right) \ , \tag{2.1}$$

where $\overline{u'v'}$ is the meridional flux of zonal momentum by eddies, $\overline{v'T'}$ is the meridional flux of sensible heat by eddies, f_0 is the Coriolis parameter, R is the gas constant for dry air, N^2 is the Brunt-Vaisala frequency, and H is the atmospheric scale height. Figure 2.5c shows the effect of lowering the AIS on the E-P flux, and Figure 2.5d shows the effect on the horizontal component of the E-P flux, the meridional flux of zonal momentum by eddies. A strong decrease in the E-P flux divergence is evident at the poleward edge of the eddy-driven jet, consistent with its weakening (Figure 2.5c). Figure 2.5d suggests that much of this decrease in the E-P flux divergence is due to an increase in the meridional eddy momentum flux divergence. Similarly, the increase in the E-P flux divergence south of 65° S is mostly due an increase in the meridional eddy momentum flux convergence; since the E-P flux divergence is negative here in C (not shown), eddies cannot de-accelerate the mean flow in this region in FA, consistent with a modest increase in the westerly winds here (Figure 2.5a).

The absence of katabatic flow in FA helps weaken the SH eddy-driven jet. When the AIS is high, katabatic winds over Antarctica are down-slope (gravity-driven) flows that arise from strong pressure gradients created by surface radiative cooling; the easterly component arises from the need to balance surface drag with the Coriolis force (Parish and Waight, 1987). When the AIS is lowered, katabatic flow ceases (Figure 2.5a), and the accompanying westerly momentum transfer from the solid earth to atmosphere above the AIS halts. As a result, northward momentum transport by atmospheric eddies near Antarctica is no longer required to balance the atmosphere's angular momentum budget (Figure 2.5c), and the SH eddy-driven jet weakens on its poleward side.

Furthermore, the E-P flux divergence suggests that the de-acceleration of the polar vortex in FA is not due to eddies, which tend to accelerate the zonal winds south of 65° S; rather, it

is due to a decreased pole-to-equator temperature gradient aloft (recall Figure 2.2c), which weakens the polar vortex through thermal wind balance. While others have postulated that momentum transfer from the solid earth via surface easterlies over the Antarctic continent (katabatic winds) maintains the polar vortex (see, e.g., Parish, 1991; Egger, 1994), our simulations suggest that eddy momentum convergence is only important for driving the eddy-driven jet. As shown in Figure 2.5d, the northward transport of zonal momentum by eddies, $\overline{u'v'}$, decreases prominently on the poleward flank of the eddy-driven jet in FA, not at the level of the polar vortex. Indeed, Simmonds and Law (1995) showed that weakening of the meridional cell by damping the katabatic flow over Antarctica without changing the orography tends to spin up the polar vortex, not weaken it as would be expected if zonal momentum transfer from the katabatic winds was responsible.

The absence of katabatic flow in FA also explains the mixed pattern of warming and cooling over West Antarctica in FA (Figure 2.6a). We define a temperature tendency due to katabatic winds as

$$\frac{dT}{dt} \equiv \frac{\vec{V} \cdot \nabla p}{\rho_0 R}, \tag{2.2}$$

where $\vec{V}$ is the surface velocity, ∇p is the climatological surface pressure gradient, ρ_0 is reference air density, and R is the gas constant for dry air. This katabatic tendency results from adiabatic compression of air parcels transported by the surface wind in the direction of the surface pressure gradient. Equation (2.2) describes a cooling tendency in FA (compared to C) that is strongest near the AIS edge where the gradient of the orography is largest (Figure 2.6b). The competing effect is warming with elevation loss at the dry adiabatic lapse rate (Figure 2.6c). Adiabatic warming dominates everywhere except over low-lying regions in West Antarctica where the difference in elevation between FA and C is small but where katabatic flows in C are substantial.

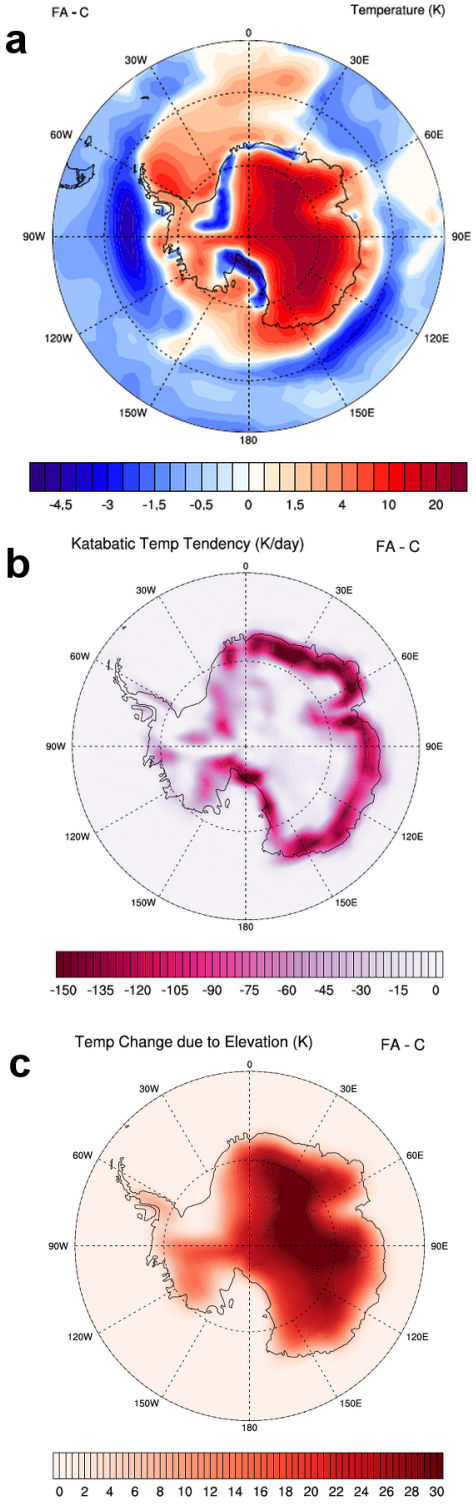

Figure 2.6: Surface temperature response in the vicinity of the AIS in FA - C: **(a)** surface temperature (in K); **(b)** temperature tendency due to katabatic winds (in K day^{-1}); and **(c)** temperature change (in K) expected from the elevation change alone, assuming a dry adiabatic lapse rate.

2.3.3 Decomposing the Atmospheric Dynamical Response

To understand why southward atmospheric energy transport increases in the SH with lowering of the AIS, we evaluate changes in atmospheric eddy activity. In FA, eddy kinetic energy (EKE) increases in the troposphere south of 30° S (Figure 2.7a). The largest increase in eddy activity is over the Antarctic continent (south of 65° S), a finding which agrees with the results of Mechoso (1981), Parish et al. (1994), Simmonds and Law (1995), and Walsh et al. (2000): while lowering the AIS decreases the rate of cyclogenesis over the Southern Ocean, it permits storms to form and intensify over the Antarctic continent itself and increases the average lifetime of storms at all latitudes (Mechoso, 1981; Walsh et al., 2000). The latter effects dominate over the former, and poleward energy transport by atmospheric eddies increases.

Enhanced cyclogenesis over the continent is made possible by enhanced baroclinic instability. Walsh et al. (2000) re-formulated the baroclinic instability criterion of the two-layer quasi-geostrophic model (see Holton, 1992) from pressure levels to sigma levels in order to compare baroclinicity in experiments with varying AIS orography. On sigma levels, the criterion for baroclinicity can be written as

$$B \equiv \frac{2\lambda^2 U_T}{\beta} > 1 \ , \tag{2.3}$$

where U_T is the vertical wind shear, β is the rate of change of the Coriolis parameter with latitude (with a correction for sigma coordinate conversion), and λ is the characteristic eddy wavelength as determined by the static stability,

$$\lambda^2 \sim \frac{\theta}{\partial\theta/\partial\sigma} \ . \tag{2.4}$$

The wind shear and the characteristic eddy wavelength are both evaluated at the $\sigma = 0.5$ vertical level. For further details on the quasi-geostrophic two-layer model and derivation of the instability criterion on σ-levels, see Holton (1992) and Walsh et al. (2000).

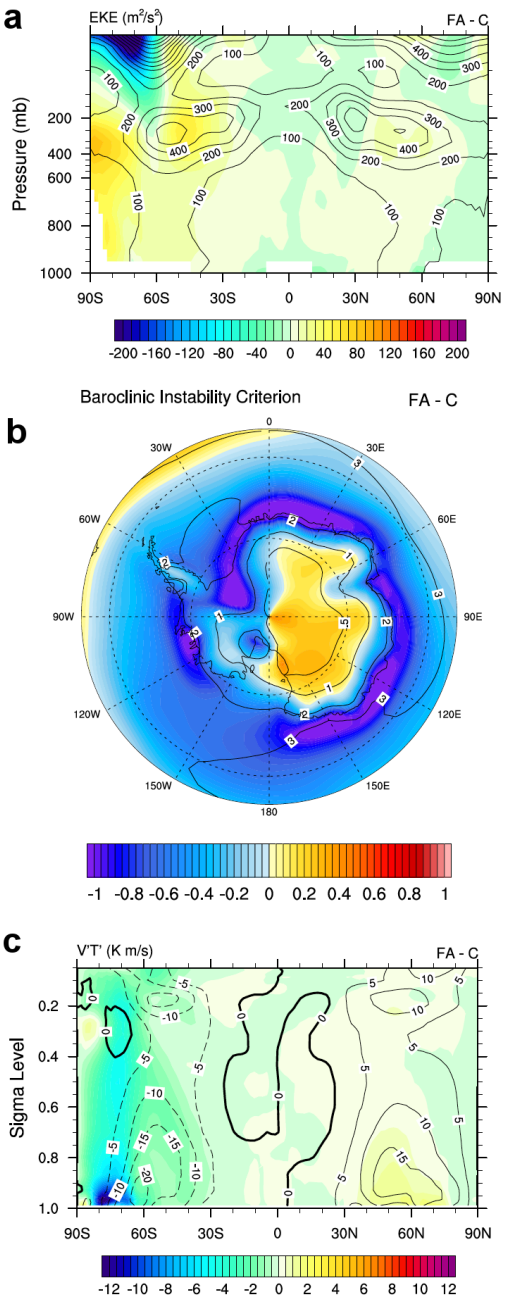

Figure 2.7: Atmospheric eddy response to lowering the AIS: **(a)** annually-averaged eddy kinetic energy (EKE) (in m^2 s^{-2}); **(b)** baroclinic instability criterion B as described in equation (2.3); and **(c)** eddy sensible heat transport, $\overline{V'T'}$ (in K m s^{-1}), computed on sigma levels. In all panels, contours depict the mean state in C, and the anomaly FA - C is shown in colors.

Figure 2.7b shows that B increases over the AIS, particularly over East Antarctica, and decreases over the Southern Ocean, particularly over the marginal ice zone around the continent. Nevertheless, regions in which B decreases in FA are also regions in which B is already large, and such decreases in B are not substantial enough to suppress instability. Overall, a larger area satisfies the baroclinic instability criterion $B > 1$ in FA.

As expected from increased baroclinicity over much of the AIS, Figure 2.7c shows that the southward sensible heat flux by atmospheric eddies ($\overline{V'T'}$) increases in FA. The increase is most pronounced on the southern flank of the climatological storm track, where $\overline{V'T'}$ doubles in FA, compared to C. Overall, the southward sensible heat flux by eddies increases at all latitudes south of 30° S. In Figure 2.7c, we show the change in eddy heat transport on sigma coordinate levels ($\sigma = p/p_s$) in order to highlight how surface-focused this anomaly is. We speculate that the greater surface pressure in FA than in C permits greater baroclinicity, explaining the surface-enhanced $\overline{V'T'}$ response in the high southern latitudes.

2.3.4 Ocean Circulation and Sea Ice Response

Significant changes in surface winds in FA (Figure 2.5c) suggest that AIS orography may be influential in shaping the ocean circulation and its energy transport. In fact, changes in surface wind stress account for changes in the wind-driven gyre circulation in FA that weaken northward energy transport by the ocean (Figure 2.4a). Over the Atlantic, anomalous surface winds (not evident in the zonal mean shown in 2.5b and 2.5c) cause the upper branch of the subtropical gyre to move southward, the Gulf Stream to weaken, and the subpolar gyre to weaken (Figure 2.8a), resulting in an equator-ward shift of the North Atlantic Drift and a decrease in ocean energy transport into the North Atlantic (Figure 2.8c).

The global oceanic meridional overturning circulation (MOC), whose streamfunction is shown in Figure 2.8b, also transports less energy northward in FA (Figure 2.8c). The upper cell of the MOC weakens over most latitudes and depths while the deep cell strengthens below 1500 m (see Marshall and Speer, 2012, for a review of the upper and lower cells), consistent with less cross-equatorial energy transport by the ocean (and in agreement with

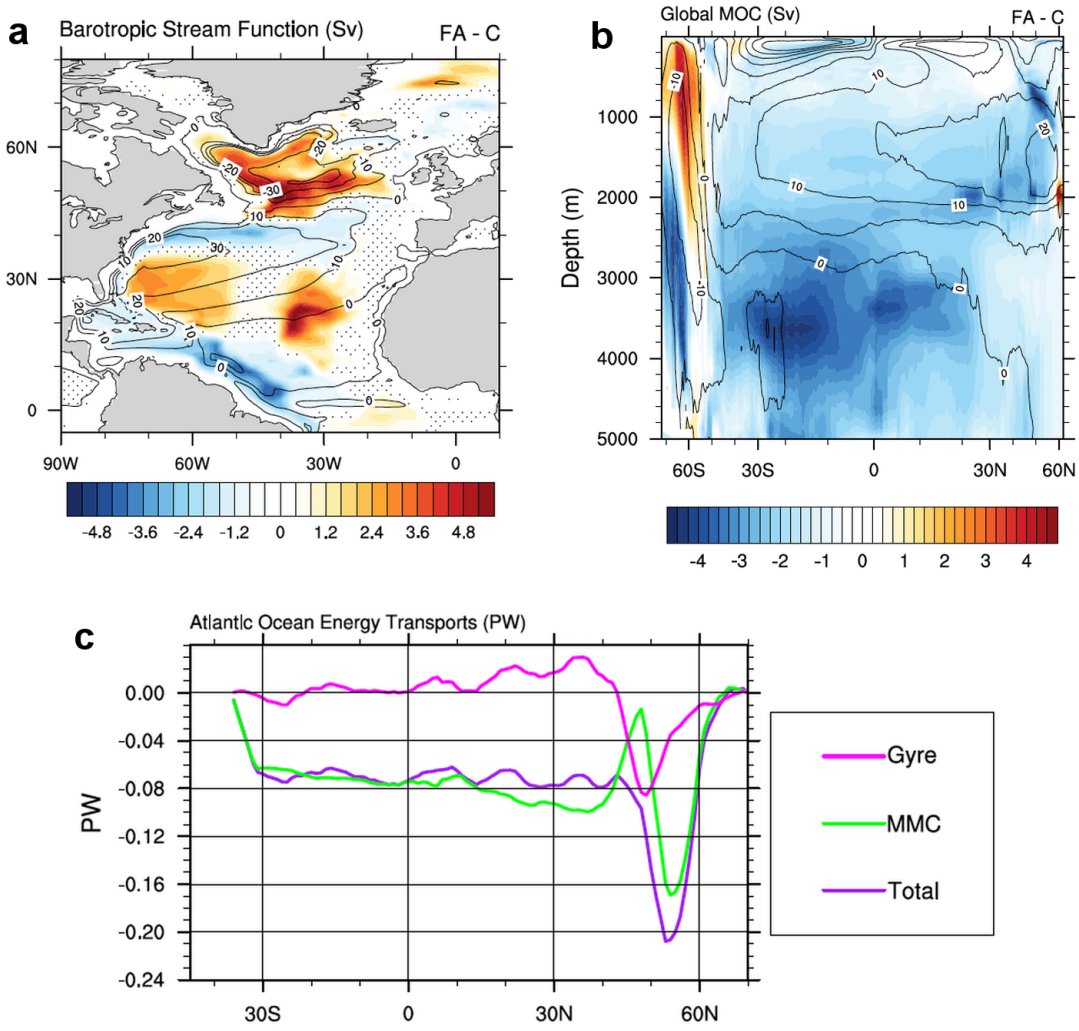

Figure 2.8: Ocean dynamic response to lowering the AIS, with labelled contours depicting the mean state in C and colors depicting the anomaly FA - C: **(a)** annually averaged barotropic streamfunction in Sv; and **(b)** annually-averaged global ocean meridional overturning streamfunction in Sv, shown as a function of depth; isopycnal flow has been removed by computing the streamfunction in potential density coordinates (σ) and converting to depth coordinates. The stippled areas in panel (a) indicate regions where the anomaly is not statistically significant at $p < 0.05$. In panel (b), the anomaly is statistically significant at $p < 0.05$ over more than 90% of the depth-latitude transect shown. Panel **(c)** displays the total change in Atlantic basin energy transport, and the partitioning of this transport into gyre and mean meridional circulation (MMC) contributions.

Figure 2.4). As a consequence, the NH mid- and high- latitudes cool, and Arctic sea ice, which depends sensitively on ocean energy transport (see Bitz et al., 2005), expands.

Sea ice, in fact, expands in both hemispheres (shown for the SH and NH in Figure 2.9a and 2.9c, respectively), although the effect is larger and more ubiquitous in the NH than the SH. In the SH, the sea ice thins and expands non-uniformly about Antarctica, with the sole region of contraction in the Weddell sector. In the NH, the sea ice expands into the Greenland Sea, Bering Sea, Barents Sea, and south of Greenland. The decrease in ocean energy transport into the northern North Atlantic is dominated by weakening of the Atlantic meridional overturning circulation.

The surface westerly winds strengthen south of 60° S over the sea ice in the Southern Ocean (Figure 2.5b). The resulting enhanced westerly momentum transfer to the ocean causes northward Ekman transport around the Antarctic margin; in such an ice-covered region, this momentum transfer also results in northward and eastward Ekman drift of sea ice (the turning angle of sea ice is approximately 45° relative to the direction of the wind, as described by Lepparanta, 2011). As a consequence, Antarctic sea ice expands in most sectors (Figure 2.9a) (Hall and Visbeck, 2002). Although sea ice expands and surface buoyancy loss increases, the deep cell weakens (above 1500 m) because the wind stress curl over the Southern Ocean decreases (Figure 2.5a), inhibiting Ekman suction of deep waters at the $\sigma = 27.6$ kg cm^{-3} isopycnal (Marshall and Speer, 2012).

2.3.5 Precipitation Response

Figures 2.10a and 2.10b show that precipitation increases over the AIS while it decreases over the Southern Ocean, the latter a result of the mid-latitude storm track shifting northward. The Inter-Tropical Convergence Zone (ITCZ) also shifts northward (Figure 2.10a), which may be surprising given the decrease in temperature difference between the NH and SH (called the "interhemispheric temperature anomaly" in Friedman et al., 2013). However, the ITCZ shift is consistent with the need to balance TOA radiative energy loss over the AIS. Similar explanations that emphasize energetics driving ITCZ shifts have been offered

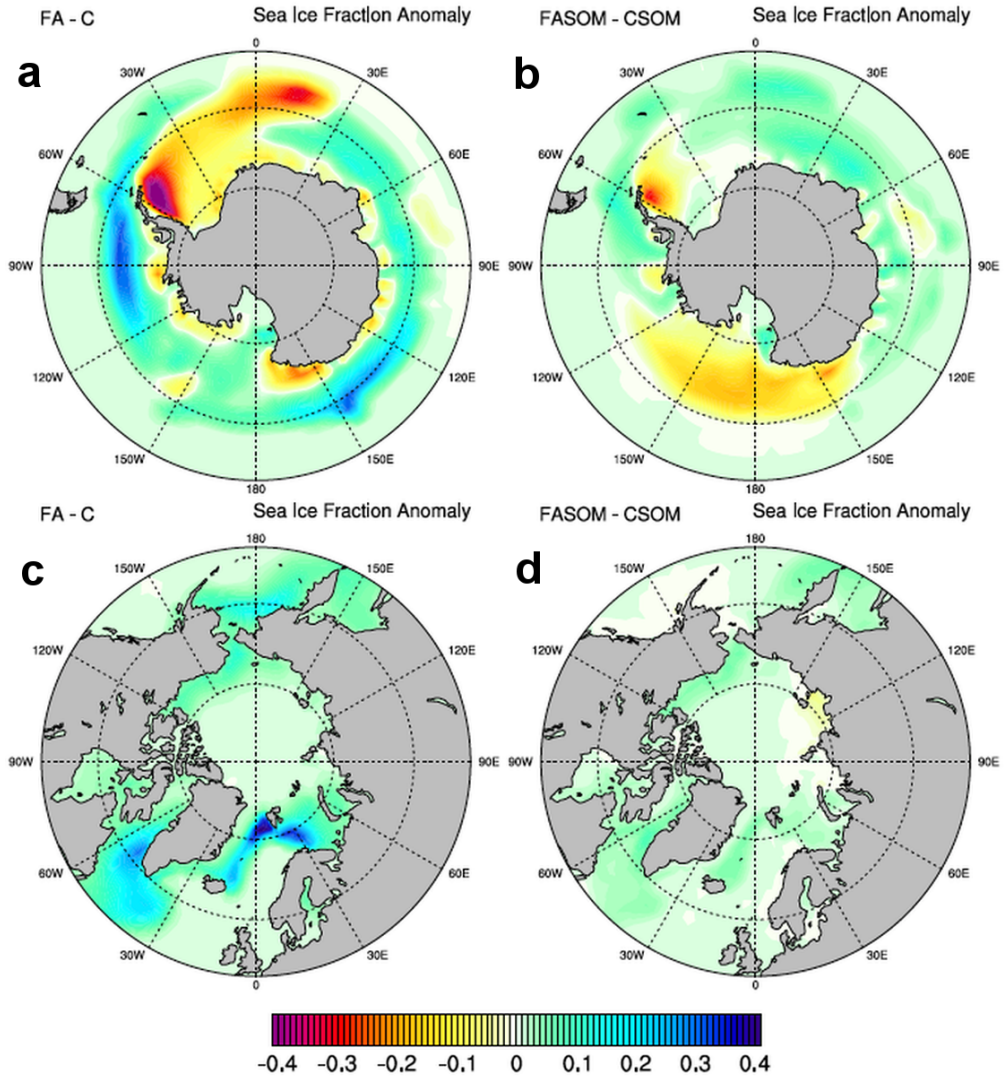

Figure 2.9: Annually averaged sea ice response to lowering the AIS: **(a)** southern hemispheric sea ice fraction in FA, expressed as FA - C; **(b)** southern hemispheric sea ice fraction in FASOM, expressed as FASOM - CSOM; **(c)** northern hemispheric sea ice fraction in FA, expressed as FA - C; and **(d)** northern hemispheric sea ice fraction in FASOM, expressed as FASOM - CSOM.

by Chiang and Bitz (2005), Cheng et al. (2007), Kang et al. (2008), and Frierson and Hwang (2012). The northward ITCZ shift in our study is associated with an anomalous southward cross-equatorial flow in the upper troposphere, which facilitates anomalous southward cross-equatorial energy transport by the atmosphere.

The ITCZ shift also introduces a small, but significant, anomalous freshwater flux into the Atlantic north of 30° S of 0.01 Sv (shown in Figure 2.10b), slowing the upper cell of the MOC (shown in Figure 2.8b) and facilitating anomalous southward energy transport by the ocean (a mechanism described by Rahmstorf, 1996). The shifting SH midlatitude storm track and its associated precipitation anomaly, on the other hand, are too far south and too weak to contribute to contribute significantly to slowing the MOC.

2.3.6 Isolating the Role of Ocean Dynamics

In order to understand the role of ocean dynamics in the climate response to lowering the AIS, we compare the response in FASOM to that in FA. In FASOM, no adjustment of ocean energy transport is permitted, so only the atmospheric energy transport may respond to TOA energy perturbations. Nonetheless, the local climate response to lowering AIS orography is similar in FA and FASOM, with strong warming over the AIS and mild cooling over the Southern Ocean. The remote response, on the other hand, particularly that at the equator and the NH high latitudes, is significantly different in FA and FASOM, which we describe below.

Because the SOM cases were run to equilibrium, there can be no difference between the annual mean net surface heat flux in FASOM and CSOM. As a result, the anomalous atmospheric energy transport anomaly in FASOM is also the total energy transport anomaly. This transport anomaly resembles the total energy transport anomaly in FA, but is smaller in magnitude from 60° N to 60° S (Figure 2.4a). As for FA, the total energy transport response in FASOM offsets the TOA radiative cooling over the AIS, resulting in a warmer troposphere above Antarctica but a cooler one globally.

The southward energy transport anomaly in FASOM is significantly greater than the

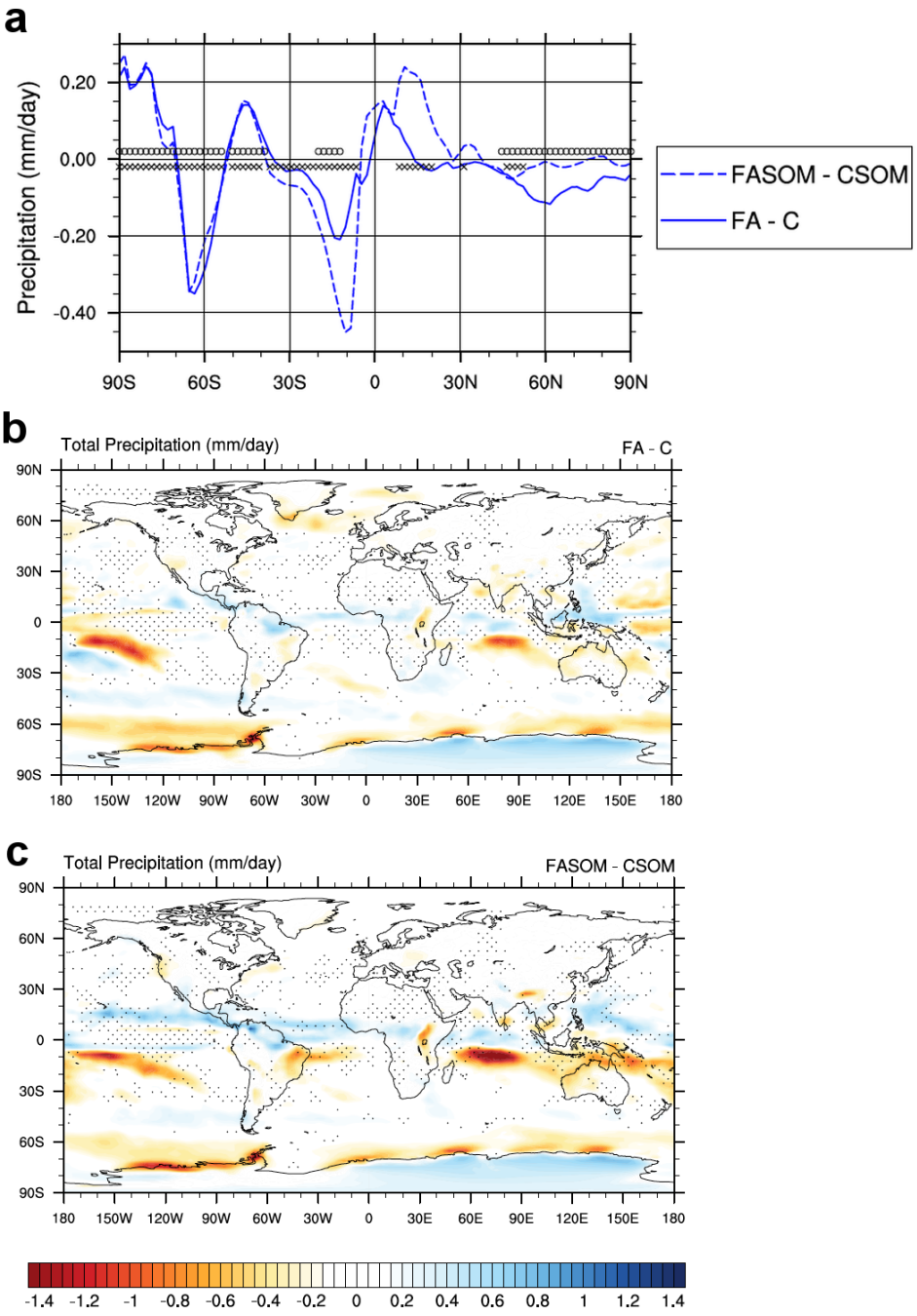

Figure 2.10: Annually averaged precipitation response (in mm/day) to lowering the AIS: **(a)** zonal mean, where circles (hatches) indicate latitudes where the precipitation anomaly in FA (FASOM) is statistically significant ($p < 0.05$); **(b)** FA - C, with stippled areas indicating regions where the anomaly is not statistically significant at $p < 0.05$; and **(c)** as in (b) but for FASOM - CSOM.

atmospheric component of the energy transport anomaly in FA from 30° N to 30° S, which corresponds to greater precipitation anomalies in the subtropics and tropics over all three ocean basins (see Figure 2.10a through 2.10c, and Figure 2.4b). The total cross-equatorial atmospheric energy transport anomaly, which is associated with the ITCZ shift and altered Hadley circulation, is about twice as large in FASOM as in FA. The magnitude of the tropical and subtropical atmospheric response must be larger in FASOM to satisfy global energy balance in the absence of ocean energy transport anomalies.

Long-range teleconnections between the lowered AIS and the NH high latitudes are also mediated by ocean dynamics. In the Arctic, surface temperature cooling in FA is greater than 2°C in the zonal average, while it is less than 1°C in FASOM (see Figure 2.2c). The larger surface temperature response in FA is due to expanding sea ice (Figure 2.9c); in FASOM, where the sea ice does not expand (Figure 2.9d), the surface temperature response is muted significantly. Sea ice expansion in FA is driven by decreased ocean energy transport into the northern high latitudes due to decreased transport by horizontal gyre and (especially) overturning circulations (Figure 2.8). In FASOM, where oceanic energy transport is held fixed, NH sea ice expansion and cooling do not occur as they do in FA.

2.4 Discussion

In undertaking this work, our objectives have been two-fold: (1) to understand how the global climate responds to lowering the AIS, and (2) to understand how incorporating ocean dynamics impacts this global climate response. By studying these climate impacts using a fully-coupled GCM, we have been able to capture the global extent of how the climate system responds to lowering the AIS; by comparing the response in a fully-coupled GCM to one in a GCM with a slab ocean, we have been able to pinpoint how coupling between the ocean and atmosphere shapes the way the global climate system responds.

We have shown that lowering the orography of the AIS has both local and global climatic consequences. While the surface and atmospheric column above the AIS warm, there is modest cooling over the Southern Ocean and globally. These temperature changes ac-

company a cessation of katabatic winds over the AIS, a weaker polar vortex, a slower jet, an equator-ward shift of the mid-latitude storm track, an expansion of the sea ice in both hemispheres, and a northward shift of the ITCZ. In the NH, northward energy transport by the oceanic MOC and wind-driven gyres decreases, and the Arctic cools. Globally, an increase in southward energy transport offsets higher TOA energy loss over the warmed AIS.

Figure 2.11 summarizes some of the energetic mechanisms at play in FA and FASOM, and illustrates the importance of atmosphere-ocean coupling in determining the cross-equatorial energy transport response to lowering the AIS. In both FA and FASOM, an increase in the OLR over the AIS prompts a net southward energy transport anomaly, which is of similar magnitude in the SH mid- and high- latitudes. The slowing of the global MOC in FA causes anomalous southward cross-equatorial energy transport by the ocean, which permits less anomalous southward cross-equatorial energy transport by the atmosphere, leading to a significantly weaker ITCZ shift in the case with a dynamical ocean response.

In the FA case the ocean response provides some of the southward energy transport needed to offset the higher TOA energy loss over the AIS. Thus, the atmospheric energy transport in FA responds not only to the TOA radiative cooling over the AIS, but it also "compensates" for the ocean energy transport anomaly. Compensation is seen in a variety of GCMs (e.g., Frierson et al., 2007; Enderton and Marshall, 2009), and is an expected result since the meridional distribution of TOA fluxes depends only weakly on the climate state (Stone, 1978). However, the compensation is imperfect in our study since the total energy transport is different between the FA and FASOM cases; specifically, the total energy transport anomaly is more southward at all latitudes in FA compared to FASOM.

The deviations from perfect compensation can be understood by considering the atmospheric energy transport anomaly spreading the TOA and surface energy flux anomalies to other regions, a framework that has been used to explain energy transport changes with global warming in midlatitudes (Hwang and Frierson, 2010) and high latitudes (Hwang et al., 2011). The weakened oceanic MOC in the FA simulation causes an anomalous surface heat flux into the atmosphere between 60° S and 20° S, while there is an anomalous surface heat

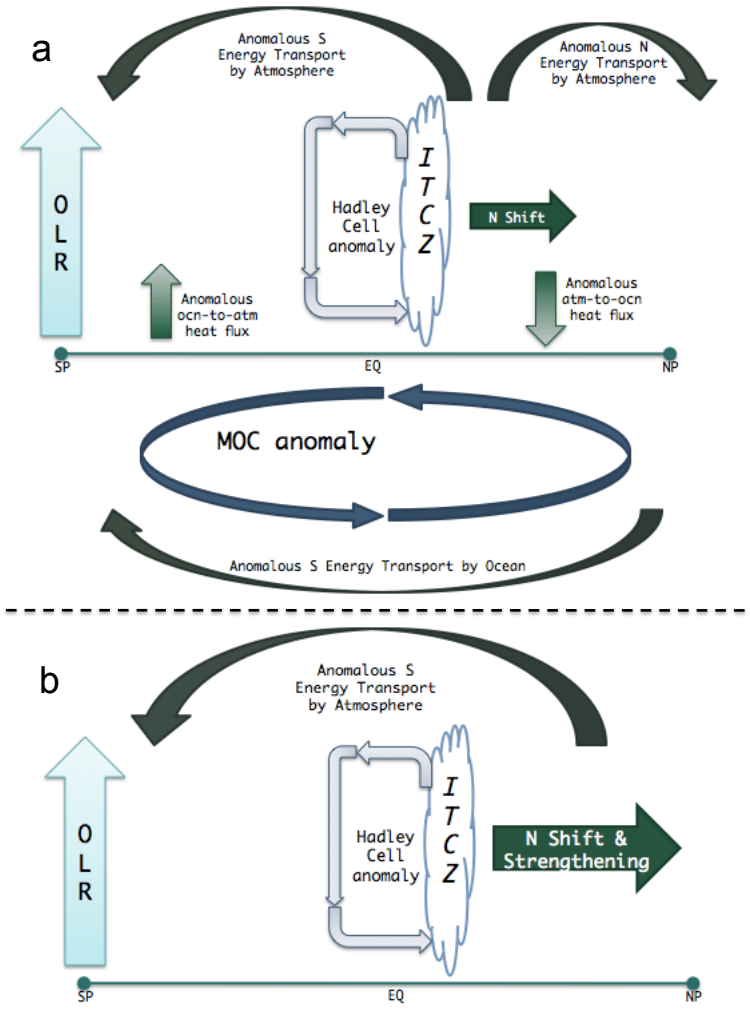

Figure 2.11: Schematics summarizing the global energetic response to lowering the orography of Antarctica. **(a)** In the case of the fully-coupled atmosphere and ocean (FA simulation), both the atmosphere and ocean energy transport processes respond to the enhanced outgoing longwave radiation over Antarctica by increasing southward energy transport. Cross-equatorial energy transport is accomplished by a northward shift in the ITCZ and decreased transport by the upper cell of the oceanic MOC. **(b)** In the case of the (uncoupled) atmosphere and slab ocean (FASOM simulation), the atmosphere must accomplish all the southward cross-equatorial energy transport by shifting the ITCZ and the rising branch of the Hadley circulation northward more than it does in the coupled case.

flux into the ocean between 50° N and 70° N (shown in Figure 2.3b). The atmosphere responds by transporting much of the energy away, but radiates some to space locally. The latter leads to the lack of perfect compensation. Furthermore, some of the surface heat flux anomaly is due to vertical mixing and diffusion (in either the atmosphere or ocean) that is unrelated to horizontal energy transport, which also results in imperfect compensation.

Overall, our results agree with other AGCM and paleoclimate studies that have explored how the climate system responds to lowering the AIS. Ogura and Abe-Ouchi (2001) showed that flattening AIS orography causes remote dynamical cooling; similarly, Knorr and Lohmann (2014) found remote dynamical warming when AIS elevation was increased. Other AGCM studies have found enhanced poleward energy and momentum transports when the AIS is flattened (e.g., Mechoso, 1981; Simmonds and Law, 1995; Quintanar and Mechoso, 1995; Walsh et al., 2000).

Enhanced southward energy transport when the AIS is lowered is a common result in AGCM studies with prescribed SSTs or slab oceans, including those of Mechoso (1981), Quintanar and Mechoso (1995), Simmonds and Law (1995), Walsh et al. (2000), and Ogura and Abe-Ouchi (2001). As shown by Ogura and Abe-Ouchi (2001), this anomalous energy transport arises to accommodate the greater TOA energy loss over the AIS. Indeed, the magnitude of the increase in southward energy transport associated with removing AIS topography reported by Ogura and Abe-Ouchi (2001) is approximately 0.25 PW, which is nearly identical to that in our FASOM experiment. All of these studies concur that the enhanced southward energy transport is accomplished by baroclinic eddies.

We have also shown that the most remote response to lowering the AIS, the cooling of the Arctic and expansion of sea ice therein, is mediated by decreased ocean energy transport into the northern high latitudes. Neither the ocean cross-equatorial energetic response nor the cooling of the Arctic are possible in the results of Mechoso (1981), Parish et al. (1994), Simmonds and Law (1995), Quintanar and Mechoso (1995), and Ogura and Abe-Ouchi (2001) because these modeling studies do not incorporate ocean and sea ice dynamics. While the results of these earlier studies are not incorrect, they are incomplete because they do not

take into account the ocean's ability to transport energy differently in response to changes in surface energy balance brought about by the dynamic atmosphere response.

Why do SH eddies transport more energy poleward when the AIS is lowered, despite the reduction in the SH meridional temperature gradient and vertical wind shear? In our study, we find that the static stability ($d\theta/dz$) decreases over the AIS, and that this decrease has a greater impact on baroclinicity than the decrease in wind shear. As a result, a greater area over the AIS satisfies the baroclinic instability criterion, permitting atmospheric eddies to grow and persist closer to the pole. These findings are similar to those of Walsh et al. (2000), who also found that baroclinically unstable regions expanded over the AIS when orography was removed. Furthermore, we note that SH atmospheric eddies are much more effective at transporting DSE poleward when the AIS is lowered since the surface pressure is much higher. Overall, eddies have a deeper atmospheric column through which to transport energy when the AIS is lowered; as a result, more energy is fluxed southward towards the AIS, offsetting the increase in OLR there and satisfying the required energy balance.

While our findings qualitatively agree with those of earlier AGCM and paleoclimate studies, they are at odds with those of Justino et al. (2014), the only other study to have considered the impact of AIS orography reduction in a fully-coupled model without confounding factors. Justino et al. (2014) found that southward atmospheric energy transport decreased when the AIS was lowered by 25%. In their case, an increase in high clouds over the lower AIS decreased TOA OLR and decreased overall cooling over the AIS. None of the earlier AGCM studies found such an increase in high clouds to counteract enhanced radiative cooling over the warmer AIS. Furthermore, we find the cloud response in our experiments has only a minor impact on the TOA radiative flux anomaly. While we cannot rule out the increase in high clouds found by Justino et al. (2014), there is also no compelling reason to expect it should dominate the outcome.

Our findings suggest that lowering the AIS, in the absence of changes in greenhouse gases or other parameters, could result in modest global cooling, a counter-intuitive result. The lowering of the AIS could act as a negative (stabilizing) feedback on anthropogenic

climate change. Similarly, Knorr and Lohmann (2014) found that growth of the AIS acts as a negative feedback on its own expansion through wind and ocean circulation changes that tended to result in modest global warming. We find that the magnitude of the negative feedback associated with AIS collapse, however, is modest, and would likely be difficult to detect against the background of changes required to cause such a catastrophic loss of the AIS (as well as the concurrent meltwater flux associated with such a loss).

The purpose of this study is to isolate the effect of flattening AIS orography on climate from the effect of other major changes (such as decreased albedo over the AIS, increased freshwater fluxes into the Southern Ocean, and global sea level rise) that would doubtlessly accompany it. We do not aim to replicate climates of the past or future, and, as such, this is not a paleoclimate study; instead, we aim to isolate and study a single element of these climates, the impact of a negative orographic anomaly over the Antarctic continent, and, by doing so, to gain insight into the working of the climate system.

Finally, it is important to note the limitations of this study. Here, we have considered the quasi-equilibrium response to lowering the AIS, while the transient response may be of more practical interest. Furthermore, we have neither accounted for the different continental margins that would result if the AIS were to melt, nor accounted for the effects of meltwater on sea surface height and oceanic static stability, nor the decreased surface albedo over the AIS with melting. We speculate that decreased surface albedo over the AIS and an anomalously positive freshwater flux over the Southern Ocean would likely increase the importance of the dynamical mechanisms we have described in this study. A lower albedo over Antarctica would enhance warming at the surface and aloft locally, while increased freshwater input into the Southern Ocean would augment remote cooling by enhancing SH sea ice growth (via increased stability of the ocean mixed layer, which would decrease the entrainment and upwelling of warmer waters from below). Despite these caveats, the results presented herein are significant to the study of climate dynamics and the response of the climate system to high latitude orography. Our study also elucidates the dynamics of past climates in which the AIS was lower or absent, and may be relevant to future climates with a lower AIS.

2.5 Conclusions

In this study, we have explored how AIS orography impacts the climate system. The high AIS orography of the present climate keeps Antarctica very cold and dry, and decreases TOA cooling; removing AIS orography, conversely, warms Antarctica at the surface and aloft, increases OLR over the continent, and enhances TOA cooling. As a result, southward energy transport towards Antarctica increases, with dynamical warming in the vicinity of the AIS but dynamical cooling over the rest of the globe.

Both atmospheric and oceanic processes contribute to increased southward energy transport. In the vicinity of the lowered AIS, the atmosphere is deep and permits baroclinic instability over a larger area, so eddies transport more DSE and zonal momentum southward. At the equator, more energy is transported southward cross-equatorially by a northward shift in the rising branch of the Hadley Cell and a weakened oceanic MOC. In the NH high latitudes, decreased northward energy transport by the ocean cools the Arctic and allows sea ice to expand into the North Atlantic and Pacific. Comparing the results from a fully-coupled experiment to those from a slab ocean experiment showed that atmosphere-ocean coupling is particularly important in determining the magnitude of the equatorial precipitation shift and the cooling of the Arctic.

In summary, we have detailed how the global climate system responds when AIS orography is reduced in the absence of confounding factors, and have identified the dynamic mechanisms involved in this response. We have studied this problem in a fully-coupled GCM, and have isolated the role of ocean energy transport. Overall, the results of this study are relevant to understanding how the climate system adjusts to a perturbation, and, in particular, how the atmosphere and ocean dynamically interact to produce a new quasi-equilibrium climate state.

Chapter 3

A MATHEMATICAL FRAMEWORK FOR ANALYSIS OF WATER TRACERS: PART I, DEVELOPMENT OF THEORY AND APPLICATION TO THE PREINDUSTRIAL MEAN STATE

3.1 Introduction

From evaporation to precipitation, a molecule of water typically spends nine days in the atmosphere (Hartmann, 1994). Numerical water vapor tracers (WTs), also known as water tags, are a powerful tool for understanding this brief period that water molecules spend in the aerial hydrological cycle. Water tagging in a global climate model (GCM) involves labeling water vapor at its point of evaporation and following its movement in an Eulerian sense through the atmosphere until it precipitates. WTs track moisture from its source region, through horizontal and vertical advection by the general circulation, through phase transitions from vapor to cloud liquid or ice, to its (eventual) point of precipitation. Once water precipitates over ocean or land (i.e. after one evaporation to precipitation cycle) the WT tag is renewed.

A handful of studies have used numerical WTs in GCMs and mesoscale models to assess the global hydrological cycle. These studies have assessed local moisture recycling (the recycling ratio, hereafter denoted RR), remote sources of precipitation and their relative importance, and the variability of local and remote precipitation sources. All of these studies have focused on precipitation over land, and have used relatively coarsely tagged regions.

The earliest studies to incorporate WTs into GCMs were those of Koster et al. (1986) and Joussaume et al. (1986). Both studies demonstrated that moisture of ocean-origin is a significant component of terrestrial precipitation. Both of these studies were limited by short

model integrations (less than one season), which were necessary to overcome the prohibitive computational cost associated with adding WTs at that time; as a result, these early studies did not account for seasonal and interannual variability in moisture transport.

Following Koster et al. (1986) and Joussaume et al. (1986), several studies implemented numerical WTs in GCMs to study precipitation RRs and remote source regions. Numaguti (1999) implemented WTs in a full GCM to study moisture source regions for the Eurasian continent, and found that oceanic source regions were particularly important in winter; using long-term tracking of water of oceanic origin, Numaguti (1999) further showed that the number of times that such water precipitated over land and re-evaporated depended on the season, with summer months associated with the greatest number of recycling events. Bosilovich and Schubert (2002) studied continental and oceanic sources of precipitation over North America and south Asia; while continental moisture sources were found to dominate precipitation over North America, particularly in the interior of the continent, oceanic sources provided most of the precipitate over the Indian subcontinent. For land regions, Bosilovich and Schubert (2002) found a strong correlation between locally-recycled precipitation and total precipitation, but little correlation between evaporation and local precipitation; they attributed the latter to regions such as the subtropical high pressure zones where there is substantial evaporation but little precipitation because the general circulation tends to diverge locally-evaporated moisture. In a related study, Bosilovich (2002) investigated the vertical distribution of moisture in the atmosphere above the interior of North America from different source regions; while there was a larger fraction of locally-sourced water vapor in the boundary layer and lower troposphere, much of the upper tropospheric water vapor was from more remote sources (including the North Pacific and tropical Atlantic).

Other studies have used WTs implemented in mesoscale weather models to consider questions relevant to regional precipitation sources and recycling (see Sodemann et al., 2009; Knoche and Kunstmann, 2013; Sodemann and Stohl, 2013). Numerical WTs have also been used to aid paleoclimate studies, many of which depend on interpreting the isotopic composition of water (both δ^{18}O and deuterium excess) in ice cores and sediments; such isotopic

records can be used to infer local temperature, salinity, and circulation (both atmosphere and ocean). The validity of such inferences, however, depends on the source region of precipitated water and the temperature of the source region relative to region of condensation. As a result, several modeling studies have used WTs to study high-latitude moisture source regions (see, e.g., Koster et al., 1992; Delaygue et al., 2000; Werner et al., 2001; Noone and Simmonds, 2002). Table 3.1 summarizes previousstudies that employ numerical WTs to investigate the aerial hydrological cycle.

Despite their limited use in the literature, numerical WTs may be used to answer many outstanding questions about the global hydrological cycle. Estimating the RR, for example, is one such topic. The current literature suggests that the geographical variations in the RR are substantial; while the global average RR is approximately 20%, the RR ranges from less than 5% over the midlatitude and equatorial oceans to greater than 30% over the subtropics (for advective length scales of 1000 km; see Trenberth (1998)). A range of analytical techniques have been used to compute the moisture RR in model output and observational reanalyses. (See the review by Eltahir and Bras (1996), and the later studies of Trenberth (1998) and Trenberth (1999) for an overview of how moisture RR calculations have evolved in the literature.) Numerical WTs, on the other hand, provide a simple means of estimating the moisture RR for a given tagged region: the RR can be calculated as the precipitation over a tagged region that bears the regional tag divided by the total precipitation over that region.

Numerical WTs may also be used to study remote precipitation sources and their variability. Indeed over most land and ocean regions, well over half of the total precipitation has a remote origin (see Eltahir and Bras, 1996; Trenberth, 1999; Bosilovich, 2002). While moisture recycling may be calculated using atmospheric moisture fluxes, differentiating between remote precipitation sources for a given region is not possible. Recently, Stohl and James (2004) and Stohl and James (2009) used Lagrangian back-trajectory methods to predict precipitation source regions in observational reanalyses; later, Sodemann and Stohl (2009) used the same methods to evaluate moisture source regions for the Antarctic. Lagrangian

Study	Model	Region	Relevant Findings
Koster et al. (1986)	NASA/GISS GCM 8°× 10°	Global	Seasonal variability in remote source regions; Low latitude land regions rely more on ocean-sourced moisture.
Joussaume et al. (1986)	AGCM	Global	Local recycling is important for inland regions in summer.
Numaguti (1999)	CCSR/NIES AGCM T21	Global (Eurasia)	80% of precipitation inland in summer is from land-sourced moisture; In winter, most inland precipitation is from ocean-sourced moisture.
Bosilovich and Schubert (2002)	GEOS-3 GCM 2°× 2.5°	Global (N. America & Eurasia)	Over the midwestern US, land-sourced moisture is most important; There is a high correlation between total precipitation and RR.
Bosilovich (2002)	(same as previous)	(same as previous)	Lower tropospheric water is more locally-sourced; Upper tropospheric water is more remotely-sourced.
Sodemann et al. (2009)	CHRM (NWPM) 0.5°× 0.5°	Europe,	Relative importance of moisture-source regions for the Elbe flood (2002) changed over the course of the event.
Sodemann and Stohl (2013)	(same as previous)	W. Europe, N. Atlantic	Moisture transport by atmospheric rivers is linked to evolution of midlatitude cyclones and upper-level flow patterns.
Knoche and Kunstmann (2013)	MM5 (NWPM)	W. Africa	Only 3% of the precipitation over the Sahel is from local moisture sources.
Koster et al. (1992)	NASA/GISS GCM 8°× 10°	Global with focus on Antarctica	Temperature is more important than source region in determining deuterium-excess.
Delaygue et al. (2000)	(same as previous)	Global, LGM and present-day	Large seasonal change in Antarctic precipitation source regions; Source regions are sensitive to prescribed low-latitude SSTs.
Werner et al. (2001)	ECHAM-5 GCM 3.75°× 3.75°	Global LGM and present-day	Antarctic moisture source regions vary by sector; Enhanced source seasonality with LGM boundary conditions.
Noone and Simmonds (2002)	Melbourne U AGCM 5.625°× 3.25	Global	Interannual variability in Antarctic precipitation source regions is coincident with the Southern Annular Mode (SAM).

Table 3.1: Synopsis of studies in the literature employing numerical WTs, including the region on which the study focuses, the model used (GCM or numerical weather prediction model, NWPM), and a one-line summary of the major findings.

back-trajectory calculations, however, are very sensitive to the temporal resolution of circulation and moisture fields; high frequency measurements are essential for minimizing errors and ensuring agreement with Eulerian diagnostics (Stohl and James, 2004), and integrations must be carried out over a time period greater than 10 days to obtain accurate estimates of precipitation origin (Sodemann and Stohl, 2009). On the other hand, numerical WTs readily reveal where moisture originates.

While WTs provide useful information, there are several problems that have curtailed their use. First, WTs are limited by the accuracy of the physics and numerics of the atmospheric models in which they are implemented; any faults and biases in evaporation, convection, cloud processes, tracer advection, and circulation will limit how applicable the WT experimental results are to the real climate system. Numerical WTs also tend to be computationally expensive. When implemented in a GCM, each tagged region requires a suite of passive tracers (representing, for example, water vapor, cloud liquid, and cloud ice that correspond to the tagged evaporative region) that must be tracked through time and recorded for each grid cell and atmospheric level. If global coverage and relatively fine resolution of source regions is required, hundreds of tracers must be used, often making the desired numerical experiment unfeasible from a computational viewpoint. Furthermore, output from WT experiments must be analyzed systematically and intuitively, which may constitute a big data problem when many tags are used.

In this study, we will confront this final difficulty by developing a mathematical framework for analyzing the output of modeling experiments that use WTs. Our framework will rely on simple assumptions, namely that in a global time-averaged sense, the amount of moisture that evaporates must be equal to the amount that precipitates. In other words, moisture must be conserved. Using basic linear algebra and analysis, we will develop a matrix formulation in which the precipitation is written as a function of evaporation from each tagged region, and in which local and remote precipitation sources are separated into distinct terms. We will apply this analysis method to a pre-industrial GCM experiment in which we have tagged the entire globe in 48 distinct regions, with 10° latitudinal resolution in each of the major

ocean basins. In the process, we will use several matrix decomposition methods to analyze the local and remote precipitation source terms, and will use these decompositions to verify old insights and gain new insights on the aerial hydrological cycle.

In this study, we focus our analysis on the part of the aerial hydrological cycle that originates from evaporation over ocean. First, analysis of several different observational reanalyses suggests that at least one-third of precipitation falling over land regions comes from evaporation over the world oceans (Trenberth et al., 2011; Gimeno et al., 2012); thus, understanding this branch of the hydrological cycle is crucial for understanding continental precipitation, a topic of great importance to human societies and natural ecosystems. Furthermore, moisture transport between ocean basins determines the salinity (and, consequently, density) of each of the basins; this, in turn, may determine where deep convection occurs and meridional overturning (see the review by Broecker, 1991, and references therein). Other studies have considered the oceanic branch of the aerial hydrological cycle, albeit without the use of numerical WTs, and have found key differences in precipitation, evaporation, and inferred moisture divergence between the Indian, Pacific, and Atlantic basins (Baumgartner and Reichel, 1975; Bryan and Oort, 1984; Schmitt, 1995; Gimeno et al., 2010). Recent work suggests that such differences may intensify in the future; using Lagrangian back-trajectory calculations of observational reanalyses, Gimeno et al. (2013) demonstrated that increases in net evaporation from oceanic source regions (as expected from surface warming due to emissions of anthropogenic greenhouse gases) can be expected to amplify precipitation over adjacent continental regions. As far as we know, no study has used numerical WTs to track the movement of evaporated water within a given ocean basin and between ocean basins.

The structure of this paper is as follows. In §3.2, we develop a concise mathematical framework with which to analyze the output of numerical WT experiments, in §3.3, we describe our model run, and in §3.4, we use the results from our run to demonstrate the utility of our mathematical framework, and to further develop it. We offer some points for discussion in §3.5 and some conclusions in §3.6.

3.2 Mathematical Development

We seek a framework for using model output from water tagging experiments to understand the natural and forced variability of atmospheric water transport in the climate system. We begin with the fundamental equation of hydrology from Peixoto and Oort (1992), which is

$$\frac{\partial Q}{\partial t} + \nabla \cdot Q = E - P \tag{3.1}$$

where Q denotes column-integrated atmospheric moisture, E denotes evaporation, and P denotes precipitation. In words, we can consider this to be a statement of conservation of Q in the atmosphere, given sources (E) and sinks (P).

For time periods greater than a year, variations in the storage of water in the atmosphere are negligible and the equation becomes

$$\overline{\nabla \cdot Q} = \overline{E} - \overline{P}, \tag{3.2}$$

where the overbars denote annual climatologies. After integrating globally and applying the divergence theorem, equation (3.2) becomes

$$\iint_{earth} \overline{\nabla \cdot Q}\ dA = \int \overline{Q \cdot \hat{n}}\ ds = \iint_{earth} (\overline{E} - \overline{P})\ dA = 0\ . \tag{3.3}$$

Thus, over a global domain we obtain the familiar equality

$$\overline{E} = \overline{P}. \tag{3.4}$$

Now, consider the hydrology equation for the case of a limited domain i, smaller than global:

$$(\nabla \cdot Q)_i = E_i - P_i. \tag{3.5}$$

For each region, a fraction of E_i will precipitate locally and contribute to P_i, while another

fraction will be exported from the region and will precipitate elsewhere. To describe this, we define an export fraction e_i, which is defined as the fraction of E_i that is precipitated elsewhere; in the hydrological literature, this value is known as the "aerial runoff." The complement of the aerial runoff term, the fraction of locally-evaporated water that precipitates locally, is $(1 - e_i)$.

Now, we consider the convergence term. Since evaporated moisture is a conservative quantity, its convergence into region i can be written as the sum of the export from all other regions multiplied by the fraction of that export that enters region i, minus the amount of locally-evaporated water that is exported:

$$-(\nabla \cdot Q)_i = \left(\sum_{j,j \neq i} e_j f_{ji} E_j \right) - e_i E_i \tag{3.6}$$

where e_j is the fraction exported from region j, f_{ji} is the fraction of the export from region j that falls in region i, and E_j is the total evaporation from region j. Note that for a given region j, the sum of these fractions must equal unity,

$$\sum_{i,i \neq j} f_{ji} = 1, \tag{3.7}$$

and that the fraction of evaporated exported from region j that falls in region j is defined to be nil:

$$f_{jj} = 0. \tag{3.8}$$

As others have noted when considering the moisture recycling ratio (see, for example, Eltahir and Bras, 1996; Trenberth, 1998, 1999), the export fraction e_i and its corollary local fraction $(1-e_i)$ are both domain-dependent quantities in that they depend on the size, shape, and spatial orientation of the region considered. If the domain i were the entire globe, for example, the e_i would be zero; decreasing the size of the domain results in e_i asymptotically approaching unity. We have designed the configuration of spatial domains in our experiment

(10° latitude bands within each ocean basin, with major continental regions tagged separately, as described in §3.3) to allow us to isolate the transport of moisture meridionally within each basin and zonally between basins. We have chosen these domains in order to resolve the most interesting physics while utilizing limited computational resources. Note that zonal transport of evaporated water within a given ocean basin is not accounted for with our choice of spatial domains, and that any evaporation within one of these domains that falls within the same domain is considered to be local despite substantial zonal transport of moisture that may have occurred.

Continuing with our mathematical development, substituting equation (3.6) into equation (3.5) yields

$$P_i = E_i + \left(\sum_{j, j \neq i} e_j f_{ji} E_j \right) - e_i E_i. \tag{3.9}$$

Now, suppose that we have n tagged regions. After a bit of rearrangement, this yields a set of equations that may be written compactly in matrix form as

$$\vec{P} = \vec{E} - (\mathbf{I} - \mathbf{F})\mathbf{T}\vec{E} \ , \tag{3.10}$$

where $\mathbf{T}$ is the export matrix, whose diagonal entries are equal to e_i, the fraction of vapor evaporated in i that diverges, and whose non-diagonal entries are nil; $\mathbf{I}$ is the identity matrix; and $\mathbf{F}$ is the convergence matrix, whose diagonal entries are zero and whose $(i, j)-$th entry $(i \neq j)$ is equal to f_{ji}, the fraction of exported atmospheric water from region j that is precipitated in region i.

Equation (3.10) may also be written as

$$\vec{P} = \vec{E} - \mathbf{T}\vec{E} + \mathbf{F}\mathbf{T}\vec{E} \ , \tag{3.11}$$

which gives three different contributions to the precipitation for a given region: the local evaporation ($\vec{E}$), the local evaporation that diverges ($-\mathbf{T}\vec{E}$), and the remote evaporation that converges ($\mathbf{F}\mathbf{T}\vec{E}$). In this framework, the RR, the fraction of the local precipitation

that originates locally, may be written as

$$RR = \frac{\vec{E} - \mathbf{T}\vec{E}}{\vec{P}} \ . \tag{3.12}$$

Furthermore, we may define the matrix operator $\mathbf{M}$ as

$$\mathbf{M} = \mathbf{I} - (\mathbf{I} - \mathbf{F})\mathbf{T} \ , \tag{3.13}$$

which we will use in conjunction with the forward and inverse methods described in §3.4.5 to compute either the evaporation $\vec{E}$ or the precipitation $\vec{P}$, given a particular spatial pattern of the other.

We consider the correspondence between the equations we have developed, (3.10) and (3.11), and the customary representation of atmospheric water conservation, equation (3.1). Equation (3.1) requires that we have some understanding of the dynamic moisture term $\nabla \cdot Q$, which, in turn, depends on knowing the specific humidity and wind velocity at different atmospheric levels and at short time intervals. In contrast, our formalism enables us to write this term as

$$-\nabla \cdot Q = (\mathbf{FT} - \mathbf{T})\vec{E}. \tag{3.14}$$

In this development, precipitation sourced from remote regions that is transported by atmospheric motions is contained in matrix $\mathbf{T}$, the export matrix, and $\mathbf{F}$, the convergence matrix. Evaporation, on the other hand, is the sole thermodynamic contribution to the precipitation; evaporation is, in effect, rearranged by atmospheric motions to produce the resulting pattern of precipitation. By synthesizing information about evaporated water from each of our source regions, we can bypass all considerations of the specific pathway by which moisture travels through the atmosphere; in effect, we only need to consider the endpoints.

3.3 Model Experiment Setup

We use the fully-coupled Community Earth System Model (CESM) version 1.2 (Hurrell et al., 2013) in which the atmosphere component, Community Atmosphere Model version 5.0 (CAM5, see Neale et al., 2012), has been refined to include water tagging capability. The methodology used to add WTs to the model is as described in Koster et al. (1986), Joussaume et al. (1986), Numaguti (1999), and Bosilovich and Schubert (2002). Being passive tracers, the WTs do not affect the mean state climate or any of the variables therein, and are effectively evolved independently of the atmospheric dynamics and physics.

Our simulation is performed with CAM5 at a $0.9^\circ \times 1.25^\circ$ spatial resolution, with the finite-volume dynamical core. Concentrations of greenhouse gases, ozone, volcanic constituents, and solar insolation are held at preindustrial levels, and atmospheric aerosols are evolved in prognostic mode. The coupled Community Land Model version 4.0 includes full carbon-nitrogen cycling. The ocean and sea ice components are on a displaced-pole grid at nominally 1° spatial resolution with the north pole singularity centered on Greenland. The ocean component is fully dynamic and is described in full by Danabasoglu et al. (2012). Subgrid-scale ocean eddies are parameterized with the GM90 eddy diffusion scheme (Gent and McWilliams, 1992), with the GM coefficient varying in space and time (Danabasoglu et al., 2012). The sea ice is fully thermodynamic and dynamic (Hunke and Lipscomb, 2004).

Tagged regions are shown in Figure 3.1, tagged ocean regions are specified in Table 3.2, and tagged land regions are specified in Table 3.3. In brief, every 10° latitude band in each of the major ocean basins (Atlantic, Pacific, and Indian) is given its own tag. For tagging purposes, the Arctic Ocean is subdivided into Atlantic and Pacific regions, and the Southern Ocean is subdivided into Indian, Pacific, and Atlantic regions. There are a total of 39 distinct tagged ocean regions. Each continent is tagged separately, with North America and Eurasia each subdivided at 45N for two tags each.

1.0

The tagged run was branched from year 1200 of an unperturbed preindustrial control

Tracer	Basin	Latitude Band	Notes
NH75P	Pacific	90N to 60N	Pacific Arctic; 100E to 260E
NH55P	Pacific	60N to 50N	
NH45P	Pacific	50N to 40N	
NH35P	Pacific	40N to 30N	
NH25P	Pacific	30N to 20N	
NH15P	Pacific	20N to 10N	
NH05P	Pacific	10N to Eq	
SH05P	Pacific	Eq to 10S	
SH15P	Pacific	10S to 20S	
SH25P	Pacific	20S to 30S	
SH35P	Pacific	30S to 40S	
SH45P	Pacific	40S to 50S	
SH55P	Pacific	50S to 60S	Pacific portion of Southern Ocean; 140E to 290E
SH65P	Pacific	60S to 90S	Pacific portion of Southern Ocean; 140E to 290E
NH80A	Atlantic	90N to 70N	Atlantic Arctic; 100W to 100E
NH65A	Atlantic	70N to 60N	
NH55A	Atlantic	60N to 50N	
NH45A	Atlantic	50N to 40N	
NH35A	Atlantic	40N to 30N	
NH25A	Atlantic	30N to 20N	
NH15A	Atlantic	20N to 10N	
NH05A	Atlantic	10N to Eq	
SH05A	Atlantic	Eq to 10S	
SH15A	Atlantic	10S to 20S	
SH25A	Atlantic	20S to 30S	
SH35A	Atlantic	30S to 40S	
SH45A	Atlantic	40S to 50S	
SH55A	Atlantic	50S to 60S	Atlantic portion of Southern Ocean; 70W to 20E
SH65A	Atlantic	60S to 90S	Atlantic portion of Southern Ocean; 70W to 20E
NH25I	Indian	30N to 20N	
NH15I	Indian	20N to 10N	
NH05I	Indian	10N to Eq	
SH05I	Indian	Eq to 10S	
SH15I	Indian	10S to 20S	
SH25I	Indian	20S to 30S	
SH35I	Indian	30S to 40S	
SH45I	Indian	40S to 50S	
SH55I	Indian	50S to 60S	Indian portion of Southern Ocean; 20E to 140E
SH65I	Indian	60S to 90S	Indian portion of Southern Ocean; 20E to 140E

Table 3.2: Description of each tagged ocean region, designated by ocean basin (Pacific, Atlantic, and Indian) and latitude band. Longitudinal limits are also included for regions in which the described tagged region is not confined to the specified ocean basin by land masses (i.e. regions that lie within the Arctic and Southern Ocean regions).

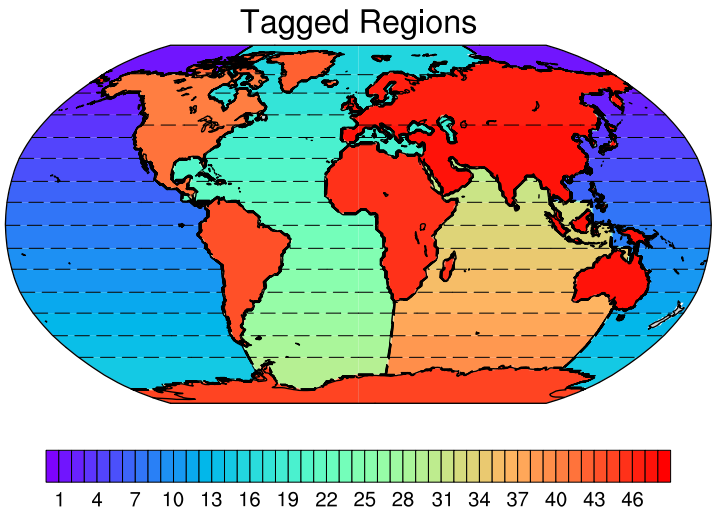

Figure 3.1: The 39 ocean regions and 9 land regions from which evaporated water is tagged. Each ocean basin is tagged separately in 10° latitude bands, with exceptions as noted in Table 3.2. Each major land mass (including Greenland) has its own tag, with North America and Eurasia subdivided at 45N to have 2 tags each; for more details, see Table 3.3.

Tracer	Continent	Latitude Limits	Notes
NA45N	North America	North of 45N	does not include Greenland
NA45S	North America	South of 45N	
GN	Greenland		
SA	South America		
AA	Antarctica		
AF	Africa		includes Madagascar
EU45N	Eurasia	North of 45N	
EU45S	Eurasia	South of 45N	includes the Maritime Continent
AU	Australia		includes New Zealand

Table 3.3: Description of each tagged land region, designated by continent and latitude limits (if applicable).

simulation, and was integrated for a total of 45 years. The first 30 years were used to construct the annually-averaged and seasonal climatologies that we use in the following analysis.

3.4 Results

Figure 3.2 displays each of the terms in equation (3.11). Over the ocean, the annual mean precipitation (Figure 3.2a) displays a strong maximum at the equator at the Inter-Tropical Convergence Zone (ITCZ), minima at the subtropics (between 10 to 30, N and S), and weaker maxima at the midlatitude storm tracks (between 40 to 60, N and S). The annual mean evaporation (Figure 3.2d) has a bimodal structure in which $\vec{E}$ peaks in each of the subtropical regions; there is a local minimum at the equator and tails on each poleward side approaching zero. The seasonal changes in $\vec{E}$ and $\vec{P}$ include a slight shift in the position of the ITCZ away from the winter hemisphere (Figure 3.2, compare panels b and c), a single Hadley cell with a strongly evaporative subsiding region in the winter hemisphere (compare panels e and f), and enhanced precipitation at the SH and NH storm tracks during their respective winters (compare panels b and c).

Though P and E over the ocean basins have many common features, there are some striking interbasin differences in how P is distributed by latitude. While the spatial structure of $\vec{E}$, both annually averaged and seasonal, is similar for the three ocean basins, the spatial structure of $\vec{P}$ is less so. The Atlantic, in particular, receives the least precipitation per unit area despite large evaporative fluxes that rival those of the other ocean basins. The region between 30N and 30S in the Atlantic is especially dry ($E-P$ is large and positive) relative to the same regions in the Indian and Pacific basins. The South Asian monsoon is also apparent in the seasonal precipitation patterns, with precipitation that is focused over the Maritime continent in DJF moving over the Indian subcontinent in JJA. These interbasin differences in precipitation and net $E - P$ are similar to those found in various observational datasets (see, e.g., Bryan and Oort, 1984; Trenberth et al., 2011), and indicate that the hydrological cycle over the world oceans is simulated reasonably well by CESM.

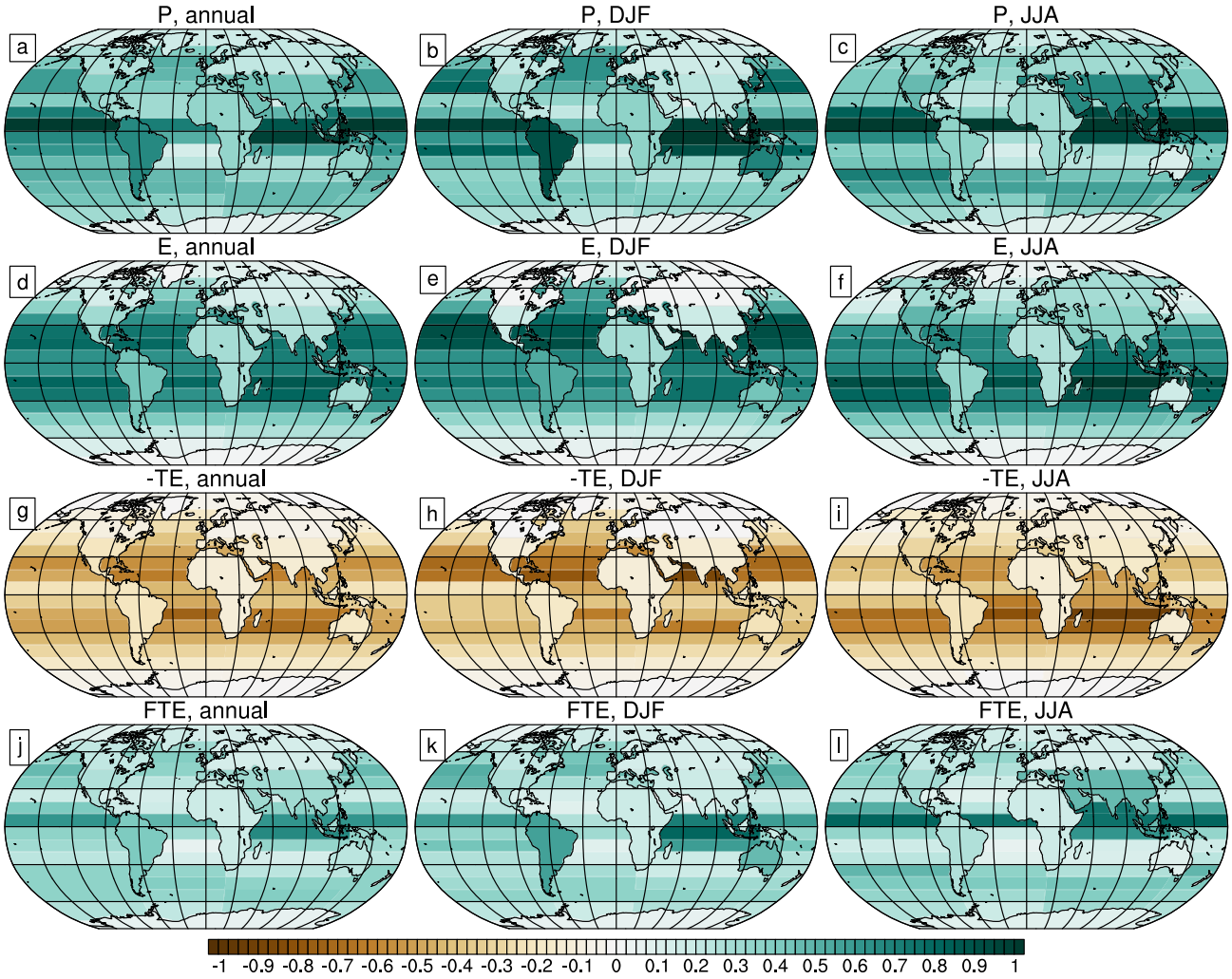

Figure 3.2: The precipitation $\vec{P}$ (panels a, b, and c), the evaporation $\vec{E}$ (panels d, e, and f), the divergence of locally-evaporated moisture $-\mathbf{T}\vec{E}$ (panels g, h, and i), and the convergence of remotely-evaporated moisture $\mathbf{FT}\vec{E}$ (panels j, k, and l), as developed in equations (3.10) and (3.11). These terms are shown in the annual mean (panels a, d, g, and j), for DJF (panels b, e, h, and k), and for JJA (panels c, f, i, and l). All quantities are in normalized units of length per area.

Nevertheless, model biases are also evident in the spatial distribution of $\vec{P}$, particularly over the tropical oceans. Of note is a prominent second precipitation maximum south of the equator over the Pacific basin in DJF. This double ITCZ problem is common to many GCMs, and may result from biases in tropical sea surface temperatures and associated cloud and radiative feedbacks (see Lin, 2007; Liu et al., 2014; Li and Xie, 2014).

Over land, areas located at the higher latitudes receive less precipitation but also evaporate less, particularly in winter. South America receives the most precipitation, especially in DJF, but also evaporates the most during this season. Southern Eurasia and North America follow a pattern similar to South America, though both E and P are smaller. Australia and Africa, on the other hand, are very arid and gain only slightly more moisture through precipitation than what they lose to evaporation.

Now, we turn to the second and third terms in equation (3.11), $-\mathbf{T}\vec{E}$ and $\mathbf{FT}\vec{E}$, whose sum constitutes the transport term $\nabla \cdot Q$ in equation (3.1). The first of the two, $-\mathbf{T}\vec{E}$, quantifies the divergence of local moisture from its region of evaporation; the second, $\mathbf{FT}\vec{E}$, quantifies the convergence and precipitation of remotely evaporated moisture. We now consider each of these terms in detail.

3.4.1 The Structure of $-\mathbf{T}\vec{E}$

The term $-\mathbf{T}\vec{E}$ quantifies the divergence of locally-evaporated moisture. By design, its contribution to the precipitation is negative, and it decreases the amount of locally-evaporated moisture available to precipitate locally by exporting away some fraction of it; this exported fraction is then allocated to other regions by the $\mathbf{FT}\vec{E}$ term. Shown in Figure 2, panels g, h, and i, the $-\mathbf{T}\vec{E}$ term has a spatial structure that is very similar to that of the evaporation (Figure 3.2, panels d, e, and f). In general, regions that are more evaporative, such as the subtropics, experience more moisture divergence than those regions that are less evaporative, such as the high latitudes. The exception to this rule is within the deep tropics (between 10N and 10S), where there is substantial evaporation but much of this locally-evaporated moisture also precipitates locally. Indeed, these are regions where there is little divergence

since moisture from the subtropics, transported by the lower (equatorward) branch of the Hadley cell, converges at the ITCZ.

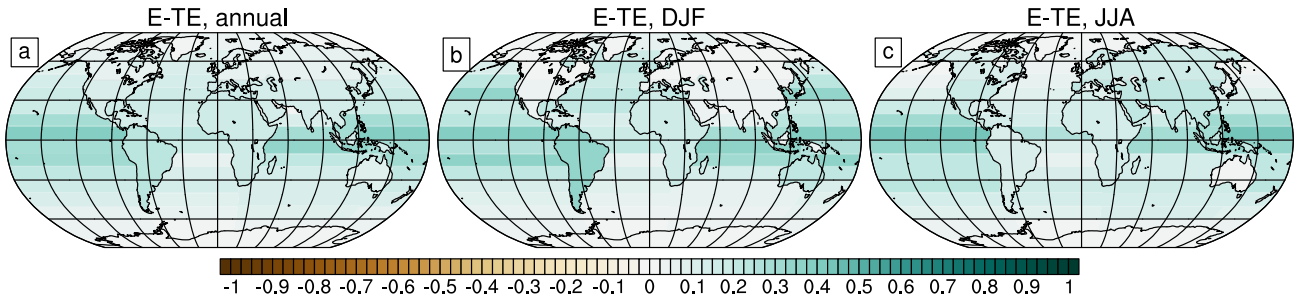

Figure 3.3: The sum of terms $\vec{E} - \mathbf{T}\vec{E} = (\mathbf{I} - \mathbf{T})\vec{E}$, which represents the locally-evaporated moisture in each tagged region that is precipitated locally. Shown for (a) the annual mean, (b) DJF, and (c) JJA. All quantities are in normalized units of length per area. For comparison purposes, the colorbar is identical to that used in Figure 3.2.

The expression $\vec{E} - \mathbf{T}\vec{E}$, shown in Figure 3.3, represents the portion of the total precipitation that is due to locally-evaporated moisture alone. For a given region i, this is $(1 - e_i)E_i$, equal to the total moisture evaporated from the region, E_i, reduced by the portion that is exported, $e_i E_i$. In the annual mean (Figure 3.3, panel a), this local contribution to the precipitation varies smoothly, with a broad maximum in the tropics. This pattern is also apparent seasonally, but includes a second, weaker maximum at the location of the midlatitude storm track in the winter hemisphere; a stronger midlatitude maximum is apparent in the NH than the SH (Figure 3.3, compare panels b and c). In most regions, the local contribution is significantly smaller than the remote contribution, $\mathbf{FT}\vec{E}$ (compare Figure 3.3, panels a, b, and c, with Figure 3.2, panels j, k, and l).

Comparing the ocean basins highlights regional asymmetries in the local divergence term (Figure 3.3, panels g, h, and i) and the local contribution to the total precipitation (Figure 3.3). The Atlantic basin has the highest local moisture divergence, particularly over the subtropics; as a result, the local contribution is also the smallest over the Atlantic compared to the local contributions over the Indian and Pacific basins. Over land areas, locally-

evaporated moisture is not very divergent, and each land region loses little locally-evaporated moisture to adjacent areas. While this is hardly surprising given the large spatial areas that each land tag covers (recall Figure 3.1 and Table 3.3), other studies have also noted that moisture recycling (i.e., precipitation sourced from local evaporation) is particularly important over large land regions, especially for those that are sufficiently removed from ocean source regions (see Eltahir and Bras, 1996; Trenberth, 1999; Gimeno et al., 2010; Trenberth et al., 2011).

Figure 3.4 shows the fraction of locally-evaporated moisture that precipitates remotely (e_i, the export fraction, shown in panels a, c, and e) and the fraction of locally-evaporated moisture that precipitates locally ($1 - e_i$, the local fraction, shown in panels b, d, and f). While these quantities are, undoubtedly, dependent upon the size and geographic orientation of the domain over which they are computed, they do provide a useful index for comparing the relative moisture divergence (and the relative size of the local contribution) between tagged regions. In the annual average, the export fraction is large and surprisingly homogeneous over ocean domains ($e_i \approx 0.75$). The smallest e_i values are found in the deep tropics over the Pacific basin and over ice-covered regions in the Arctic and Antarctic; the largest values ($e_i \approx 1.0$) are found over the Atlantic basin subtropics, particularly south of the equator. Over ocean, the gross spatial structure of the export and local fractions agree with our intuition of how the atmospheric circulation moves moisture around: the export fraction is smallest (and the local fraction is largest) where there is little divergence of moisture, at the equator and the poles; analogously, the export fraction is largest (and the local fraction is smallest) in the subtropics, where the mean circulation diverges moisture equatorward and midlatitude eddies move moisture (and latent heat) poleward.

The local and export fractions are more heterogeneous over land than ocean. Africa, South America, and Eurasia export less moisture than much of the surrounding ocean (0.5 for these land regions compared to 0.75 over ocean). Over some land areas, the export fraction varies dramatically by season: 0.3 in DJF compared to 0.65 in JJA for South America; and 0.8 in DJF compared to 0.4 in JJA for southern Eurasia; and 0.5 in DJF compared to 0.9 in

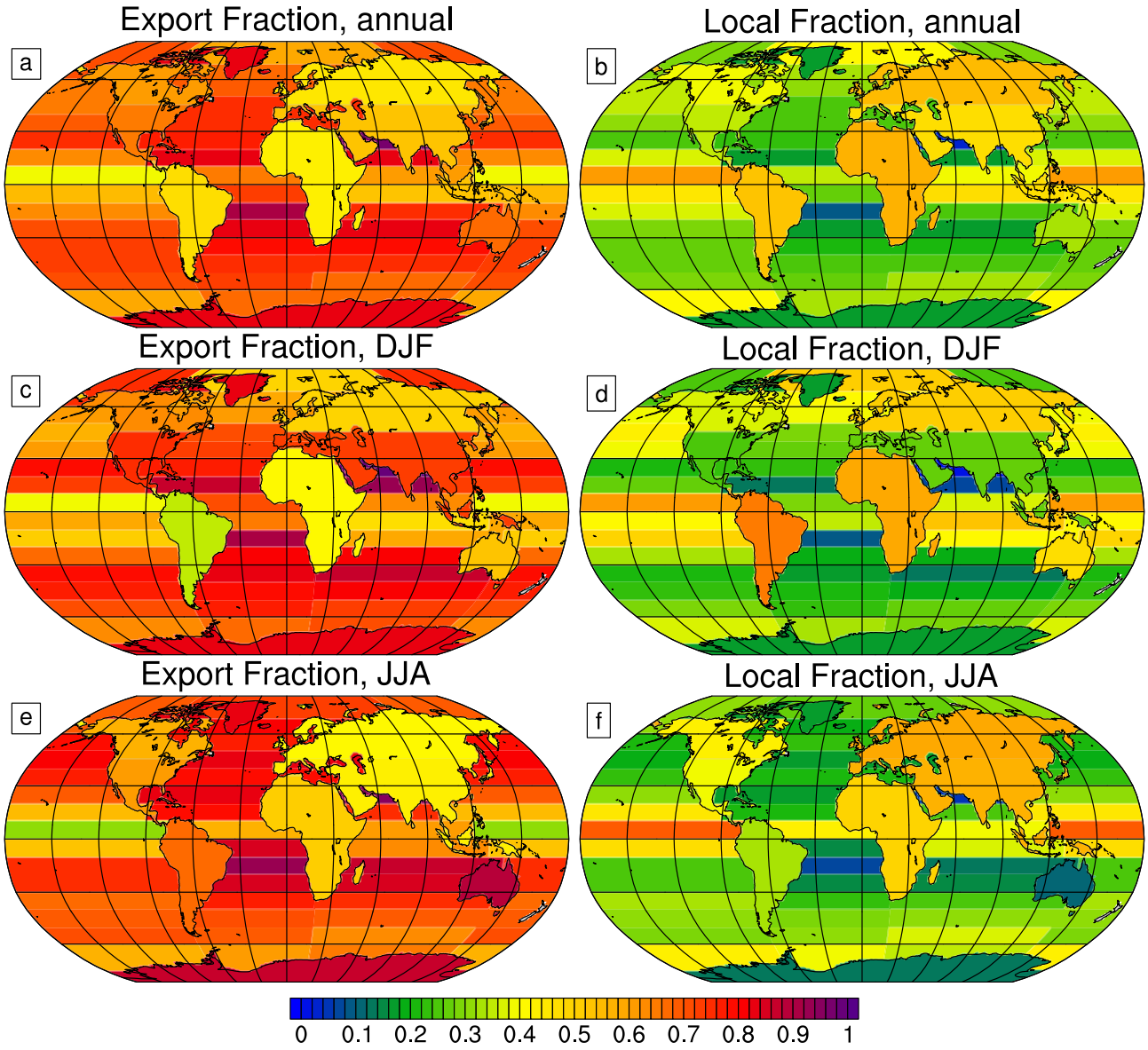

Figure 3.4: The export fraction e_i (the fraction of locally-evaporated moisture that diverges and precipitates remotely) is shown in panels (a), (c), and (e), and the local fraction, $(1-e_i)$ (the fraction of locally-evaporated moisture that precipitates locally) is shown in panels (b), (d), and (f). These quantities are shown in the annual mean (panels a and b), for DJF (panels c and d), and for JJA (panels e and f).

JJA for Australia. Over others, particularly Africa, northern Eurasia, and North America, the export fraction remains relatively constant year-round. For Greenland and Antarctica, the export fraction remains large year-round ($e_i \approx 0.8$) due to large-scale subsidence and downslope flow over these elevated ice sheets that tend to advect locally-evaporated (or locally-sublimated) moisture away.

3.4.2 The Structure of $\mathbf{FT}\vec{E}$

The moisture convergence term $\mathbf{FT}\vec{E}$ (shown in Figure 3.2, panels d, h, and l) quantifies how water evaporated remotely converges and precipitates over region i. By design, this term increases the total precipitation over region i by adding moisture sourced from other regions. $\mathbf{FT}\vec{E}$ has a spatial pattern similar to $\vec{P}$, a result that is not surprising given that the difference $\vec{E} - \mathbf{T}\vec{E}$ amounts to a modest residual (compare Figure 3.3, panels a, b, and c to Figure 3.2, panels d, h, and l). Indeed, the convergence of remote moisture must play a significant role in creating the distinct spatial pattern of $\vec{P}$ since the local contribution to the total precipitation is small.

Figure 3.5 shows that the convergence term $\mathbf{FT}\vec{E}$ and the total precipitation $\vec{P}$ are highly correlated and are close in value. The local contribution to the precipitation (which can be inferred as the vertical distance between each point and the one-to-one line) is modest, and the contribution from remotely-evaporated moisture accounts for over 60% of the total precipitation (as shown by the proximity of the scattered $\vec{P}$ versus $\mathbf{FT}\vec{E}$ points to the one-to-one line).

The relationship between $\vec{P}$ and $\mathbf{FT}\vec{E}$, seasonally and in the annual mean, can be described succinctly by a least-squares regression of the form

$$\mathbf{FT}\vec{E} \approx \alpha\vec{P} + \beta \ , \tag{3.15}$$

where $\alpha \approx 0.6$ and $\beta \approx 0.05$. That equation (3.15) approximates the relationship between moisture convergence and the total precipitation so well is consistent with the spatial simi-

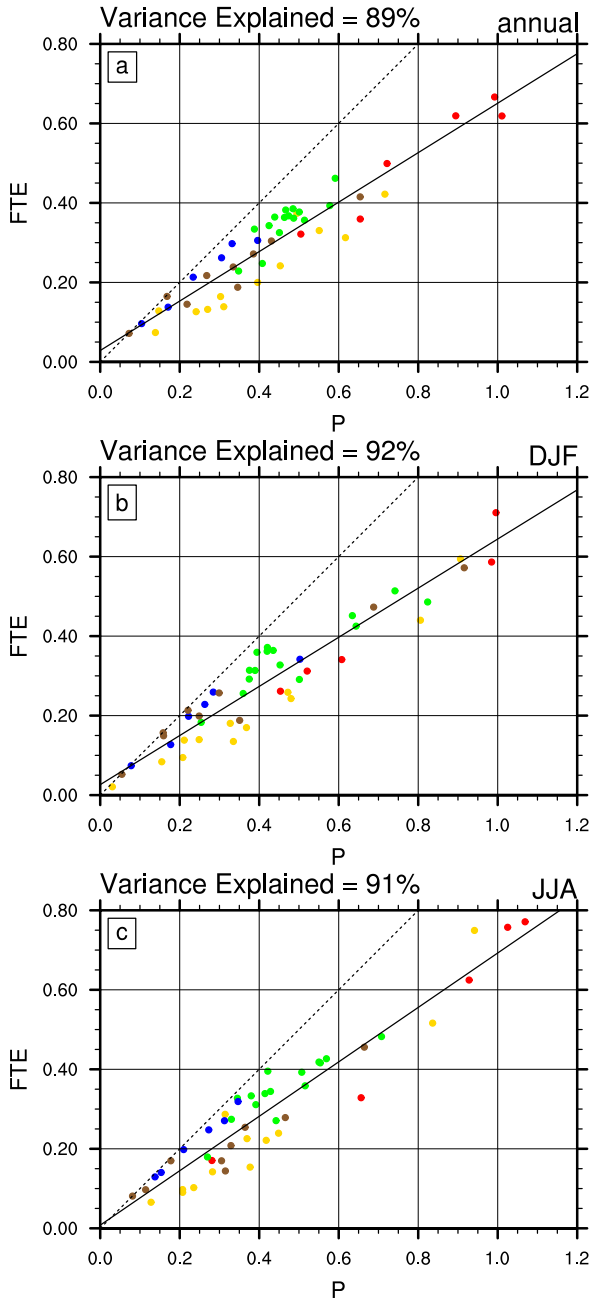

Figure 3.5: The values of $(\mathbf{FT}E)_i$ as a function of P_i for each tagged region i in (a) the annual mean, (b) DJF, and (c) JJA. The markers denote different tagged regions, with regions between 10N and 10S (the deep tropics) shown in red; regions between 10N and 40N and between 10S and 40S (the subtropics) shown in gold; regions between 40N and 60N and between 40S and 60S (the midlatitudes) shown in green; regions poleward of 60S and 60N shown in blue; and land areas shown in brown. Also shown are the least squares regression best-fit line (solid) and the one-to-one line (dashed).

larity of the $\mathbf{FT}\vec{E}$ term to $\vec{P}$, as shown in Figure 3.2. As stated earlier, the distinct spatial structure of $\vec{P}$ is mostly determined by the convergence of remotely-evaporated moisture. Furthermore, wet regions (those that receive lots of precipitation per unit area) receive proportionately more remotely-sourced moisture while dry regions receive proportionately less, consistent with a roughly linear relationship between precipitation and the remote convergence term.

Figure 3.5 also highlights regional differences in the relationship between $\vec{P}$ and $\mathbf{FT}\vec{E}$ over ocean. The high latitude data points (defined as those whose delineated regions are poleward of 60N or 60S, shown in blue in Figure 3.5) lie the closest to the one-to-one line in the annual mean, DJF, and JJA. This means that the precipitation in the high latitudes is almost completely determined by the convergence of remotely-evaporated moisture (rather than by local evaporation). The local contribution to precipitation in the high latitudes is smallest in JJA (see panel c in Figure 3.5), suggesting that remotely-evaporated moisture convergence still dominates the precipitation in NH summer despite higher local temperatures, more open ocean, and more shortwave energy available at the surface for evaporation.

The midlatitudes (between 30N and 60N in the NH and between 30S and 60S in the SH, shown in green in Figure 3.5) also exhibit a similar tendency in that $\vec{P}$ versus $\mathbf{FT}\vec{E}$ points lie between the one-to-one line and the line of best-fit (albeit less so than the high latitude points discussed earlier). Therefore, remotely-evaporated moisture that converges into these latitudes contributes a greater fraction to the total precipitation here than it does on average, highlighting the important role that subtropical water sources play in providing moisture to the midlatitudes.

At what latitudes is the local contribution to the precipitation more important (on average) than the remote contribution? Figure 3.5 shows that nearly all points representing latitudes equatorward of 30S and 30N (shown in gold and red) lie to the right of the best-fit line. In regions equatorward of 10N and 10S (shown in red), the total precipitation per unit area tends to be large, and locally-evaporated moisture and remotely-evaporated moisture make nearly equal contributions to the total precipitation. Even in the ITCZ, where moisture

evaporated in the subtropics converges via the Hadley cell, nearly half of what precipitates originates locally.

In the subtropics (the regions from 10S to 30S and from 10N to 30N, shown in gold), the total precipitation per unit area is generally less than it is in the deep tropics, but there is a similar tendency for a larger fraction of precipitation to originate from local sources. This is consistent with high evaporation rates in the subtropics and divergence of this moisture with the mean flow around the subtropical highs.

Most land areas (shown in brown in Figure 3.5) lie close to the line of best fit, suggesting that these areas are as dependent on remotely-converging moisture as the average area. In general, land regions with less precipitation per unit area rely more on remotely-evaporated moisture, and tend to lie closer to the one-to-one line.

3.4.3 Decompositions of the Convergence Term $\mathbf{FT}\vec{E}$

In the following sections, we present various decompositions of the matrix $\mathbf{F}$ and their respective contributions to the $\mathbf{FT}\vec{E}$ term. Such decompositions provide insight into the mechanisms by which spatial patterns of moisture convergence give rise to precipitation. The singular value decomposition of $\mathbf{F}$ is presented in §3.4.3, and various physical decompositions of $\mathbf{F}$ are presented in §3.4.3.

Singular Value Decomposition of $\mathbf{F}$

We write the singular value decomposition (SVD) of $\mathbf{F}$ as

$$\mathbf{F} = \mathbf{U}\mathbf{\Sigma}\mathbf{V}^T \ , \tag{3.16}$$

where $\mathbf{U}$ is the matrix whose columns are the left singular vectors of $\mathbf{F}$, $\mathbf{\Sigma}$ is a diagonal matrix whose entries are the singular values of $\mathbf{F}$ (ordered from largest to smallest), and $\mathbf{V}^T$ is a matrix whose rows are the right singular vectors of $\mathbf{F}$. Let $\vec{u}_m$ be the m-th left singular vector, $\vec{v}_m$ by the m-th right singular vector, and let σ_m be the m-th singular value. Then,

we may write matrix $\mathbf{F}$ exactly as the sum of rank-one matrices formed by the outer product of $\vec{u}_m$ and $\vec{v}_m$ weighted by the respective singular value σ_m:

$$\mathbf{F} = \sum_m \sigma_m \vec{u}_m \otimes \vec{v}_m = \sum_m \mathbf{F}_m \ , \tag{3.17}$$

where the matrices $\mathbf{F}_m$ are the successive rank-one approximations to $\mathbf{F}$.

If the matrix $\mathbf{F}$ has a structure dominated by a few of these orthogonal modes, only the first few $\mathbf{F}_m$ are required to make a reasonable approximation to $\mathbf{F}$ since subsequent singular values will be small. If only the first two terms in equation (3.17) are retained, for example, $\mathbf{F}$ may be approximated as

$$\mathbf{F} = \mathbf{F}_1 + \mathbf{F}_2 + \mathbf{F}_{\mathbf{res}} \approx \mathbf{F}_1 + \mathbf{F}_2 \ , \tag{3.18}$$

where $\mathbf{F}_{res}$ is the residual formed from the subsequent (smaller) terms in equation (3.17). Using equation (3.18) for $\mathbf{F}$ yields the following expression for the convergence term:

$$\mathbf{F}\mathbf{T}\vec{E} = \sum_{m=1,2} \mathbf{F}_\mathbf{m}\mathbf{T}\vec{E} + \mathbf{F}_\mathbf{res}\mathbf{T}\vec{E} \approx \sum_{m=1,2} \mathbf{F}_\mathbf{m}\mathbf{T}\vec{E}. \tag{3.19}$$

Figure 3.6 shows the contribution of the first two rank-one updates of the SVD of $\mathbf{F}$ to the $\mathbf{F}\mathbf{T}\vec{E}$ term in the annual mean (as described in equation 3.19), and the first two left and right singular vectors that are used to create this decomposition (as described in equation 3.17). Remarkably, Figure 3.6 shows that the matrix $\mathbf{F}$ is well-approximated by the first rank-one update matrix; the second rank-one update and all remaining contributions to $\mathbf{F}$ are small (not shown). In effect, $\mathbf{F}$ has a rank of one, suggesting that there is only one degree of freedom in the way that moisture is partitioned between the regions in which it precipitates. Therefore, partitioning of remotely evaporated moisture is a non-random process; in effect, there is only one underlying mathematical rule that governs this moisture transport.

The first of the rank-one update matrices of $\mathbf{F}$ produces a precipitation pattern very

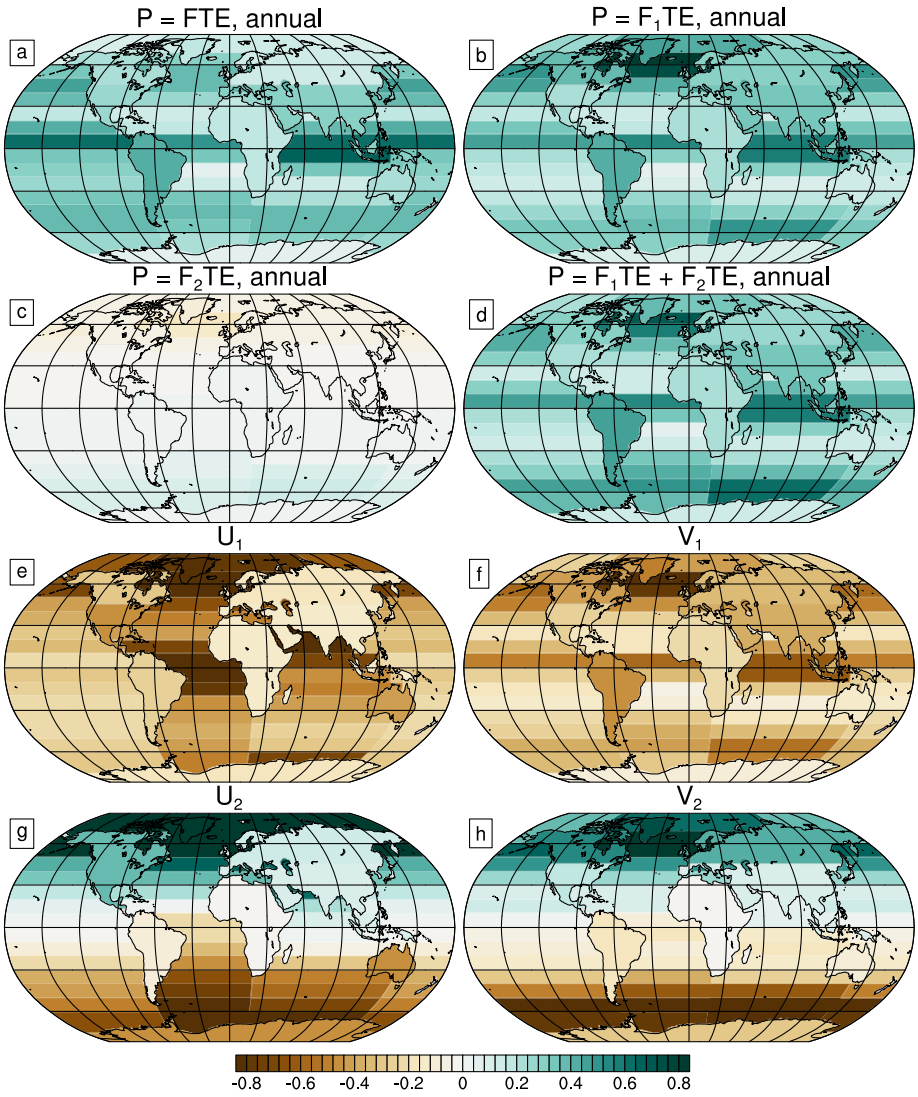

Figure 3.6: Decomposition of the $\mathbf{FT}\vec{E}$ term using the SVD: (a) the full $\mathbf{FT}\vec{E}$ term (shown for comparison purposes), (b) the contribution from the first rank-one update of $\mathbf{F}$, (c) the contribution from the second rank-one update of $\mathbf{F}$, and (d) the contribution from the sum of the first and second rank-one update terms. The first and second left and singular vectors of the SVD of $\mathbf{F}$ are also shown: (e) first left singular vector of $\mathbf{F}$, (f) first right singular vector of $\mathbf{F}$, (g) second left singular vector of $\mathbf{F}$, and (h) second right singular vector of $\mathbf{F}$.

similar to the total $\mathbf{FT}\vec{E}$ term (panel b), while the second produces a weak NH - SH dipole pattern (panel c). The left singular vector corresponding to $\mathbf{F}_1$ (panel e) is an evaporation pattern that is focused over the Arctic, Atlantic, and equatorial Indian basins; this indicates that the most parsimonious way of re-creating $\mathbf{F}$ is through evaporation sourced from these regions. The sinks, which correspond to the right singular vector (shown in panel f), appear much like the full precipitation signal (compare panels f and a).

Physical Decompositions of $\mathbf{F}$

Alternatively, matrix $\mathbf{F}$ may be decomposed using physical, rather than mathematical, considerations. Since all the entries of matrix $\mathbf{F}$ describe the convergence of remotely-evaporated moisture from some region j into some (different) region i, $\mathbf{F}$ may be written as a finite sum of matrices $\mathbf{F}_p$, where p represents some special physical property that is satisfied by i and j:

$$\mathbf{F} = \sum_p \mathbf{F}_p \ , \tag{3.20}$$

where

$$\mathbf{F}_p = \begin{cases} f_{ij} & \text{if } i \text{ and } j \text{ satisfy some criterion} \\ 0 & \text{if } i = j \\ 0 & \text{otherwise.} \end{cases} \tag{3.21}$$

As demonstrated with the SVD, the decomposition of $\mathbf{F}$ in equation (3.20) may be used to subdivide the convergence term into distinct parts due to each of the sub-matrices $\mathbf{F}_p$:

$$\mathbf{FT}\vec{E} = \sum_p \mathbf{F}_p\mathbf{T}\vec{E} = \sum_p \left(\mathbf{FT}\vec{E}\right)_p \ . \tag{3.22}$$

First, we consider a decomposition in which $\mathbf{F}$ is separated into a set of sub-matrices depending on whether the areas of evaporation and precipitation are over ocean or land: (1) a submatrix in which moisture that evaporates from the ocean also precipitates over the ocean, $\mathbf{F}_{OO}$; (2) another in which moisture that evaporates from the ocean precipitates

over land, $\mathbf{F}_{OL}$; (3) another in which moisture that evaporates from land precipitates over the ocean, $\mathbf{F}_{LO}$; and (4) a final submatrix in which moisture evaporating from land also precipitates over land, $\mathbf{F}_{LL}$. In other words $\mathbf{F}$ may be written as the exact sum

$$\mathbf{F} = \mathbf{F}_{OO} + \mathbf{F}_{OL} + \mathbf{F}_{LO} + \mathbf{F}_{LL} \ . \tag{3.23}$$

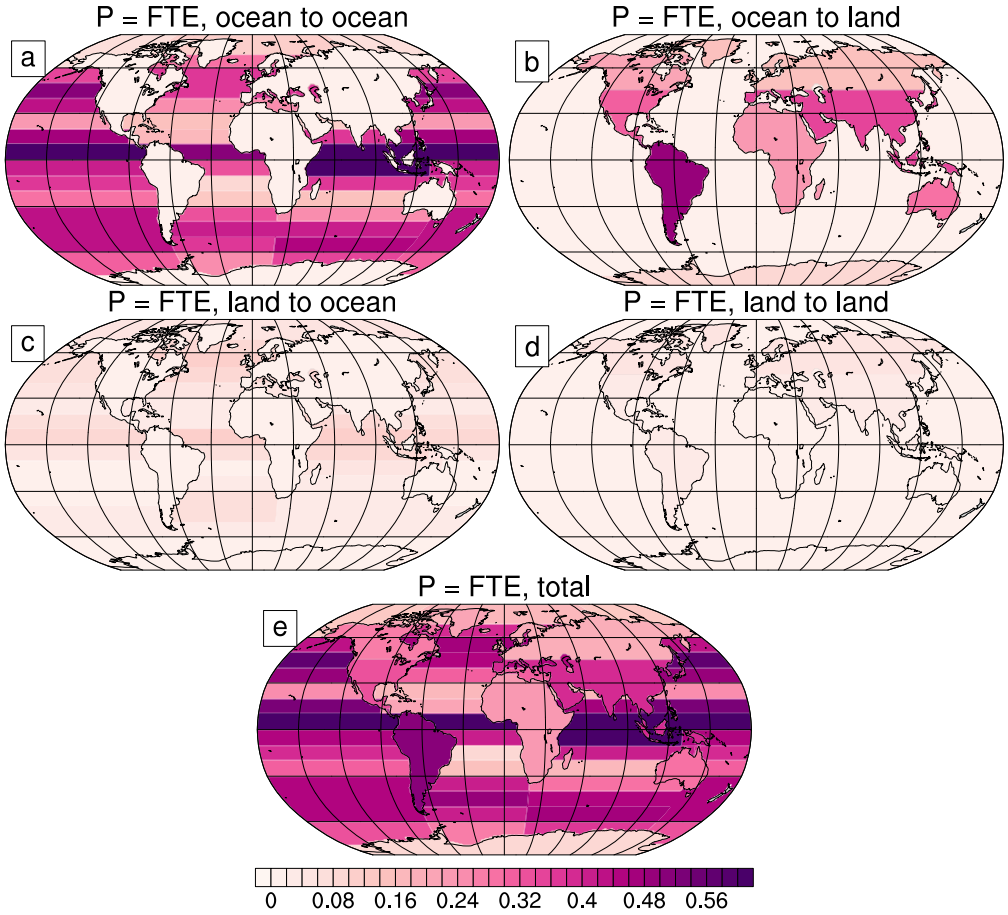

Figure 3.7: Physics-based decomposition of $\mathbf{FT}\vec{E}$ in the annual average. The top row shows decomposition of the remote convergence term $\mathbf{FT}\vec{E}$ into components as described in equation (3.23): (a) ocean to ocean, (b) ocean to land, and (c) land to ocean, and (d) land to land components. The full $\mathbf{FT}\vec{E}$ term is shown in panel (e).

Substituting components of $\mathbf{F}$ from equation (3.23) into equation (3.22) yields the com-

ponents of $\mathbf{FT}\vec{E}$ shown in Figure 3.7. Immediately apparent is that $\mathbf{F}_{OO}\mathbf{T}\vec{E}$, the portion of the remote convergence term due to evaporation and precipitation over ocean (panel a), is much greater in magnitude than $\mathbf{F}_{LO}\mathbf{T}\vec{E}$, the portion due to evaporation over land and precipitation over ocean (panel c). Likewise, $\mathbf{F}_{OL}\mathbf{T}\vec{E}$, the portion of the remote convergence term due to evaporation from ocean and precipitation over land (panel b), is much greater in magnitude than $\mathbf{F}_{LL}\mathbf{T}\vec{E}$, the portion of the remote convergence term due to evaporation and precipitation over land (panel d). Neither of these results are surprising, given that evaporation over the world oceans greatly exceeds evaporation over land as it is not limited by surface moisture availability (Trenberth et al., 2011). In addition, each individual land tag covers a large geographic area, a feature of the experiment design that minimizes moisture transfer among tagged land regions.

Nevertheless, Figure 3.7 illustrates that most remotely-sourced moisture evaporates from the global ocean, not land. In the following analysis, the ocean-to-ocean term (panel a) will be further subdivided using physically-motivated considerations; we consider the ocean-to-land term (panel b) further in §3.4.4.

We present three physical decompositions of matrix $\mathbf{F}_{OO}$. In the first, $\mathbf{F}_{OO}$ is subdivided into (1) a component in which moisture precipitates north of its point of evaporation, $\mathbf{F}_{SN}$, (2) one in which moisture precipitates south of its point of evaporation, $\mathbf{F}_{NS}$, and (3) one in which moisture precipitates within the same latitude band (but different ocean basin) as where it evaporated, $\mathbf{F}_{zon}$:

$$\mathbf{F}_{OO} = \mathbf{F}_{SN} + \mathbf{F}_{NS} + \mathbf{F}_{zon} \ . \tag{3.24}$$

In the second, $\mathbf{F}_{OO}$ is subdivided into an interbasin component $\mathbf{F}_{inter}$ (where moisture evaporates in one ocean basin and precipitates in another) and an intrabasin component $\mathbf{F}_{intra}$ (where moisture evaporates and precipitates in the same basin):

$$\mathbf{F}_{OO} = \mathbf{F}_{inter} + \mathbf{F}_{intra} \ . \tag{3.25}$$

In the third, $\mathbf{F}_{OO}$ is subdivided into (1) a pure meridional component in which moisture

travels meridionally within the basin in which it evaporated to its point of precipitation, $\mathbf{F}_{merid}$, (2) a pure zonal component in which moisture evaporates within a given latitude band and precipitates in the same latitude band but in a different basin, $\mathbf{F}_{zon}$, and (3) a cross component in which moisture travels both meridionally and zonally from its region of evaporation to its region of precipitation, $\mathbf{F}_{cross}$:

$$\mathbf{F}_{OO} = \mathbf{F}_{merid} + \mathbf{F}_{zon} + \mathbf{F}_{cross} \ . \tag{3.26}$$

Applying equation (3.22) to each of these three decompositions yields the various components of the remote convergence term in the annual mean (Figure 3.8) and by season (Figure 3.9).

First, we consider the decomposition of $\mathbf{F}_{OO}$ given in equation (3.24), which separates the northerly and southerly components of meridional moisture convergence. Panels a, b, and c of Figure 3.8 show that moisture converging into the midlatitude and subpolar oceans mostly originates equatorward of where it precipitates. This result is true for all ocean basins, which suggests that moisture transport into the mid- and high-latitudes varies little by basin. Seasonal changes in this moisture convergence are apparent in Figure 3.9 (compare panels a, b, c with panels i, j, k). In the NH, there is a clear seasonality to moisture convergence, in that convergence is much stronger in DJF than it is in JJA (compare panels b and j). In the SH, on the other hand, there is much less of a seasonal difference; moisture convergence into the SH midlatitudes is substantial in both DJF and JJA (compare panels a and i), though there is slightly less northerly moisture transport and convergence in DJF than in JJA.

Unlike the mid- and high-latitudes, moisture convergence into the deep tropics has a distinct spatial and seasonal pattern that varies by basin. In the annual mean, moisture converging over the equatorial Indian ocean originates mostly from the south, which is expected due to the geographical constraints of the basin, namely that its northernmost extent lies at approximately 30N. The SH Hadley cell, which transports latent heat northward in JJA, is responsible for most equatorward moisture transport in the Indian basin since there

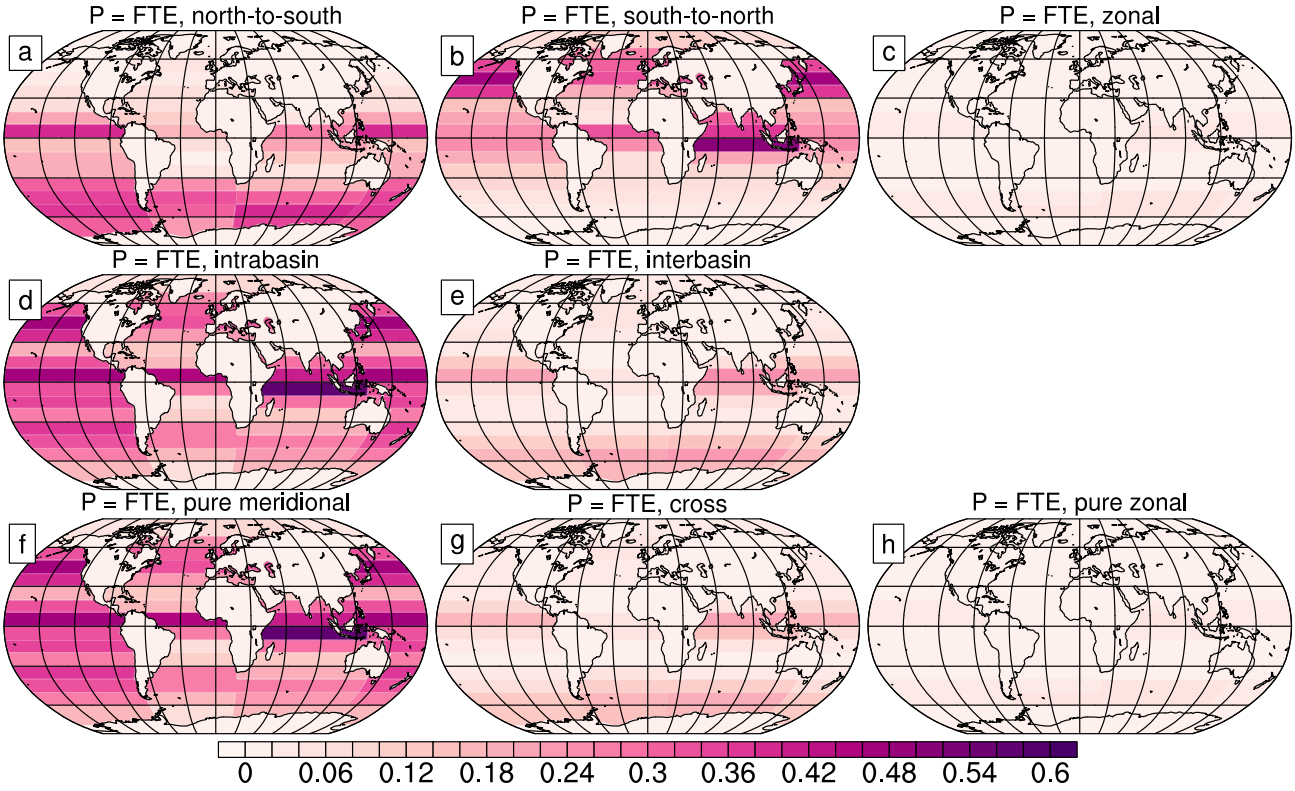

Figure 3.8: Physics-based decomposition of $\mathbf{F}_{OO}\mathbf{T}\vec{E}$ in the annual average. The top row shows decomposition into (a) northward, (b) southward, and (c) zonal components, as in equation (3.24); the middle row shows decomposition into (d) intrabasin and (e) interbasin components, as in equation (3.25); and the bottom row shows decomposition into (f) a purely meridional component, (g) a cross component (both meridional and zonal), and (h) a purely zonal component, as in equation (3.26). As described in the text, each row sums to the total ocean-to-ocean convergence term, $\mathbf{F}_{OO}\mathbf{T}\vec{E}$.

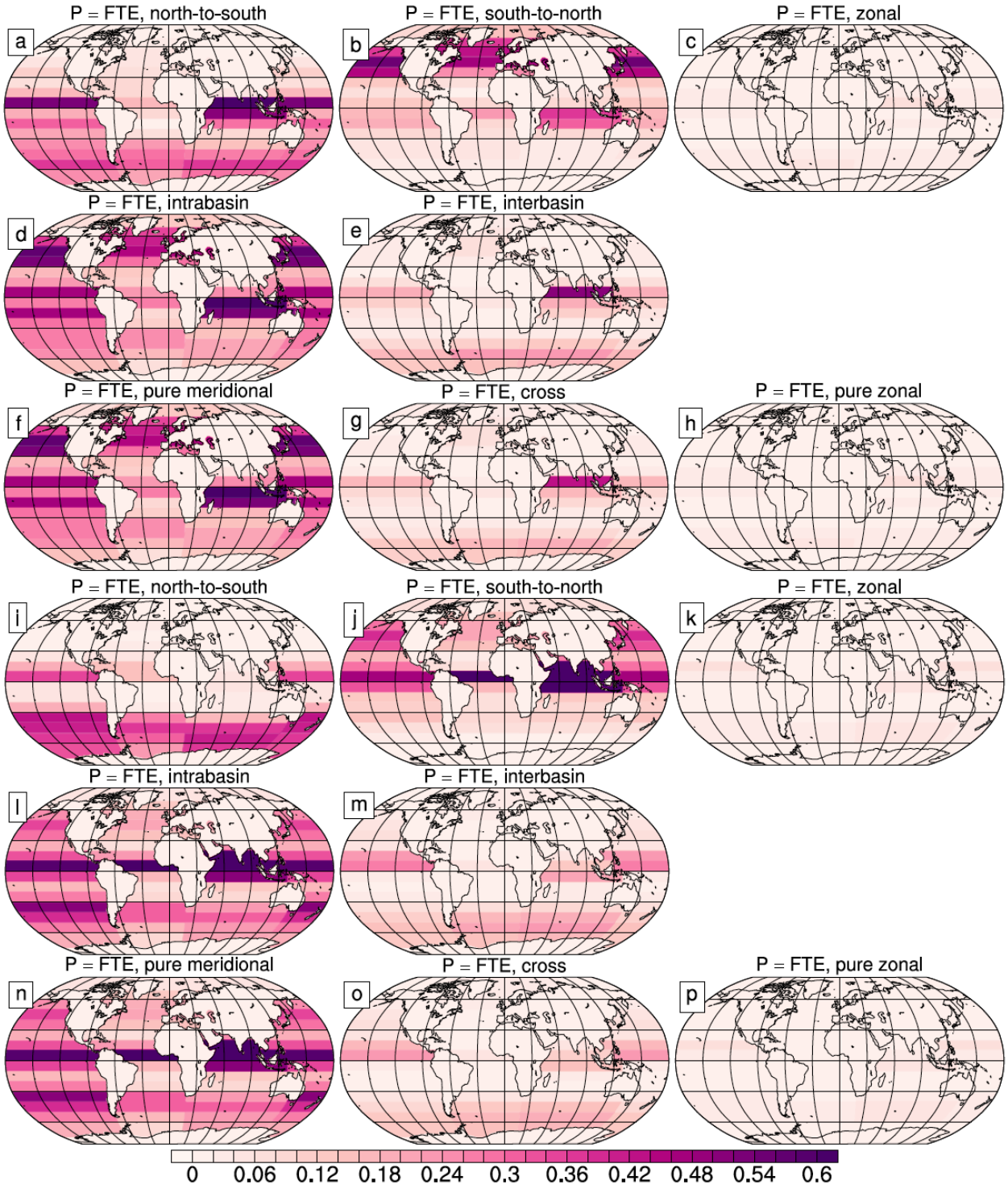

Figure 3.9: Physics-based decomposition of $\mathbf{FT}\vec{E}$ for DJF (panels a through h) and for JJA (panels i through p). The decompositions are the same as described for Figure 3.8.

is not much ocean area available for evaporation in the NH subtropics. As a result, northerly moisture convergence over the equatorial Indian is modest in DJF (Figure 3.9, panel a), while southerly moisture convergence is substantial in JJA (Figure 3.9, panel j).

Over the Atlantic basin, equatorial precipitation tends to be dominated by the SH Hadley cell rather than the NH one, though this seasonal difference in the atmospheric moisture transport is not due to obvious geographical constraints, as they are for the Indian basin. In the Pacific basin, on the other hand, both the NH and SH Hadley cells are equally responsible for creating the equatorial precipitation maximum (compare panels a and j in Figure 3.9), with north-to-south (south-to-north) moisture transport from the NH (SH) Hadley cell dominating DJF (JJA) as expected.

Next, we consider the decomposition of $\mathbf{F}_{OO}$ given in equation (3.25), which separates the intrabasin and interbasin components of the moisture convergence. In general, the intrabasin moisture convergence greatly exceeds the interbasin contribution (compare panels d and e in Figure 3.8; compare panels d and e, and panels l and m in Figure 3.9). Given that distance and orography separate the ocean basins at most latitudes, it is not surprising that intrabasin convergence exceeds interbasin convergence.

There are, however, a few regions where interbasin moisture transport is significant. Over the equatorial Pacific and Indian basins, interbasin moisture convergence is significant year-round (see Figure 3.8 panel e, and Figure 3.9 panels e and m), with larger interbasin moisture convergence over the equatorial Pacific (Indian) in JJA (DJF). In the tropics, equatorial easterlies advect moisture westward; when land distances are sufficiently small and orography is low, these winds can transport moisture between basins. Thus, moisture evaporated from the Atlantic basin can travel over the Isthmus of Panama to precipitate over the Pacific, and moisture evaporated from the Pacific basin can travel over the Maritime continent to precipitate over the Indian. On the other hand, the African continent is too great a land barrier, and little moisture is transported from the Indian basin to the Atlantic.

Over the Southern Ocean (south of 50S), the relative absence of land and orographic barriers allows for significant interbasin moisture convergence year-round. Here, surface

westerlies freely advect evaporated moisture eastward, and midlatitude eddies in the storm-track also transport moisture poleward. In the NH storm track, conversely, there is little transport of moisture across basins due to blocking by the North American and Eurasian continents.

Finally, we may further decompose interbasin moisture convergence by using equation (3.26). The first term in this decomposition corresponds to the intrabasin moisture convergence, while the latter two sum to the interbasin moisture convergence. These latter terms allow the interbasin component to be separated further into a purely zonal part (where moisture evaporates from and precipitates in the same latitude band) and a cross part (where moisture evaporates from a different latitude band than the one it precipitates in). Overall, the purely zonal component is very small (see panel h in Figure 3.8 and panels h and p in Figure 3.9), and most of the interbasin convergence is encompassed in the cross term (see panel g in Figure 3.8 and panels g and o in Figure 3.9). This suggests that over all regions where interbasin moisture transport is important (i.e. in the tropics and over the Southern Ocean), this transport nearly always has a meridional component. Thus, both zonal and meridional advection are required to precipitate moisture in a basin that is different from its basin of origin.

3.4.4 Indentifying Precipitation Source Regions using $\mathbf{FT}\vec{E}$

How much precipitation over a region is remotely sourced from every other tagged region? While $\mathbf{FT}\vec{E}$ gives the total precipitation that originates remotely, it does not provide any information on which tagged regions this precipitation came from. Remote source regions are particularly interesting over land since a substantial fraction of terrestrial precipitation originates from the global ocean (recall Figure 3.5).

To visualize remote moisture convergence into one particular region, we consider individual terms in the product of matrices $\mathbf{FT}$ with $\vec{E}$. Consider the product of the i-th row of

FT with $\vec{E}$. This is the sum

$$\sum_{j,j\neq i} f_{ji} e_j E_j = \sum_{j,j\neq i} \tilde{E}_{ji} \ , \tag{3.27}$$

where each $\tilde{E}_{ji}$ represents the part of the precipitation over region i that originated in region j. The sum of the $\tilde{E}_{ji}$ yields the portion of the total precipitation over region i that originated remotely, P_i^r:

$$\sum_{j,j\neq i} \tilde{E}_{ji} = P_i^r \ . \tag{3.28}$$

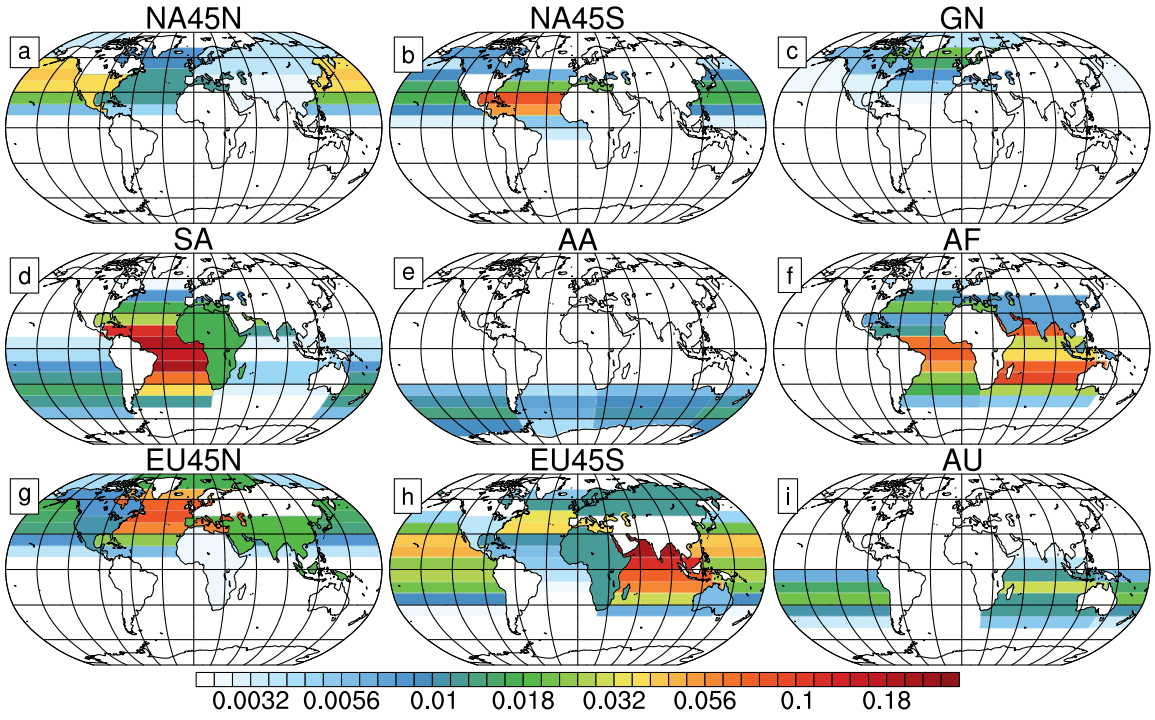

Figure 3.10: Sources of precipitation from remote regions $\tilde{E}_{ji}$, annually averaged and in normalized units of length per unit area of source region, for each of the tagged land areas: (a) North America, north of 45N, (b) North America, south of 45N, (c) Greenland, (d) South America, (e) Antarctica, (f) Africa, (g) Eurasia, north of 45N, (h) Eurasia, south of 45N, and (i) Australia. Note that the color bar is shown on a log scale.

The individual precipitation contributions $\tilde{E}_{ji}$ to each tagged land area i from all other

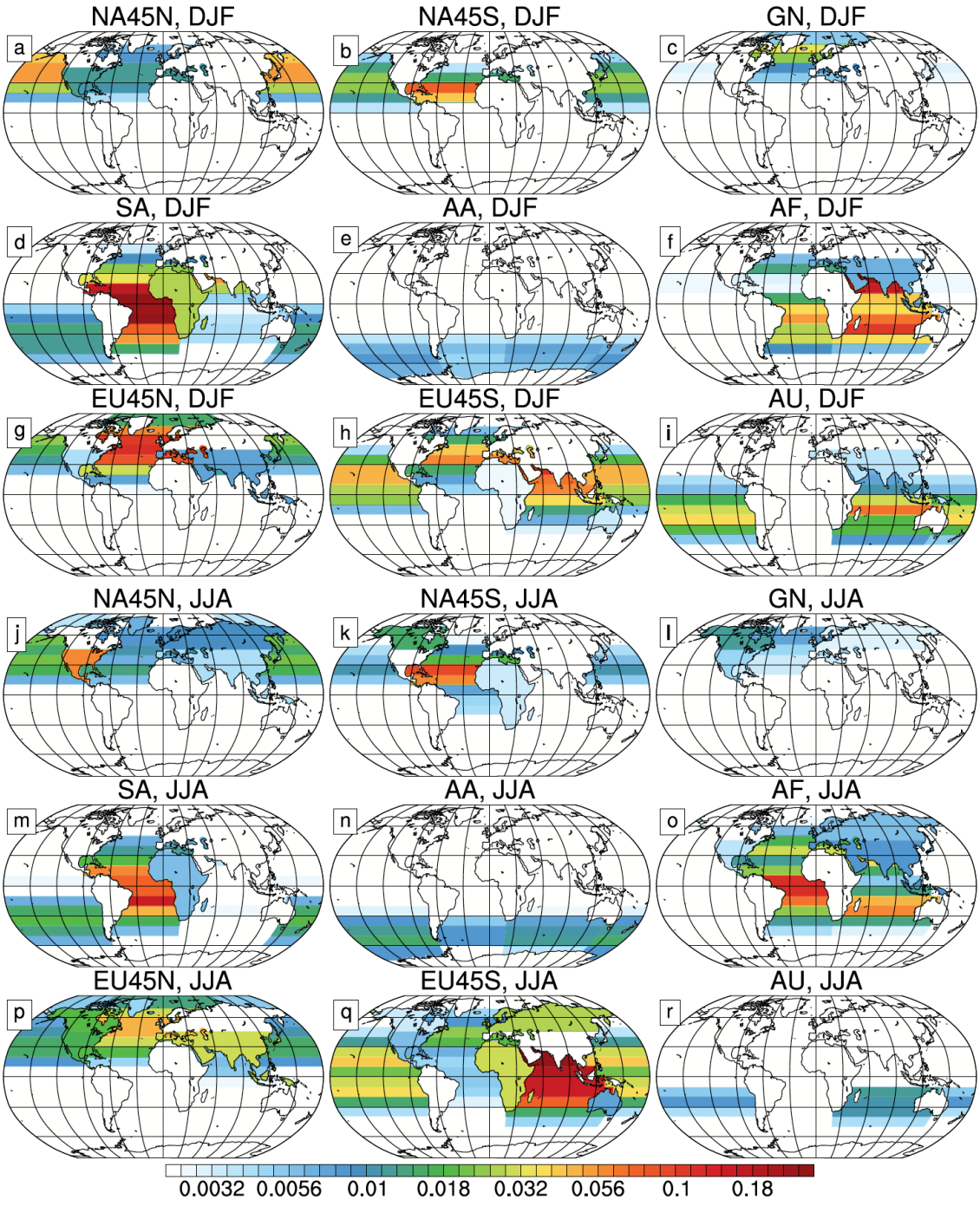

Figure 3.11: As in Figure 3.10, but for DJF (panels a through i) and JJA (panels j through r).

tagged areas j is shown for the annual mean in Figure 3.10 and by season in Figure 3.11. Predictably, in the annual average and seasonally, ocean areas provide moisture to land areas that are down-wind. Thus, land regions in the tropics receive moisture from ocean that is to the west (via the equatorial easterly winds), while land regions in the midlatitudes receive moisture from ocean that is to the east (via the midlatitude westerly winds). Midlatitude cyclones transport moisture poleward to high-latitude regions, such as Greenland, northern Eurasia, northern North America, and Antarctica. Almost all of this moisture originates poleward of 30N or 30S, and very little moisture from the tropics precipitates in these mid- and high-latitude regions.

Figures 3.10 and 3.11 both reveal substantial differences in the amount of moisture each ocean basin contributes to terrestrial precipitation. Year-round, the Atlantic basin contributes the most moisture (per unit area) to precipitation over southern North America, Greenland, South America, and northern Eurasia. The Atlantic basin is also the most important source of precipitation for Africa in JJA, though the Indian basin dominates in the annual average and in DJF. In addition to Africa, the Indian basin is also the most important moisture source region for southern Eurasia and Australia. Surprisingly, the Pacific basin is the dominant moisture source for only two regions, northern North America and Antarctica. The Pacific basin, however, is an important moisture source for northern and southern Eurasia, southern North America, South America, and Australia, albeit a less important one than the other basins noted earlier.

3.4.5 Forward and Inverse Methods using the Operator $\mathbf{M}$

Recall that the matrix operator $\mathbf{M} : \vec{E} \rightarrow \vec{P}$, which operates on some spatial pattern of evaporation to create some unique spatial pattern of precipitation, is defined as

$$\mathbf{M} = \mathbf{I} - \mathbf{T}(\mathbf{I} - \mathbf{F}) \ , \tag{3.29}$$

and the evaporation and precipitation are related by $\mathbf{M}$ as

$$\mathbf{M}\vec{E} = \vec{P} \ . \tag{3.30}$$

Equation (3.30) may be used to compute the associated precipitation pattern $\vec{P}$ given any spatial evaporation pattern $\vec{E}$. We refer to this use of $\mathbf{M}$ as a forward calculation.

Fortuitously, matrix $\mathbf{M}$ possesses special properties that facilitate the use of forward and inverse methods. We may show that *matrix* $\mathbf{M}$ *is area-preserving* by noting that the sum of all the entries of $\vec{E}$ must equal the sum of all the entries of $\vec{P}$, i.e.

$$||\vec{E}||_1 = ||\vec{P}||_1 \ . \tag{3.31}$$

This is merely a statement of the conservation of atmospheric water in a global sense, as expressed in equation (3.4). Thus, we may write the induced operator 1-norm of $\mathbf{M}$ as

$$||\mathbf{M}||_1 = \sup_{\vec{E}\neq 0} \frac{||\mathbf{M}\vec{E}||_1}{||\vec{P}||_1} = 1 \ , \tag{3.32}$$

from which it follows that $\mathbf{M}$ must be area-preserving since

$$\det(\mathbf{M}) = 1 \ . \tag{3.33}$$

We further note that $\mathbf{M}$ is a function of the climate state, which determines how evaporated moisture moves through the climate system and, eventually, condenses to produce precipitation. As a result, $\mathbf{M}$ will also be variable on any time scales that are inherent to the climate system, such as seasonal time scales and interannual ones, and will also change if the climate system is subject to some external forcing.

In the case where the number of tagged evaporative regions is equal to the number of regions over which precipitation is evaluated, the transformation matrix $\mathbf{M}$ (which has full

rank but may be ill-conditioned) can be inverted to give

$$\vec{E} = \mathbf{M^{-1}}\vec{P}. \tag{3.34}$$

Given a particular state of the climate system, the distribution of evaporation may be derived if the precipitation is known. We refer to the use of $\mathbf{M}^{-1}$ to compute $\vec{E}$ given a prescribed $\vec{P}$ as an inverse calculation.

We now use these forward and inverse prediction methods to study how a particular spatial pattern of evaporation creates a corresponding spatial pattern of precipitation (§3.4.5), and, conversely, how a particular spatial pattern of precipitation corresponds to a given spatial pattern of evaporation (§3.4.5). In all ensuing analyses, the matrix $\mathbf{M}$ is the one computed from the annual mean model output.

Results from Forward Experiments

Figures 3.12 and 3.13 show various prescribed spatial patterns of evaporation $\vec{E}$ and corresponding patterns of precipitation $\vec{P}$, computed using equation (3.30). Panels a through d of Figure 3.12, in which $\vec{E}$ is prescribed in distinct latitudinal bands, show that moisture evaporated in the deep tropics and high latitudes tends to precipitate locally, while moisture evaporated in the subtropics and midlatitudes tends to precipitate remotely. Panels e through g, where $\vec{E}$ is prescribed uniformly over each ocean basin, show that moisture evaporated within each basin tends to precipitate within the same basin and over adjacent land masses.

Regions where locally-evaporated moisture precipitates locally are those where moisture converges. Moisture that evaporates in the deep tropics remains mostly within this region (Figure 3.12 panel a) because the lower tropospheric mean meridional circulation, the lower branch of the Hadley cell, converges here; this, in turn, pushes moist air upwards at the ITCZ, resulting in convection and precipitation *in situ*.

Moisture that originates in the high latitudes also precipitates locally (Figure 3.12, panel

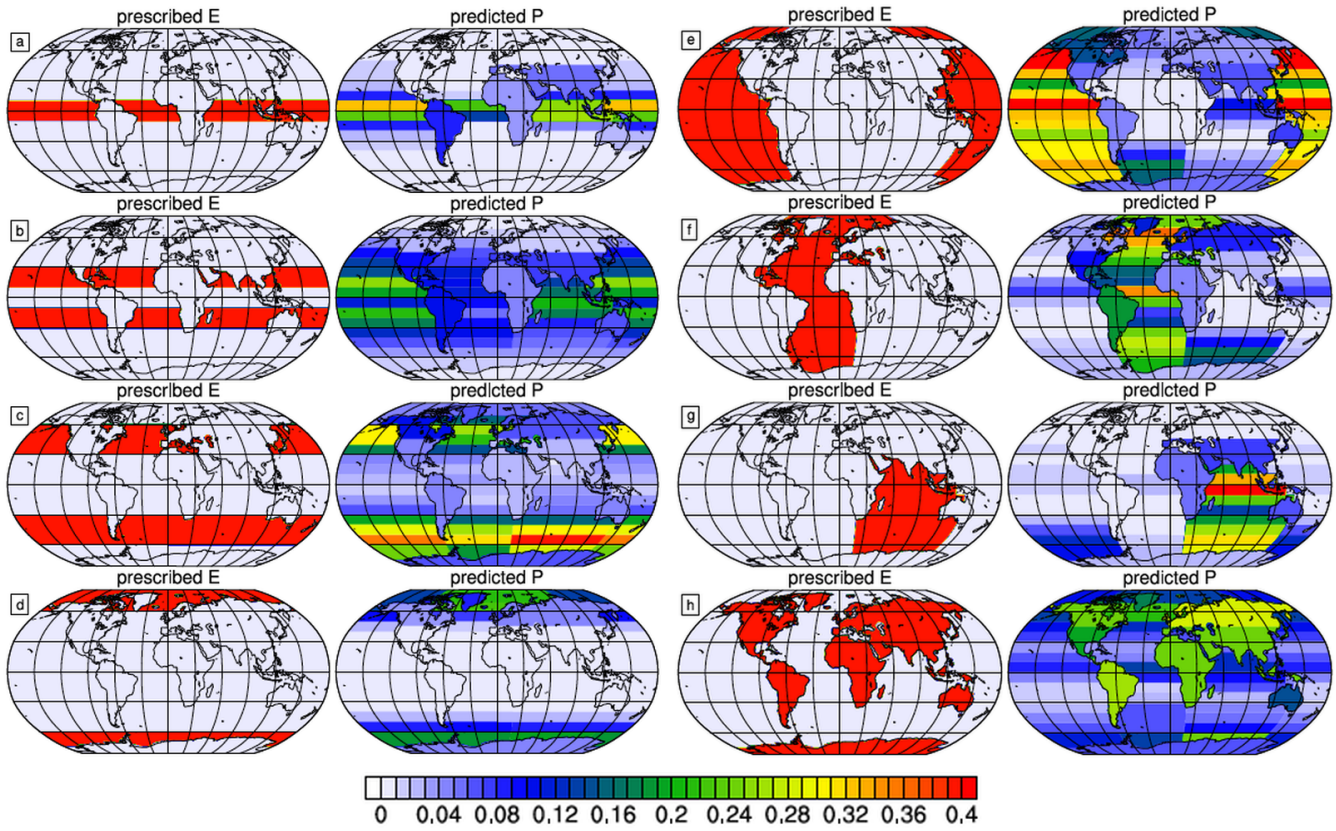

Figure 3.12: Predicted precipitation patterns corresponding to prescribed evaporation patterns. The predicted precipitation $\vec{P}$ is computed from substituting the prescribed evaporation $\vec{E}$ in equation (3.30). Prescribed evaporation regions in each panel are as follows: (a) equatorial (10N to 10S), (b) subtropics (10N to 30N and 10S to 30S), (c) midlatitudes (30N to 60N and 30S to 60S), (d) subpolar and polar (poleward of 60N and 60S), (e) the Pacific basin, (f) the Atlantic basin, (g) the Indian basin, and (h) all land regions.

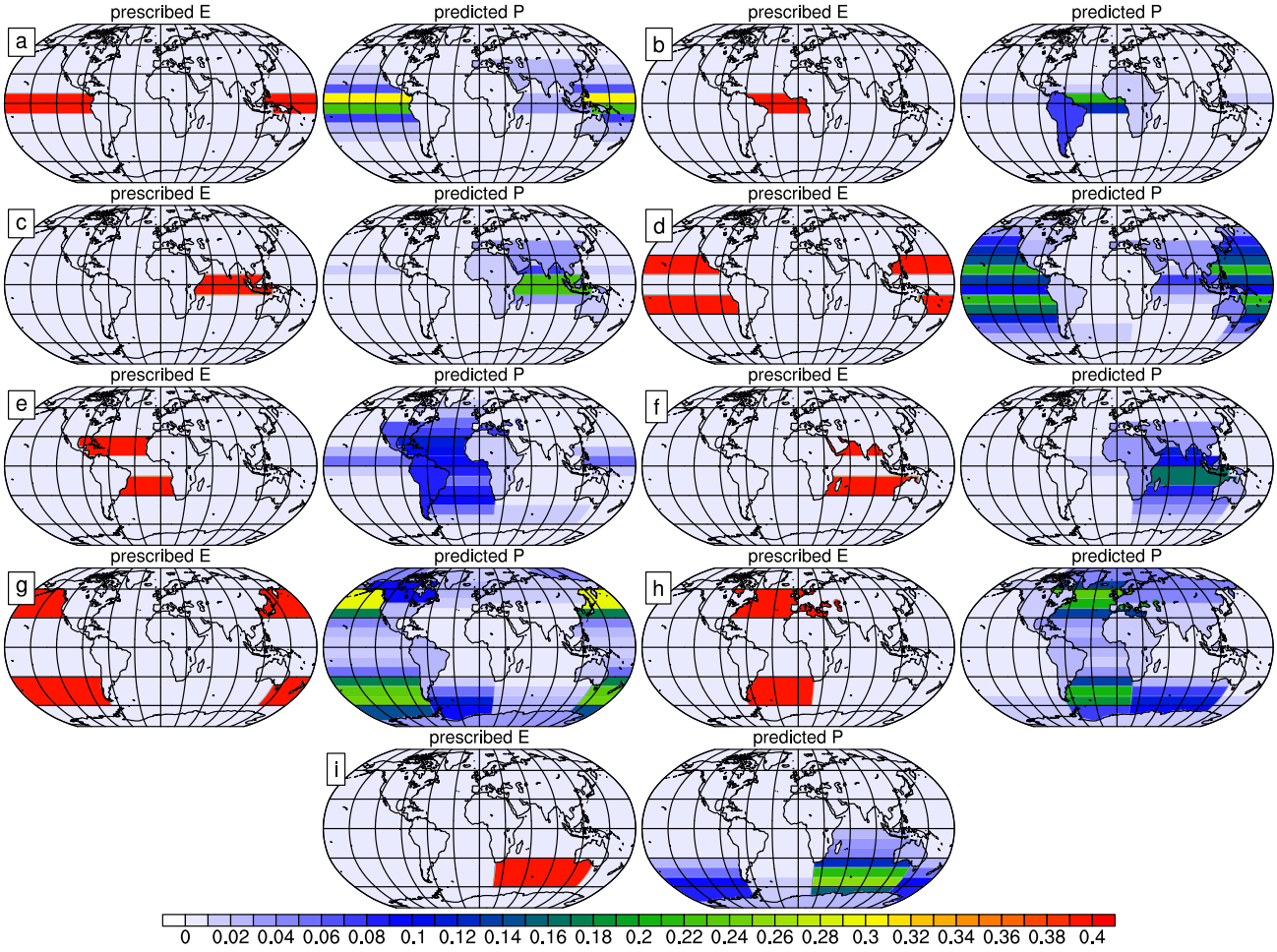

Figure 3.13: As for Figure 3.12, but for prescribed localized evaporation patterns over ocean. Prescribed evaporation regions in each panel are as follows: (a) equatorial Pacific, (b) equatorial Atlantic, (c) equatorial Indian, (d) subtropical Pacific, (e) subtropical Atlantic, (f) subtropical Indian, (g) midlatitude Pacific, (h) midlatitude Atlantic, and (i) midlatitude Indian.

d), and increasing evaporation in the high latitudes will mostly increase precipitation *in situ*, not remotely. Nevertheless, most high latitude precipitation ($> 90\%$, see Figure 3.5) originates in the midlatitudes and moves poleward in midlatitude eddies. Indeed, the high-latitude evaporation rate is very small compared to the rate in the midlatitudes where most polar precipitation originates.

In contrast, moisture evaporated from regions where there is net moisture divergence, such as the subtropics (Figure 3.12, panel b), mostly precipitates outside its source region. Moisture from the subtropical oceans is an important source of precipitable water for land areas in the tropics and midlatitudes. Generally, moisture that evaporates from the subtropics travels both equatorward and poleward before precipitating. The equatorward branch of this circulation is the lower limb of the Hadley cell, which transports warm, moist air towards the ITCZ. Poleward moisture transport is accomplished by midlatitude eddies, whose equatorward excursions pull subtropical moisture poleward; the poleward-eastward slope of the midlatitude geopotential height field facilitates this transport. Poleward movement of subtropical moisture is also important in the global energy budget, as transport of latent heating is an important component of meridional moist static energy transport.

In the midlatitudes, eddies transport locally-evaporated moisture poleward (Figure 3.12, panel c, and Figure 3.13, panels g to i). There is substantial hemispheric asymmetry in moisture transport from the mid- to high- latitudes in that transport in the SH greatly exceeds transport in the NH in the annual mean. The Arctic (north of 60N), in particular, receives little moisture from the NH midlatitude oceans, despite the fact that the majority of precipitation in the Arctic is remotely-sourced (rather than local); the Antarctic (south of 60S), on the other hand, receives a substantial amount of moisture from the SH midlatitudes, though precipitation over Antarctica itself is small. This hemispheric asymmetry is partly due to the intervening land masses that surround the Arctic and intercept moisture from the midlatitude ocean; the absence of such obstacles in the SH allows greater meridional moisture transport in the Antarctic than the Arctic. Furthermore, since there is more land area in the NH, there is also correspondingly more midlatitude ocean area in the SH; thus, there is

more moisture is available for poleward transport to the Antarctic than the Arctic. Unlike the subtropics, where a large fraction of locally-evaporated moisture diverges and there is very little precipitation, a larger fraction of the moisture evaporated within the midlatitudes remains in the midlatitudes to precipitate within the storm tracks (compare panels b and c in Figure 3.12).

Next, we consider prescribed evaporation patterns that are limited to each ocean basin (Figure 3.12, panels e to g). Prescribing a spatially-uniform evaporative flux in a given basin results in precipitation that has a strong maximum at the equator (where the ITCZ is located) and weaker maxima in the midlatitudes; there are corresponding precipitation minima in the subtropics. The midlatitude maxima are weakest over the Pacific basin since the subtropical minima are least pronounced here compared to the Indian and Atlantic basins. The reason for this becomes clear when precipitation resulting from evaporation in the Pacific subtropics is compared to that in the Indian and Atlantic subtropics (Figure 3.13, panels d, e, f). Given a uniform surface evaporation per unit area, the most pronounced subtropical precipitation minimum is found in the South Atlantic. The North Atlantic subtropics and the South Indian subtropics follow closely behind. The Pacific subtropics, on the other hand, are distinct in that they retain significant precipitation maxima (Figure 3.13, panel d). Indeed, the Pacific subtropics provide much less precipitable water (per unit area) to surrounding land masses than the Atlantic and Indian subtropics.

Evaporation patterns confined to a particular basin also help pinpoint where moisture moving between basins comes from. As noted earlier, all basins 'leak' moisture into adjacent basins, particularly when the distance between basins is short and intervening orography is low. This is true over the Southern Ocean, where the absence of land barriers allows evaporated moisture to move eastward in the midlatitude storm tracks. In this case, since all basins contribute moisture to the downwind basin, and since all basins receive moisture from the upwind basin, there is little net gain or loss of freshwater in a particular basin.

At the equator, however, interbasin moisture convergence is not uniform across basins. The Pacific basin leaks moisture into the Indian basin (via low-level easterly winds that

transport moisture over the Maritime continent) and receives moisture from the Atlantic. The Atlantic leaks moisture into the equatorial Pacific (via low-level easterly winds that transport moisture over the Isthmus of Panama), but does not receive any compensating moisture from the Indian basin (compare panels f and g in Figure 3.12). The Indian basin, on the other hand, receives moisture evaporated from the Pacific basin, but leaks little to the Atlantic. Comparing panels b and e in Figure 3.13 reveals that the Atlantic subtropics, not the deep tropics, are mostly responsible for the interbasin contribution to equatorial precipitation in the Pacific. Climatological winds advect this subtropical moisture equatorwards and westwards. The interbasin-sourced precipitation in the Indian basin is also (mostly) from the Pacific subtropics, not the deep tropics (compare panels a and d in Figure 3.12).

Results from Inverse Experiments

Now we turn to the inverse problem as outlined in equation (3.34), in which we predict the spatial pattern of evaporation that would give rise to a prescribed spatial pattern of precipitation, and whose results are shown in Figures 3.14 and 3.15. The first thing to note is that most of the experiments predict regions of negative evaporation; these are areas in which evaporation would have to decrease in order to create the given precipitation pattern. An insight from these inverse experiments, then, is that *localized precipitation patterns are difficult to create with given spatial patterns of evaporation*, since increasing evaporation at a given location will tend to increase precipitation both locally and remotely.

The extent to which a localized precipitation pattern is difficult to create depends on the extent to which evaporation in a given region precipitates locally versus the extent to which it precipitates remotely. In those regions where most locally evaporated water also precipitates locally, a localized evaporation pattern easily corresponds to the prescribed precipitation pattern. On the other hand, localized precipitation patterns are difficult to create in those regions where most locally evaporated water is transported elsewhere.

Localized precipitation patterns in the deep tropics and the high latitudes (Figure 3.14, panels a and d, respectively) correspond to increased evaporation in these very same lo-

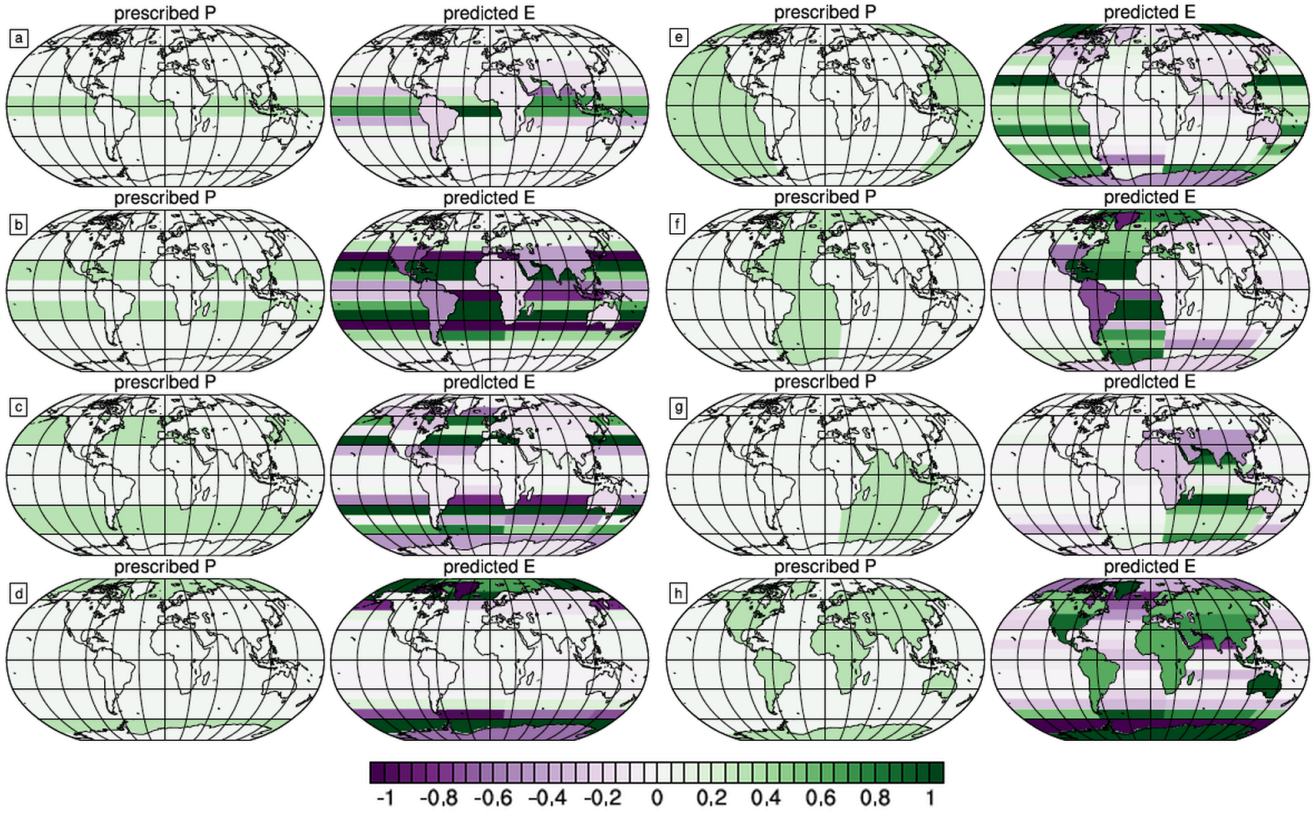

Figure 3.14: Predicted evaporation patterns corresponding to prescribed precipitation patterns. The predicted evaporation $\vec{E}$ is computed from substituting the prescribed precipitation $\vec{P}$ in equation (3.34). Prescribed precipitation regions in each panel are as follows: (a) equatorial (10N to 10S), (b) subtropics (10N to 30N and 10S to 30S), (c) midlatitudes (30N to 60N and 30S to 60S), (d) subpolar and polar (poleward of 60N and 60S), (e) the Pacific basin, (f) the Atlantic basin, and (g) the Indian basin.

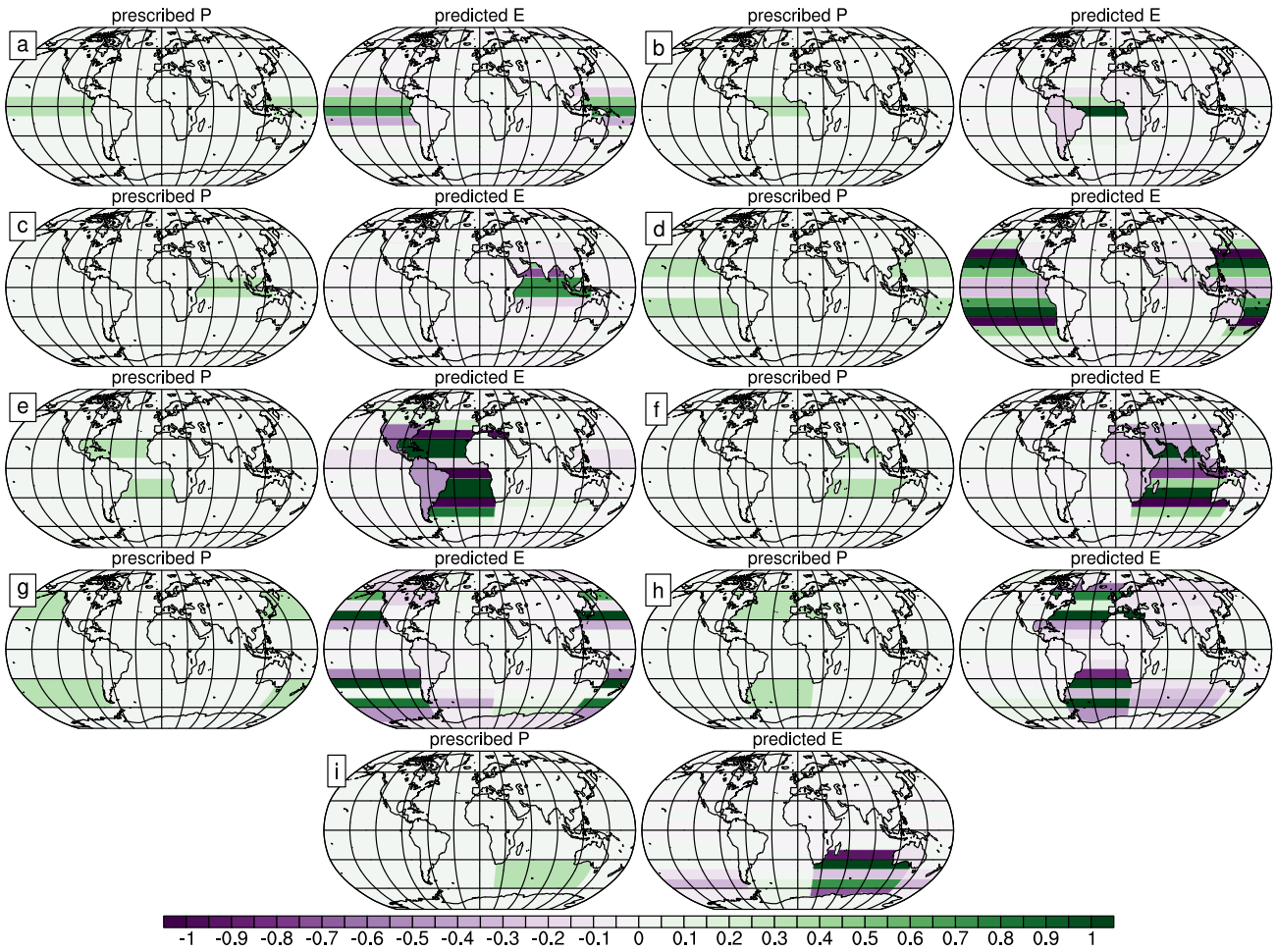

Figure 3.15: As for Figure 3.14, but for prescribed localized precipitation patterns. Prescribed precipitation regions in each panel are as follows: (a) equatorial Pacific, (b) equatorial Atlantic, (c) equatorial Indian, (d) subtropical Pacific, (e) subtropical Atlantic, (f) subtropical Indian, (g) midlatitude Pacific, (h) midlatitude Atlantic, and (i) midlatitude Indian.

cations; because water evaporated within each of these regions mostly precipitates locally, increasing local evaporation is sufficient to create a localized increase in precipitation. Even within these relatively self-contained regions, however, a small amount of locally-evaporated moisture is exported, requiring that the evaporation in the flanking latitude band must decrease slightly to compensate. In other words, no regions are self-contained such that all evaporated water precipitates locally.

Localized precipitation patterns in the subtropics and midlatitudes are more challenging to create. Panels b and c of Figure 3.14 show the evaporation pattern that would be required to create bands of precipitation that are localized in the subtropics and midlatitudes, respectively. The complexity of these spatial patterns of evaporation, with their neighboring regions of increased and decreased evaporation, show that extensive compensation (i.e. regions of decreasing evaporation) is required to produce precipitation that is localized in these regions. Furthermore, a large amount of evaporation is required within these regions in order to create the prescribed precipitation patterns, and evaporation in neighboring regions (where much of the water evaporated from the subtropics and midlatitudes tends to precipitate) must decrease proportionately in order to compensate.

Basin-wide precipitation patterns, on the other hand, are relatively straightforward to create in that increasing evaporation within a given basin will tend to increase precipitation mostly within that basin. This is evident in Figure 3.14, panels e through g, where a uniform pattern of precipitation in a given basin corresponds to a spatially heterogeneous pattern of evaporation that is (mostly) confined to that basin. For a given basin, it is clear that the greatest amount of evaporation must occur in the subtropics (between 20 to 30 N or S) while the least generally occurs in the tropics (between 10N and 10S) and the midlatitudes (between 30 to 50 N or S). Moisture that evaporates in the subtropics tends to diverge before precipitating, and there is little compensating moisture convergence from neighboring regions; as a result, there must be a high evaporative flux in the subtropics, and smaller fluxes in adjacent regions that receive moisture from the subtropics. There are also differences between the basins, with the subtropics in the Atlantic basin requiring the

greatest amount of evaporation to produce the prescribed basin-wide precipitation pattern, while the subtropical latitudes in the Indian and Pacific basins require a smaller amount.

Interbasin differences are also apparent in Figure 3.15, with the Atlantic basin subtropics and tropics contrasting with those in the Indian and Pacific basins. Prescribed precipitation patterns confined to the deep tropics in each of the basins (panels a, b, and c) show that the greatest evaporative flux is found south of the equator in the Atlantic basin, while fluxes in the Pacific and Indian basins are equally distributed north and south of the equator. Precipitation patterns confined to the subtropics (Figure 3.15, panels d, e, and f), require the greatest evaporative fluxes in the Atlantic (compared to the Indian and Pacific basins), and evaporation over the equatorial Pacific must decrease to compensate for moisture transport from the Atlantic subtropics. Precipitation patterns confined to the midlatitudes (panels g, h, and i), on the other hand, require very similar evaporation patterns in all three basins: more evaporation in the midlatitudes and less in evaporation towards the pole.

3.5 Discussion

In this study, we have presented a new mathematical framework for linking precipitation and evaporation that exploits data made available by implementing numerical WTs in a fully-coupled GCM. Our mathematical framework uses straightforward techniques from linear algebra and analysis, and allows us to separate contributions to precipitation from the divergence of locally-evaporated moisture and convergence of remotely-evaporated moisture. Within this framework, we have used matrix decomposition methods to gain further insight into how remotely-evaporated moisture converges differentially to create the distinct spatial pattern of global precipitation. We have also used the results from our tagging experiment to define a full-rank matrix operator that can be used to compute how a given spatial pattern of evaporation maps to a unique spatial pattern of precipitation. Such an operator may also be inverted, allowing us to predict the spatial pattern of evaporation required to create a prescribed spatial pattern of precipitation.

The mathematical development that we have presented here is, by no means, only relevant

to numerical WTs. We envision that these techniques could also be used in other regional or GCM tracer studies, such as those that tag dust, biogenic substances, sea spray, trace gases, or other climate- or meteorologically-relevent variables that have a spatially-heterogeneous source-to-sink relationship. The utility of this framework lies in its simplicity and physical relevance. Being linear, all coefficients are simple to compute; being cast into a linear algebra framework, many powerful matrix decomposition methods may be used to analyze the results. Being able to separate the divergence of local sources from the convergence of remote sources allows both short- and long-range influences to be evaluated. Allowing sinks to be predicted, given a set of sources (and vice-versa), offers a starting point for computing how each of these quantities evolves, given the other.

We have applied our mathematical framework to the results of our GCM experiment in which we have tagged evaporated water in 10° latitude bands in each of the major ocean basins, and where each major land region is tagged separately. We have chosen to focus our attention on the aerial hydrological cycle sourced from the world's oceans, which move about four times more water than that sourced from land. Given that at least one-third of precipitation over land originates in the ocean, and that the ocean circulation depends on asymmetries in the net freshwater input between the ocean basins, understanding the aerial hydrological cycle over the global ocean is relevant to global climate and human societies.

By applying our methods to the hydrological cycle in our model run, we have confirmed old insights and gained new insights on how moisture moves from local and remote sources of precipitation. These findings can be summarized in the following major points:

1. Over the world ocean, the contribution of remotely-evaporated moisture (i.e. moisture that has travelled more than 10 ° meridionally) to the total precipitation is more important than the contribution of locally-evaporated moisture. This is very evident in the high- and mid-latitudes, and less so in the tropics and subtropics. The distinct spatial pattern of precipitation mostly arises from the convergence of remotely-evaporated moisture, not the locally-evaporated moisture that precipitates *in situ*.

2. Interbasin contributions to precipitation are small, except over the Southern Ocean (where there are no land barriers to zonal flow), across the Isthmus of Panama, and across the Maritime continent.

3. Moisture evaporated in the high latitudes and deep tropics tends to precipitate *in situ*. In contrast, the general circulation transports moisture evaporated in the subtropics both equatorward and poleward and transports moisture evaporated in the midlatitudes poleward.

4. The Atlantic basin is unique in several ways: the Atlantic subtropics are the most divergent, as far as locally-evaporated moisture is concerned; the Atlantic basin provides precipitable water to the largest land area; little remotely-evaporated moisture converges over the Atlantic basin; the ITCZ over the Atlantic is very weak in DJF, with little north-to-south remote moisture convergence compared to that over the Pacific and Indian basins; and the Atlantic loses a significant amount of (subtropical) moisture to the equatorial Pacific, but doesn't regain any of this lost moisture from either the Pacific or Indian basins.

One interesting insight from this work is that remote evaporation contributes more to the precipitation at a given locale than local evaporation. We have shown that the contribution of the local evaporation to the total precipitation is, on average, about one-third. Given that the large spatial scales we have chosen for our tagged regions should bias our estimate on the high side, the modest size of the local contribution is somewhat surprising. This result, however, agrees qualitatively with that of other studies that have considered various land areas and their precipitation source regions (see Numaguti, 1999; Bosilovich, 2002; Bosilovich and Schubert, 2002; Stohl and James, 2009; Gimeno et al., 2010). While landlocked regions in the the centers of the large continents (i.e. Eurasia, North America, and Africa) depend largely on this local contribution, particularly in the summer season, most other regions receive much of their locally-precipitating moisture from a variety of remote

source regions (Gimeno et al., 2010, 2012). Indeed, Gimeno et al. (2013) suggest that regions that receive moisture from a variety of sources will be more resilient to perturbations in the hydrological cycle in a changing climate.

As far as the oceans are concerned, some regions are sources of moisture ($E > P$), while others are sinks ($E < P$). The subtropics and the midlatitudes are the former, while the deep tropics and the high latitudes are the latter. The general circulation is responsible for the spatial heterogeneity of these sources and sinks; some regions are convergent while others are divergent, and the former are moisture sinks while the latter are moisture sources. The circulation, which acts along some component of the atmospheric moisture gradient, partitions moisture evaporated from a given region into components that precipitate remotely in other regions. In general, our results show that the distinct spatial pattern of precipitation is created by the convergence of remotely-evaporated moisture which is made possible by atmospheric motions, not by *in situ* evaporation.

Our results show that each of the ocean basins, Pacific, Atlantic and Indian, exhibits distinct tendencies in how much moisture they evaporate, and where this moisture travels before it precipitates. While the broad paradigm of the rainy ITCZ, the dry subtropics, and the stormy midlatitudes is a reasonable approximation to $E - P$ in the global sense, it does not take into account the distinct nature of each of the basins. The Atlantic basin is the most divergent (in terms of locally-evaporated moisture) and least convergent (in terms of remotely-evaporated moisture); in contrast, the Pacific basin is the least divergent and most convergent. The Indian basin is set apart by the South Asian monsoon, whose seasonal movements are made possible by the sizeable subtropical land mass at its northern flank.

The results from this work confirm that the Atlantic basin is unique in terms of its net surface freshwater flux. Qualitatively, our results agree with that of Broecker (1991), who found a substantial flux divergence of moisture from the Atlantic drainage basin. Our WT experiment shows that moisture evaporated from the Atlantic basin is very divergent, and that much of what is evaporated from the Atlantic subtropics precipitates over adjacent landmasses and over the equatorial Pacific. At the same time, the African continent blocks

most moisture fluxes from the Indian basin to the Atlantic. Precipitation over the tropical Atlantic is also minimal, especially during DJF. Though we have not considered runoff and river output from the surrounding continents, we suspect that the high salinity of the Atlantic basin results from an excess of evaporation over precipitation that is uncompensated by moisture input from an adjacent basin. This result echoes that of Ferreira et al. (2010), who studied the impact of ocean basin length scales on salinity in a series of idealized GCM experiments; they found a similar asymmetry in freshwater export between basins of different sizes, in that freshwater export from the smaller basin to the larger basin was always larger than that from the larger basin to the smaller basin. Unlike Ferreira et al. (2010), who argue that the storm tracks are responsible for net vapor transport from the smaller to larger basin in their idealized experiments, we find that it is moisture from the subtropical Atlantic that is being exported to the Pacific over Central America. While the results of Ferreira et al. (2010) relied on idealized continents with no longitudinal extent, we find that the width of the continents in the NH midlatitudes are sufficient to block interbasin moisture exchange here.

Our results show that precipitation in the mid- and high-latitudes depends strongly on the convergence of remotely-evaporated moisture: precipitation in the midlatitude storm tracks is mostly sourced from moisture evaporated in the subtropics and the lower midlatitudes, and precipitation in the high latitudes is mostly sourced from moisture evaporated in the midlatitudes. On the other hand, the export fraction (the fraction of locally-evaporated moisture that diverges) of the midlatitudes is approximately 0.5, which suggests that about half of what evaporates in the midlatitudes precipitates locally. This apparent paradox can be reconciled by considering that a vast amount of moisture is evaporated in the subtropics and precipitates remotely; thus, the substantial fraction of midlatitude precipitation that is from remote sources, approximately 80%, dwarfs the contribution from local sources since the local evaporation is substantially smaller than the total evaporation in the subtropics. This is true even though about half of what evaporates locally tends to precipitate locally. The same is true for the high-latitudes, where evaporation is even lower; even though much

of the moisture that evaporates in the high latitudes remains in the high latitudes, the contribution from remote sources (dominated by the midlatitudes) still provides over 90% of the precipitating moisture in the high latitudes. While our results appear to disagree with those of Bengtsson et al. (2011), who used observational reanalyses to show that only 50% of the total precipitation north of 60N originated remotely, we point out that our calculation does not take precipitation sourced from high-latitude land regions into account. If land sources are considered, which our results show are the dominant precipitation source for the Arctic in the summer, our relative partitioning between local and remote sources is similar to the value reported by Bengtsson et al. (2011).

Finally, we reiterate the major caveat associated with this study and its findings: while numerical WTs may be a powerful tool, they are also a highly model-dependent one. It is likely that some of our results are specific to the aerial water advection and condensation schemes in CAM5, and to all model biases in E and P. While CESM 1.0 produces the spatial patterns of E and P over the world oceans relatively favorably (see the climatologies of freshwater input into the world oceans compiled by Bryan and Oort (1984) and Ganachaud and Wunsch (2003); also see Trenberth et al. (2011)), there are still substantial differences between the modeled hydrological cycle and that in the real world, particularly in the tropics. Determining which, if any, of our results are robust will depend on future work, in which we apply the mathematical methods presented here to results from several different models. Alternatively, we may also use numerical WTs in a data assimilation framework, and a GCM equipped with numerical WTs may be used in conjunction with observational hydrological data. Such a study would allow us to evaluate how well GCMs can capture evaporation, precipitation, and moist processes in the aerial hydrological cycle, and could provide some clues on how the hydrological cycle is changing in response to anthropogenic perturbations.

3.6 Concluding Points

In this study, we have presented a linear algebra framework for analyzing the results of numerical WT experiments. This framework permits local and remote contributions to

the total precipitation to be evaluated systematically using matrix methods, rather than through an *ad hoc* approach. Furthermore, the mathematical development we have presented here may be generalized to tagging experiments that focus on any geophysical quantity, particularly those that have a spatially-heterogeneous source-to-sink relationship.

We have applied these methods to a numerical WT experiment performed with CESM 1.0, and have found that most moisture sourced from the global ocean travels long distances before precipitating. In general, remotely-sourced moisture (i.e. moisture that has travelled more than 1,000 km meridionally) is a larger contributor to precipitation than locally-sourced moisture; this is particularly true in the high latitudes, which receive most of their precipitable water from the midlatitudes, and the midlatitudes, which receive most of their moisture from the subtropics. At the ITCZ, at least half of what precipitates is locally-sourced while the remainder originates in the subtropics. Overall, the highly-evaporative subtropics are the most important remote moisture source.

Our results also show that little moisture travels between basins, except in the tropics where land barriers do not impede moisture convergence. Furthermore, each of the ocean basins is distinct: the Atlantic basin, particularly at subtropical latitudes, provides the most moisture to other regions (per unit area), including surrounding land regions as well as other basins; on the other hand, the Pacific basin provides the least amount of moisture to surrounding land regions, despite its large area.

We envision future work with numerical WTs that evaluates the robustness of the findings described in this study. Furthermore, a similar mathematical framework may be used to study the response of the aerial hydrological cycle to perturbations, particularly anthropogenic ones.

Chapter 4

A MATHEMATICAL FRAMEWORK FOR ANALYSIS OF WATER TRACERS: PART II, PERTURBATION STUDIES OF THE CO_2-DOUBLING SCENARIO

4.1 Introduction

This is the second part of a study in which we use numerical water tracers (WTs) implemented in a global climate model (GCM) to understand the aerial hydrological cycle. In Part I of this study (Chapter 3), we developed a mathematical framework that allowed for systematic analysis of results from global WT experiments, and applied this framework to a simulation of the pre-industrial mean-state hydrological cycle. Here in Part II, we use the mathematical framework developed in Part I to analyze perturbations to the aerial hydrological cycle in simulations subject to CO_2-doubling, and, thereby, gain new insights on the response of the aerial hydrological cycle to CO_2-induced warming.

4.1.1 Observational and Modeling Evidence of Hydrological Cycle Changes

The hydrological cycle over land is, undoubtedly, a subject of great importance to human societies and natural ecosystems. As a consequence, changes in the hydrological cycle due to anthropogenic CO_2 emissions, both present and in the projected future, have been, and continue to be, studied extensively. Several lines of observational evidence suggest that the hydrological cycle has shifted relative to its preindustrial state in response to anthropogenic perturbations. Observed ocean salinities appear to be trending upward in the tropics and downward in the high latitudes, suggesting that the climatological difference between evaporation and precipitation has increased and the hydrological cycle has intensified (Helm et al., 2010; Durack et al., 2012). Observations also show that surface specific humidity has in-

creased in response to increased surface temperatures (Willett et al., 2007), and terrestrial precipitation over the NH subtropics has declined (Zhang et al., 2007).

Nevertheless, anthropogenic perturbations to the hydrological cycle are difficult to discern in the observational data, which are limited by incomplete spatial coverage and short time series (Sarojini et al., 2012). GCM studies, on the other hand, predict a medley of hydrologic changes with continued anthropogenic greenhouse gas emissions. In the tropics, models predict enhanced precipitation seasonality (Chou et al., 2007) and more heavy precipitation events (Meehl et al., 2005; Hu et al., 2012; Lau et al., 2013). The subtropics are expected to dry (Allan et al., 2010) and widen (Seager et al., 2007; Seidel et al., 2008). The midlatitude storm tracks are expected to shift poleward (Hall et al., 1994; Yin, 2005; Bengtsson et al., 2006; Chang et al., 2012) and intensify (O'Gorman, 2010; Chang et al., 2012), the characteristic length scale of atmospheric eddies is expected to increase (Kidston et al., 2010; Riviere, 2011), and moisture transport into the polar regions is expected to increase (Hwang and Frierson, 2010). In the high latitudes, precipitable water is projected to increase (Serreze et al., 2012) and the hydrological cycle to intensify (Bengtsson et al., 2011). As land areas become more arid globally(Dai, 2012; Sherwood and Fu, 2014), the relative importance of oceanic moisture sources for continental precipitation is expected to increase (Gimeno et al., 2013).

On a global scale, predictions of hydrological cycle change by GCMs are in agreement with observed perturbations (Seager and Naik, 2012; Allan et al., 2014). Nevertheless, significant mean-state spatial biases in precipitation plague all GCMs (Lin, 2007; Liu et al., 2014; Li and Xie, 2014), and such mean-state biases have been shown to account for the wide range of future hydrological cycle predictions made by different GCMs (Mitchell et al., 1987; Knutti and Sedlacek, 2013; Bony et al., 2013). As a result, confidence in GCM precipitation predictions is low, particularly in terms of regional changes (Stocker et al., 2013).

4.1.2 Theoretical Underpinnings of Hydrological Cycle Changes with Warming

From a global perspective, there are two important principles that govern how the hydrological cycle responds to anthropogenic greenhouse gas emissions. First, tropospheric water vapor must increase as the atmosphere warms, and this rate is dictated by the Clausius-Clapeyron (C-C) equation, approximately 7% increase in specific humidity per °C of warming (Manabe and Wetherald, 1975; Held and Soden, 2006). Second, precipitation and evaporation, by themselves, can't increase at the C-C rate due to energetic constraints. In particular, evaporation is limited by the surface energy budget, while precipitation is limited by the atmospheric longwave radiative cooling rate and the dry static energy (DSE) flux divergence; as a result, both precipitation and evaporation increase with temperature at a slower rate, globally approximately 1% to 3% per °C of warming, which varies depending on the GCM and emissions scenario (Mitchell et al., 1987; Stephens et al., 1994; Allen and Ingram, 2002).

Clausius-Clapeyron Scaling

The most influential study attributing changes in the hydrological cycle to C-C scaling of atmospheric moisture with temperature (the thermodynamic hypothesis) is that of Held and Soden (2006). While neither P nor E scale at the C-C rate, Held and Soden (2006) showed that the change in $P - E$ scales with the change in temperature times the C-C scaling rate, both in magnitude and spatial arrangement. Poleward moisture transport can also be shown to increase with temperature at the C-C rate, given a small correction factor for compensation between poleward sensible and latent energy transports. According to the thermodynamic argument of Held and Soden (2006), increased atmospheric specific humidity, as is expected with increased surface and lower tropospheric temperatures that accompany increased CO_2, will tend to amplify the mean state evaporation-precipitation cycle and transport more moisture meridionally. As a result, areas where P exceeds E in the climatology will get wetter, while areas where E exceeds P will dry.

The thermodynamic argument put forth by Held and Soden (2006) has a great deal of

explanatory power on the global scale. And at first glance, the spatial pattern of $P - E$ changes in GCM simulations is strikingly similar to the mean state $P - E$. Other studies have also confirmed the importance of increased specific humidity in determining hydrological cycle changes in the CMIP5 archive (see, e.g., (see, e.g., Li et al., 2013).

Nevertheless, the changes in the atmospheric moisture divergence, $\nabla \cdot Q$ $\left(Q = \int vqdp/p_0\right)$, which are responsible for the change in $P - E$, are not solely due to increased atmospheric moisture. Indeed, many studies since Held and Soden (2006) have qualified the results presented therein, particularly in regards to the importance of dynamic (rather than thermodynamic) drivers of hydrological cycle changes seen in GCMs. Many of these studies suggest that changes in circulation (i.e. dynamics) are as important (or nearly so) as thermodynamics in determining the hydrological cycle response to warming. Seager et al. (2010) decomposed the response of the atmospheric moisture flux divergence term to CO_2-induced warming in the CMIP5 archive into components due to changes in mean circulation ($\Delta\bar{v}$), thermodynamics (increased atmospheric humidity, $\Delta\bar{q}$), and eddy moisture fluxes ($\Delta\overline{v'q'}$); while the importance of the thermodynamic term was confirmed, changes in the mean circulation were found to be equally important as the increase in atmospheric humidity in the tropics and subtropics, while the eddy moisture flux term dominated the sum in the mid- and high-latitudes (Seager et al., 2010).

Others argue that closer inspection of the spatial pattern of precipitation change reveals inconsistencies with the thermodynamic argument of Held and Soden (2006). Scheff and Frierson (2012b) and Scheff and Frierson (2012a) point out that precipitation doesn't decrease uniformly within the subtropics in CMIP5 models as would be expected from the thermodynamic argument. Instead, the subtropics dry preferentially on their poleward flanks as the subtropical dry zones expand, suggesting that this and the the accompanying poleward shift of the storm tracks and jets are a dynamic response to CO_2-induced warming. The accompanying changes in precipitation are not a simple result of increased atmospheric moisture, but are rather a result of these poleward shifts in general circulation features that are common to most GCM predictions and that are not easily explained by a single, unifying

theory (see, e.g., Vallis et al., 2014; Lorenz, 2014). Changes in precipitation, then, may primarily be a tracer of these poleward shifts.

Furthermore, it is clear that changes in the hydrological cycle at regional scales cannot be explained by thermodynamic arguments alone. The correlation between changes in atmospheric moisture and changes in precipitation increases with length scale (Held and Soden, 2006), suggesting that the thermodynamic argument may only explain hydrological cycle changes at the largest scales. In the tropics, Chou and Neelin (2004) and Chou et al. (2009) propose several distinct mechanisms for increased $P - E$ in convergence zones and decreased $P - E$ over subsidence regions that vary depending on whether areas of ascent, descent, or their boundaries are being considered. While increasing atmospheric moisture does, undoubtedly, play a role in these mechanisms of regional precipitation change, the interaction between increased moisture, temperature, and the atmospheric motions required for convection suggest a more complex, dynamic mechanism than the simple thermodynamic argument described above. Chadwick et al. (2013) suggest that because thermodynamic and dynamic changes mostly oppose and cancel each other in the tropics, shifts in convergence zones that follow changes in P are a better marker of hydrological cycle change than either dynamics or thermodynamics.

Moreover, weakening of the atmospheric circulation in the tropics cannot be inferred *a priori* from the thermodynamic argument. This weakening is a robust result in GCM simulations of elevated CO_2 scenarios (Vecchi and Soden, 2007; Chou et al., 2009; He et al., 2014)), and is more pronounced in zonal circulations, such as the Walker Circulation, than meridional ones (Vecchi and Soden, 2007). Bony et al. (2013) showed that the tropical circulation weakens because of decreased outgoing longwave radiation (OLR) coincident with rising CO_2, which tends to increase tropospheric temperatures more than surface temperatures; the resulting enhanced static stability decreases the strength of deep convection, which weakens the tropical circulation. Unlike moisture increase, which requires the surface temperature to increase and is, therefore, associated with slower timescales, this dynamic response to increased CO_2 is rapid and is immediately apparent in GCM simulations as a

transient suppression of precipitation (Andrews et al., 2010; Bony et al., 2013).

Energetic Constraints

Both surface and atmospheric energetics constrain the precipitation response to greenhouse warming below the C-C rate. Suppression of longwave cooling, as noted by Andrews et al. (2010) and Bony et al. (2013), is one mechanism by which precipitation is limited by energetics. The idea that CO_2-induced precipitation changes could be constrained energetically began with the work of Mitchell et al. (1987), who showed that both increased CO_2 and increased temperatures were important components of this radiative cooling limit. Mitchell et al. (1987), and, later, Sugi and Yoshimura (2004) showed that increasing CO_2 in GCMs tended to decrease longwave cooling while increased temperatures increased it, albeit more slowly due to OLR suppression by CO_2; as a result, the hydrological cycle responds to CO_2-induced warming over at least two distinct time scales. These ideas were further developed by Stephens et al. (1994), who demonstrated suppression of atmospheric longwave cooling by greenhouse gases in satellite observations from the Earth Radiation Balance Experiment (ERBE). Allen and Ingram (2002) proposed that energetic constraints on precipitation could be used to improve predictions of short- and long-term hydrological cycle change due to anthropogenic forcing.

Nevertheless, changes in longwave atmospheric cooling are not only dictated by changes in temperature and atmospheric CO_2. Longwave cooling is also suppressed by clouds (Stephens and Ellis, 2008; Pendergrass and Hartmann, 2014). Furthermore, Pendergrass and Hartmann (2014) have shown that the subdued clear-sky longwave cooling rate in CMIP5 models can only be explained by moistening of the atmospheric column at constant relative humidity, concomitant with increased CO_2 and surface-amplified warming.

The local radiative cooling rate, however, is not the only element of the energy balance that constrains precipitation changes. Any energy that can not be radiated to space locally can be moved to another region where it can be radiated to space more efficiently. Thus, Muller and O'Gorman (2011) argue out that from a regional perspective, it is not only the

longwave cooling rate that matters, but the divergence of dry static energy (DSE). Indeed, the spatial pattern of precipitation change is well-described by the change in the DSE flux, with a moderate correction associated with changes in sensible heat flux. Since shortwave and longwave radiative fluxes largely cancel each other out, Muller and O'Gorman (2011) suggest that it is the change in DSE divergence that mostly determines the spatial pattern of precipitation change.

While precipitation is constrained by atmospheric energetics, namely DSE divergence and TOA radiative cooling, the surface energy budget constrains evaporation below the C-C rate. Boer (1993) noted that GCM precipitation increases depended sensitively on the change in the amount of energy available at the surface; in the tropics, the increased cloud albedo, combined with changes in the Bowen ratio (the ratio of the sensible to latent heat flux) act to constrain evaporation below the C-C rate. Richter and Xie (2008) and Lorenz et al. (2010) showed that from the surface evaporation perspective, increased relative humidity, increased static stability due to an increase in the surface - boundary layer temperature contrast, and decreased wind speeds, tended to constrain evaporation rates well below C-C. Lorenz et al. (2010) further suggested that the relative importance of these different factors varied with the time scale considered.

4.1.3 A Context for the Present Study

As described above, perturbations in the hydrological cycle due to CO_2-induced warming have been described in the context of thermodynamics versus dynamics (changes in atmospheric moisture content versus changes in circulation), or, alternatively, have been described in terms of energetic constraints on precipitation or evaporation. In this study, we will use numerical WTs to present a complementary framework to these existing paradigms that relies on moisture conservation. In a steady state, global evaporation must balance global precipitation, and perturbations to this steady-state, provided that they are in quasi-equilibrium, must also satisfy moisture conservation.

So far, only one other study has used numerical WTs to study changes in the aerial

hydrological cycle caused by anthropogenic CO_2 emissions. Bosilovich et al. (2005) used a 50-year GCM integration with WTs to show that the cycling rate of water in the atmosphere decreased, and the residence time scale increased. Such changes have also been predicted by other studies, who have shown that increasing atmospheric moisture at a higher rate than evaporation or precipitation requires that atmospheric moisture residence times must increase (see Trenberth, 1998; Held and Soden, 2006; van der Ent and Savenije, 2011). However, while they have been noted, the implications of these increased residence times for changes in the hydrological cycle are less clear.

In this study, we use numerical WTs implemented in a state-of-the-art GCM to study how the aerial hydrological cycle changes with CO_2-doubling, and, thereby, to examine the implications of this increased atmospheric moisture residence time scale. We use the mathematical framework developed in Part I of this study to analyze perturbations in the hydrological cycle due to quasi-equilibrium CO_2-doubling. The change in the precipitation is decomposed into changes due to evaporation (both local and remote) and changes due to moisture transport. Further decompositions reveal how precipitation perturbations are related to changes in the divergence of locally-evaporated moisture versus the convergence of remotely-evaporated moisture, how the amount of moisture precipitating locally (rather than remotely) changes, and how the partitioning of remotely-evaporated moisture between precipitating regions shifts. To understand the latter, we use several physically-motivated decompositions of the remote moisture convergence. Finally, we present and analyze a series of heuristic models of moisture transport in order to establish a context for our findings.

This chapter is structured as followed. In §4.2, we review the mathematical development presented in Chapter 3 and introduce notation for applying it to perturbation studies. In §4.3, we describe the setup of our GCM WT experiments, and in §4.4, we analyze the results of these experiments using the mathematics developed earlier. In §4.5, we present and analyze several heuristic models of atmospheric moisture transport to support and clarify the results from our GCM experiments. We discuss our results and consider further implications of our work in §4.6, and offer some concluding remarks in §4.7.

4.2 Overview of Mathematical Framework and Perturbation Methods

In Part I, we developed a linear algebra framework for analyzing the output from experiments employing numerical water tracers (WTs). We review this framework here, and introduce some additional notation for analyzing perturbations to the mean state.

In general, the difference between the precipitation and evaporation in a tagged region (P_i and E_i, respectively) is due to divergence of locally-evaporated moisture from the tagged region and convergence of remotely-evaporated moisture from all other tagged regions (denoted E_j) such that tagged regions cover the entire globe:

$$P_i - E_i = -e_i E_i + \sum_{i \neq j} e_j f_{ji} E_j \tag{4.1}$$

where e_i is the fraction of moisture evaporated in the i-th region that precipitates elsewhere (and is, therefore, not available to precipitate locally), e_j is the fraction of moisture evaporated in the j-th region that precipitates outside the j-th region, and f_{ji} is the fraction of total moisture exported from region j that falls in region i. Thus, the product $e_j f_{ji} E_j$ represents the fraction of E_j (the total moisture evaporated from region j) that is exported from the j-th region and subsequently precipitates in the i-th region. Summing the contributions from all regions j to region i gives the total amount of remotely-evaporated moisture that converges into region i.

In matrix form, we can write equation (4.1) compactly as

$$\vec{P} = \vec{E} - \mathbf{T}\vec{E} + \mathbf{F}\mathbf{T}\vec{E}. \tag{4.2}$$

In equation (4.2), $\mathbf{T}$ is a diagonal matrix whose entries e_j represent the fraction of moisture evaporated from region j that precipitates outside region j; and $\mathbf{F}$ is a hollow matrix (diagonal entries are zero) whose i, j-th entry is equal to f_{ji}, the fraction of the exported moisture evaporated from the j-th region that precipitates in the i-th region. By definition, the diagonal entries of $\mathbf{F}$ must be nil (i.e., $f_{ii} = 0$), since any moisture that both evaporates and

precipitates in region i is accounted for in the $E_i - e_i E_i$ term, which is the contribution of locally-evaporated moisture to the local precipitation. In brief, equation (4.2) states that $\vec{P}$ is composed of contributions from the local evaporation ($\vec{E}$), decreased by the amount of this local evaporation that diverges ($\mathbf{T}\vec{E}$), and increased by the amount of remote evaporation that converges ($\mathbf{FT}\vec{E}$).

This matrix operator framework corresponds to the fundamental equation of hydrology,

$$E - P = \nabla \cdot Q \ , \tag{4.3}$$

by equating the moisture flux divergence, $\nabla \cdot Q$ to the difference between the local divergence ($\mathbf{T}\vec{E}$) and the remote convergence ($\mathbf{FT}\vec{E}$) terms:

$$\nabla \cdot Q = \mathbf{T}\vec{E} - \mathbf{FT}\vec{E}!. \tag{4.4}$$

We may also write equation (4.2) more compactly as

$$\vec{P} = \mathbf{M}\vec{E} \tag{4.5}$$

where the operator $\mathbf{M}$ is defined as

$$\mathbf{M} = \mathbf{I} - \mathbf{T} + \mathbf{FT} \ . \tag{4.6}$$

In the ensuing perturbation analysis, we will decompose equation (4.2) into mean state and perturbation quantities to compute how changes in the local evaporation, the divergence of locally-evaporated moisture, and the convergence of remotely-evaporated moisture all contribute to changes in the precipitation. In terms of notation, we will use the Δ operator to denote a difference between the CO_2-doubling experiment and the control, i.e.

$$\Delta X = X_{2\times CO_2} - X_{control} \ , \tag{4.7}$$

where X is either a vector quantity (such as $\vec{P}$ or $\vec{E}$) or a matrix (such as $\mathbf{T}$ or $\mathbf{F}$).

In our perturbation analysis, we will also assume that perturbed quantities can be decomposed linearly. In other words, we assume that for a given product, XY, we can write the perturbation decomposition as

$$\Delta(XY) \approx (\Delta X)Y + X(\Delta Y) \ , \tag{4.8}$$

and that the nonlinear term $(\Delta X)(\Delta Y)$ is negligible. In all the following analyses, we have found that the nonlinear terms are very small ($< 5\%$ of the total perturbation), and have neglected them. It should be noted, though, that these terms should be checked carefully in any analysis where the difference between the control experiment and the anomaly experiment is large and nonlinearities may be significant.

4.3 Model Experiments

The control experiment (C) is as described in Part I of this study. In brief, an equilibrium pre-industrial mean state experiment was conducted using the fully-coupled Community Earth System Model 1.0 (CESM1) with all model components at 1° spatial resolution. Aerial water was tagged with its region of origin in 10° latitude bands over each ocean basin. Each continent was tagged separately, with Eurasia and North America subdivided in two parts each. There are 49 distinct tagged regions in total, encompassing the entire globe.

For Part II, a second experiment was branched from the pre-industrial control simulation in which atmospheric CO_2 was doubled from its preindustrial concentration in the model of 290 parts per million (ppm) to 580 ppm. The simulation was allowed to run without WTs for 270 years to approach a quasi-equilibrium state. For a final 30 years, WTs with the same spatial configuration as for C were introduced. We refer to the final 30 years of this run, years 270 to 300, as the equilibrium CO_2-doubling experiment (Eqm2×CO_2). The net TOA energetic imbalance in Eqm2×CO_2 is less than 0.1 W m^{-2}.

Climatologies are created from 30 years of model output with WTs. All quantities

are given as the difference between that in the CO_2-doubling experiment and the control, Eqm2×CO_2 - C, as described in equation (4.7).

4.4 Results

4.4.1 Decomposing the Total Change in Precipitation

We begin by considering how changes in evaporation and changes in transport each contribute to the total precipitation change with CO_2-doubling. Given that we can write the relationship between evaporation and precipitation as $\vec{P} = \mathbf{M}\vec{E}$, we may write the perturbation of the precipitation as the sum

$$\Delta\vec{P} \approx (\Delta\mathbf{M})\vec{E} + \mathbf{M}(\Delta\vec{E}) \ , \tag{4.9}$$

where $\mathbf{M}$ is the transport operator as defined in equation (4.6) and $\vec{E}$ is the evaporation vector. According to equation (4.9), the total change in the precipitation in Eqm2×CO_2 can be decomposed into two terms: $\mathbf{M}(\Delta\vec{E})$, the change in precipitation due to changes in evaporation given that transport remains constant, and $(\Delta\mathbf{M})\vec{E}$, the change in precipitation due to changes in transport, given that evaporation remains constant. Shown in Figure 4.1 are the total precipitation perturbation $\Delta\vec{P}$ in Eqm2×CO_2 (panels a, b, and c), the change in precipitation due to changes in the transport matrix $\Delta\mathbf{M}$ (panels d, e, and f), and the change in precipitation due to changes in evaporation $\Delta\vec{E}$ (panels g, h, and i).

From Figure 1, it is evident that the change in precipitation, $\Delta\vec{P}$, has the canonical spatial pattern associated with CO_2-induced climate change: regions that already receive abundant precipitation, like the inter-tropical convergence zone (ITCZ) and storm tracks, become wetter, while those that receive little precipitation, the subtropics in particular, become drier. This view of $\Delta\vec{P}$ associated with CO_2-doubling is spatially-smoothed since it has been averaged over each of the tagged regions. As a result, this view conceals many of the model-specific small-scale features (likely a result of model biases) found in the precipitation field simulated in this particular GCM.

Substantial spatial inhomogeneities are present in the precipitation field. First, while

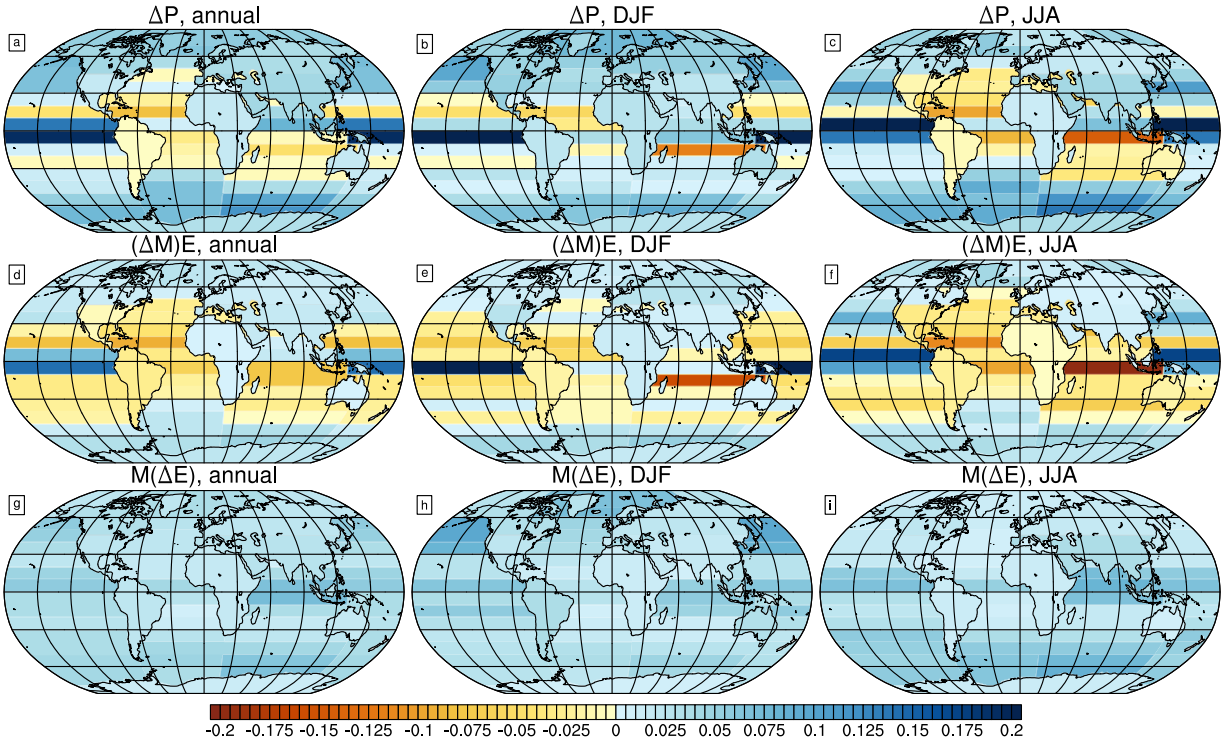

Figure 4.1: Perturbation analysis of the contribution of $\Delta\mathbf{M}$ and $\Delta\vec{E}$ to the change in precipitation with CO_2-doubling: panels a, b, and c show the change in precipitation; panels d, e, and f show the change in precipitation due to changes in the transport operator $\mathbf{M}$; and panels g, h, and i show the change in precipitation due to changes in $\vec{E}$. Each of these quantities is shown in the annual average (panels a, d, g), averaged over DJF (panels b, e, h), and averaged over JJA (panels c, f, i).

equatorial precipitation over the Pacific increases substantially in Eqm2×CO_2, it increases only modestly over the equatorial Indian basin and remains constant over the Atlantic. Second, the decrease in precipitation over the subtropics also appears to vary between basins; it is most pronounced over the Atlantic and (South) Indian basins, while relatively modest over the Pacific. Indeed, there is very little decrease in precipitation over the entire Pacific basin, suggesting that mechanisms involved in the drying of the subtropics may be operating very differently over each of the ocean basins; the same may be true for increases in equatorial precipitation. Third, the precipitation over the midlatitude storm tracks and high latitudes increases over all ocean basins and both hemispheres; for a given season, this increase in precipitation in Eqm2×CO_2 is most dramatic in the respective winter hemisphere.

Now, we turn to the decomposition of this total precipitation change into the components given in equation (4.9). Comparing how changes in $\mathbf{M}$ (Figure 4.1, panels d, e, f) and changes in $\vec{E}$ (Figure 4.1, panels g, h, i) contribute to the change in precipitation, several features of this partitioning become apparent. These can be summarized as follows:

- The change in precipitation due to changes in evaporation is always positive, and is relatively spatially homogeneous in the annual mean. This can only be true if the change in evaporation is (mostly) positive, which it is (see Figure 2, panels d, e, f).

- The change in precipitation due to changes in the transport (both changes in the convergence of remotely-evaporated moisture and the divergence of locally-evaporated moisture) is spatially-inhomogeneous compared to the change due to increasing evaporation. Broadly, this term is positive over the equatorial Pacific and Indian basins, negative over the subtropics and portions of the midlatitudes, and moderately positive over the high-latitudes.

- Over the tropics and subtropics, the change in the precipitation due to the transport term is greater than that due to the evaporation term. In the analysis that follows, we will show that precipitation decreases over the subtropics because the overall con-

vergence of remotely-evaporated moisture declines, while it increases over the deep tropics (primarily over the Pacific and Indian basins) mostly because a greater amount of remotely-evaporated moisture converges at the equator.

- In the annual mean, increased precipitation in the mid- and high-latitudes are due to increases in both the transport and evaporation terms. Intensified precipitation in the winter hemisphere, however, is dominated by the evaporation term, which is more seasonally variable in these regions.

In order to understand why these terms partition the total precipitation change as they do, we substitute the definition of the operator $\mathbf{M}$ given by equation (4.6) into $\vec{P} = \mathbf{M}\vec{E}$ and compute its perturbation:

$$\Delta P = \Delta(\mathbf{I} - \mathbf{T} + \mathbf{FT})\vec{E} + (\mathbf{I} - \mathbf{T} + \mathbf{FT})\Delta\vec{E} \ . \tag{4.10}$$

A bit of rearrangement gives

$$\Delta\vec{P} = \Delta\vec{E} - \Delta(\mathbf{T}\vec{E}) + \Delta(\mathbf{FT}\vec{E}) \ , \tag{4.11}$$

where the total change in the precipitation $\Delta\vec{P}$ is subdivided as follows: the part due to the change in local evaporation, $\Delta\vec{E}$; the part due to the change in the divergence of locally-evaporated moisture, $-\Delta(\mathbf{T}\vec{E})$; and the part due to the change in the convergence of remotely-evaporated moisture, $\Delta(\mathbf{FT}\vec{E})$.

Figure 4.2 displays each of the terms in equation (4.11). The change in evaporation is positive everywhere and nearly spatially homogeneous (Figure 4.2 panels d, e, f). In the annual average, the evaporation increase is muted over the continents and intensified over the equatorial regions, particularly over the Indian basin; the only region in which evaporation decreases in the annual average is over the North Atlantic, where this decline is due to cooler SSTs and weakened surface winds. Seasonally, evaporation increases significantly over the mid- and high-latitude oceans in winter (panels e, f).

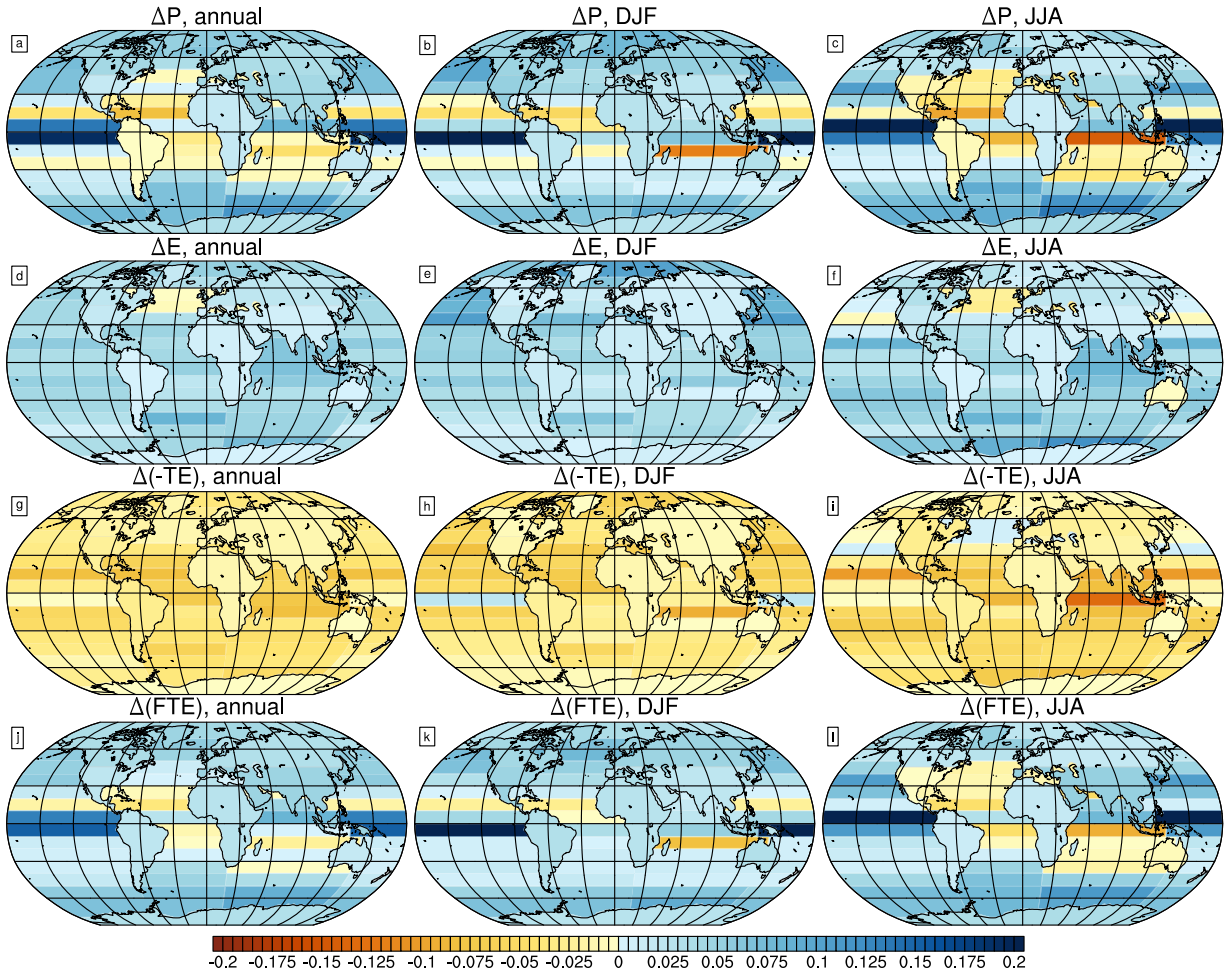

Figure 4.2: Perturbation analysis of changes in the aerial hydrological cycle with CO_2-doubling, with the total change in precipitation decomposed as in equation (4.11): the (local) change in evaporation (panels d, e, f), the change in the divergence of locally-evaporated moisture (panels g, h, i), and the change in the convergence of remotely-evaporated moisture (panels j, k, l). The total change in precipitation is shown for comparison purposes (panels a, b, c). All quantities are shown in the annual average (panels a, d, g, j), averaged over DJF (panels b, e, h, k), and averaged over JJA (panels c, f, i, l).

The change in the local divergence term, $\Delta(-\mathbf{T}\vec{E})$, is negative globally in the annual average (shown in Figure 4.2 panels g, h, i). Physically, this indicates that less locally-evaporated moisture precipitates locally across the globe, or, equivalently, more locally-evaporated moisture precipitates remotely everywhere (i.e. moisture originating in one tagged region that precipitates in another increases everywhere). Like the change in $\Delta\vec{E}$ discussed previously, this term is also relatively spatially homogeneous; continental regions lose less locally-evaporated moisture, while the tropics and subtropics over the Atlantic and Indian basins lose the most. Seasonally, more locally-evaporated moisture is exported from the subtropics, midlatitudes, and high latitudes over ocean in the winter hemisphere. Over much of the globe, the decline in the amount of locally-evaporated moisture that precipitates locally appears equal and opposite to the local increase in evaporation (compare panels d, e, f with panels g, h, i). Indeed, as Figure 4.4 shows, and as we describe further in §4.4.3, the change in precipitation due to the change in the *in situ* precipitation of locally-evaporated moisture (i.e. the local contribution to the precipitation), which is the sum of the $\Delta\vec{E}$ and $\Delta(\mathbf{T}\vec{E})$ terms, is very small.

From Figure 4.2, we see that while $\Delta\vec{E}$ and $-\Delta(\mathbf{T}\vec{E})$ are relatively homogenous and do not have the distinct spatial structure of $\Delta\vec{P}$, the change in the convergence of remotely-evaporated moisture, $\Delta(\mathbf{FT}\vec{E})$ (panels j, k, l) is similar spatially to $\vec{P}$. The largest differences between these terms are over the deep tropics and subtropics, where changes in precipitation due to enhanced export of locally-evaporated moisture are also important. In general, the deep tropics tend to become wetter because both the local contribution to the total precipitation, $\Delta(\vec{E}-\mathbf{T}\vec{E})$, and the remote contribution to the total precipitation, $\Delta(\mathbf{FT}\vec{E})$, increase. On the other hand, the subtropics tend to become drier because the local contribution declines; in some areas, the remote contribution declines and augments this tendency, while in others, the remote contribution increases modestly. Nevertheless, in most of the subtropics, the remote contribution does not increase sufficiently to compensate for the decline in the local contribution.

Over the mid- and high-latitudes, the change in the remote contribution is positive in

both the SH and NH, both annually and seasonally. The remote contribution increases slightly in the respective winter hemisphere, compared to the annual mean. This increased convergence of remotely-evaporated moisture into the mid- and high-latitudes is consistent with increased poleward transport of latent heat in a warming climate (Held and Soden, 2006; Hwang and Frierson, 2010).

There are also noteworthy interbasin differences in the relative importance of these various terms to the precipitation perturbation. First, the change in precipitation is most negative over the Atlantic basin, which results from a substantial decline in the local contribution (see Figure 4.4) accompanied by modest changes (both increases and decreases) in the remote contribution; the southern Indian basin also experiences a net decline in total precipitation for similar reasons. The Pacific basin, on the other hand, experiences a substantial increase in precipitation over the deep tropics and a very modest decline over the subtropics. Here, precipitation over the deep tropics increases mostly because the remote contribution increases; precipitation over the subtropical Pacific only declines slightly because a decrease in the local contribution is nearly fully compensated for by an increase in the remote contribution.

4.4.2 Another Decomposition of the Total Precipitation Change

Alternately, the total change in precipitation $\Delta\vec{P}$ may be subdivided as

$$\Delta\vec{P} = (\mathbf{I} - \mathbf{T} + \mathbf{FT})\Delta\vec{E} + (-\mathbf{I} + \mathbf{F})(\Delta\mathbf{T})\vec{E} + (\Delta\mathbf{F})\mathbf{T}\vec{E} \ , \tag{4.12}$$

where the right-hand-side terms are the portion of the total precipitation change (1) due to changes in evaporation, $\Delta\vec{E}$, (2) due to changes in moisture export, $\Delta\mathbf{T}$, and (3) due to changes in the way remotely-evaporated moisture is partitioned between the regions in which it precipitates, $\Delta\mathbf{F}$.

Shown in Figure 4.3, the evaporation term (panels d, e, f) is identical to that shown in Figures 4.1 and 4.2, and, as noted previously, is positive everywhere and relatively spatially uniform. The export term (shown in panels g, h, i) and the remote moisture partitioning term

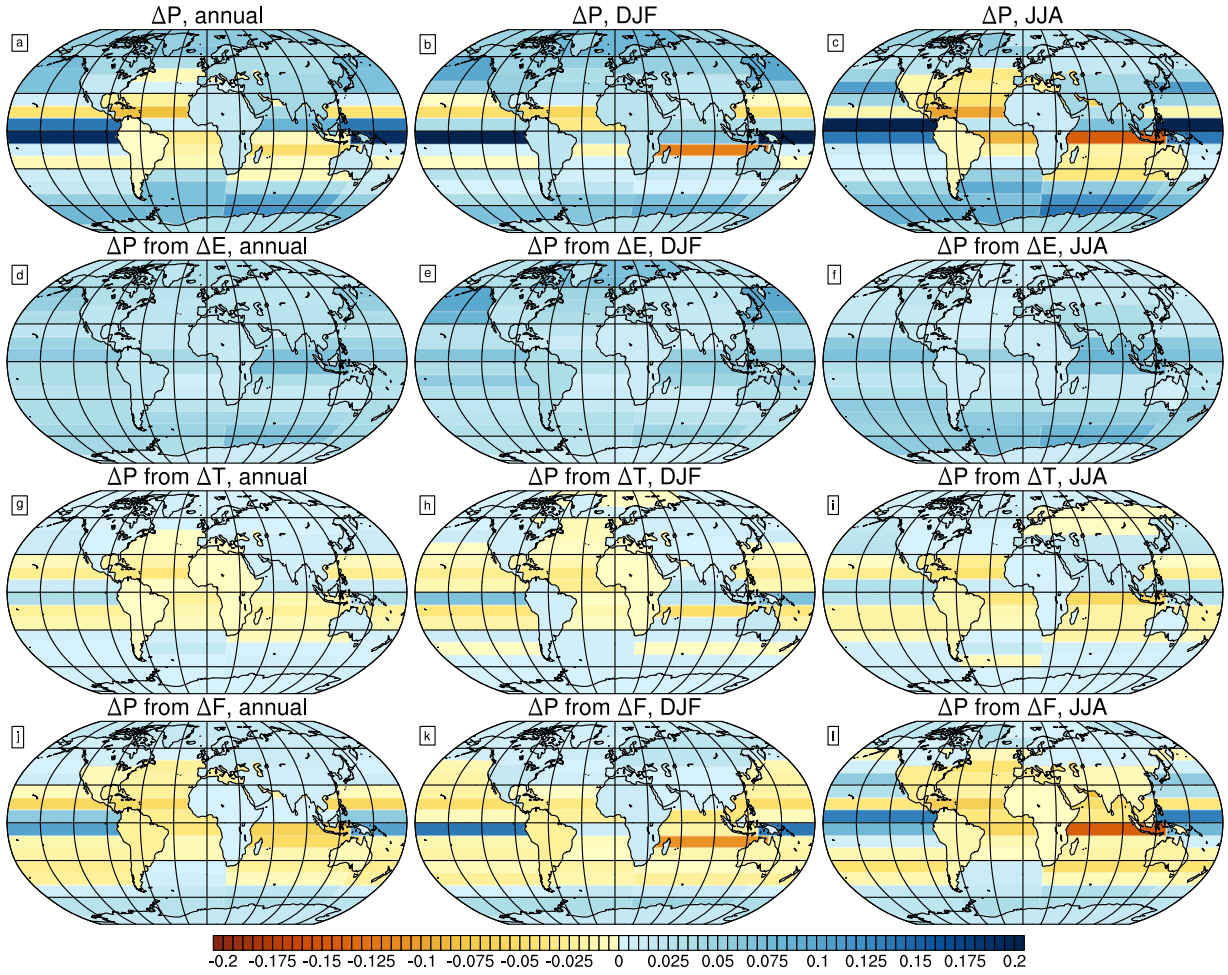

Figure 4.3: An alternative decomposition of the total precipitation change $\Delta\vec{P}$ (panels a, b, c) into the change due to $\Delta\vec{E}$ (panels d, e, f), the change due to $\Delta\mathbf{T}$ (panels g, h, i), and the change due to $\Delta\mathbf{F}$ (panels j, k, l). Each term is shown for the annual mean (panels a, d, g, j), DJF (panels b, e, h, k), and JJA (panels c, f, i, l).

(panels j, k, l), on the other hand, both display a varied spatial structure. Both changes in export and shifts in remote moisture partitioning contribute to precipitation decreases in the subtropics and increases in the mid- and high-latitudes. As pointed out earlier, without changes in the export fraction and the relative partitioning of remotely-evaporated moisture, precipitation could not decrease anywhere in the Eqm2×CO_2 experiment, since more evaporation everywhere would ensure that precipitation also increased everywhere.

Here, we discuss the annual mean terms in this decomposition unless otherwise specified. Overall, the export and remote moisture partitioning terms have a similar spatial structure in the annual mean, with decreases in the tropics and subtropics and increases in the mid- and high-latitudes. As shown in equation (4.12), the export term is a sum of two terms, one that is related to changes in the local divergence of moisture, $-(\Delta\mathbf{T})\vec{E}$, and another that is due to changes in the remote convergence of moisture, $\mathbf{F}(\Delta\mathbf{T})\vec{E}$. Note that these two terms tend to act in opposition: an increase in the export fraction will decrease the former, but will also enhance the latter. Therefore, for a given region, the magnitude of the export term depends on how well changes in the export of locally-evaporated moisture are compensated for by changes in the import of remotely-evaporated moisture. In general, as we will show in §4.4.3, the export fraction e_i increases almost everywhere, and the sign of the export term depends on how effectively increases in remote moisture convergence can compensate. Overall, the increase in local divergence due to enhanced export wins out in the tropics and subtropics, and the $\Delta\mathbf{T}$ component of the precipitation declines; in contrast, increased remote convergence due to increasing moisture export in remote regions wins out in the mid- and high-latitudes, leading to an increase in the $\Delta\mathbf{T}$ term.

Figure 4.3 also shows that in the tropics and subtropics, precipitation changes in each basin are varied, and the relative importance of each term in equation (4.12) also varies. Increased precipitation over the equatorial Pacific is due to a change in the partitioning of remotely-evaporated moisture that favors more convergence. Over the subtropical Pacific, on the other hand, precipitation only declines modestly because increased evaporation, both local and remote, compensates for declines due to the export and remote moisture partitioning

terms. Over the tropical Indian basin, the precipitation maximum shifts northward and the southern part of the basin dries. The former is due in nearly equal measure to all three terms, though it is dominated by increases in local and remote evaporation; the latter is mostly due to changes in export and partitioning of remotely-evaporated moisture that increases export from this region but does not favor convergence. Over the Atlantic, increases in local and remote evaporation tend to increase precipitation uniformly, but enhanced moisture export and decreased moisture convergence both have a drying effect and dominate the sum.

In the mid- and high-latitudes, all three terms increase precipitation. In the NH, all three terms are almost equally important for increasing precipitation, while in the SH, the evaporation term is most important. For both hemispheres, the evaporation term is the most important for increasing mid- and high-latitude precipitation in the winter hemisphere, while the export and moisture partitioning terms do not display such seasonality.

Over most land regions, including Greenland, Eurasia, northern North America, and Antarctica, all three terms act to increase precipitation year-round. Over South America, Africa, Australia, and southern North America, on the other hand, these terms act in different directions. Over South America, the change in remote moisture partitioning tends to decrease remote moisture convergence. Increased moisture export also tends to decrease precipitation, and increasing evaporation is not able to offset these. As a result, South America is the only land region where precipitation decreases in the annual mean. Southern North America and Australia also experience a similar precipitation decrease in JJA that can be attributed to changes in remote moisture partitioning that favor decreased moisture convergence; increased evaporation and increased convergence due to increasing export are not able to counteract the decrease due to moisture partitioning changes.

4.4.3 The Change in the Local Contribution to the Precipitation

We now consider the local contribution to the total precipitation changes in the $2\times CO_2$ experiment relative to C. When the first two terms on the RHS of equation (4.11) are

summed, they produce

$$\Delta\vec{E} - \Delta(\mathbf{T}\vec{E}) = \Delta(\vec{E} - \mathbf{T}\vec{E}) \ , \tag{4.13}$$

which quantifies how changes in precipitation due to locally-evaporated moisture contribute to the total precipitation change. Shown in Figure 4.4 (panels a, b, c), the change in the local contribution to the precipitation is substantially smaller than the change in the remote contribution (compare Figure 4.4 to Figure 4.2 panels j, k, l). Overall, as we detail further in §4.4.4, the change in the local contribution makes up less than 25% of the total precipitation change, while the change in the remote contribution accounts for the much larger remainder.

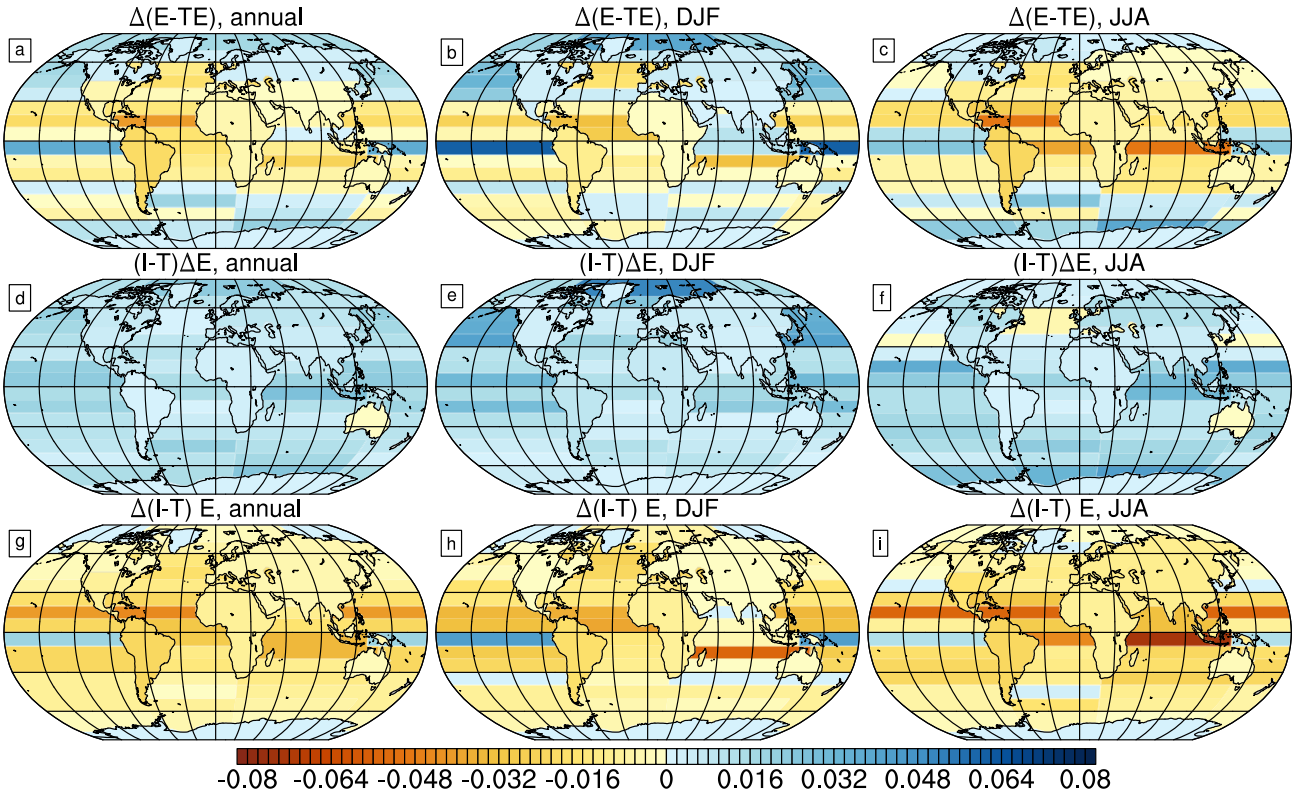

Figure 4.4: The change in the local precipitation contribution $\Delta(\vec{E} - \mathbf{T}\vec{E})$ (panels a, b, c), decomposed into the part of the local precipitation change due to the change in the evaporation $(\mathbf{I} - \mathbf{T})\Delta\vec{E}$ (panels d, e, f) and the part due to changes in moisture export fraction $\Delta(\mathbf{I} - \mathbf{T})\vec{E}$ (panels g, h, i). Quantities are shown for the annual mean (panels a, d, g), DJF (panels b, e, h), and JJA (panels c, f, i).

Generally, the local contribution decreases in the tropics and subtropics over both land and ocean, and increases in the mid- and high-latitudes. There are, however, many exceptions. Over the oceans, the local contribution decreases over the Atlantic from 60N to 40S in the annual mean; on the other hand, the local contribution increases over the equatorial Pacific (from Eq to 10° S) and Indian (from Eq to 10° N) basins. For land regions, the local contribution decreases over South America, Africa, southern Eurasia, and southern North America, while it increases over remaining land areas.

The change in the local contribution can be decomposed into a part due to changes in evaporation, and another due to changes in the moisture export fraction:

$$\Delta(\vec{E} - \mathbf{T}\vec{E}) = (\mathbf{I} - \mathbf{T})\Delta\vec{E} + \Delta(\mathbf{I} - \mathbf{T})\vec{E} \ . \tag{4.14}$$

An assessment of these terms reveals that the change in the local component of the precipitation is made up of two larger terms that are nearly equal in magnitude but opposite in sign. The change in the local contribution due to changes in evaporation (Figure 4.4, panels d, e, f) is positive almost everywhere and nearly spatially homogeneous in the annual mean; it is magnified in the mid- and high-latitudes in the winter hemisphere, particularly over the Arctic Ocean and North Pacific. On the other hand, the change in the local contribution due to changes in the export fraction (Figure 4.4, panel g, h, i) is negative almost everywhere, and is most prominent over the tropical oceans. It is most pronounced in JJA.

The change in the local contribution to the precipitation is small because it is the residual sum of these two larger, opposing terms. Overall, evaporation increases almost everywhere, which tends to increase precipitation from local moisture sources. On the other hand, the export fraction also increases almost everywhere, which tends to decrease locally-sourced precipitation. In the tropics and subtropics, the increased export wins out, and the local contribution to the precipitation decreases modestly the Eqm2×CO_2. In the mid- and high-latitudes, on the other hand, the local evaporation increase dominates over the effect of increased in local moisture export, and the local contribution increases.

From equation (4.13), it is clear that the change in the local contribution is the sum of the change in evaporation, $\Delta\vec{E}$, and the change in the divergence of locally-evaporated moisture, $\Delta(\mathbf{T}\vec{E})$. The latter term can be further subdivided into changes in moisture divergence due to changes in moisture export, $(\Delta\mathbf{T})\vec{E}$, and changes in moisture divergence due to changes in evaporation, $\mathbf{T}(\Delta\vec{E})$:

$$-\Delta(\mathbf{T}\vec{E}) = -\mathbf{T}(\Delta\vec{E}) - (\Delta\mathbf{T})\vec{E} \tag{4.15}$$

The results of this decomposition, shown in Figure 4.5, suggest that the change in the divergence of locally-evaporated moisture is mostly due to increased *in situ* evaporation, i.e. the $\mathbf{T}(\Delta\vec{E})$ term (Figure 4.5, panels d, e, f). As expected, increased evaporation with warming will lead to increased moisture divergence, even if the fraction of the total evaporation that is exported remains constant. Overall, increases in the moisture divergence due to increased *in situ* evaporation tend to be spatially homogenous, with a smaller increase over land than ocean. Over ocean, the largest increases in moisture divergence are over the mid- and high- latitudes in the winter season. In the annual mean, the north Atlantic is the only region where evaporation decreases, and, consequently, the moisture divergence also decreases here.

Changes in the export fraction, however, also contribute non-negligibly to the increased moisture divergence (Figure 4.5, panels g, h, i). The largest increases in moisture divergence due to export fraction changes are over the tropical and subtropical oceans, while the smallest increases are over the the mid-latitude oceans and land areas. Interestingly, the high latitudes are the sole region where the export contribution to the moisture divergence is positive, i.e. there is less divergence in these regions because a smaller fraction of locally-evaporated moisture is exported.

The change in the export fraction (the change in the fraction of locally-evaporated moisture that is exported, Δe_i), and the change in the local fraction (the change in the fraction of locally-evaporated moisture that precipitates locally, $\Delta(1 - e_i)$), is shown in Figure 4.6. Most striking is the homogeneity of the export fraction change, which is positive nearly ev-

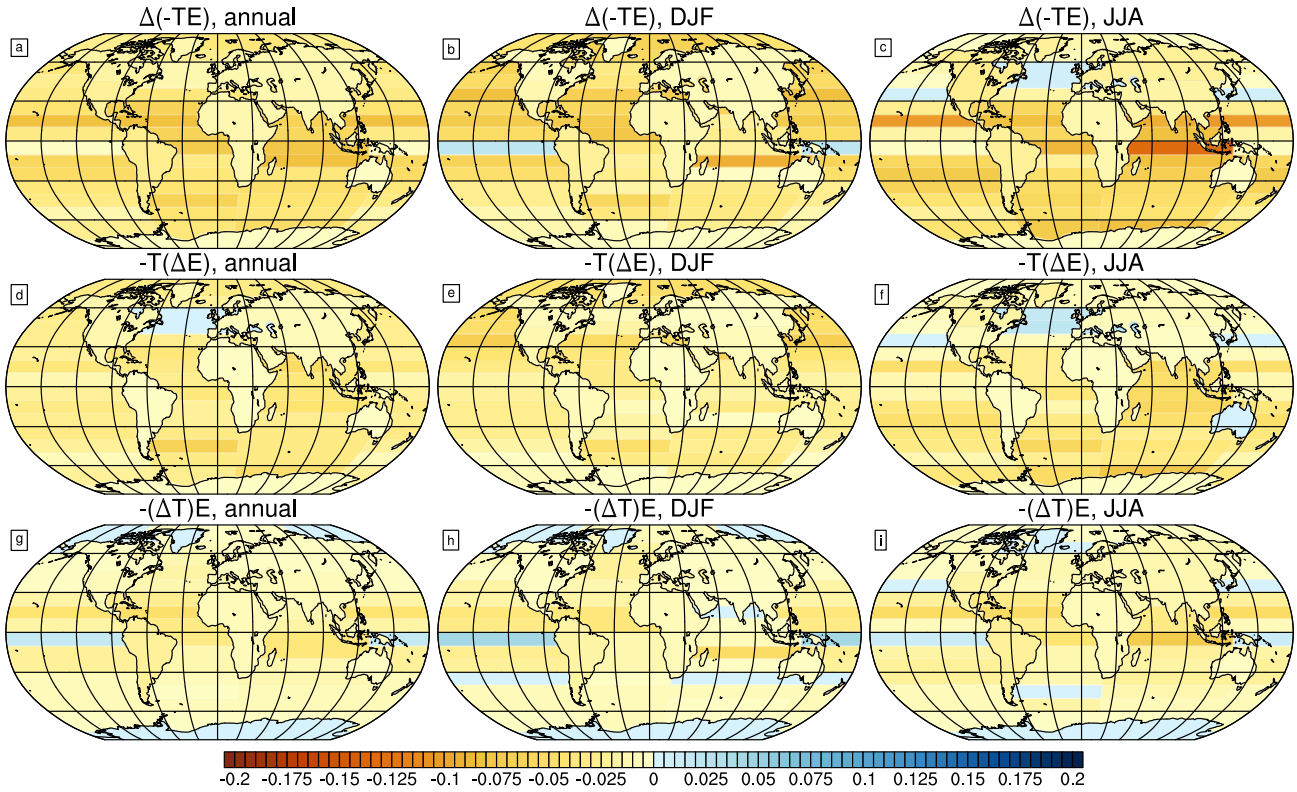

Figure 4.5: The change in the local moisture divergence term, $\Delta(-\mathbf{T}\vec{E})$ (panels a, b, and c), decomposed into changes due to $\Delta\vec{E}$ (panels d, e, and f), and changes due to $\Delta\mathbf{T}$ (panels g, h, and i). Each contribution is shown in the annual mean (panels a, d, and g), DJF (panels d, e, and f), and JJA (panels g, h, and i).

erywhere (Figure 4.6, panels a, c, e). Indeed, the only areas over which the export fraction decreases in the annual mean are Antarctica, Greenland, the Pacific sector of the Arctic, and the tropical Pacific from 10S to the equator. Similarly, the local fraction change is negative nearly everywhere (Figure 4.6, panels b, d, f).

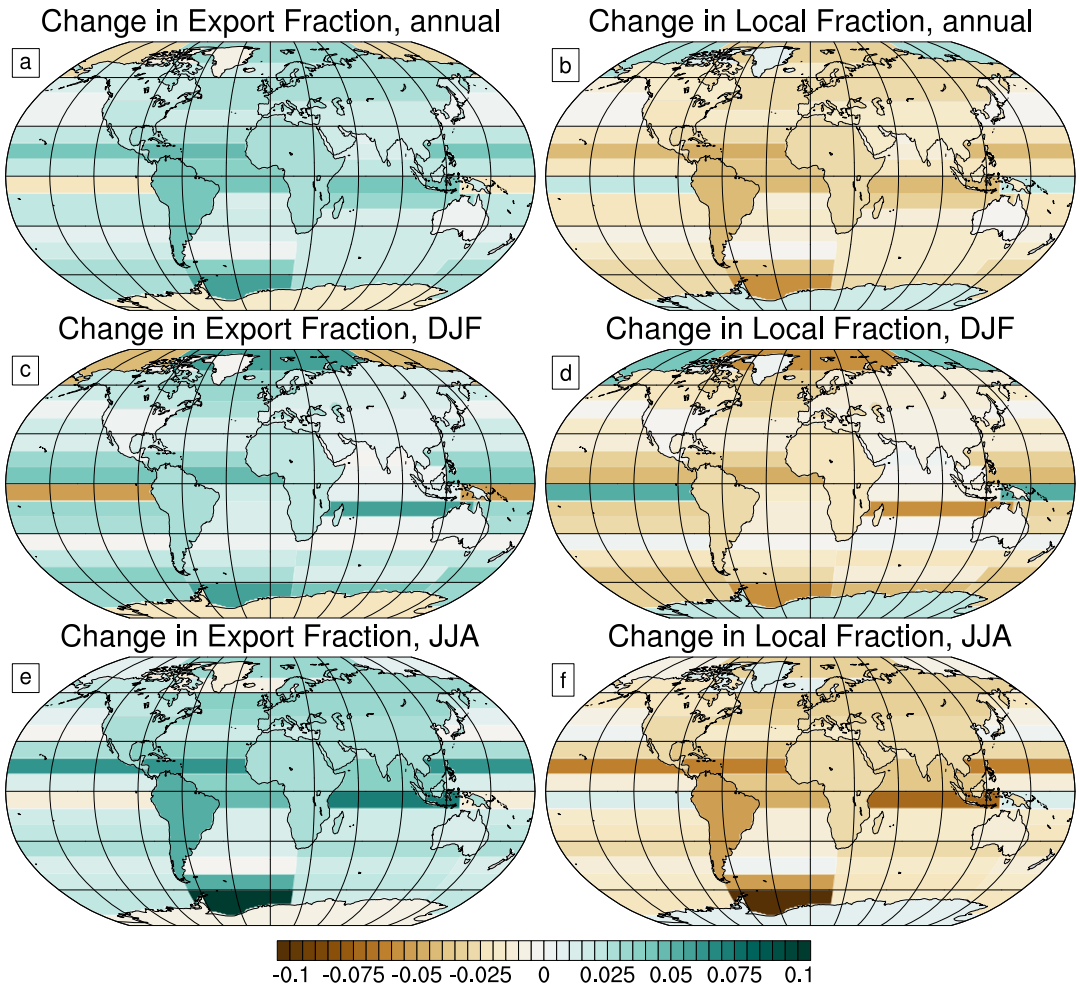

Figure 4.6: The change in the export fraction e_i (panels a, c, and e) and the local fraction $1 - e_i$ (panels b, d, and f). Fractions are shown for the annual mean (panels a and b), DJF (panels c and d), and JJA (panels e and f).

As expected, a robust increase in moisture export from each tagged region means that there is an increase in moisture convergence into other regions. We assess these changes in

the remote moisture convergence in the following section.

4.4.4 The Change in the Remote Contribution to the Precipitation

How does the change in the remote contribution to the precipitation compare to the change in the local contribution discussed earlier? Figure 4.7 shows $\Delta\vec{P}$ plotted against $\Delta(\mathbf{FT}\vec{E})$, the change in the remote contribution to the precipitation, revealing that the change in the precipitation over each tagged region is well-approximated by a linear relation,

$$\Delta\vec{P} \approx \alpha\Delta(\mathbf{FT}\vec{E}) + \delta \tag{4.16}$$

where $\alpha \approx 0.75$ and $\delta < 0.01$. Approximately three-quarters of the change in precipitation over each tagged region is due to changes in remote moisture convergence while only one-quarter is due to changes in the local contribution. Furthermore, on average, changes in the remote contribution and the local contribution tend to be in the same direction: over most of the tropics and subtropics, the precipitation decreases because both the local and remote contributions decrease, while over the mid- and high-latitudes, the precipitation increases because both of these components increase.

Figure 4.7 also reveals regional differences in the relative contributions of changing moisture convergence and changes in the local contribution. In the subtropics (shown in gold), $\Delta\vec{P} < 0$ and changes in the local contribution tend to be more important than on average. Likewise, areas in the deep tropics (shown in red), where $\Delta\vec{P}$ increases in some regions and decreases in others, also tend to have a higher than average change in the local contribution. In the mid- and high- latitudes (shown in green and blue, respectively), on the other hand, there is little systematic change in the local and remote contributions to the total precipitation, and most regions fall close to the best-fit line.

Now, we decompose the change in the $\mathbf{FT}\vec{E}$ term itself. The total change in this term may be written as

$$\Delta(\mathbf{FT}\vec{E}) = \mathbf{FT}(\Delta\vec{E}) + \mathbf{F}(\Delta\mathbf{T})\vec{E} + (\Delta\mathbf{F})\mathbf{T}\vec{E} \ , \tag{4.17}$$

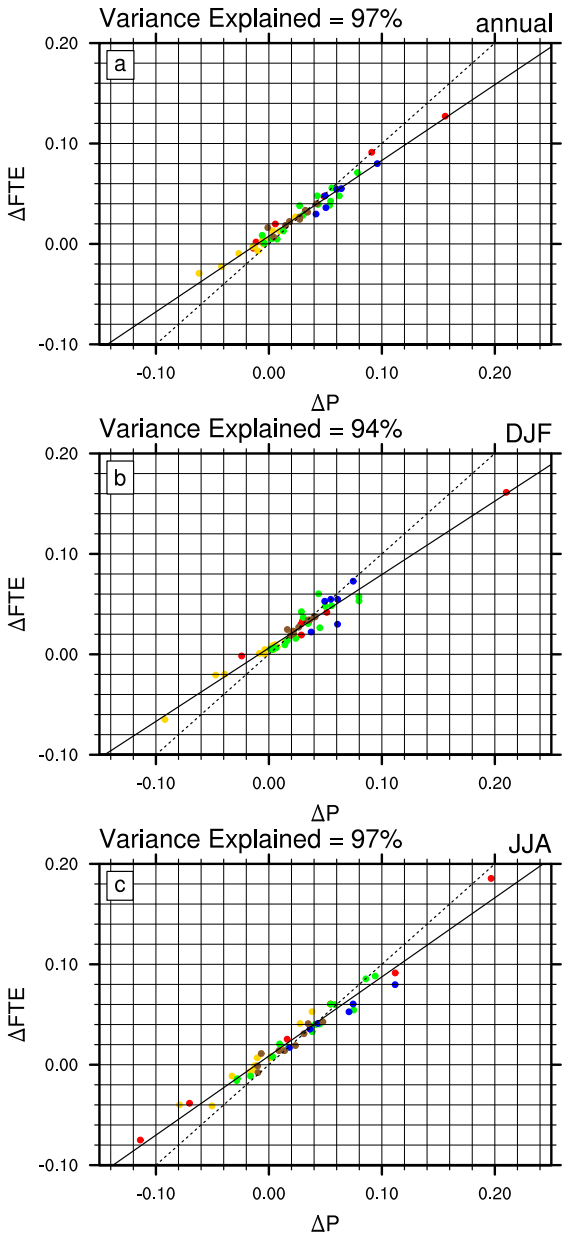

Figure 4.7: The relation between the change in the precipitation, $\Delta\vec{P}$, and the change in the convergence of remotely-evaporated moisture, $\Delta(\mathbf{FT}\vec{E})$ for each tagged region, shown for (a) the annual mean, (b) DJF, and (c) JJA. The color of the point indicates the location of the point, with all land regions in brown, ocean regions in the tropics (between 10° N and 10° S) in red, ocean regions in the subtropics (between 10°and 30° N and S) in gold, ocean regions in the midlatitudes (between 30°and 60° N and S) in green, and ocean regions in the high latitudes (between 60°and 90° N and S) in blue. The line of best fit (solid) and the one-to-one line (dotted) are also shown, with the slope α of the former equal to 0.754, 0.731, and 0.788 for panels a, b, and c, respectively.

so that the remote moisture convergence perturbation is subdivided into components due to changes in evaporation, changes in the remote moisture export fraction, and changes in moisture convergence partitioning, respectively. These contributions, shown in Figure 4.8, have several interesting features. First, changes in the evaporation tend to increase remote moisture convergence everywhere (panels d, e, f), since more evaporation provides more moisture for converging elsewhere. The change in the remote convergence due to increased evaporation is spatially uniform, though there is a slightly larger contribution in the midlatitudes over the winter hemisphere, and over the tropics, particularly over the Indian basin and southern Eurasia in JJA. Second, changes in the moisture export fraction also tend to increase remote moisture convergence (panels g, h, i), though the increase is slightly less than that due to enhanced evaporation. Since the export fraction increases nearly everywhere (recall Figure 4.6), less moisture precipitates locally and more moisture is available for converging remotely. Though the export fraction does not increase uniformly, the precipitation increase due to remote convergence of this exported moisture does increase relatively uniformly, though there is a slightly greater increase over the tropics than elsewhere.

Finally, we assess the change in the remote moisture convergence due to changes in the partitioning of remotely-evaporated moisture, $\Delta\mathbf{F}$. Figure 4.8 (panels j, k, l) shows that changes in this term are much more spatially heterogeneous than the previous two. In the high latitudes and much of the midlatitudes, this term tends to increase remote moisture convergence; in the subtropics and tropics, on the other hand, this term tends to decrease it. This spatial pattern is consistent with enhanced poleward moisture transport with CO_2-induced warming (Hwang and Frierson, 2010). The major exceptions are over the equatorial Pacific and Indian basins, with the increase in precipitation in the Pacific greatly exceeding that in the Indian, and over Africa and southern Eurasia. Moreover, this term tends to decrease precipitation preferentially over much of the Atlantic basin, compared to the Pacific and Indian basins.

To gain further insight on how changes in the convergence remotely-evaporated moisture contribute to precipitation changes, we subdivide this term using various physically-

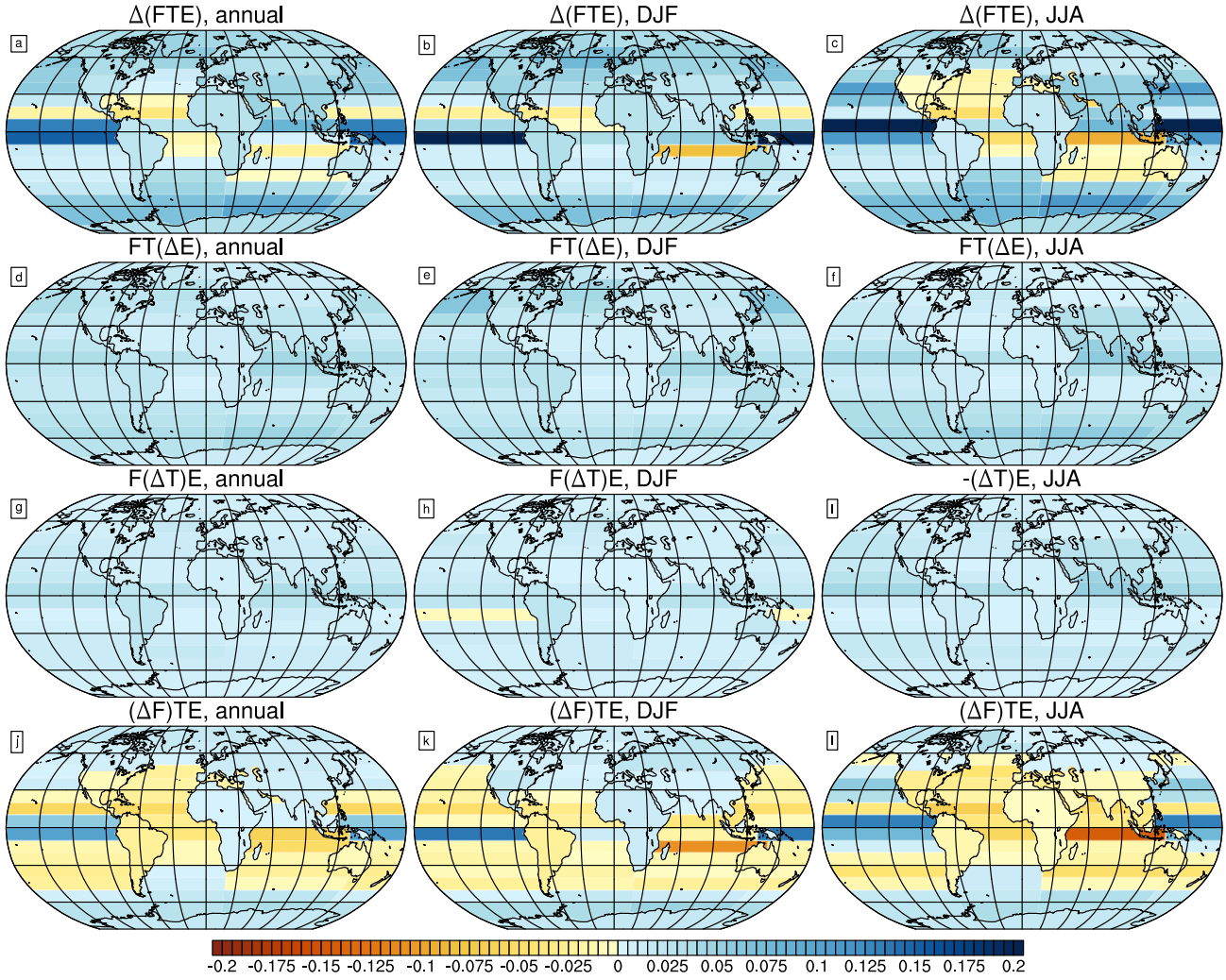

Figure 4.8: Decomposition of the remote moisture convergence term, $\Delta(\mathbf{FT}\vec{E})$, as given in equation (4.17: the entire term (panels a, b, c), that due to changes in evaporation $\mathbf{FT}(\Delta\vec{E})$ (panels d, e, f), that due to changes in moisture export $\mathbf{F}(\Delta\mathbf{T})\vec{E}$ (panels g, h, i), and that due to changes in the partitioning of remotely-evaporated moisture between sink regions $(\Delta\mathbf{F})\mathbf{T}\vec{E}$ (panels j, k, l). Each term is shown for the annual mean (panels a, d, g, and j), DJF (panels b, e, h, and k), and JJA (panels c, f, i, and l).

motivated decompositions of matrix $\mathbf{F}$. In general, $\mathbf{F}$ is subdivided into some n contributions such that

$$\mathbf{F} = \sum_n \mathbf{F}_n \ . \tag{4.18}$$

Using equation (4.18), $\Delta(\mathbf{FT}\vec{E})$ can be subdivided into n terms, each of which is due to some component $\mathbf{F}_n$:

$$\Delta(\mathbf{FT}\vec{E}) = \sum_n \Delta(\mathbf{F}_n\mathbf{T}\vec{E}) \ . \tag{4.19}$$

We begin with a decomposition in which $\mathbf{F}$ has been subdivided as

$$\Delta(\mathbf{FT}\vec{E}) = \Delta(\mathbf{F}_{O-O}\mathbf{T}\vec{E}) + \Delta(\mathbf{F}_{O-L}\mathbf{T}\vec{E}) + \Delta(\mathbf{F}_{L-O}\mathbf{T}\vec{E}) + \Delta(\mathbf{F}_{L-L}\mathbf{T}\vec{E}) \ , \tag{4.20}$$

where the terms on the right-hand-side are due to (1) moisture sourced from the ocean that also converges over the ocean, (2) moisture sourced from the ocean that converges over land, (3) moisture sourced from land that converges over the ocean, and (4) moisture sourced from land that also converges over land. Figure 4.9 shows each of these contributions to the total change in remote moisture convergence, and reveals that only the first two are substantive. While it is hardly surprising that the land-to-land term is small (panel d), given the large size of the tagged land regions in our experiments, it is somewhat surprising that there is only a slight increase in the amount of moisture evaporated over land that precipitates over the ocean (panel c). However, given that the land-to-ocean term is also very small in the mean state, the modest increase in this term most likely reflects the mean state.

We now assess changes in the ocean-to-ocean and ocean-to-land convergence terms (Figure 4.9, panels a and b, respectively). The latter is positive over all land areas, indicating that precipitation over land increases because moisture of ocean origin tends to converge more over it. Furthermore, some land areas experience larger precipitation increases, primarily southern Eurasia and Greenland, while others experience very little, like Australia and South America. Compared to the ocean-to-land convergence term, the change in the ocean-to-ocean convergence term is more spatially-heterogeneous. Ocean-to-ocean moisture convergence in-

creases strongly over the tropical Pacific and Indian basins, and over the Southern Ocean. In the NH, the ocean-to-ocean term increases over the Arctic, Pacific basin north of 30° N, and Atlantic basin north of 50° N. Decreased moisture convergence over the subtropics is evident over all the basins, though the decrease is least pronounced in the Pacific basin and most pronounced over the Indian. Over the south Atlantic, moisture convergence remains relatively unchanged, though it decreases over the north Atlantic between 10° N and 30° N. The remote moisture convergence over the equatorial Atlantic is substantially smaller than it is over the equatorial Pacific and Indian basins.

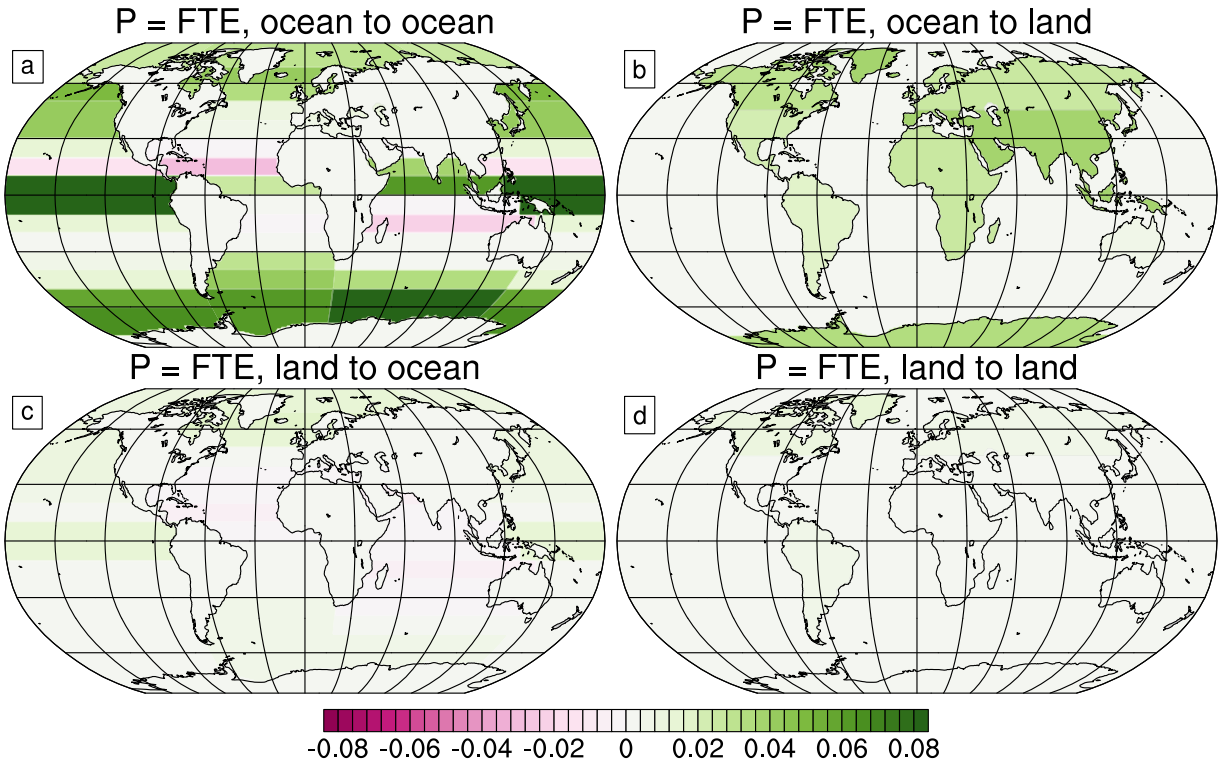

Figure 4.9: Decomposition of the change in the remote moisture convergence, $\Delta(\mathbf{F}\mathbf{T}\vec{E})$, as in equation (4.20), for the annual mean. Panels show (a) the ocean-to-ocean contribution, $\Delta(\mathbf{F}_{O-O}\mathbf{T}\vec{E})$, (b) the ocean-to-land contribution, $\Delta(\mathbf{F}_{O-L}\mathbf{T}\vec{E})$, (c) the land-to-ocean contribution, $\Delta(\mathbf{F}_{L-O}\mathbf{T}\vec{E})$, and (d) the land-to-land contribution, $\Delta(\mathbf{F}_{L-L}\mathbf{T}\vec{E})$.

In subsequent decompositions, we seek to understand the complex spatial structure of the

change in the ocean-to-ocean moisture convergence (Figure 4.9 panel a). First, $\Delta(\mathbf{F}_{O-O}\mathbf{T}\vec{E})$ is decomposed into components in which (1) moisture precipitates south of its source region, $\Delta(\mathbf{F}_{NtoS}\mathbf{T}\vec{E})$, (2) moisture precipitates north of its source region, $\Delta(\mathbf{F}_{StoN}\mathbf{T}\vec{E})$, and (3) moisture precipitates at the same latitude as its source region, $\Delta(\mathbf{F}_{zon}\mathbf{T}\vec{E})$:

$$\Delta(\mathbf{F}_{O-O}\mathbf{T}\vec{E}) = \Delta(\mathbf{F}_{NtoS}\mathbf{T}\vec{E}) + \Delta(\mathbf{F}_{StoN}\mathbf{T}\vec{E}) + \Delta(\mathbf{F}_{zon}\mathbf{T}\vec{E}) \ . \tag{4.21}$$

Shown in Figure 4.10 (panels a, b, c), this decomposition reveals that north-to-south moisture convergence increases most dramatically over the Southern Ocean and equatorial Pacific Ocean, while south-to-north moisture convergence increases over the mid- and high-latitude Pacific and Atlantic basins and near the equator over all three basins. On the other hand, both north-to-south and south-to-north moisture convergence decrease over the north Atlantic and south Indian basins, while south-to-north moisture convergence also decreases over the south Atlantic. This spatial pattern is consistent with increased moisture convergence from the subtropics to the ITCZ, though the increase is most pronounced over the Pacific basin and is least pronounced over the Atlantic basin. It is also consistent with increased poleward transport of moisture sourced from the subtropics and tropics over all three basins, with greater moisture convergence over the mid- and high-latitudes in the SH than the NH, likely due to the larger area of ocean moisture source regions in the former.

Another decomposition of $\Delta(\mathbf{F}_{O-O}\mathbf{T}\vec{E})$ subdivides it into an intrabasin term, $\Delta(\mathbf{F}_{intrabasin}\mathbf{T}\vec{E})$, where moisture precipitates in the same basin in which it evaporates, and an interbasin term $\Delta(\mathbf{F}_{interbasin}\mathbf{T}\vec{E})$, where moisture precipitates in a different basin than the basin where it evaporates:

$$\Delta(\mathbf{F}_{O-O}\mathbf{T}\vec{E}) = \Delta(\mathbf{F}_{intrabasin}\mathbf{T}\vec{E}) + \Delta(\mathbf{F}_{interbasin}\mathbf{T}\vec{E}) \ . \tag{4.22}$$

Shown in Figure 4.10 (panels d, e), the changes in the interbasin and intrabasin moisture convergence are of roughly similar magnitude globally, although the latter greatly dominates the mean state (recall the previous chapter). Furthermore, the interbasin moisture convergence increases globally, with the largest increases over the Southern Ocean and equatorial Pacific,

and smaller increases over the Pacific and the northern Indian basins. The smallest increases in the interbasin moisture convergence are over the Atlantic and south Indian basins. In contrast, the intrabasin moisture convergence term is more spatially heterogeneous, with decreased convergence over the subtropics over all three basins and increased convergence over the mid- and high-latitudes. Intrabasin-sourced equatorial precipitation increases most strongly over the Pacific, modestly over the Indian, and not at all over the Atlantic. As noted earlier, the change in the remote moisture convergence is consistent with a pattern of increased convergence over the equatorial regions, midlatitudes, and polar regions, and decreased convergence over the subtropics. Indeed, the major difference between the intrabasin and interbasin components of the remote moisture convergence change is the change in the subtropics, which is weakly positive in the interbasin component, but mostly negative in the intrabasin component. Thus, precipitation decreases in the subtropics due to decreasing intrabasin moisture convergence that is incompletely compensated for by increasing interbasin moisture convergence.

A third decomposition of $\Delta(\mathbf{F}_{O-O}\mathbf{T}\vec{E})$ is given by

$$\Delta(\mathbf{F}_{O-O}\mathbf{T}\vec{E}) = \Delta(\mathbf{F}_{merid}\mathbf{T}\vec{E}) + \Delta(\mathbf{F}_{cross}\mathbf{T}\vec{E}) + \Delta(\mathbf{F}_{zon}\mathbf{T}\vec{E}) \ , \tag{4.23}$$

where the ocean-to-ocean remote moisture convergence is subdivided into (1) a pure meridional component, $\Delta(\mathbf{F}_{merid}\mathbf{T}\vec{E})$, where moisture only travels meridionally between its source and sink tagged regions, (2) a cross component, $\Delta(\mathbf{F}_{cross}\mathbf{T}\vec{E})$, where moisture travels meridionally and zonally between its source and sink regions, and (3) a pure zonal component $\Delta(\mathbf{F}_{intrabasin}\mathbf{T}\vec{E})$, where moisture only travels zonally between its source and sink regions.

Shown in Figure 4.10 (panels f, g, h), this decomposition appears nearly identical to the interbasin-intrabasin decomposition given by equation (4.22). Given that the specific spatial domains tagged are 10° latitude bands that cover each basin, it is evident that the pure meridional term must correspond to the intrabasin term, while the interbasin term is a sum of the cross and pure zonal terms. This decomposition reveals that nearly all of the increase

in interbasin moisture convergence is due to both meridional and zonal transport (the cross term), and that the change in interbasin moisture convergence due to interbasin transport without a meridional component is negligible.

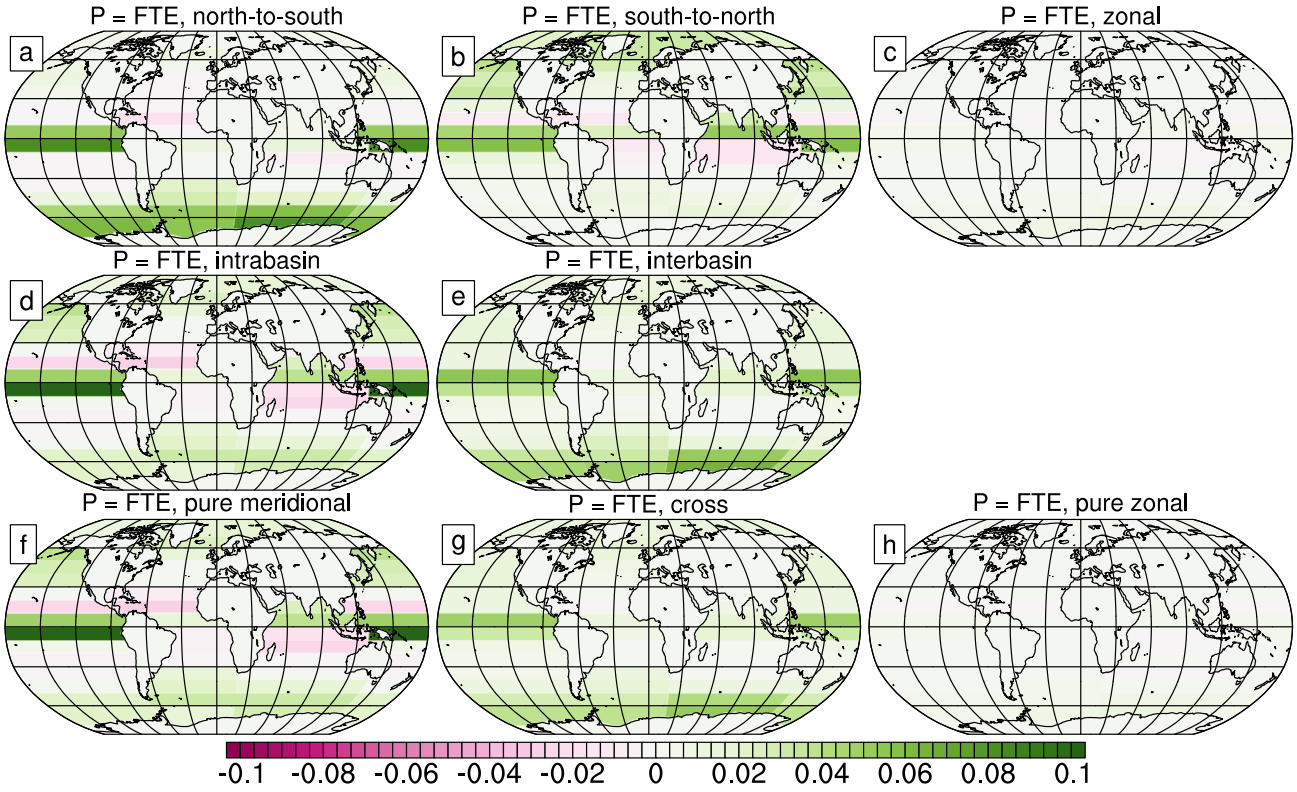

Figure 4.10: Three physics-based decompositions of $\Delta(\mathbf{F}_{O-O}\mathbf{T}\vec{E})$, the change in the ocean-to-ocean component of the remote moisture convergence, as given in equation (4.21) (panels a, b, c), equation (4.22) (panels d, e), and equation (4.23) (panels f, g, h). All decompositions are shown for the annual mean.

Finally, we present an extension of the decomposition from equation (4.22), where the intrabasin component is further subdivided into a "near" component, where moisture originates in a latitude band adjacent to where it precipitates, and a "far" component, where moisture originates in a latitude band that is not adjacent to the one in which it precipitates:

$$\Delta(\mathbf{F}_{O-O}\mathbf{T}\vec{E}) = \Delta(\mathbf{F}_{inter}\mathbf{T}\vec{E}) + \Delta(\mathbf{F}_{intra,\ near}\mathbf{T}\vec{E}) + \Delta(\mathbf{F}_{intra,\ far}\mathbf{T}\vec{E}) \ . \tag{4.24}$$

Shown in Figure 4.11, this decomposition successfully separates the intrabasin moisture convergence into one in which convergence decreases over much of the globe (the "near" component) and another in which convergence increases over much of the globe (the "far" component). Indeed, the former decreases everywhere except over the north and equatorial Pacific, the Atlantic sector of the Southern Ocean, and a small swath of the equatorial Indian; the latter increases everywhere, except for a small region over the subtropical Atlantic and equatorial Indian basins. That the intrabasin moisture convergence can be separated into such opposing components suggests that there is a systematic decrease in moisture convergence from adjacent regions, and a corresponding increase in moisture convergence from more remote regions. Combined with the increasing interbasin moisture convergence, this indicates that *moisture is transported further in the Eqm2×CO_2 experiment relative to C.*

Indeed, the increase in the moisture transport length scale is also evident in the change in the mean latitude of the moisture source region, as shown in Figure 4.12. Calculated as

$$\Delta\overline{\phi} = \Delta\left(\frac{\sum_i P_i\phi_i}{\sum_i P_i}\right) \ , \tag{4.25}$$

where the mean latitude of the precipitation source, $\overline{\phi}$ is computed as the average of the central latitude of each tagged region i weighted by the precipitation from that tagged region. In general, Figure 4.12 shows that precipitation over the NH tends to originate further south in the Eqm2×CO_2 experiment relative to C, while precipitation over the SH tends to originate further north. The tendency is more pronounced in the summer hemisphere, and is most prominent over the mid- and high-latitudes. The effect is more homogeneous over the NH than the SH.

In general, Figure 4.12 shows that precipitation at a given location originates more equatorward in the Eqm2×CO_2 experiment. This result further supports our contention that the distance between source (evaporation) and sink (precipitation) regions in Eqm2×CO_2 increases relative to C. In the following subsection, we further assess this increase in the

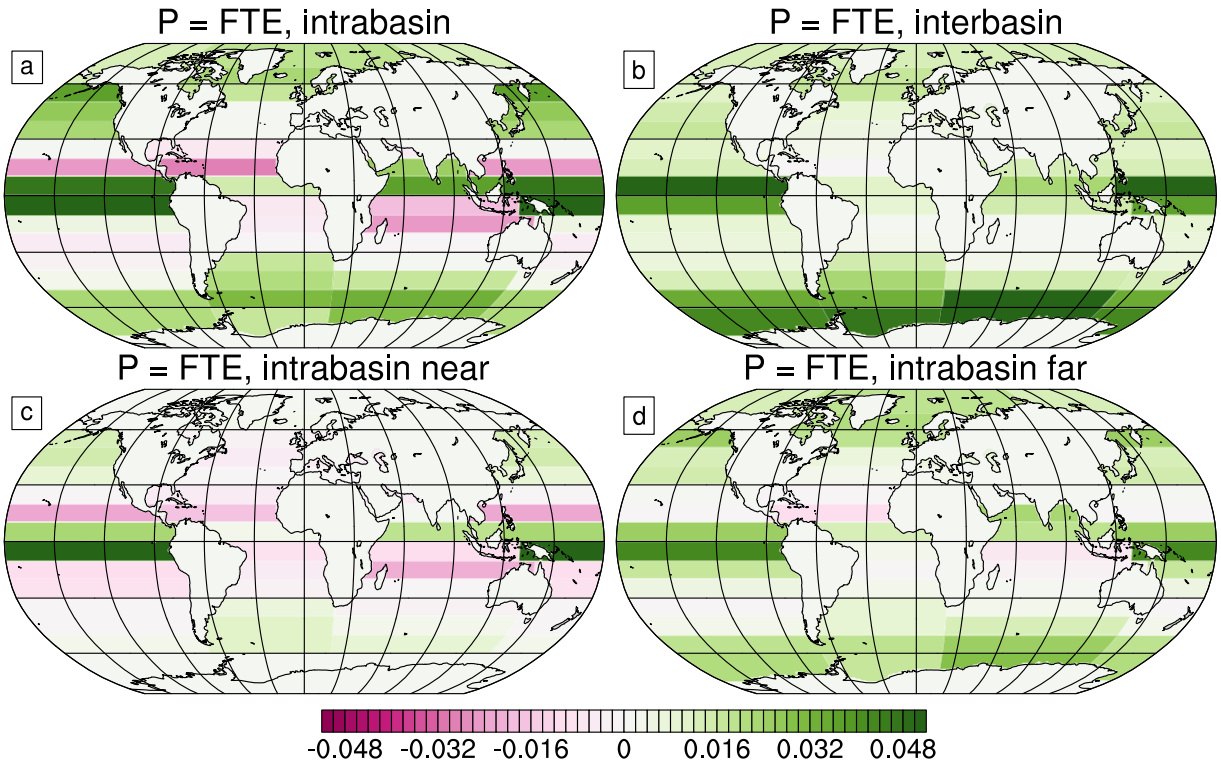

Figure 4.11: Another decomposition of the $\Delta(\mathbf{F}_{O-O}\mathbf{T}\vec{E})$ into intrabasin (panel a) and interbasin (panel b) components, with the intrabasin component further subdivided into "near" (panel c) and "far" (panel d) components as in equation (4.24).

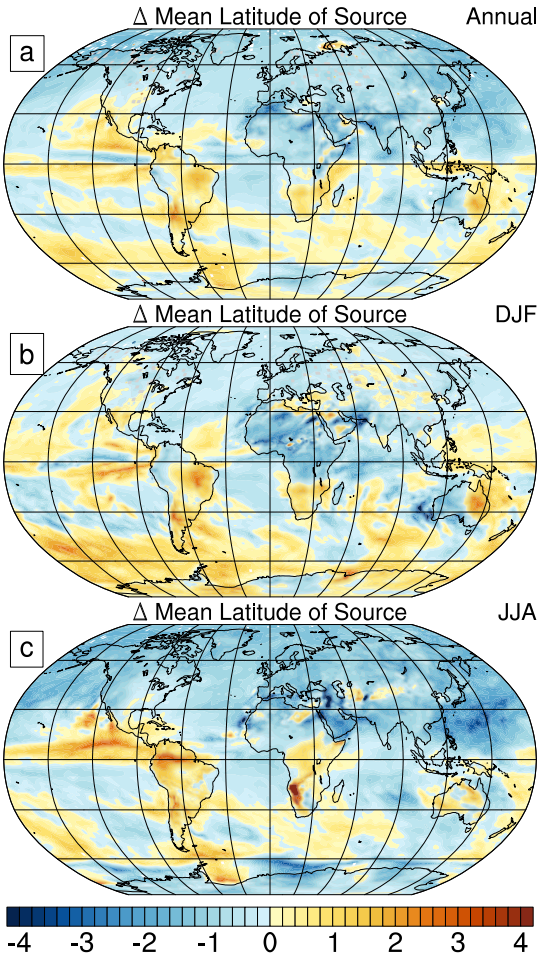

Figure 4.12: The change in the mean latitude of the ocean moisture source region, computed for the total precipitation in each model grid box in (panel a) the annual mean, (panel b) DJF, and (panel c) JJA.

moisture transport length scale with the aid of heuristic models.

4.5 Understanding Enhanced Moisture Transport in Eqm2×CO_2 using Heuristic Models

As described above, several lines of evidence point to enhanced moisture transport in the Eqm2×CO_2 experiment relative to C. First, the fraction of locally-evaporated moisture that is exported increases globally (recall Figure 4.6). As a result, a smaller fraction of the total precipitation originates as locally-evaporated moisture, while a larger fraction originates remotely. Second, the convergence of remotely-evaporated moisture shifts towards longer distances between source (evaporative) and sink (precipitation) regions. This increase in the moisture transport length scale results in an increase in interbasin moisture convergence everywhere (Figure 4.10, panel e). Furthermore, the part of the intrabasin moisture convergence that originates as evaporation from an adjacent latitude band decreases almost everywhere (Figure 4.11, panel c), while the part that originates as evaporation from more distant latitude bands increases (Figure 4.11, panel d). Finally, the average latitude of the moisture source region consistently moves equatorward in the mid- and high-latitudes in both hemispheres, indicating that moisture source regions become more distant from sink regions (Figure 4.12).

Why is a greater fraction of locally-evaporated moisture exported in the Eqm2×CO_2 experiment? And why does exported moisture travel a greater distance before precipitating? The global extent of these changes suggests that a simple, robust mechanism is responsible for lengthening the moisture transport length scale. In the ensuing analysis, we show that this increase in the length scale of moisture transport corresponds to an increase in the moisture residence time scale. Such an increase in time scale increases the relative importance of remotely-evaporated moisture sources to the total *in situ* precipitation at the expense of locally-evaporated moisture, thereby increasing the atmospheric moisture transport length scale.

4.5.1 Adjustment Time Scales in a One-Box Model

First, consider a self-contained domain with an evolving atmospheric moisture content $Q(t)$ and (constant) evaporation rate E_0. Following Trenberth (1998) and Bosilovich et al. (2005), the precipitation can be written as a depletion tendency γ multiplied by the total moisture. Thus, the time evolution of Q must satisfy the ordinary differential equation (ODE)

$$\frac{dQ}{dt} = E_0 - \gamma Q \ . \tag{4.26}$$

If $Q(t = 0) = 0$, the solution is

$$Q(t) = \frac{E_0}{\gamma}(1 - e^{-\gamma t}) \ . \tag{4.27}$$

The adjustment time scale τ for Q is

$$\tau = \frac{1}{\gamma} \ . \tag{4.28}$$

Several other studies have shown that increasing atmospheric moisture content with temperature at the C-C rate while limiting evaporation and precipitation increases to some lower rate requires that the precipitation tendency γ must decrease (see Trenberth, 1998; Bosilovich et al., 2005; van der Ent and Savenije, 2011). This, in turn, corresponds to a decrease in the rate of moisture cycling, or, analogously, an increase in the atmospheric moisture residence time scale τ, as we have shown above.

4.5.2 Time Scales and Length Scales in an n-Box Model

We now show how this moisture residence time scale increase directly corresponds to a greater fraction of moisture originating further afield, and a correspondingly smaller fraction originating nearby. Ponder a system of three atmospheric boxes of length L, as shown on the left side of Figure 4.13. Each box has some moisture content $Q_i(t)$ and some characteristic evaporation rate E_i. As for the single box model above, the precipitation is proportional to

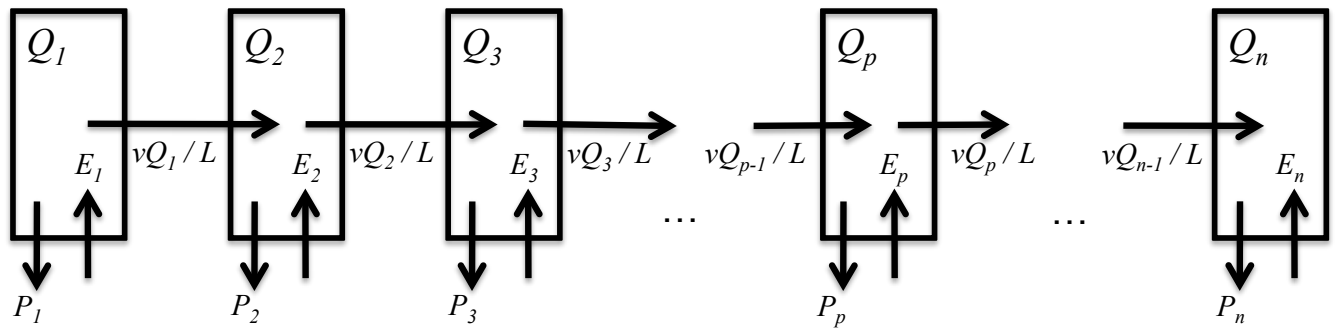

Figure 4.13: Schematic of the n-box model used to study moisture transport length scales. The length of each box is L and the moisture content is Q_i. Moisture is replenished by evaporation E_i and is depleted by precipitation $P_i = \gamma Q_i$. Moisture flux between boxes is uni-directional at some uniform advective velocity v. A smaller 3-box model, as described in the text, consists of only the first 3 boxes on the left-hand-side.

the box's moisture content and is written as γQ_i. Additionally, moisture is advected between boxes by some advective velocity v. This yields a system of three coupled ODEs

$$\begin{aligned} \frac{dQ_1}{dt} &= E_1 - \gamma Q_1 - \frac{v}{L} Q_1 \\ \frac{dQ_2}{dt} &= E_2 - \gamma Q_2 - \frac{v}{L} Q_2 + \frac{v}{L} Q_1 \\ \frac{dQ_3}{dt} &= E_3 - \gamma Q_3 - \frac{v}{L} Q_3 + \frac{v}{L} Q_2 \ , \end{aligned} \tag{4.29}$$

with an advective time scale of

$$\tau = \frac{1}{\gamma + v/L} \ . \tag{4.30}$$

Once again, it is clear that decreasing the precipitation tendency would increase the residence time scale. Additionally, the moisture residence time may also be increased by decreasing the advection velocity v or increasing the box length L.

The steady state solution ($dQ_i/dt = 0$) of the system of equations (4.29) may be written

as

$$Q_1 = \frac{1}{\beta}E_1 \tag{4.31}$$

$$Q_2 = \frac{1}{\beta}\left(E_2 + \frac{v}{L\beta}E_1\right) \tag{4.32}$$

$$Q_3 = \frac{1}{\beta}\left(E_3 + \frac{v}{L\beta}E_2 + \left(\frac{v}{L\beta}\right)^2 E_1\right) \quad , \tag{4.33}$$

where $\beta = \gamma + v/L$ is the moisture cycling rate and $1/\beta$ is the timescale τ. Indeed, the general solution for the n-th box may be written as the finite series

$$Q_n = \frac{1}{\beta}\sum_{i=1}^{n}\left(\frac{v}{L\beta}\right)^{n-i} E_i \ . \tag{4.34}$$

Consider the steady-state solution for Q_3 in equation (4.33). The fraction of moisture in box 3 that comes from box 1, $F_{3,1}$ is

$$F_{3,1} = \frac{\left(\frac{v}{L\beta}\right)^2 E_1}{E_3 + \frac{v}{L\beta}E_2 + \left(\frac{v}{L\beta}\right)^2 E_1} \ , \tag{4.35}$$

With some algebraic manipulation, it can be shown that $(\partial F_{3,1}/\partial\gamma) < 0$ for all physical values of β (i.e. $\beta > 0$). In other words, decreasing the precipitation tendency will increase the fraction of moisture in box 3 that comes from box 1. Correspondingly, the fraction of moisture that originates in boxes 2 and 3 must decrease.

Indeed, a similar proof can be used to show that the fraction of moisture in the n-th box coming from the p-th (where p is sufficiently small) increases as γ decreases. In the general case, the fraction of moisture in the n-th box that comes from the p-th box is

$$F_{n,p} = \frac{\left(\frac{v}{L\beta}\right)^{n-p} E_p}{\sum_{i=1}^{n}\left(\frac{v}{L\beta}\right)^{n-i} E_i} \ . \tag{4.36}$$

To simplify the mathematics, let all $E_i = E_0$. This gives

$$F_{n,p} = \frac{\left(\frac{v}{L\beta}\right)^{n-p}}{\sum_{i=1}^{n}\left(\frac{v}{L\beta}\right)^{n-i}} \ . \tag{4.37}$$

Now, define the non-dimensional parameter ξ as

$$\xi \equiv \frac{v/L}{\gamma + v/L} = \frac{v}{L\beta} \ , \tag{4.38}$$

and note that $|\xi| < 1$ for all $\gamma > 0$. Then, $F_{n,p}$ can be written as

$$F_{n,p} = \frac{(\xi)^{n-p}}{\sum_{i=1}^{n}(\xi)^{n-i}} \ . \tag{4.39}$$

Using the Taylor series expansion, valid for $|x| < 1$,

$$\frac{1}{1-x} = 1 + x + x^2 + x^3 + ... \ , \tag{4.40}$$

equation (4.39) may be well-approximated as

$$F_{n,p} \approx \xi^{n-p}(1-\xi) \ . \tag{4.41}$$

Taking the partial derivative of $F_{n,p}$ with respect to β yields

$$\frac{\partial F_{n,p}}{\partial \beta} = \frac{1}{\beta}\left[(n-p+1)\left(\frac{v}{L\beta}\right)^{n-p+1} - (n-p)\left(\frac{v}{L\beta}\right)^{n-p}\right] \ , \tag{4.42}$$

which is less than zero when p is less than some critical value p_c:

$$p_c = n - \frac{v}{L\beta - v} = n - \frac{v}{L\gamma} \ . \tag{4.43}$$

Therefore, for boxes that satisfy $1 \leq p < p_c$, $F_{n,p}$ increases as γ decreases, indicating that

decreasing the precipitation tendency and, thereby, the moisture cycling rate, will increase the fraction of moisture in box n that comes from these distant boxes. Conversely, for boxes that satisfy $p_c < p \leq n$, the same decrease of the precipitation tendency will decrease the fraction of moisture in box n that comes from these proximal boxes. Furthermore, decreasing γ will decrease this critical value p_c; in other words, decreasing the precipitation tendency will also tend to shift the range of boxes at which $\partial F_{n,p}/\partial\gamma < 0$ to boxes that are even more distant.

In Figure 4.14, we present some distributions of $F_{n,p}$ as a function of box p, using several different values of the precipitation tendency γ; results are shown for a standard case in which $n = 50$ boxes, L =100 m, and $v = 10$ m s^{-1}. In panel a, where evaporation is constant across boxes, it is clear that decreasing γ tends to flatten the distribution of $F_{n,p}$, decreasing the fraction of moisture in box n that originates in proximal boxes and increasing the fraction that originates in distant boxes. Furthermore, Figure 4.14a shows that decreasing γ tends to decrease the value of p_c that separates regions where $F_{n,p}$ increases and where it decreases; in particular, the intersection between the $\gamma = 0.01$ s^{-1} and the $\gamma = 0.02$ s^{-1} distributions occurs at larger p than the intersection between the $\gamma = 0.005$ s^{-1} and the $\gamma = 0.01$ s^{-1} distributions.

In Figure 4.14, panel b, the evaporation is allowed to vary between boxes such that

$$E_p = (0.9)^{p-1} E_0 \ , \tag{4.44}$$

giving a geometric decrease in evaporation with box number, giving a zero-th order approximation to atmospheric moisture transport from a warm, highly evaporative region to a cool one. Clearly evident in this case is an increase in the moisture fraction from distant boxes, and a corresponding decrease in moisture fraction from proximal boxes, as γ decreases; also evident is a decrease in p_c as γ decreases, indicating a shift towards more distant source regions with decreased γ. In the varying evaporation case, however, both these effects are amplified, and $\partial F_{n,p}/\partial\gamma$ is clearly larger in magnitude than in the constant evaporation case.

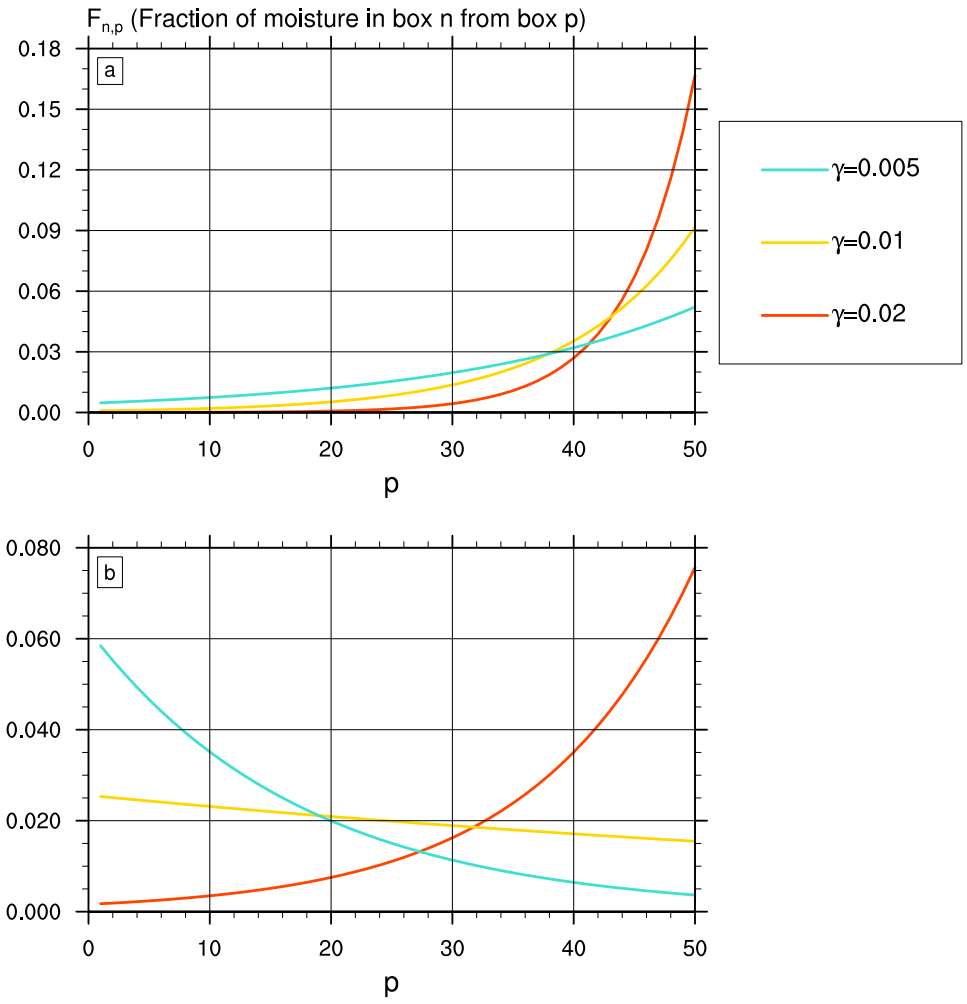

Figure 4.14: $F_{n,p}$, the fraction of moisture in box n originating from box p, for three different values of the precipitation tendency γ (given in s^{-1}): (panel a) with constant evaporation in each box (i.e. $E_p = E_0$); and (panel b) with evaporation decreasing geometrically with the box number, $E_p = (0.9)^{p-1}E_0$. Other constants are as follows: $v = 10$ m/s, $L = 100$ m, and $n = 50$.

Thus, small changes in the precipitation tendency have a much larger effect on the moisture source region distribution for the n-th box when the evaporation is allowed to decrease with box number, compared to the case when the evaporation is held constant.

In summary, we have used a simple n-box model to show that decreasing the precipitation tendency γ, which increases the residence time of atmospheric water and decreases the atmospheric moisture cycling rate, also tends to increase the fraction of the precipitation in the n-th box that originates further afield, while decreasing the fraction that originates nearby. Thus, increasing the time scale also increases the advective length scale of moisture transport through the atmosphere, and, as a result, the distance between where water evaporates and where it precipitates will increase.

4.5.3 The Length Scale in a Spatially-Continuous Model

Finally, we show that an analogous result can be obtained in a spatially-continuous model. Ponder a one-dimensional continuous spatial domain in which the vertically-integrated atmospheric moisture is $Q(x)$. Over this domain, the atmospheric moisture increases due to evaporation, decreases due to depletion by precipitation, and is subject to advection by atmospheric motions. In this case, the equation governing the time evolution of $Q(x)$ is

$$\frac{\partial Q}{\partial t} = E(x) - \nabla \cdot (vQ) - \gamma Q \ , \tag{4.45}$$

where $E(x)$ is the evaporation as a function of spatial position, $\nabla \cdot (vQ)$ is the advection term, and $v(x)$ is the advection velocity. If v is assumed to be constant over the spatial domain, equation (4.45) may be written as

$$\frac{\partial Q}{\partial t} = E(x) - v\frac{\partial Q}{\partial x} - \gamma Q \ . \tag{4.46}$$

We find steady-state solutions to equation (4.46). If the evaporation rate is spatially-invariant over the domain (i.e. $E(x) \equiv E_0$), and if $Q(x = 0) = 0$, we obtain the steady-state

solution

$$Q(x) = \frac{E_0}{\gamma}(1 - e^{-\gamma x/v}) \ , \tag{4.47}$$

which tends to E_0/γ when x greatly exceeds the advective length scale

$$\lambda \equiv \frac{v}{\gamma} \ . \tag{4.48}$$

Clearly, the advective length scale λ increases as the precipitation depletion rate γ declines. This is equivalent to the result from the n-box model, namely that a decline in the precipitation depletion rate will cause the moisture transport length scale to increase, thereby shifting the aerial hydrological cycle towards greater distances between source (evaporation) and sink (precipitation) regions.

4.6 Discussion

In this chapter, we have introduced a new framework for considering perturbations in the aerial hydrological cycle, and have applied it to the problem of quasi-equilibrium CO_2-doubling. Existing perspectives have focused on hydrological cycle amplification, and energetic constraints on precipitation and surface evaporation. The present work aims to create a complementary perspective for evaluating hydrological cycle changes due to climate perturbations. This perspective systematically utilizes the information made available by numerical WTs implemented in a GCM, and decomposes the change in precipitation into those due to increased evaporation (both local and remote) and those due to changes in moisture transport from source (evaporation) to sink (precipitation) regions. The precipitation perturbation can be further decomposed into a part due to changes in the local contribution to the precipitation (the part of the precipitation over a tagged region that originates from evaporation in that tagged region itself) and changes in the remote contribution to the precipitation (the part of the precipitation over a tagged region that originates from evaporation in all other tagged regions). Using matrix operator decompositions, the change in the remote contribution to the precipitation may be further decomposed in a variety of ways.

In this chapter, we present a complementary view on how the hydrological cycle changes with CO_2-induced warming. This perspective does not challenge existing paradigms of hydrological cycle change. Instead, it synthesizes the two governing principles of CO_2-induced hydrological cycle change: that atmospheric moisture increases at the C-C rate with temperature (approximately 7% $^{\circ}C^{-1}$), and that energetic constraints on E and P cap their increase well below below the C-C rate. Both of these principles are linked by the precipitation depletion tendency γ (Trenberth, 1998; Bosilovich et al., 2005), which must decline if both are to be satisfied simultaneously. A decline in the precipitation depletion tendency corresponds to an increase in moisture residence time, and, as we have shown using both GCM results and heuristic models, an increase in the advective length scale of moisture transport.

If E, P, and specific humidity q all increased at the same rate with increasing temperature, γ would remain constant and much of the change in precipitation would arise from the evaporation change itself, i.e.

$$\Delta\vec{P} \approx \mathbf{M}(\Delta\vec{E}) \; . \tag{4.49}$$

In other words, the total precipitation change would only depend on changes in the spatial pattern of evaporation, which depends on how the part of the surface energy budget allocated for evaporation changes. In reality, both precipitation and evaporation increase with temperature at a slower rate than the specific humidity; as a result of this incongruity, the rate at which moisture is removed from the atmosphere must slow, or, equivalently, γ must decrease. The decrease in the precipitation depletion tendency, then, increases the export fraction, and shifts the precipitation contribution due to remotely-evaporated moisture towards longer distances between source and sink regions. This manifests itself in the $(\Delta\mathbf{M})\vec{E}$ term, which is equally important to the total precipitation change as the $\mathbf{M}(\Delta\vec{E})$ term.

As our results show, increasing evaporation without changing moisture transport results in a nearly uniform pattern of increased precipitation, with a notable maximum in the mid- and high-latitudes in winter. In fact, much of the increased precipitation in the extra-tropics in Eqm2×CO_2 is due to increased evaporation in the subtropics and mid-latitudes that is

transported poleward in a manner similar to that in the mean state. In the tropics, however, changes in evaporation cannot explain the pattern of strengthening equatorial precipitation and decreasing subtropical precipitation. In this regard, changes in moisture transport are essential for creating the distinct spatial pattern of precipitation change associated with CO_2-induced warming.

Recalling equation (4.48), it would also be possible to increase the advective length scale of moisture transport if the circulation were to intensify at constant γ. However, studies of general circulation perturbations with CO_2-induced warming suggest that its tendency in the tropics and subtropics is to slow, not speed up (see, e.g., Vecchi and Soden, 2007). Thus, perturbations in the general circulation tend to decrease the advective length scale of moisture transport, at least at lower latitudes, and counteract the effect of the decreasing precipitation tendency γ. The results from our WT experiments suggest, however, that weakening of the general circulation does not negate the effect of decreased γ, and the advective length scale of moisture increases nearly everywhere. This result, however, may be model-dependent, in that the competing effects of a weakening circulation and decreased precipitation depletion tendency may favor the former in some models. In such models, the advective length scale of moisture transport would decrease, distances between moisture source and sink regions would shorten, and the precipitation perturbation, particularly in the tropics, would likely look very different. In the following chapter, however, we show that this result is unlikely, in that analysis of CMIP5 perturbation experiments are suggestive of a robust increase in the advective moisture length scale over much of the globe in all state-of-the-art GCMs.

We also note that the change in precipitation due to $\Delta\vec{E}$ is not equivalent to the so-called thermodynamic effect of increased atmospheric moisture. As others have already shown, increased atmospheric moisture cannot account for how E and P change independently (Allen and Ingram, 2002; Held and Soden, 2006). Nevertheless, as we have shown, increasing atmospheric moisture at a faster rate than either E or P also alters moisture transport by decreasing the precipitation depletion rate γ, thereby increasing the advective length scale of moisture transport. In other words, *the increased moisture residence timescale, or,*

equivalently, the increased transport length scale, which result from atmospheric moisture increasing at a faster rate with temperature than either E or P, manifests as a change in moisture transport. As we have shown, this change in moisture transport corresponds to increased moisture export from its region of evaporation, and an overall increase in long-range remote moisture convergence at the expense of short-range convergence. The latter is evident in a robust increase in interbasin moisture convergence (moisture precipitating in a different basin than where it evaporated), and shift in intrabasin moisture convergence to longer distances between source and sink regions.

A corollary of this finding is that dynamic shifts in general circulation features, particularly the expansion of the subsiding regions of the Hadley circulation and the poleward shift in the storm track that accompanies it, are also an expected result of this increase in the advective length scale of moisture. Widening of the subtropics corresponds to a larger source region from which water can evaporate and reach the deep tropics, which is consistent with an increased transport length scale. Additionally, increasing the transport length scale will also push the midlatitude precipitation maximum poleward, since water from subtropical source regions will travel further. In other words, increasing the advective length scale of moisture transport produces hydrological cycle perturbations with CO_2-induced warming that are consistent with the dynamical perturbations observed in a wide range of GCMs.

The local and remote contributions to the precipitation perturbation are each impacted differently by this advective length scale increase. Surprisingly, we find that the local contribution to the precipitation changes very little in the Eqm2×CO_2 experiment relative to C, despite the fact that the export fraction increases almost everywhere. This can be explained, however, by a compensating increase in the local evaporation: even though more locally-evaporated moisture is transported away from where it evaporates as the advective length scale of moisture transport increases, local evaporation increases sufficiently to counteract this. As a result, the change in the local contribution makes up less than 25% of the total precipitation perturbation. This leaves the change in the convergence of remotely-evaporated moisture (the remote contribution) as the dominant component of the total precipitation

perturbation.

As we have already noted, changes in the convergence of remotely-evaporated moisture are partly due to increased export of a larger amount of evaporated moisture, and partly due to changes in how remotely-evaporated moisture is partitioned between sink regions. The former tends to increase precipitation globally, and is relatively spatially homogeneous; the latter is spatially heterogeneous, and tends to increase precipitation at the equator, decrease it over the subtropics, and increase it over the extra-tropics. The former effect, greater export of more evaporated moisture, is most important over the extra-tropics. Over the tropics, however, the change in moisture partitioning is essential for creating a spatial pattern where equatorial precipitation increases and the subtropics dry.

These changes in the local and remote contributions, however, are not uniform among the basins. Overall, the Atlantic basin dries the most while the Pacific dries the least. Over the Atlantic, surprisingly, changes in remote moisture do not favor convergence over the deep tropics. Thus, even though the Atlantic experiences subtropical drying similar to the other basins, there is no increasing equatorial precipitation to compensate for this drying. Over the Pacific, equatorial precipitation increases primarily because changes in moisture partitioning favor convergence over this area. In addition, the effect of increasing the advective length scale of moisture transport is least apparent over the subtropical and midlatitude Pacific, with intrabasin moisture convergence from adjacent tagged regions relatively unaffected compared to the other basins. We speculate that the Pacific is relatively impervious to this elongating moisture transport length scale, in part, because of its substantial zonal extent; any moisture evaporated over the Pacific basin that is advected zonally likely remains over the Pacific basin when it precipitates, despite any modest length scale changes.

Over the continents, the relative contribution of the local and remote portions of the precipitation perturbation varies depending on the region. Over most land areas, the local contribution to the precipitation declines. The exception to this finding is in the high latitudes, where the local contribution actually increases modestly. The remote contribution, on the other hand, increases over all land regions primarily because ocean-to-land moisture

convergence increases. In general, the sum of these two competing tendencies determines whether precipitation increases or decreases over a given land mass. Over the polar regions, where both the local and remote contributions increase, precipitation always increases. Over most other land masses, the increase in the remote contribution wins out over the declining local contribution, and precipitation increases year-round. The exception to this general finding is over South America, and, seasonally, over southern North America and Australia. In these regions, the declining local contribution is not sufficiently compensated for by the increasing remote contribution, and the precipitation over these land masses declines.

We end by assessing the implications of our findings. We speculate that the increase in the advective length scale of precipitable water may have significant climate consequences, some of which may be unexpected. For one, we have shown that an increase in the advective length scale of moisture can be expected to increase interbasin moisture transport. In the event that this transport between ocean basins isn't reciprocal, it may lead to long-term trends in basin salinity, which may impact the ocean circulation. Indeed, as we will show in the following chapter, amplified transport of moisture from the subtropical Atlantic into the equatorial Pacific is a robust result in GCMs subject to increased CO_2, and acts to freshen the tropical Pacific and salinize the tropical Atlantic. Observations of ocean surface salinity show that such changes are already underway. Model and observational paleo-proxy records suggest that the meridional overturning circulation in the Atlantic is sensitive to this salinization of subtropical surface waters (Thorpe et al., 2001), but the extent to which the meridional circulation is sensitive to this salinization, relative to freshening in the mid- and high-latitudes, has not yet been determined. Further study is warranted.

Furthermore, changes in this length scale may affect the findings of isotope studies, and, thereby, how results from isotope proxy records are used to infer information about climates of the past. Our GCM WT experiments suggest that the advective length scale of moisture transport changes with temperature. In warmer temperatures, as in the Eqm2$\times CO_2$ experiment, the advective length scale increases relative to C; similarly, in cooler temperatures, the advective length scale is expected to decrease. From the perspective of moisture from

the subtropics that is transported poleward, both the temperature at which it evaporated and the time spent in the aerial hydrological cycle impact the isotopic signature; both of these components however, depend on temperature in both a local and global sense. This suggests, then, that back-of-the-envelope calculations of state variables from isotope data are ill-advised, as these secondary effects of temperature and its impact on transport may not be easily distilled into a simple model. Thus, we contend that isotope-enabled GCM studies are essential for interpreting isotope proxy records, particularly those in which global temperatures are very different from that in the present climate.

Finally, we point out the major caveat associated with this and any study using numerical WTs in GCMs, namely that the findings we present here are limited by the ability of our GCM to model the aerial hydrological cycle with fidelity. Thus, the conclusions presented here are tentative, and should be verified with additional GCM modeling studies, including those that are isotope-enabled.

4.7 Conclusions

We summarize the four major takeaway points of thus study as follows:

- Both changes in evaporation, local and remote, and changes in moisture transport are important components of the total precipitation perturbation associated with CO_2-doubling. The former is most important in the high latitudes, while the latter is most important in the subtropics.

- The change in the contribution of locally-evaporated moisture to the precipitation change is small, while the change in the contribution of remotely-evaporated moisture to the precipitation change is substantial and constitutes most of the total precipitation perturbation.

- The part of the precipitation perturbation due to transport changes are mostly attributable to an increase in the moisture residence time, or, equivalently, an increase in

the advective length scale. Such an increase in residence time and length scale results in greater distances between moisture source (evaporation) and sink (precipitation) regions.

- The increased advective length scale of moisture transport results in the export of a greater fraction locally-evaporated moisture, an increase in the interbasin moisture convergence, and a shift towards greater distances between intrabasin moisture source and sink regions.

Chapter 5

THE AERIAL HYDROLOGICAL CYCLE AND THE SALINITY OF THE ATLANTIC IN PRE-INDUSTRIAL AND HIGH-CO_2 SIMULATIONS

5.1 Introduction

The Atlantic basin has the highest salinity waters of the world's oceans, with zonal mean salinity differences between Atlantic and Pacific of at least 1.0 psu between 30° S and 65° N at depths above 1000 m (Peixoto and Oort, 1992; Levitus et al., 2013; Boyer et al., 2013). Observational studies suggest that the upper ocean salinity of the Pacific basin is decreasing while that of the tropical and subtropical Atlantic basin is increasing (see Curry et al., 2003; Boyer et al., 2005; Grodsky et al., 2006; Hosoda et al., 2009; Durack et al., 2012), with the most pronounced increases occurring in the subtropical mode waters (Curry et al., 2003; Durack and Wijffels, 2010). These basin-scale salinity trends have been attributed to intensification of the aerial hydrological cycle as greenhouse gas concentrations increase in the atmosphere from anthropogenic activities (Durack et al., 2012).

Experiments with global climate models (GCMs) suggest that lowering the salinity of the tropical Atlantic, either by artificially enhancing the surface freshwater flux or by directly reducing the upper-ocean salinity, can substantially weaken deep convection in the North Atlantic (e.g. Rahmstorf, 1996; Vellinga and Wu, 2004; Haupt and Seidov, 2007); conversely, increasing the salinity of the tropical Atlantic strengthens deep convection and its associated meridional circulation (Thorpe et al., 2001). As such, understanding why the Atlantic basin has such a high upper-ocean salinity, and, thereby, accurately projecting future upper-ocean salinity changes, are paramount for understanding the mean state ocean circulation and any expected future perturbations. Such changes will have important implications for the global

climate system (Seager et al., 2002; Sutton and Hodson, 2003, 2005) and, by extension, the many natural systems on which human societies depend. The steady-state salinity of an ocean basin arises from a dynamic balance between the surface freshwater input (evaporation minus precipitation, hereafter $E - P$) and advective fluxes of freshwater by the ocean circulation through any open lateral boundaries (Schmitt, 2008). In addition, surface freshwater fluxes themselves give rise to haline circulations, which compete with thermal, wind-driven, and surface height effects to produce the circulation (Huang, 1993). The Atlantic is a net evaporative basin, i.e $E - P > 0$ (Bryan and Oort, 1984), and aerial transport of freshwater over the Isthmus of Panama by prevailing easterly winds has long been implicated in the Atlantic-Pacific salinity contrast (Weyl, 1968). Indeed, planktonic δ^{18}O records suggests that the salinity difference between the tropical Atlantic and Pacific basins developed some 4.7 to 4.2 mya with the uplift of the Panamanian seaway (Haug et al., 2001); the lack of salinity contrast prior to this uplift suggests that the presence of the Isthmus of Panama is necessary, though possibly not sufficient, for the comparatively high salinity of the Atlantic. Furthermore, changes in the interbasin moisture transport have been proposed as a possible mechanism for abrupt climate change events evident in the paleoclimate record (see, e.g., Lohmann, 2003; Leduc et al., 2007; Prange et al., 2010, and others).

Broecker et al. (1990) and Broecker (1991) quantified this Atlantic-to-Pacific interbasin freshwater transport, and showed that at least half of the 0.5 Sv (1 Sv = 10^6 m^3/s) freshwater deficit of the Atlantic basin was due to aerial transport of freshwater over the Isthmus of Panama and into the equatorial Pacific by the prevailing easterlies; this export was not compensated by similar moisture import from the Indian basin over the African continent. Zaucker and Broecker (1992) showed that this interbasin freshwater transport intensified with increased atmospheric CO_2 in a coarse-resolution GCM.

Nevertheless, there remains some disagreement in the literature over the relative role of subtropical atmospheric moisture transport as the driver of interbasin salinity contrasts. More recently, Ferreira et al. (2010) have suggested that the interbasin salinity contrast is a result of water residence times in midlatitude storms, not the equatorial circulation; using

an idealized basin configuration in a GCM, they concluded that a small basin (i.e., the Atlantic) adjacent to a larger basin (i.e., the Pacific) became more salty over time because of a precipitation deficit at midlatitudes.

Evaporation at midlatitudes, surface winds, and natural variability may also play a role in the high salinity of the Atlantic. The low temperature of the Pacific midlatitudes decreases buoyancy loss by evaporation (Warren, 1983), while the higher temperatures at similar latitudes in the Atlantic facilitate buoyancy loss (Emile-Geay et al., 2003). Furthermore, there is no Pacific analog to the pronounced northward flow of warm, high-salinity water from the subtropical to subpolar gyres in the North Atlantic. This transport is made possible by the positioning and north-east tilt of the line of zero wind stress curl (Warren, 1983; Emile-Geay et al., 2003), which results from orographic forcing (Manabe and Terpstra, 1974). Czaja (2009) argued that the relationship between the line of zero wind stress curl and the line of zero $E - P$ was crucial; while these lines do not coincide in the Pacific, they are spatially coincident in the Atlantic, and stochastically variable winds facilitate transport of warm, salty Atlantic water northwards into the subpolar gyre.

In this study, we examine the comparatively high salinity of the Atlantic through the lens of the aerial hydrological cycle, which transports moisture away from the Atlantic drainage basin. Using observational data and reanalyses, we estimate the present-day surface salinity of the Atlantic, and use two independent hydrologic cycle estimates to constrain the surface freshwater flux. We use ouput from the fifth Climate Model Intercomparison Project (CMIP5) to show that Atlantic surface salinity perturbations are strongly linked to changes in $E-P$ over the Atlantic drainage basin. Then, we use a pair of GCM experiments employing numerical water tracers (WTs) to examine the mechanism of net moisture export from the Atlantic basin in the pre-industrial mean state climate, and predict how this mechanism may change in a doubled-CO_2 world. We determine whether the driver of this change is increased evaporation or altered transport, and conclude with a discussion of the implications of our findings.

5.2 Experimental Setup and Methods

5.2.1 Observations and Reanalyses

We consider the observed moisture fluxes into and out of the Atlantic drainage basin from atmospheric reanalyses and how well this moisture flux divergence agrees with observational estimates of evaporation and precipitation over the Atlantic. The vertically integrated atmospheric moisture fluxes are calculated using the velocity and specific humidity fields from the ERA interim analysis (Dee et al., 2011). We use the 6-hourly instantaneous fields with a horizontal resolution of 1.5° and 37 vertical levels. The atmospheric mass budget is constrained with a barotropic wind correction (Trenberth and Caron, 2001) prior to performing the moisture flux calculations, which enforces conservation of mass on latitude circles over the period of our analysis. Time integrated moisture fluxes are calculated for each month between 1979 and 2009. We report here on the annual mean climatological moisture fluxes and their divergence with a focus on the Atlantic drainage basin (defined as in §5.2.2).

Atmospheric moisture flux divergence must be balanced by $E - P$, neglecting the small moisture tendency in the column. Therefore, we compare the divergence of the vertically integrated moisture fluxes calculated from the reanalyses to independent estimates of $E-P$. Precipitation data is from the National Oceanographic and Atmospheric Administration's Climate Prediction Center's (NOAA CPC) merged analysis (Xie and Arkin, 1996) – derived from gauge measurements, satellite observations, and numerical models – averaged over the period 1979-2009. Evaporation is taken from the ERA interim reanalysis latent heat flux; the spatial correlation of this globally gridded product compares favorably with the evaporative fluxes from the WHOI OA fluxes (Woods Hole Oceanographic Institute Ocean Atlas, Yu et al., 2004) over the common ocean domain (R = 0.99).

In the calculation of $E - P$ and the atmospheric moisture flux divergence, the Atlantic drainage basin is designated as follows: the northern edge is at 70° N; the western edge is the longitude of maximum topography over either North or South America at each latitude from 70° N to 35° S; the southern edge is at 35° S; and the eastern edge is defined as the

maximum topography between the prime meridian and 30° E.

5.2.2 CMIP5 Models

We compare evaporation minus precipitation ($E - P$) and sea surface salinity (SSS) in the preindustrial control (piC) with the final 50 years of the abrupt CO_2-quadrupling simulation (ab4×CO_2) in thirteen CMIP5 models. Models used are listed in supplemental material S1. The Atlantic drainage basin is as defined in §ObsMethods.

5.2.3 Simulations with Water Tags

We use the state-of-the-art Community Earth System Model version 1.1 (CESM 1.1, Hurrell et al., 2013) with the Community Atmosphere Model version 5 (CAM5, Neale et al., 2012) at 1° spatial resolution. Water tracing capability was added to CAM5, with water entering the atmosphere tagged at its region of evaporation (or sublimation) and followed in a bulk sense during its transit through the atmosphere (as vapor, liquid, or ice); tags are re-initialized when water precipitates and is absorbed by the land or ocean model components.

Water was tagged in 10° latitude bands in each of the major ocean basins (Atlantic, Pacific, and Indian); continents have one tag each, with the exception of Eurasia and North America, which have two tags each. There are 48 tags in total. The area of each tagged region is as detailed in supplemental material S2.

Two thirty-year experiments were performed with numerical WTs: the first branched from an equilibrated pre-industrial control experiment (piC-WT), and the second branched from year 270 of a doubled-CO_2 experiment in which all other constituents and parameters were set at preindustrial conditions (Eqm2×CO_2-WT). The latter run is at quasi-equilibrium with the net top-of-atmosphere flux not exceeding 0.1 W/m^2 in magnitude. Results are presented as annual mean climatologies of these final 30-year segments.

5.3 Results

5.3.1 Observations and Reanalyses

Now, we demonstrate that two different and independent estimates concur that the atmosphere exports moisture away from the Atlantic basin. The spatial patterns of vertically integrated atmospheric moisture flux divergence (from the reanalyses) and precipitation minus evaporation (from the satellites/gauge measurements and latent heat fluxes) agree remarkably well (c.f. the colors and contours in Figure 5.1a); the annual mean spatial variations of the two fields have an area-weighted correlation coefficient of 0.90 with a regression coefficient near unity (0.91). The vertically integrated moisture flux integrated around the Atlantic basin boundary (thick colored lines on the continental divides) give 0.45 Sv of moisture export from the basin, whereas the spatial integral of $E - P$ show 0.51 Sv of moisture loss from the surface of the Atlantic basin.

We determine which regions contribute to the atmospheric moisture export from the Atlantic basin. More specifically, is the moisture loss a consequence of (1) more export across tropical Central and South America than import across tropical Africa, (2) more export across Europe than import across North America in the northern hemisphere (NH) extratropics, (3) more export across southern Africa than import across South America in the southern hemisphere (SH) extratropics, or (4) export across the boundaries with the Arctic and Southern Oceans? These different regions are demarcated by the colored boundaries and their respective moisture fluxes (in Sv) in Figure 5.1a.

We find that the export of moisture across Panama (0.46 Sv) greatly exceeds the import across Africa (0.29 Sv) in the same latitude range (20N to 15S). This is due to the relatively low orography of the Panama Isthmus, in contrast to the higher topography of eastern and southern Africa. Southward moisture transport into the Southern Ocean also leads to substantial moisture export from the Atlantic. Indeed, southward moisture transport in the SH storm track region is evident over all longitudes, though the moisture export is slightly stronger in the Atlantic than in the zonal mean.

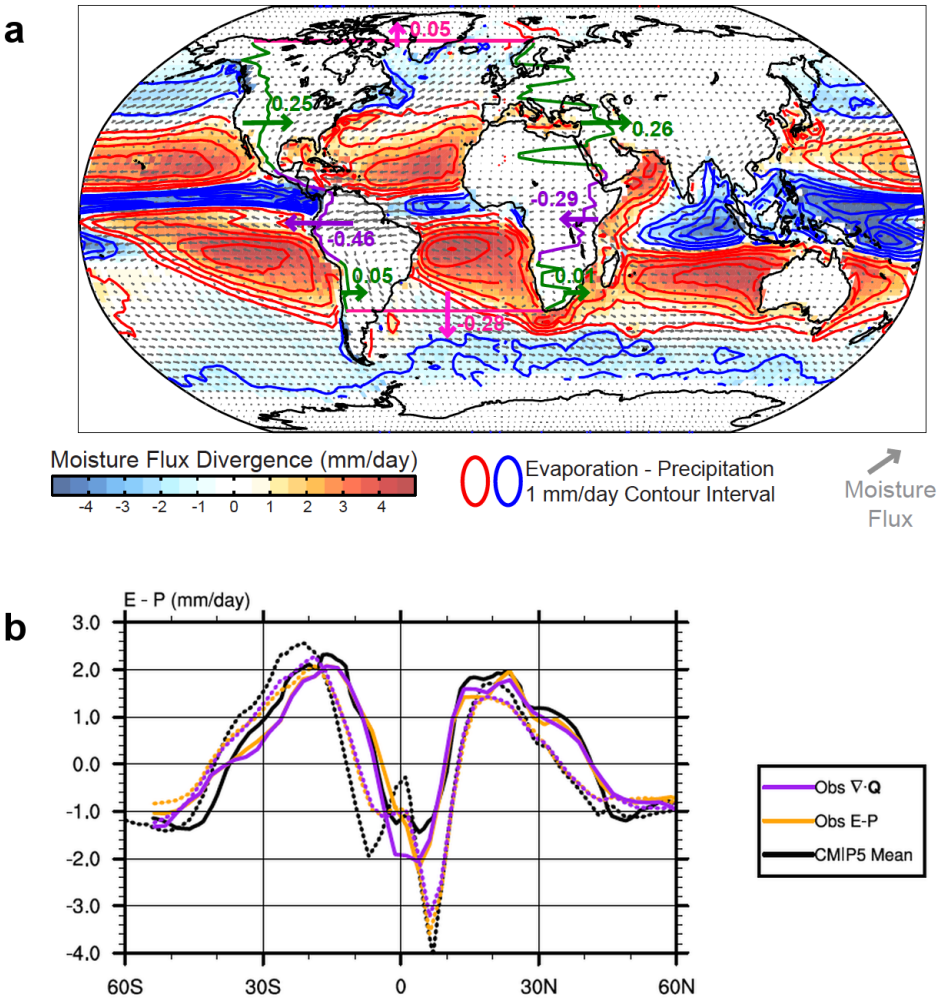

Figure 5.1: Panel (a): vertically integrated moisture flux divergence climatology from ERA interim reanalysis (colors) and evaporation minus precipitation (contours at intervals of 1 mm day^{-1}). The gray vectors show the moisture flux vectors; the colored arrows with accompanying moisture fluxes in Sv (1 Sv = 10^9 kg s^{-1}) give the moisture fluxes across the boundaries of the Atlantic drainage basin, with green arrows and numbers corresponding to extratropics, purple for the tropics, and pink for the northern and southern boundaries. Panel (b): comparison of $E - P$ from the two observational estimates shown in panel a with the CMIP5 multimodel mean. Solid lines denote $E - P$ over the Atlantic drainage basin and dashed lines denote $E - P$ over the rest of the globe.

In contrast, the difference between import into and export out of the Atlantic basin in the extratropical latitudes leads to a modest net import of moisture into the extratropical Atlantic: the westerly import across North America (0.25 Sv) is nearly identical to the export across Europe (0.26 Sv) over the same latitudes (20N to 70N) wheres as the moisture import across South America (0.05 Sv) slightly exceeds the export across Africa (0.01 Sv) in the same latitude bands (20S to 35S). Thus, our observational estimates do not support the hypothesis that extratropical zonal transports are responsible for salinity anomalies in the Atlantic. Overall, there is strong observational evidence of atmospheric moisture export out of the Atlantic basin by easterly advection across the Panama Isthmus.

5.3.2 CMIP5 Models

We now use the CMIP5 archive to identify any robust relationships between SSS, $E - P$, and their responses to increased CO_2. In all models, the climatological SSS is higher in the Atlantic basin than it is in the rest of the world ocean (Figure 5.2a). Atlantic SSS peaks between 30° S and 40° N in individual models, and the multimodel mean agrees reasonably well with Boyer et al. (2013) (Figure 5.2a). Furthermore, Atlantic SSS increases in all models in response to abruptly quadrupling CO_2 (Figure 5.2b), particularly between 30° S and 40° N, while SSS decreases in the Indo-Pacific. The striking intermodel agreement in the SSS response suggests that the mechanism driving this increase is both simple and robust across models.

In the climatology, $E - P$ over the Atlantic drainage basin exceeds that over much of the rest of the globe from 20° S to 40° N, and there is strong intermodel agreement between 5° N and 40° N (Figure 5.2c). Integrated over the basin, the multimodel mean $E - P$ deficit over the Atlantic is 0.46 Sv, which agrees well with observations (Table 5.1). As Figure 5.2d reveals, $E - P$ increases over much of the Atlantic drainage basin in response to quadrupling CO_2; over the rest of the globe, all models have a strong equatorial minima in the $E - P$ response, a feature notably absent over the Atlantic in most models. The integrated change in $E - P$ in Sv for the Atlantic drainage basin is positive for all models, with a multimodel

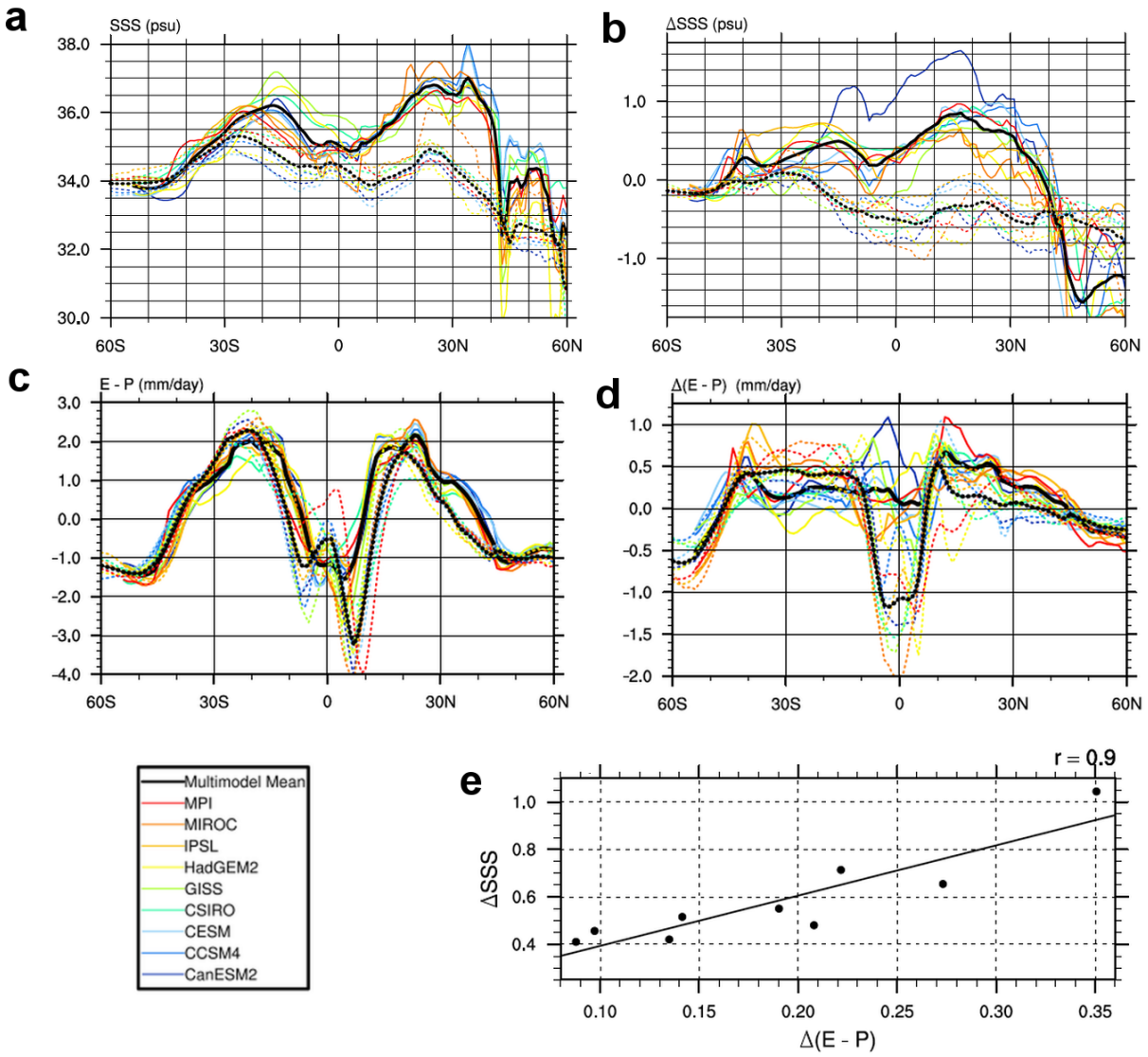

Figure 5.2: Panels a through d show the zonal averages of 9 CMIP5 models: (a) $E - P$ over the Atlantic drainage basin (solid lines) and the rest of the globe (dotted lines) in the preindustrial control run (piC); (b) $\Delta(E - P)$ over the Atlantic drainage basin (solid lines) and the rest of the globe (dotted lines), where Δ denotes the difference between the abrupt 4XCO2 run (Ab4xCO2) and piC; (c) SSS in the Atlantic basin (solid lines) and over the rest of the world ocean (dotted lines) in piC; and (d) Δ SSS over the Atlantic basin (solid lines) and over the rest of the world ocean (dotted lines), where Δ denotes Ab4xCO2 minus piC. Panel (e) shows the intermodel correlation between the change in $E - P$ over the Atlantic drainage basin and the change in Atlantic SSS; both $\Delta(E - P)$ and ΔSSS are recorded as an area-weighted mean between 10° S and 20° N.

Table 5.1: Evaporation minus precipitation ($E-P$) in Sverdrups over the Atlantic drainage basin from 9 models in the CMIP5 archive and in the observations. $E-P$ is shown for the preindustrial control simulation (piC), and the change in $E-P$ is shown for ab4×CO_2 − piC. Two independent observational estimates of $E-P$ are also given, using the atmospheric moisture flux divergence and surface estimates of E and P, respectively.

Model	piC	ab4×CO_2 - piC
CanESM2	0.44 Sv	0.13 Sv
CCSM4	0.49 Sv	0.13 Sv
CESM	0.44 Sv	0.097 Sv
CSIRO	0.42 Sv	0.098 Sv
GISS	0.44 Sv	0.067 Sv
HadGEM2	0.57 Sv	0.15 Sv
IPSL	0.41 Sv	0.095 Sv
MIROC	0.45 Sv	0.10 Sv
MPI	0.46 Sv	0.14 Sv
Multimodel Mean	0.46 Sv	0.11 Sv
Observations, $\nabla \cdot Q$		0.45 Sv
Observations, $E-P$		0.51 Sv

mean of 0.11 Sv (Table 5.1).

In Figure 5.2e, we note a strong intermodel relationship between the $E-P$ response over the Atlantic drainage basin for a given model and the equatorial Atlantic SSS response (Figure 5.2e). Indeed, using SSS to calculate $E-P$ over the world's oceans is one strategy for observing the hydrological cycle (Bryan and Oort, 1984; Schmitt, 2008) and perturbations to its climatology (see, i.e., Terray et al., 2012). To first order, SSS does not affect the hydrological cycle; therefore, we may understand SSS and perturbations in SSS as responses to $E-P$ and its perturbations.

The agreement between these independent observational datasets is also evident in the zonal mean, shown in Figure 5.1b. The largest discrepancy between the two is over the equatorial Atlantic basin, where the ERA reanalysis product predicts more precipitation than

does the observational $E-P$ estimate. Indeed, these independent observational estimates are in better agreement with each other than with the CMIP5 pre-industrial control multi-model mean (compare the black line with the orange and purple lines in Figure 5.1b). Compared to the observational estimates, the CMIP5 mean over-estimates $E-P$ in the equatorial Atlantic (likely due to under-estimating precipitation), while overestimating the magnitude of $E-P$ over the remainder of the globe, particularly in the SH.

5.3.3 Water Tracer Experiments

The Preindustrial Control Experiment

We now consider the mechanism of net freshwater loss from the Atlantic drainage basin in the preindustrial climate. Our WT control experiment confirms that water evaporating from (and hence "originating" from) the Atlantic basin precipitates not only within the Atlantic drainage basin, but also over the equatorial Pacific (Figure 5.3a); this is most apparent over the eastern Pacific circa 5° N. On the other hand, substantially less moisture evaporating from the rest of the globe precipitates in the Atlantic drainage basin (Figure 5.3b). Integrating these two quantities, we find that ∼1.1 Sv of moisture evaporated from the Atlantic basin precipitates outside the Atlantic drainage, while only ∼0.5 Sv of moisture evaporated from outside the Atlantic drainage basin falls within the Atlantic drainage basin. As a result, the Atlantic drainage basin has a net freshwater deficit of ∼0.6 Sv, which agrees well with the moisture flux calculations of Broecker (1991) as well as those performed with the two independent present-day estimates (Figure 5.1a).

In piC-WT, most of this moisture transported to the Pacific from the Atlantic originally evaporates from the NH Atlantic subtropics. This contribution varies little seasonally, and peaks in the 10° N to 20° N latitude band (Figure 5.3c). Indeed, our WT experiment suggests that nearly 0.4 Sv of freshwater precipitating in the eastern Pacific intertropical convergence zone (ITCZ) originally evaporates between the equator and 30° N in the Atlantic basin. Figure 5.3c also reveals a smaller, more seasonally varying contribution from the southern

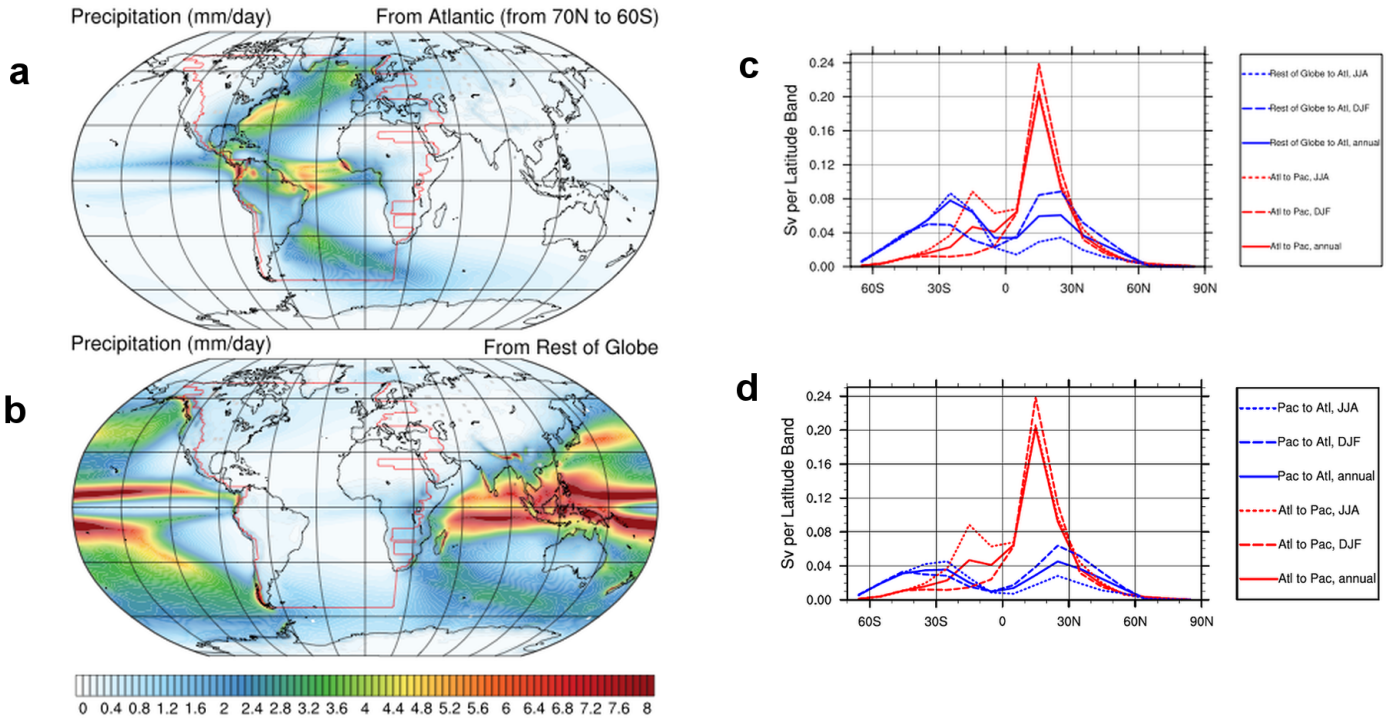

Figure 5.3: Results from water-tagging experiments in the pre-industrial control (piC) run: (a) annually-averaged precipitation from moisture originating in the Atlantic basin; (b) annually-averaged precipitation from moisture originating in the rest of the world ocean (except Atlantic); (c) annual and seasonal moisture source regions for interbasin exchange, where red denotes source regions of moisture transfer from the Atlantic to the Pacific basin, and blue denotes source regions of moisture transfer from the rest of the world ocean to the Atlantic; (d) as in panel c, but with blue denoting source regions of moisture transfer from the Pacific basin to the Atlantic. The red contour in panels (a) and (b) represents the Atlantic drainage basin used in the analysis.

hemisphere (SH) Atlantic subtropics, though this contribution is smaller in magnitude (but not in magnitude per unit area) than the contribution from the rest of the globe to the Atlantic drainage basin.

Comparing these results to moisture flux calculations using ERA interim (Figure 5.1a), we find that precipitable water from the NH subtropical Atlantic follows a north-easterly route over the Isthmus of Panama and over other low-lying regions of Central America to the equatorial Pacific, where it preferentially precipitates in the east Pacific ITCZ near 5° N.

Changes in Eqm2×CO_2-WT

We assess changes in net freshwater loss from the subtropical basin Atlantic in a doubled-CO_2 world. Results from Eqm2×CO_2-WT show that the amount of moisture that originates evaporates in the Atlantic and falls in the Pacific increases by 0.2 Sv relative to piC-WT, while the amount of moisture that originally evaporates over the rest of the globe and falls in the Atlantic increases by only 0.1 Sv. This leaves the Atlantic drainage basin with an increased freshwater deficit of 0.1 Sv, which is consistent with changes in $E - P$ over the Atlantic drainage basin in ab4×CO_2 − piC in the CMIP5 archive (Table 5.1, right column).

In a warmer world, E increases globally and P, in an integrated sense, must follow suit. From Figure 5.4a, we see that P arising from moisture that originally evaporated from the Atlantic basin decreases over much of the Atlantic drainage basin itself (with modest increases over eastern North America, the South American Andes, the African Sahel, and the Atlantic ITCZ), while P arising from moisture that originally evaporated from the Atlantic basin increases significantly over the eastern Pacific ITCZ. On the other hand, P arising from moisture evaporated from the rest of the globe does not appreciably increase over the Atlantic drainage basin (Figure 5.4b), indicating no compensating freshwater gain from the rest of the globe.

From Figure 5.4c, we see that this increase in the Atlantic contribution to the eastern Pacific ITCZ arises mostly from moisture originally evaporated from the NH Atlantic subtropics, with a substantial peak in the 10° N to 20° N latitude band. Indeed, comparing

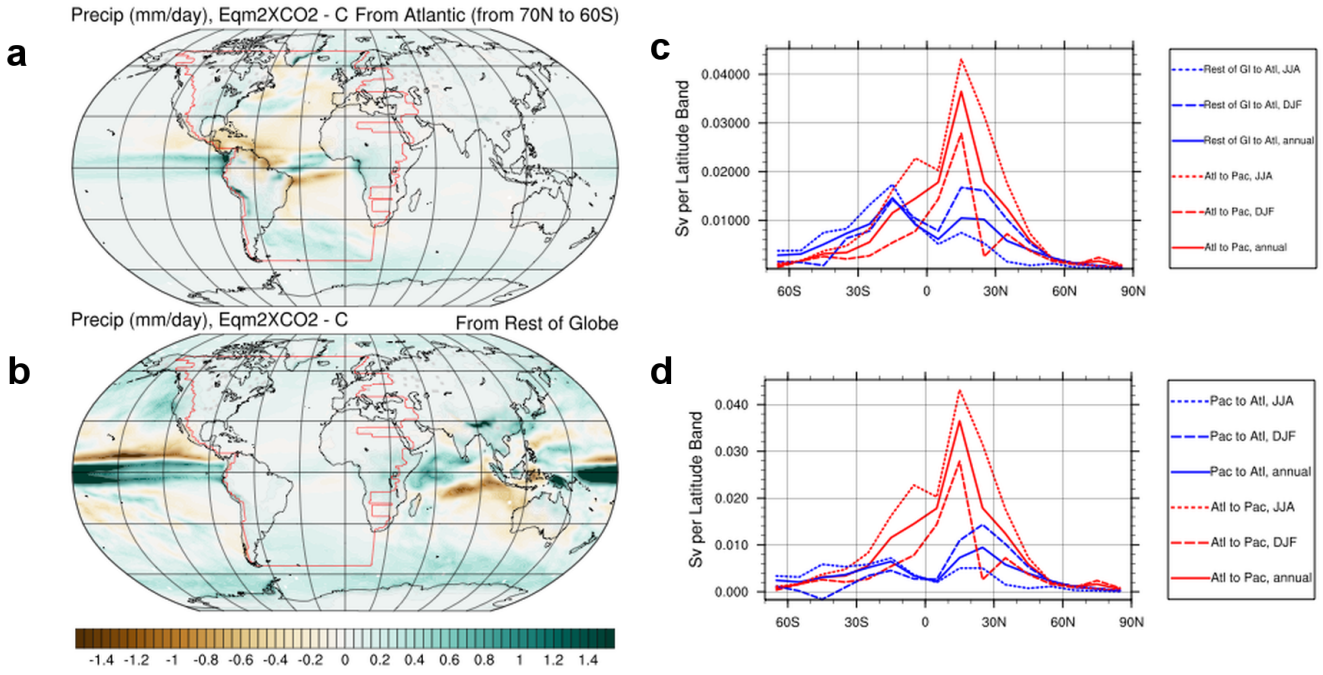

Figure 5.4: Panels (a) through (d) as in Figure 5.3, but for results from the equilibrium CO_2-doubling experiment (Eqm2$\times CO_2$) minus piC.

Figure 5.3c with Figure 5.4c shows that this increase is approximately 20% of the Atlantic-to-Pacific export in piC-WT, and that the spatial pattern of the increased Atlantic-to-Pacific moisture export looks similar to that in piC-WT. There is also a substantial increase in Atlantic-to-Pacific moisture transport that originates in the SH subtropics; this increased contribution amounts to 35% of the Atlantic-to-Pacific export from this region in piC-WT. We also note that Figure 5.4c shows an increase in moisture transport from the rest of the globe, particularly the NH and SH subtropics, to the Atlantic drainage basin, but that this increase is still smaller in magnitude (as well as magnitude per unit area) than the increase in Atlantic-sourced moisture export.

Finally, we compare regions of increased moisture export from the Atlantic (Figure 5.4c) to changes in Atlantic SSS in CESM1-CAM5 and the CMIP models (Figure 5.2b). Our water tracer experiments show that increased Atlantic-to-Pacific moisture export peaks in the NH and SH subtropics in the 10° to 20° latitude band, and that this peak (where moisture export increases the most) also coincides well with the (NH and SH) peaks in SSS increase in the Atlantic in the CMIP Ab4XCO_2 - piC multimodel mean (which occur at 15° N and 15° S). This supports our claim that increased SSS in the subtropical Atlantic is due to increased moisture export from the Atlantic subtropics to the equatorial Pacific that is robust across CMIP5 models.

Attribution of Increased Atlantic-to-Pacific Moisture Export

There are two possible explanations of why Atlantic-to-Pacific moisture export increases in Eqm2×CO_2-WT: (1) the Atlantic-to-Pacific moisture export scales with increased evaporation over the equatorial Atlantic basin (the increased evaporation hypothesis), and (2) the Atlantic-to-Pacific moisture export increases substantially beyond what would be expected from increased evaporation alone, implicating changes in how moisture is transported (the altered transport hypothesis).

To distinguish between these hypotheses, we decompose the precipitation perturbation

$\Delta\vec{P}$ as

$$\Delta\vec{P} = \mathbf{M}(\Delta\vec{E}) + (\Delta\mathbf{M})\vec{E} \ , \tag{5.1}$$

where $\mathbf{M}$ is the transport operator, $\vec{E}$ is the evaporation vector, and Δ is used to denote the difference between Eqm2×CO_2-WT and piC-WT. (See Supplementary Materials S3 for further details on the matrix operator framework for tracers.) If the evaporation hypothesis is correct, most of the increase in Atlantic-to-Pacific moisture export will be contained in the first term, which is the portion of $\Delta\vec{P}$ due to the change in evaporation alone. On the other hand, if changes in transport are responsible for the increase in Atlantic-to-Pacific moisture export, the latter term (which encompasses the portion of $\Delta\vec{P}$ due to changes in the transport operator) will dominate the sum.

We now show that the substantial increase in Atlantic-to-Pacific moisture export is better explained by the transport hypothesis rather than the evaporation hypothesis, that changes in the transport operator $\mathbf{M}$ are more important than changes in evaporation $\vec{E}$. Figure 5.5a shows the precipitation perturbation induced by enhanced evaporation ΔE over the Atlantic basin in Eqm2×CO_2-WT, given a constant transport operator $\mathbf{M}$. Increased evaporation over the Atlantic basin increases precipitation most appreciably over South America, with smaller precipitation enhancements over southern North America, northern Eurasia, and Africa. Precipitation also increases modestly over the Atlantic basin itself, over the equatorial Pacific, and over the Indian sector of the Southern Ocean.

Similarly, Figure 5.5b shows the portion of the precipitation perturbation due to changes in transport $\Delta\mathbf{M}$, given that evaporation over the Atlantic basin is held at piC-WT levels (i.e. the $(\Delta\mathbf{M})\vec{E}$ term). This term is negative over South America and the Atlantic basin itself, with the largest precipitation decline in the NH subtropics. In contrast, precipitation increases most substantially over the equatorial Pacific (from 10° S to 10° N), with more modest increases over Africa, northern Eurasia, and the Indian sector of the Southern Ocean.

This decomposition of Atlantic-sourced precipitation is also shown Figure 5.5e, where each term is separated into a part that falls over Atlantic drainage basin and a part that falls

over the eastern Pacific drainage basin. It is clear that the $(\Delta\mathbf{M})\vec{E}$ term accounts for both a decrease in precipitation over the Atlantic drainage basin and a corresponding increase in precipitation over the eastern Pacific. Indeed, increased evaporation over the Atlantic basin accounts for <10% of the total increase in Atlantic-to-Pacific moisture transport; the remaining >90% is due to changes in the transport operator $\mathbf{M}$. Moreover, comparing the spatial patterns of each of these terms (Figures 5.5a and c) with the total change in precipitation sourced from the Atlantic basin (Figure 5.4a), it is clear that only the change in transport can account for the decrease in Atlantic-sourced precipitation over much of the Atlantic basin, as well as the pronounced increase in Atlantic-sourced moisture that precipitates over the equatorial Pacific. Therefore, we reject the increased evaporation hypothesis in favor of the altered transport hypothesis.

A similar decomposition performed for moisture sourced from the remainder of the globe (Figure 5.5b and c) reveals that neither increased evaporation over the rest of the globe nor changes in transport affect precipitation over the Atlantic appreciably (see Figure 5.5f, red lines). Furthermore, it is clear that both increased evaporation and intensified transport serve to increase Pacific-sourced precipitation over the equatorial Pacific; while the former mechanism increases precipitation modestly over the entire Pacific basin, the latter serves to increase precipitation at the equator while decreasing it over the subtropics.

Comparing Figure 5.5e to Figure 5.5f reveals that at least one-quarter of the precipitation increase over the equatorial Pacific in Eqm2×CO_2-WT is Atlantic-sourced. In other words, a smaller fraction of Atlantic-sourced moisture precipitates locally (over the Atlantic) while a larger fraction precipitates remotely (over the Pacific), and this enhanced interbasin moisture transport is responsible for approximately one-quarter of the increased rainfall over the eastern Pacific ITCZ in Eqm2×CO_2-WT. This shift in moisture transport results in increasing $E - P$ over the Atlantic drainage basin, leading to increased SSS over the Atlantic basin and decreased SSS over the Pacific.

In the following discussion, we delve further into the question of why transport is altered in Eqm2×CO_2-WT, and, by extension, the CMIP5 Ab4×CO_2 experiments.

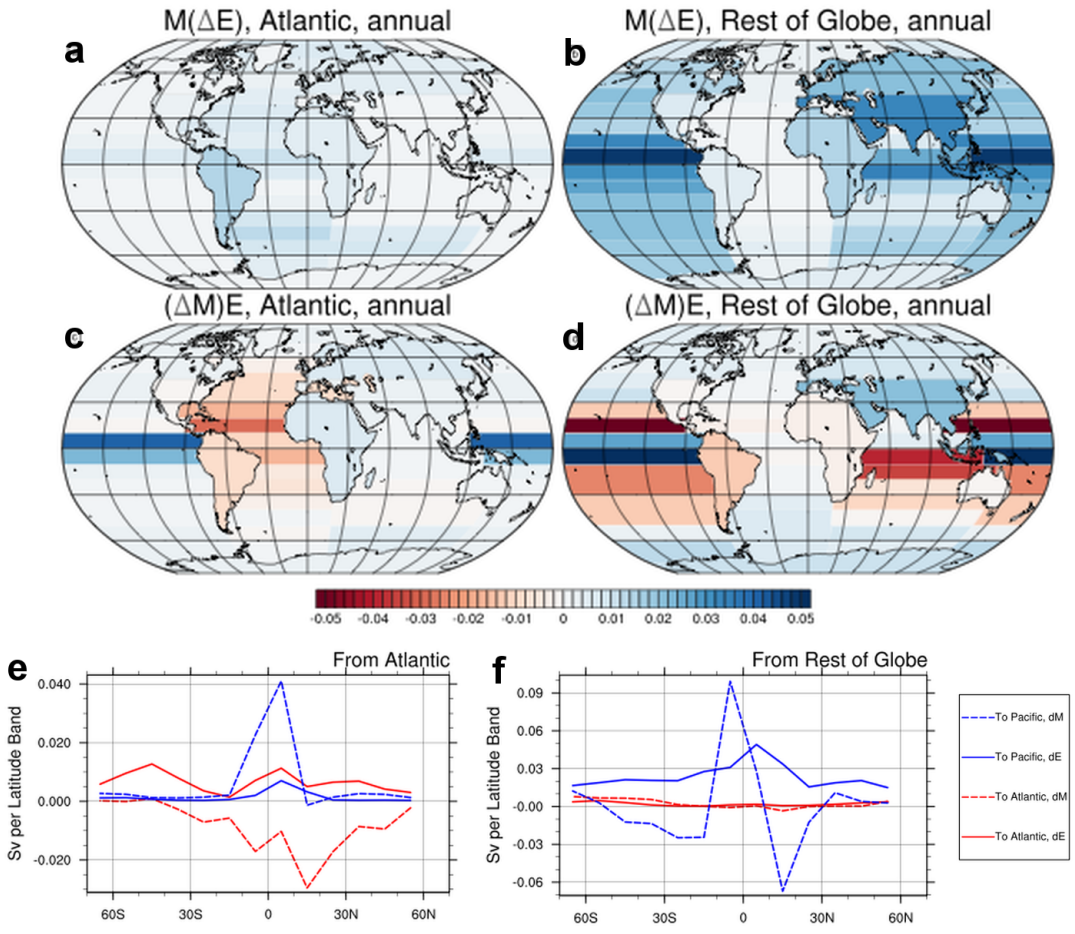

Figure 5.5: Decomposition of results from Eqm2×CO_2 minus piC: (a) change in precipitation originating from moisture evaporated from the Atlantic basin, due to changes in E; (b) change in precipitation originating from moisture evaporated from the rest of the globe, due to changes in E; (c) change in precipitation originating from moisture evaporated from the Atlantic basin, due to changes in the transport operator $\mathbf{M}$; (d) change in precipitation originating from moisture evaporated from the rest of the globe, due to changes in $\mathbf{M}$; (e) change in precipitation originating from the Atlantic and falling on the Atlantic (red lines) and falling on the Pacific (blue lines); and (f) change in precipitation originating from the rest of the globe (excluding the Atlantic) and falling on the Atlantic (red lines) and falling on the Pacific (blue lines). In (e) and (f), dashed lines denote changes due to differences in the transport operator $\mathbf{M}$, and solid lines denote changes due to differences in evaporation $\vec{E}$.

5.4 Discussion and Conclusions

In this study, we have provided further support for the theory of Broecker (1991), namely that the anomalously high salinity of the Atlantic is due to approximately 0.5 Sv of aerial freshwater export of Atlantic-sourced moisture across the Panama Isthmus into the Pacific, and that this moisture export is a necessary condition for deep sinking of surface waters in the North Atlantic. We have shown remarkable agreement between two observational estimates of net moisture loss from the Atlantic drainage basin, as well as agreement between these observational estimates and those from the CMIP5 preindustrial control experiments. With the aid of numerical WTs implemented in a GCM, we have also shown that most of this moisture is exported from the NH Atlantic tropics, from the equator to 30° N, with maximum export in the 10° N to 20° N latitude band. This moisture exported from the subtropical Atlantic mostly falls in the eastern Pacific ITCZ.

Furthermore, we have shown a strong link between increased SSS in the subtropical Atlantic and increased $E - P$ in the CMIP5 ab4×CO_2 experiment, and confirmed that intermodel changes in the surface freshwater input are well-correlated with changes in basin surface salinity. In the CMIP5 multimodel mean, $\Delta(E-P)$ and ΔSSS attain their maximum near 15° N; similarly, in our Eqm2×CO_2-WT experiment, we find that it is from near this latitude (within 10° N to 20° N) that moisture sourced from the Atlantic that precipitates in the Pacific increases most dramatically. Indeed, Atlantic-to-Pacific moisture export increases by 20% in Eqm2×CO_2, and approximately one-quarter of the precipitation increase in the Pacific ITCZ is sourced from the Atlantic. Further analysis points to altered transport, not increased evaporation, as the mechanism for increased Atlantic-to-Pacific moisture export in Eqm2×CO_2 relative to piC.

An important question that remains is how altered transport increases Atlantic-to-Pacific moisture export in the Eqm2×CO_2 experiment. As noted earlier, there is remarkable intermodel agreement in the CMIP5 ab4×CO_2 experiment in increased salinity in the tropical Atlantic, suggesting a common and simple mechanism. Furthermore, other analyses of the

CMIP models indicate that increased CO_2 tends to decrease the strength of the atmospheric circulation in the tropics (see Vecchi and Soden, 2007), suggesting that enhanced interbasin transport cannot be explained by more vigorous easterly winds.

We propose that increased Atlantic-to-Pacific moisture transport is due to increased atmospheric moisture with increased atmospheric CO_2. Increased specific humidity increases the residence time of atmospheric moisture (Trenberth, 1998; Bosilovich et al., 2005; Held and Soden, 2006), thereby also increasing its advective length scale (Held and Soden, 2006). As a result, moisture transport is altered such that the distance between where moisture evaporates and where it precipitates increases. In Supplemental Material S4, we consider evidence of increased advective moisture length scales, both in terms of changes in the Eqm2×CO_2-WT experiment and evidence from heuristic models. In general, there is greater moisture export, more interbasin moisture transport, and an increase (decrease) in interbasin moisture transport from distant (adjacent) tagged regions in Eqm2×CO_2-WT relative to piC-WT. Furthermore, heuristic models suggest that decreased precipitation efficiency (as would be necessary to increase atmospheric moisture at a faster rate than either E or P, see Trenberth, 1998) corresponds to an increased residence time scale, a decreased cycling rate, and an increased advective length scale for atmospheric moisture. Therefore, increased moisture results in altered moisture transports, particularly a shift towards longer distances between moisture source and sink regions. Consequently, long-range moisture transport increases, including Atlantic-to-Pacific moisture export, at the expense of short-range transport, including intrabasin moisture convergence within the Atlantic itself.

To conclude, we briefly consider the significance of the salinity of the subtropical Atlantic. In general, the salinity of surface waters advected poleward determine the maximum density attainable at high latitudes. Indeed, as several GCM studies have shown (see, e.g. Rahmstorf, 1996; Vellinga and Wu, 2004; Haupt and Seidov, 2007), freshwater forcing at low latitudes can weaken deep ocean convection at high latitudes. At all salinities, seawater freezes near $T = -1.8$ °C, and the maximum possible density ρ is a (nearly) linear function of salinity S of the waters at the northernmost latitudes of the basin ($\partial\rho/\partial S|_{T=-1.8} \approx 0.8$ kg m^{-3} psu^{-1} at

all physically-relevant S). All basins experience substantial net freshwater input at mid- and high-latitudes, which tends to decrease the salinity of surface waters as they are advected poleward. Thus, the maximum salinity attained in the subtropics determines the salinity in the mid- and high-latitudes, which subsequently determines whether surface waters are sufficiently dense to sink as they lose buoyancy from surface heat loss.

The previous train of reasoning requires that ocean hydrography (the variation of T and S with depth, which determines ρ *in situ*) is set by remote processes rather than local ones. In fact, ρ as a function of depth is determined remotely, as the properties of water in the deep and abyssal ocean are set by formation and sinking of dense waters in the Southern Ocean (i.e. in the deep cell, as described by Marshall and Speer, 2012). Antarctic Bottom Water (AABW) formed by brine rejection in coastal polyñas sets S (and therefore ρ) for nearly all deep waters in the global ocean; these waters, then may be further modified by local processes, particularly mixing near topography or due to tides. If, in contrast, hydrographic properties were set solely by local processes, buoyancy loss by surface cooling could result in deep ocean convection irrespective of the maximum surface density achieved, as the salinity at depth would be comparable to that at the surface.

Our results also indicate that increased salinity in the subtropical Atlantic is a robust outcome in GCM experiments with increased CO_2. By itself, such a salinity increase would be expected to enhance sinking of surface waters in the North Atlantic, and, thereby, to increase the strength of the meridional circulation. GCM experiments, however, also project an increase in precipitation in the mid- and high-latitudes that offsets this salinity increase at low latitudes. Taken together, these two effects (increased $E - P$ at low latitudes, decreased $E - P$ at high latitudes) result in less vigorous sinking in the North Atlantic in most GCMs (Cheng et al., 2013). Nevertheless, if SSS did not increase at low latitudes, sinking in the North Atlantic would be expected to weaken even more. Thus, considering the salinity of the Atlantic subtropics, and changes therein, are necessary, though not sufficient, for predicting the strength of the overturning circulation in the Atlanic, and how it may respond to future climate perturbations.

Chapter 6

CONCLUSIONS

We present the following major points, distilled from the four studies described in this thesis:

1. A forcing applied at one of the poles, orographic or otherwise, can affect climate both locally and remotely. In the case of Antarctic orography lowering, remote effects are mediated by both atmosphere and ocean responding in concert, and extend to the opposite pole. Such remote effects have the ability to modify the local response beyond that dictated by the thermodynamic effect of lower orography. Much of this response can be attributed to energy balance requirements that arise from tropospheric warming over the Antarctic, which locally increases outgoing longwave emission to space. At the equator, the ocean energy transport response helps diminish the atmospheric energy transport response, which corresponds to a shift in the intertropical convergence zone. [Chapter 2]

2. In the preindustrial mean state, most moisture precipitates great distances from where it originally evaporated (or sublimated). While moisture recycling is important over the continents, moisture precipitating over the ocean usually originates from far-removed regions. Furthermore, the extent to which evaporated moisture moves zonally and meridionally before precipitating is strongly dependent on the ocean basin from where it originates. In terms of moisture transport, the Atlantic basin is the most divergent, while the Pacific is the most convergent. [Chapter 3]

3. When the climate system is perturbed by doubling CO_2, moisture transport changes substantially while evaporation increases relatively uniformly. Many of the cannonical

changes in precipitation associated with CO_2-induced warming, including the 'wet get wetter, the dry get dryer', are actually a result of altered moisture transport, not merely a manifestation of greater evaporation that is transported as in the mean state. Many of the changes in moisture transport evident in our CO_2-doubling experiment, which result in precipitation anomalies, are attributable to an increase in the moisture transport length scale with warming. A simple box model can be used to show that the increase in advective length scale, in turn, corresponds to a decrease in precipitation efficiency with warming that arises from the energetic constraints on evaporation and precipitation such that they increase more slowly with temperature than specific humidity. Thus, such changes in moisture transport are not indicators of changes in circulation, but rather are a fundamental characteristic of how the Earth system responds to warming. [Chapter 4]

4. In the present-day, moisture evaporated from the Atlantic basin precipitates both over the Atlantic basin itself, over surrounding land masses, and over the eastern Pacific ITCZ. We find that moisture export from the Atlantic to the Pacific originates mostly in the subtropical Atlantic, between 10N and 20N, and is transported to the Pacific by the prevailing easterlies over Central America. With CO_2-induced warming, this transport pathway becomes more important as the moisture transport length scale increases, and leads to robust salinization of the tropical Atlantic and freshening of the equatorial Pacific. [Chapter 5]

The major caveat associated with the results of these studies is that all rely on results from a series of GCM experiments. Given that the hydrological cycle, in particular, is very poorly represented in most GCMs, attempting to reproduce these findings using other state-of-the-art GCMs, or observational reanalyses with water tags incorporated, will help to identify which of the findings are robust.

On the other hand, we have attempted to focus on mechanisms and attribution in this thesis. Therefore, while the particular results we have presented may depend on model pecu-

liarities, attribution of coupling, energy balance, and cause-and-effect do not. For example, with regards to the results of Chapter 2, we have argued that many of the Earth system responses to lowering the AIS can be explained by changes in energy transport that arise from the need to balance the increase in the outgoing TOA flux over Antarctica. If the TOA energy flux over Antarctica responded differently, however, the specifics of our analysis would likely change, but the same mode of analysis, revolving around energy balance, atmosphere-ocean coupling, and energy transport, would still apply. Thus, while some of the results we have described here are model-dependent, our framework for understanding the responses of the climate system and our modes of analysis are not, and are fundamental to the study of climate dynamics.

Chapter 7
FUTURE DIRECTIONS

In this thesis, we have considered the interconnectedness of the climate system, and the many ways in which energetics and moisture transport mediate these connections. There are several possible directions in which the work we have described may be extended. A brief description of salient short- and long-term research projects, and the fundamental concerns that motivate them, are presented here.

7.1 Near-Term Projects

7.1.1 Tracers in the Climate System

There are many tracer species of great climatic interest in the atmosphere, substances which are advected by the general circulation, have short atmospheric residence times, and display a heterogeneous source-to-sink relationship. Aerosols, such as dust, black carbon, sea spray, sulfates, and biogenic particulates, represent a whole class of tracer species which affect the climate system by directly impacting atmospheric radiative transfer and indirectly affecting planetary energy balance through cloud nucleation. Other tracers of interest in global and regional climate include short-lived greenhouse gases, such as tropospheric ozone, methane, and nitrous oxide, substances emitted by vegetation including organic volatiles, and various other pollutants. In Chapter 3 of this thesis, we presented a new matrix operator framework for systematically analyzing results from water tracer experiments, and have demonstrated the utility of this framework for understanding moisture transport in the climate system, both mean state and perturbed by CO_2-doubling. One simple extension of this work would be to apply the matrix operator framework developed here to analyze model results for other tagged tracer species. Such an application would be relatively straightforward, and would require

minimal modifications of the matrix operator framework presented here. A study of the mean state and perturbation transport of such species may appear very similar to the analysis we have outlined in Chapters 3 and 4. To this end, we have already initiated collaborations with Phil Rasch and his group at the Department of Energy's Pacific Northwest National Laboratory, whose current research interests include aerial water and aerosol species tagging.

Another possible project involves streamlining tracer advection in CAM5. One difficulty in using tagging to study transport of tracer species and their role in the climate system has been the high computational cost of adding tagged tracers. In order to facilitate further study of tracers using tags, the efficiency of tracer advection must be improved. The incremental remapping tracer advection scheme of Dukowicz and Baumgardner (2000), which is already used to advect tracer species in the Community Ice Model (CICE), may be implemented in a separate CAM5 module and used to advect tracer species of all types, including precipitable water and aerosols, tagged or otherwise. While the initial cost of incremental remapping is substantial, adding more tagged species comes at a negligible computational cost, making it ideal for experiments where there are many tagged tracer species. Indeed, Dukowicz and Baumgardner (2000) showed that the computational cost of a two-dimensional incremental remapping scheme may be re-couped when the number of tracers exceeded 7.

7.1.2 Moisture Transport Variability

In Chapters 3 and 4, we focused on atmospheric water transport in the climate system in the mean state and in the quasi-equilibrium CO_2-doubling scenario. Additionally, we may also use the matrix operator framework to investigate interannual variability in moisture transport. Consider, for example, the matrix operator $\mathbf{M}$, and its constituents $\mathbf{T}$ and $\mathbf{F}$. We have shown that all of these operators vary seasonally, and respond strongly to CO_2-doubling. We have not, however, considered other canonical forms of climate system variability that may affect these operators, including the annular modes (the SAM and NAM), the El Nino - Southern Oscillation (ENSO), and the Pacific-North American pattern (PNA), which have all been linked to distinct precipitation patterns in the literature (Dai and Wigley, 2000;

Thompson and Wallace, 2001; Gillett et al., 2006; Leathers et al., 1991).

In order to understand variability in moisture transport, we propose two distinct approaches that are complementary to each other. First, compositing analysis may be used to create pairs of the matrix operator **M** (or, alternatively, **T** or **F**), where each member in the pair corresponds to the positive and negative phases of each of the modes of canonical variability of the climate system. Each of these pairs may be further decomposed and assessed in order to understand the moisture transport patterns that characterize each of these modes of variability. Next, the major interannual forms of **M** may be extracted by computing **M** yearly, and using a singular value decomposition (SVD) to extract the most significant modes. Comparing the forms of **M** derived from compositing with those derived from the SVD of the set of annually-computed **M** operators will allow assessment of which modes of variability play the largest role in moisture transport, both globally and regionally.

7.1.3 Polar Orographic Influences on Climate

In Chapter 2, we investigated the effect of high latitude orography, particularly that of the Antarctic Ice Sheet (AIS), on global climate. We found substantial, global-scale teleconnections from the Antarctic, through the tropics, all the way to the Arctic. Furthermore, we found that energetic requirements and atmosphere-ocean coupling explained the scope of these global teleconnections. What remains in question, however, is the extent to which these teleconnections depend on the climate mean state. In particular, how would these global-scale climate responses to lowering Antarctic orography change if the mean-state climate were one in which CO_2 were doubled? Likewise, how would the climate system respond if the mean-state climate were cooler than the pre-industrial one? These questions may be answered by similar GCM experiments to those described in Chapter 2, but in which Antarctic orography were flattened in either of these alternate climate states. Preliminary results from such experiments suggest that some of the teleconnections, particularly the global-scale responses mediated by the ocean, depend strongly on the climate state. Understanding the state-dependence of the climate response may also be useful for understanding the hetero-

geneity of how global and regional climates respond to a forcing.

Another related question is the extent to which the response to Antarctic orography flattening is thermodynamically-driven versus dynamically-driven. Lowering the AIS has two distinct effects: (1) surface warming of the AIS, with the surface temperature decreasing at the dry adiabatic lapse rate by the extent that orography is reduced; and (2) reduction of the surface orography gradient, resulting in a cessation of katabatic flow and its associated meridional cell, and a decrease in transfer of easterly angular momentum from the solid earth to atmosphere. We refer to responses to the former as thermodynamically-driven, and responses to the latter as dynamically-driven. In order to decompose the climate response into thermodynamically- and dynamically-driven parts, two additional experiments may be conducted: (1) to model the dynamically-driven response, the orography of the AIS is lowered, but the surface temperature is kept at that in the control experiment where the AIS is high; and (2) to model the thermodynamically-driven response, the orography of the AIS is untouched, but the temperature at the surface is increased at the dry adiabatic lapse rate as though it had been lowered. The difference between the sum of these responses and the response in the AIS lowering experiment (described in Chapter 2) would give the nonlinear part of the response to orography-lowering, the portion that is due to both thermodynamic- and dynamic-driving in concert. Such a sequence of experiments would also further understanding of how the AIS creates both global and local conditions that allow for its maintenance, and why the Antarctic and Arctic may respond differently to a climate perturbation.

7.2 Long-Term Directions

In *Principles of Planetary Climate*, author Ray Pierrehumbert describes the Big Questions that characterize the climate system, those related to the evolution of climate, both on Earth and other planets further removed, and how a general theory of planetary climate may be developed to encompass all possible worlds in all phases of their climate evolution (Pierrehumbert, 2010). Indeed, as the number of known extrasolar planets increases, and as observational technology evolves, understanding the climates of these alien worlds is expected

to be of general interest, highlighting the need for an all-encompassing theory of planetary climate. In this thesis, we have demonstrated through careful analysis of GCM experiments, observations, and the CMIP5 model archive, that the Earth system is highly interconnected, from pole to equator to pole, through both energetics and transport. We find that many of the broader questions that remain, however, relate to overarching questions of planetary climate as described in Pierrehumbert (2010), and the extent to which transport and energetics, as essential components of the climate system, may be distilled in the most general way possible. We briefly describe some of the Big Questions highlighted by our work below.

7.2.1 Precipitable Water in the Climate System

Precipitable water plays an important role in the climate system, as a conveyer of energy and surface moisture, and as a condensable greenhouse gas that modulates the global surface and top-of-atmosphere (TOA) energy budgets. Indeed, many argue that the habitability of our planet depends upon the existence of surface reservoirs of liquid water, and the greenhouse warming provided by its atmospheric store. As we have shown in Chapters 2 and 3, aerial moisture transport is complex, seasonally variable, and responds strongly to a change in climate state. However, the extent to which atmospheric moisture and its transport generally respond to a forcing, while also modifying the response of other system components to that forcing, remains an open one. How much of this response is a function of the peculiarities of the Earth system itself, such as continental configurations, orography, , and how much of it is general to the theory of planetary climate?

Moreover, while we have shown that an increase in the advective length scale of moisture transport and atmospheric moisture residence time is a robust result when the Earth's climate warms, given an increase in atmospheric moisture storage that exceeds the increase in either evaporation or precipitation, it remains an open question whether the disparity between these rates of increase is a general facet of climate systems with a large liquid water reservoir. Do the moisture residence time and transport length scale always increase in a warming world, or must this finding be qualified? Furthermore, to what extent are these findings state-

dependent?

Furthermore, the role of atmospheric precipitable water transport on the ocean circulation is another open question. In Chapter 5, we have argued that moisture transport between basins is important in that such transport is necessary for understanding the current state of the ocean, in which a robust meridional overturning circulation exists over the length of the Atlantic basin, but not the Indo-Pacific. The extent to which surface freshwater forcing of the ocean by the atmosphere is important for ocean circulation is still unknown. While a range of studies have shown that the ocean circulation is sensitive to anomalous atmospheric freshwater forcing (e.g., Rahmstorf, 1996; Thorpe et al., 2001), the state-dependence of this sensitivity, particularly with regards to ocean basin configurations and orography, remains an open question.

Finally, we point out that water is not the only liquid substance that is volatile and acts as a greenhouse gas in vapor form. The Saturnian moon Titan, for example, has a moisture cycle that is dominated by methane and other hydrocarbons which appears strikingly similar to the hydrological cycle of Earth. Are there other compounds, like methane, that can serve a similar function to water in the climate system, moderating both energy transport and energy balance? If so, can these different substances also be incorporated into a general understanding of planetary climate? These queries, and more, are relevant to the Big Questions that relate to the role of precipitable water, and other volatile liquid substances, in planetary climate.

7.2.2 Towards a General Theory of Energy Transport and its Partitioning in the Climate System

One of the most interesting aspects of climate concerns how energy transport is partitioned between the various components of the climate system, and, for the atmosphere, into different energy types. Both the ocean and atmosphere transport energy, and atmospheric energy transport itself is partitioned into moist and dry parts. Generally, energy diverges from the tropics and converges at the poles; however, the drift of sea ice may diverge energy from the

pole, as energy released when sea ice forms in one location must be re-absorbed from the surrounding environment when sea ice melts at another.

In his seminal study of planetary climate and energy balance, Stone (1978) argued that since TOA fluxes only weakly depend upon the climate state, the climate system must respond to a forcing in such way that the sum of the atmosphere and oceanic energy transport anomalies are close to zero. Equivalently, the atmosphere and ocean energy transport responses must compensate for each other such that the total energy transport is only minimally perturbed.

In Chapter 2 of this thesis, we have shown that TOA fluxes may, in fact, be profoundly affected when the climate system is perturbed, as when the AIS is lowered. In such a case, atmosphere and ocean do not compensate for each other, but rather act in unison. Two big questions are highlighted by this result:

1. When will a perturbation to the climate system significantly change the net TOA energy flux, such that energy transport is altered, and when will it resemble the the assumptions of Stone (1978) and not?

2. In a case where TOA energy fluxes are significantly affected by a perturbation, how much of the required total energy transport anomaly will be relegated to the ocean and how much to the atmosphere? Additionally, how will the energy transport anomaly of the atmosphere by subdivided into dry and latent heat components?

The second of the above points also involves peculiarities of the Earth's atmospheric general circulation, the latitudinal extent of the atmospheric meridional circulation cells and eddies, and the extent to which latent heat release is an effective medium for transporting energy poleward in a given mean state. Such queries regarding how energy is transported within an arbitrary climate system, are some of the Big Questions whose answers will allow us to develop a fundamental understanding of energy transport in planetary climate.

7.2.3 Polar Amplification and its Manifestations

Another interesting question concerns the way that polar climates respond to a forcing. Polar amplification refers the the regional climate sensitivity of the polar regions, which many researchers have argued is greater than that of extra-polar regions (Serreze and Barry, 2011). Furthermore, theoretical arguments suggest that polar amplification may be a robust characteristic of a climate system in which moist static energy is transported poleward, with poleward latent heat transport proportional to the temperature of the tropics (Langen and Alexeev, 2007). Similarly, it is clear that there are regional positive feedbacks, such as the ice-albedo feedback, which amplify the surface temperature response only over the poles (Screen and Simmonds, 2010).

Nevertheless, there are interesting questions posed by the Earth system itself regarding the generality of polar amplification. While the Arctic is warming at a rate faster than the rest of the globe in response to anthropogenic greenhouse gas emissions (as well as other anthropogenic forcings, including black carbon), the Antarctic has remained relatively impervious. The reason for this difference has been attributed to the particular land-ocean configurations that characterize each of the poles, configurations which lead to isolation of the Antarctic that is not seen in the Arctic. This isolation effect, however, has never been quantified in the literature. Furthermore, to what extent does the atmosphere contribute to this isolation, and to what extent is it the ocean? Moreover, to what extent is the delayed warming of the Antarctic due to the thermal inertia of the AIS itself?

Furthermore, given that polar amplification is due to regional feedbacks in the high latitudes that exceed those seen globally, it is not clear that polar amplification is a general feature of planetary climate. For example, a planet orbiting around an M-dwarf star with liquid water at its surface will experience a negative ice-albedo feedback over its polar regions: the emissions spectrum of such a star is shifted towards the IR, relative to the sun, and over such wavelengths, the albedo of liquid water exceeds that of snow and ice (Shields et al., 2013). Other feedbacks which contribute to polar amplification over the Arctic, such as

the lapse rate feedback, may also be anomalously strong when pre-industrial mean state conditions over the Arctic, which favor a low-level atmospheric temperature inversion, are perturbed (Bintanja et al., 2011).

Therefore, just as one may have a general theory of planetary climate, one may have a general theory that encompasses polar climate and how it responds to a forcing. Is polar amplification a robust characteristic of polar climate? If not, when is polar amplification observed and when is it not observed? And, finally, if polar amplification is a universal characteristic of planetary climate, to what extent can forcing and feedback response time scales be used to quantify how the Arctic and Antarctic respond to greenhouse gas-induced perturbations differently?

BIBLIOGRAPHY

Allan, R., C. Liu, M. Zahn, D. Lavers, E. Koukouvagias, and A. Bodas-Salcedo, 2014: Physically consistent responses of the global atmospheric hydrological cycle in models and observations. *Surveys in Geophysics*, **35**, 533–552.

Allan, R., B. Soden, V. John, W. Ingram, and P. Good, 2010: Current changes in tropical precipitation. *Environmental Research Letters*, **5 (025205)**.

Allen, M. and W. Ingram, 2002: Constraints on future changes in climate and the hydrologic cycle. *Nature*, **419**, 224–232.

Andrews, T., P. Forster, O. Boucher, N. Bellouin, and A. Jones, 2010: Precipitation, radiative forcing and global temperature change. *Geophysical Research Letters*, **37 (L14701)**.

Baumgartner, A. and E. Reichel, 1975: *The world water balance: Mean annual global continental and maritime precipitation, evaporation and run-off*. Elsevier Science Inc.

Bengtsson, L., K. Hodges, S. Koumoutsaris, M. Zahn, and N. Keenlyside, 2011: The changing atmospheric water cycle in Polar Regions in a warmer climate. *Tellus A*, **63 (5)**, 907–920.

Bengtsson, L., K. Hodges, and E. Roeckner, 2006: Storm tracks and climate change. *Journal of Climate*, **19**, 3518–3543.

Bintanja, R., R. Graverson, and W. Hazeleger, 2011: Arctic winter warming amplified by the thermal inversion and consequent low infrared cooling to space. *Nature Geoscience*, **4**, 758–761.

Bitz, C., M. Holland, E. Hunke, and R. Moritz, 2005: Maintenance of the sea-ice edge. *Journal of Climate*, **18 (15)**, 2903–2921.

Bitz, C., K. Shell, P. Gent, D. Bailey, G. Danabasoglu, K. Armour, M. Holland, and J. Kiehl, 2012: Climate sensitivity of the community climate system model, version 4. *Journal of Climate*, **25 (9)**, 3053–3070.

Boer, G., 1993: Climate change and the regulation of the surface moisture and energy budgets. *Climate Dynamics*, **8**, 225–239.

Bony, S., G. Bellon, D. Klocke, S. Sherwood, S. Fermepin, and S. Denvil, 2013: Robust direct effect of carbon dioxide on tropical circulation and regional precipitation. *Nature Geoscience*, **6**, 447–451.

Bosilovich, M., 2002: On the vertical distribution of local and remote sources of water for precipitation. *Meteorology and Atmospheric Physics*, **80**, 31–41.

Bosilovich, M. and S. Schubert, 2002: Water vapor tracers as diagnostics of the regional hydrologic cycle. *Journal of Hydrometeorology*, **3**, 149–165.

Bosilovich, M., S. Schubert, and G. Walker, 2005: Global changes in water cycle intensity. *Journal of Climate*, **18**, 1591–1608.

Boyer, T., S. Levitus, J. Antonov, R. Locarnini, and H. Garcia, 2005: Linear trends in salinity for the world ocean, 1955-1998. *Geophysical Research Letters*, **32 (L01604)**.

Boyer, T., et al., 2013: World ocean database 2013. Tech. rep., NOAA.

Broecker, W., 1991: The great ocean conveyor. *Oceanography*, **4 (2)**, 79–89.

Broecker, W., T.-H. Peng, J. Jouzel, and G. Russell, 1990: The magnitude of global fresh-water transports of importance to ocean circulation. *Climate Dynamics*, **4**, 73–79.

Bryan, F. and A. Oort, 1984: Seasonal variation of the global water balance based on aerological data. *Journal of Geophysical Research*, **89 (D7)**, 11 717–11 730.

Chadwick, R., I. Boutle, and G. Martin, 2013: Spatial patterns of precipitation change in cmip5: Why the rich do not get richer in the tropics. *Journal of Climate*, **26**, 3803–3822.

Chang, E., Y. Guo, and X. Xia, 2012: Cmip5 multimodel ensemble projection of storm track change under global warming. *Journal of Geophysical Research*, **117 (D23118)**.

Cheng, W., C. Bitz, and J. Chiang, 2007: *Past and future changes in the ocean's meridional overturning circulation: mechanisms and impacts*, american geophysical union monograph 19: Adjustment of the global climate to an abrupt slowdown of the Atlantic mericional overturning circulation, 295–313. American Geophysical Union.

Cheng, W., J. Chiang, and D. Zhang, 2013: Atlantic meridional overturning circulation (amoc) in cmip5 models: Rcp and historical simulations. *Journal of Climate*, **26**, 7187–7197.

Chiang, J. and C. Bitz, 2005: Influence of high latitude ice cover on the marine intertropical convergence zone. *Climate Dynamics*, **25 (5)**, 477–496.

Chou, C. and J. Neelin, 2004: Mechanisms of global warming impacts on regional tropical precipitation. *Journal of Climate*, **17**, 2688–2701.

Chou, C., J. Neelin, C.-A. Chen, and J.-Y. Tu, 2009: Evaluating the "rich-get-richer" mechanism in tropical precipitation change under global warming. *Journal of Climate*, **22**, 1982–2005.

Chou, C., J.-Y. Tu, and P.-H. Tan, 2007: Asymmetry of tropical precipitation change under global warming. *Geophysical Research Letters*, **34 (17)**.

Ciais, P., J. White, J. Jouzel, and R. Petit, 1995: The origin of present-day antarctic precipitation from surface snow deuterium excess data. *Journal of Geophysical Research: Atmospheres*, **100 (D9)**, 18 917–18 927.

Curry, R., B. Dickson, and I. Yashayaev, 2003: A change in the freshwater balance of the Atlantic Ocean over the past four decades. *Nature*, **426**, 826–829.

Czaja, A., 2009: Atmospheric control on the thermohaline circulation. *Journal of Physical Oceanography*, **39**, 234–247.

Dai, A., 2012: Increasing drought under global warming in observations and models. *Nature Climate Change*, **3**, 52–58.

Dai, A. and T. Wigley, 2000: Global patterns of enso-induced precipitation. *Geophysical Research Letters*, **27 (9)**, 1283–1286.

Danabasoglu, G., S. Bates, B. Briegleb, S. Jayne, M. Jochum, W. Large, S. Peacock, and S. Yeager, 2012: The CCSM4 ocean component. *Journal of Climate*, **25**, 1361–1389.

de Q. Robin, G., 1988: The Antarctic ice sheet, its history and response to sea level and climatic changes over the past 100 million years. *Palaeogeography, Palaeoclimatology, Palaeoecology*, **67 (1-2)**, 31–50.

DeConto, R. and D. Pollard, 2003: Rapid Cenozoic glaciation of Antarctica induced by declining atmospheric co2. *Nature*, **421**, 245–249.

Dee, D., et al., 2011: The era-interim reanalysis: configuration and performance of the data assimilation system. *Quarterly Journal of the Royal Meteorological Society*, **137**, 553–597.

Delaygue, G., V. Mason, J. Jouzel, R. Koster, and R. Healy, 2000: The origin of antarctic precipitation: a modelling approach. *Tellus B*, **51 (1)**, 19–36.

Ding, Q., E. Steig, D.S., and M. Kuttel, 2011: Winter warming in west antarctica caused by central pacific warming. *Nature Geoscience*, **4**, 398–403.

Dukowicz, J. and J. Baumgardner, 2000: Incremental remapping as a tracer advection algorithm. *Journal of Computational Physics*, **160**, 318–335.

Durack, P. and S. Wijffels, 2010: Fifty-year trends in global ocean salinities and their relationship to broad-scale warming. *Journal of Climate*, **23**, 4342–4362.

Durack, P., S. Wijffels, and R. Matear, 2012: Ocean salinities reveal strong global water cycle intensification during 1950 to 2000. *Science*, **336**, 455–458.

Egger, J., 1994: Antarctic slope winds and the polar stratospheric vortex. *Journal of Atmospheric and Terrestrial Physics*, **56 (9)**, 1067–1072.

Eltahir, E. and R. Bras, 1996: Precipitation recycling. *Reviews of Geophysics*, **34 (3)**, 367–378.

Emile-Geay, J., M. Cane, N. Naik, R. Seager, A. Clement, and A. van Geen, 2003: Warren revisited: Atmospheric freshwater fluxes and "why is no deep water formed in the north pacific". *Journal of Geophysical Research*, **108 (C6)**.

Enderton, D. and J. Marshall, 2009: Explorations of atmosphere-ocean-ice climates on an aquaplanet and their meridional energy transports. *Journal of the Atmospheric Sciences*, **66**, 1593–1611.

Ferreira, D., J. Marshall, and J.-M. Campin, 2010: Localization of deep water formation: Role of atmospheric moisture transport and geometrical constraints on ocean circulation. *Journal of Climate*, **23**, 1456–1476.

Friedman, A., Y.-T. Hwang, J. Chiang, and D. Frierson, 2013: Interhemispheric temperature asymmetry over the Twentieth century and in future projections. *Journal of Climate*, **26**, 5419–5433.

Frierson, D., I. Held, and P. Zurita-Gotor, 2007: A gray-radiation aquaplanet moist GCM. part ii: Energy transports in altered climates. *Journal of the Atmospheric Sciences*, **64**, 1680–1693.

Frierson, D. and Y.-T. Hwang, 2012: Extratropical influence on ITCZ shifts in slab ocean simulations of global warming. *Journal of Climate*, **25**, 720–733.

Ganachaud, A. and C. Wunsch, 2003: Large-scale ocean heat and freshwater transports during the world ocean circulation experiment. *Journal of Climate*, **16**, 696–705.

Gent, P. and J. McWilliams, 1992: Isopycnal mixing in ocean circulation models. *Journal of Physical Oceanography*, **20**, 150–155.

Gent, P., et al., 2011: The community climate system model version 4. *Journal of Climate*, **24 (19)**, 4973–4991.

Gillett, N., T. Kell, and P. Jones, 2006: Regional climate impacts of the southern annular mode. *Geophysical Research Letters*, **33 (L23704)**.

Gimeno, L., A. Drumond, R. Nieto, R. Trigo, and A. Stohl, 2010: On the origin of continental precipitation. *Geophysical Research Letters*, **37 (L13804)**.

Gimeno, L., R. Nieto, A. Drumond, R. Castillo, and R. Trigo, 2013: Influence of th intensification of the major oceanic moisture sources on continental precipitation. *Geophysical Research Letters*, **40 (7)**, 1443–1450.

Gimeno, L., et al., 2012: Oceanic and terrestrial sources of continental precipitation. *Reviews of Geophysics*, **50 (RG4003)**, 1–41.

Gloersen, P., 1996: Modulation of hemispheric sea-ice cover by enso events. *Nature*, **373**, 503–506.

Goldner, A., N. Herold, and M. Huber, 2014: Antarctic glaciation caused ocean circulation changes at the eocene-oligocene transition. *Nature*, **511**, 574–577.

Grodsky, S., J. Carton, and F. Bingham, 2006: Low frequency variation of sea surface salinity in the tropical atlantic. *Geophysical Research Letters*, **33 (L14604)**.

Hahn, D. and S. Manabe, 1975: The role of mountains in the South Asian monsoon circulation. *Journal of the Atmospheric Sciences*, **32**, 1515–1541.

Hall, A. and M. Visbeck, 2002: Synchronous variability in the southern hemisphere atmosphere, sea ice, and ocean resulting from the annular mode. *Journal of Climate*, **15 (21)**, 3043–3057.

Hall, N., B. Hoskins, P. Valdes, and C. Senior, 1994: Storm tracks in a high-resolution gcm with doubled carbon dioxide. *Quarterly Journal of the Royal Meteorological Society*, **120 (519)**, 1209–1230.

Hartmann, D., 1994: *Global Physical Climatology*, International Geophysics, Vol. 56. Academic Press.

Haug, G., R. Tiedemann, R. Zahn, and A. Ravelo, 2001: Role of panama uplift on oceanic freshwater balance. *Geology*, **29 (3)**, 207–210.

Haupt, B. and D. Seidov, 2007: Strengths and weaknesses of the global ocean conveyor: Inter-basin freshwater disparities as the major control. *Progress in Oceanography*, **73**, 358–369.

He, J., B. Soden, and B. Kirtman, 2014: The robustness of the atmospheric circulation and precipitation response to future anthropogenic surface warming. *Geophysical Research Letters*, **41**, 2614–2622.

Held, I. and B. Soden, 2006: Robust reponses of the hydrological cycle to global warming. *Journal of Climate*, **19**, 5686–5699.

Helm, K., N. Bindoff, and J. Church, 2010: Changes in the global hydrological-cycle inferred from ocean salinity. *Geophysical Research Letters*, **37 (L18701)**.

Holton, J. R., 1992: *An Introduction to Dynamic Meteorology*, International Geophysics, Vol. 48. 3d ed., Academic Press.

Hosoda, S., T. Suga, N. Shikama, and K. Mizuno, 2009: Global surface layer salinity change detected by argo and its implications for hydrological cycle intensification. *Journal of Oceanography*, **65**, 579–586.

Hu, P., T. Li, J.-J. Luo, H. Murakami, A. Kitoh, and M. Zhao, 2012: Increase of global monsoon area and precipitation under global warming: a robust signal. *Geophysical Research Letters*, **39 (6)**.

Huang, R., 1993: Real freshwater flux as a natural boundary condition for the salinity balance and thermohaline circulation forced by evaporation and precipitation. *Journal of Physical Oceanography*, **23 (11)**, 2428–2446.

Hunke, E. and W. Lipscomb, 2004: Cice: the los alamos sea ice model, documentation and software, version 3.1. Tech. Rep. CC-98-16, Los Alamos National Laboratory.

Hunke, E. and W. Lipscomb, 2008: Cice: the los alamos sea ice model, documentation and software, version 4.0. Tech. Rep. LA-CC-06-012, Los Alamos National Laboratory.

Hurrell, J., et al., 2013: The community earth system model: A framework for collaborative research. *Bulletin of the American Meteorological Society*, **94**, 1339–1360.

Hwang, Y.-T. and D. Frierson, 2010: Increasing atmospheric poleward energy transport with global warming. *Geophysical Research Letters*, **37 (L24807)**.

Hwang, Y.-T., D. Frierson, and J. Kay, 2011: Coupling between Arctic feedbacks and changes in poleward energy transport. *Geophysical Research Letters*, **38 (L17704)**.

Johnsen, S. and J. White, 1989: The origin of arctic precipitation under present and glacial conditions. *Tellus*, **41B**, 452–468.

Joussaume, S., R. Sadourny, and C. Vignal, 1986: Origin of precipitating water in a numerical simulation of july climate. *Ocean-Air Interactions*, **1**, 43–56.

Justino, F., J. Marengo, F. Kucharski, F. Stordal, J. Machado, and M. Rodrigues, 2014: Influence of Antarctic ice sheet lowering on the Southern Hemisphere climate: modeling experiments mimicking the mid-Miocene. *Climate Dynamics*, **42**, 843–858.

Kang, S., I. Held, D. Frierson, and M. Zhao, 2008: The response of the ITCZ to extratropical thermal forcing: idealized slab-ocean experiments with a GCM. *Journal of Climate*, **21**, 3521–3532.

Kennett, J., 1977: Cenezoic evolution of Antarctic glaciation, the circum-Antarctic Ocean, and their impact on global paleoceanography. *Journal of Geophysical Research*, **82**, 3843–3860.

Kidston, J., S. Dean, J. Renwick, and G. Vallis, 2010: A robust increase in the eddy length scale in the simulation of future climates. *Geophysical Research Letters*, **37 (L03806)**.

Knoche, H. and H. Kunstmann, 2013: Tracking atmospheric water pathways by direct evaporation tagging: A case study for West Africa. *Journal of Geophysical Research: Atmospheres*, **118**, 12 345–12 358.

Knorr, G. and G. Lohmann, 2014: Climate warming during antarctic ice sheet expansion at the middle miocene transition. *Nature Geoscience*, **7 (2119)**, 376–381.

Knutti, R. and J. Sedlacek, 2013: Robustness and uncertainties in the new cmip5 climate model projections. *Nature Climate Change*, **3**, 369–373.

Koster, R., J. Jouzel, R. Suozzo, and G. Russell, 1992: Origin of july antarctic precipitation and its influence on deuterium content: a gcm analysis. *Climate Dynamics*, **7**, 195–203.

Koster, R., J. Jouzel, R. Suozzo, G. Russell, W. Broecker, D. Rind, and P. Eagleson, 1986: Global sources of local precipitation as determined by the nasa/giss gcm. *Geophysical Research Letters*, **13 (1)**, 121–124.

Langen, P. and V. Alexeev, 2007: Polar amplification as a preferred response in an idealized aquaplanet gcm. *Climate Dynamics*, **29**, 305–317.

Lau, W., H.-T. Wu, and K.-M. Kim, 2013: A canonical response of precipitation characteristics to global warming from cmip5 models. *Geophysical Research Letters*, **40**, 3163–3169.

Leathers, D., B. Yarnal, and M. Palecki, 1991: The pacific / north american teleconnection pattern and united states climate. part i: Regional temperature and precipitation associations. *Journal of Climate*, **4**, 517–528.

Leduc, G., L. Vidal, K. Tachikawa, F. Rostek, C. Sonzogni, L. Beaufort, and E. Bard, 2007: Moisture transport across central america as a positive feedback on abrupt climatic changes. *Nature*, **445**, 908–911.

Lepparanta, M., 2011: *The Drift of Sea Ice*. Springer-Praxis Books in Geophysical Sciences, Springer-Verlag.

Levitus, S., et al., 2013: The world ocean database. *Data Science Journal*, **12**, 229–234.

Li, G., S. Harrison, P. Bartlein, K. Izumi, and I. Prentice, 2013: Precipitation scaling with temperature in warm and cold climates: An analysis of cmip5 simulations. *Geophysical Research Letters*, **40**, 4018–4024.

Li, G. and S.-P. Xie, 2014: Tropical biases in cmip5 multimodel ensemble: The excessive equatorial pacific cold tongue and double itcz problems. *Journal of Climate*, **27**, 1765–1780.

Lin, J.-L., 2007: The double-itcz problem in ipcc ar4 coupled gcms: Ocean-atmosphere feedback analysis. *Journal of Climate*, **20 (18)**, 4497–4525.

Lisiecki, L. E. and M. E. A. Raymo, 2005: Pliocene-pleistocene stack of 57 globally distributed benthic [dgr]18o records. *Paleoceanography*, **20**, URL `http://dx.doi.org/10.1029/2004PA001071`.

Liu, Z., A. Mehran, T. Phillips, and A. AghaKouchak, 2014: Seasonal and regional biases in cmip5 precipitation simulations. *Climate Research*, **60**, 35–50.

Lohmann, G., 2003: Atmospheric and oceanic freshwater transport during weak atlantic overturning circulation. *Tellus*, **55A**, 438–449.

Lorenz, D., 2014: Understanding midlatitude jet variability and change using rossby wave chromatography: Poleward-shifted jets in response to external forcing. *Journal of the Atmospheric Sciences*, **71 (7)**, 2370–2389.

Lorenz, D., E. DeWeaver, and D. Vimont, 2010: Evaporation change and global warming: The role of net radiation and relative humidity. *Journal of Geophysical Research*, **115 (D20118)**.

Manabe, S. and A. Broccoli, 1985: The influence of continental ice sheets on theclimate of an ice age. *Journal of Geophysical Research*, **90**, 2167–2190.

Manabe, S. and A. Broccoli, 1990: Mountains and arid climates of the middle latitudes. *Science*, **247 (4939)**, 192–195.

Manabe, S. and T. Terpstra, 1974: The effects of mountains on the general circulation of the atmosphere as identified by numerical experiments. *Journal of the Atmospheric Sciences*, **31**, 3–42.

Manabe, S. and R. Wetherald, 1975: The effects of doubling the co2 concentration on the climate of a general circulation model. *Journal of the Atmospheric Sciences*, **32 (1)**, 3–15.

Marshall, J. and K. Speer, 2012: Closure of the meridional overturning circulation through Southern Ocean upwelling. *Nature Geoscience*, **5**, 171–180.

Mechoso, C., 1980: The atmospheric circulation around Antarctica: Linear stablity and finite amplitude interactions with migrating cyclones. *Journal of the Atmospheric Sciences*, **37**, 2209–2233.

Mechoso, C., 1981: Topographic influences on the general circulation of the Southern Hemisphere: A numerical experiment. *Monthly Weather Review*, **109**, 2131–2139.

Meehl, G., J. Arblaster, and C. Tebaldi, 2005: Understanding future patterns of increased precipitation intensity in climate model simulations. *Geophysical Research Letters*, **32 (L18719)**.

Mitchell, J., C. Wilson, and W. Cunnington, 1987: On co_2 climate sensitivity and model dependence of results. *Quarterly Journal of the Royal Meteorological Society*, **113 (475)**, 293–322.

Muller, C. and P. O'Gorman, 2011: An energetic perspective on the regional response of precipitation to climate change. *Nature Climate Change*, **1**, 266–271.

Mysak, L., R. Ingram, J. Wang, and A. van der Baaren, 1996: The anomalous sea-ice extent in hudson bay, baffin bay, and the labrador sea during three simultaneous nao and enso episodes. *Atmosphere-Ocean*, **34 (2)**, 313–343.

Neale, R., et al., 2012: Description of ncar community atmosphere model (cam 5.0). NCAR Technical Note TN-486+STR, NCAR.

Noone, D. and I. Simmonds, 2002: Annular variations in moisture transport mechanisms and the abundance of δ^{18}o in antarctic snow. *Journal of Geophysical Research: Atmospheres*, **107 (D24)**.

Numaguti, A., 1999: Origin and recycling processes of precipitating water over the eurasian continent: Experiments using an atmospheric general circulation model. *Journal of Geophysical Research*, **104 (D2)**, 1957–1972.

O'Gorman, P., 2010: Understanding the varied response of the extratropical storm tracks to climate change. *Proceedings of the National Academy of Sciences*, **107 (45)**, 19 176–19 180.

Ogura, T. and A. Abe-Ouchi, 2001: Influence of the Antarctic ice sheet on souther high latitude climate during the Cenozoic: albedo vs topography effect. *Geophysical Research Letters*, **28 (4)**, 587–590.

Parish, T., 1991: On the role of antarctic katabatic winds in forcing large-scale tropospheric motions. *Journal of the Atmospheric Sciences*, **49 (15)**, 1374–1385.

Parish, T., D. Bromwich, and R.-Y. Tzeng, 1994: On the role of the antarctic continent in forcing large-scale circulations in the high southern latitudes. *Journal of the Atmospheric Sciences*, **51 (24)**, 3566–3579.

Parish, T. and K. I. Waight, 1987: The forcing of antarctic katabatic winds. *Monthly Weather Review*, **115**, 2214–2226.

Peixoto, J. and A. Oort, 1992: *Physics of Climate*. American Institute of Physics.

Pendergrass, A. and D. Hartmann, 2014: The atmospheric energy constraint on global-mean precipitation change. *Journal of Climate*, **27**, 757–768.

Pierrehumbert, R., 2010: *Principles of Planetary Climate*. Cambridge University Press, New York.

Pollard, D. and R. DeConto, 2009: Modelling West Antarctic ice sheet growth and collapse through the past five million years. *Nature*, **458 (7236)**, 329–332.

Prange, M., S. Steph, M. Schulz, and L. Keigwin, 2010: Inferring moisture transport across central america: Can modern analogs of climate variability help reconcile paleosalinity records? *Quaternary Science Reviews*, **29 (11-12)**, 1317–1321.

Quintanar, A. and C. Mechoso, 1995: Quasi-stationary waves in the southern hemisphere. part ii: Generation mechanisms. *Journal of the Atmospheric Sciences*, **8**, 2673–2690.

Rahmstorf, S., 1996: On the freshwater forcing and transport of the atlantic thermohaline circulation. *Climate Dynamics*, **12**, 799–811.

Richter, I. and S. Xie, 2008: Muted precipitation in global warming simulations: a surface evaporation perspective. *Journal of Geophysical Research: Atmospheres*, **113 (D24)**.

Riviere, G., 2011: A dynamical interpretation of the poleward shift of the jet streams in global warming scenarios. *Journal of the Atmospheric Sciences*, **68**, 1253–1272.

Sarojini, B., P. Stott, E. Black, and D. Polson, 2012: Fingerprints of changes in annual and seasonal precipitation from cmip5 models over land and ocean. *Geophysical Research Letters*, **39 (21)**.

Scheff, J. and D. Frierson, 2012a: Robust future precipitation declines in CMIP5 largely reflect the poleward expansion of model subtropical dry zones. *Geophysical Research Letters*, **39 (L18704)**.

Scheff, J. and D. Frierson, 2012b: Twenty-first century multimodel subtropical precipitation declines are mostly midlatitude shifts. *Journal of Climate*, **25**, 4330–4347.

Scherer, R. P., 1991: Quaternary and tertiary microfossils from beneath ice stream-b - evidence for a dynamic west antarctic ice-sheet history. *Glob. Planet. Change*, **90**, 395–412, URL `http://dx.doi.org/10.1016/0921-8181(91)90005-H`.

Schmitt, R., 1995: The ocean component of the global water cycle. *Reviews of Geophysics*, **(95RG00184)**, 1895–1409.

Schmitt, R., 2008: Salinity and the global water cycle. *Oceanography*, **21 (1)**, 12–19.

Screen, J. and I. Simmonds, 2010: The central role of diminishing sea ice in recent arctic temperature amplification. *Nature*, **464**, 1334–1337.

Seager, R., D. Battisti, J. Yin, N. Gordon, N. Naik, A. Clement, and M. Cane, 2002: Is the gulf stream responsible for Europe's mild winters? *Quarterly Journal of the Royal Meteorological Society*, **128**, 2563–2586.

Seager, R. and N. Naik, 2012: A mechanisms-based approach to detecting recent anthropogenic hydroclimate change. *Journal of Climate*, **25**, 236–261.

Seager, R., N. Naik, and G. Vecchi, 2010: Thermodynamic and dynamic mechanisms for large-scale changes in the hydrological cycle in response to global warming. *Journal of Climate*, **23**, 4651–4668.

Seager, R., et al., 2007: Model projections of an imminent transition to a more arid climate in southwestern north america. *Science*, **316 (5828)**, 1181–1184.

Seidel, D., Q. Fu, W. Randel, and T. Reichler, 2008: Widening of the tropical belt in a changing climate. *Nature Geoscience*, **1**, 21–24.

Serreze, M., A. Barrett, and J. Stroeve, 2012: Recent changes in tropospheric water vapor over the arctic as assessed from radiosondes and atmospheric reanalyses. *Journal of Geophysical Research*, **117 (D10104)**.

Serreze, M. and R. Barry, 2011: Processes and impacts of arctic amplification: A research synthesis. *Global and Planetary Change*, **77**, 85–96.

Sherwood, S. and Q. Fu, 2014: A drier future? *Science*, **343 (737)**, 2014.

Shields, A., V. Meadow, C. Bitz, R. Pierrehumbert, M. Joshi, and T. Robertson, 2013: The effect of host star spectral energy distribution and ice-albedo feedback on the climate of extrasolar planets. *Astrobiology*, **13 (8)**, 715–739.

Simmonds, I. and R. Law, 1995: Associations between Antarctic katabatic flow and the upper level winter vortex. *International Journal of Climatology*, **15 (4)**, 403–421.

Sodemann, H. and A. Stohl, 2009: Asymmetries in the moisture origin of antarctic precipitation. *Geophysical Research Letters*, **36 (L22803)**.

Sodemann, H. and A. Stohl, 2013: Moisture origin and meridional transport in atmospheric rivers and their association with multiple cyclones. *Monthly Weather Review*, **41**, 2850–2868.

Sodemann, H., H. Wernli, and C. Schwierz, 2009: Sources of water vapour contributing to the elbe flood in august 2002 - a tagging study in a mesoscale model. *Quarterly Journal of the Royal Meteorological Society*, **135 (638, Part A)**, 205–223.

Stephens, G. and T. Ellis, 2008: Controls of global-mean precipitation increases in global warming gcm experiments. *Journal of Climate*, **21**, 6141–6155.

Stephens, G., A. Slingo, M. Webb, P. Minnett, P. Daum, L. Kleinman, I. Wittmeyer, and D. Randall, 1994: Observations of the earth's radiation budget in relation to atmospheric hydrology; 4. atmospheric column radiative cooling over the world's oceans. *Journal of Geophysical Research*, **99 (D9)**, 18 585–18 604.

Stocker, T., et al., (Eds.), 2013: *Climate Change 2013: The Physical Science Basis. Contribution of Working Group I to the Fifth Assessment Report of the Intergovernmental Panel on Climate Change*, Cambridge University Press, Cambridge UK and New York, NY USA.

Stohl, A. and P. James, 2004: A lagrangian analysis of the atmospheric branch of the global water cycle. Part I: method description, validation, and demonstration for the August 2002 flooding in Central Europe. *Journal of Hydrometeorology*, **5**, 656–678.

Stohl, A. and P. James, 2009: A lagrangian analysis of the atmospheric branch of the global water cycle. part ii: moisture transports between earth's ocean basins and river catchments. *Journal of Hydrometeorology*, **6 (6)**, 961–984.

Stone, P., 1978: Constraints on dynamical transports of energy on a spherical planet. *Dynamics of Atmospheres and Oceans*, **2**, 123–139.

Sugi, M. and J. Yoshimura, 2004: A mechanism of tropical precipitation change due to co2 increase. *Journal of Climate*, **17**, 238–243.

Sutton, R. and D. Hodson, 2003: Influence of the ocean on north atlantic climate variability. *Journal of Climate*, **16**, 3296–3313.

Sutton, R. and D. Hodson, 2005: Atlantic ocean forcing of north american and european summer climate. *Science*, **309**, 115–118.

Takahashi, K. and D. Battisti, 2007: Processes controlling the mean tropical pacific precipitation pattern. part I: the Andes and the eastern Pacific ITCZ. *Journal of Climate*, **20**, 5696–5706.

Terray, L., L. Corre, S. Cravatte, T. Delcroix, G. Reverdin, and A. Ribes, 2012: Near-surface salinity as nature's rain gauge to dect human influence on the tropical water cycle. *Journal of Climate*, **25**, 958–977.

Thompson, D. and J. Wallace, 2001: Regional climate impacts of the northern hemisphere annular mode. *Science*, **293 (5527)**, 85–89.

Thorpe, R., J. Gregory, T. Johns, R. Wood, and J. Mitchell, 2001: Mechanisms determining the atlantic thermohaline circulation response to greenhouse gas forcing in a non-flux-adjusted coupled climate model. *Journal of Climate*, **14**, 3102–3116.

Trenberth, K., 1998: Atmospheric moisture residence times and cycling: Implications for rainfall rates and climate change. *Climatic Change*, **39 (4)**, 667–694.

Trenberth, K., 1999: Atmospheric moisture recycling: role of advection and local evaporation. *Journal of Climate*, **12**, 1368–1381.

Trenberth, K. and J. Caron, 2001: Estimates of meridional atmosphere and ocean heat transports. *Journal of Climate*, **14**, 3433–3443.

Trenberth, K., J. Fasullo, and J. Mackaro, 2011: Atmospheric moisture transports from ocean to land and global energy flows in reanalyses. *Journal of Climate*, **24**, 4907–4925.

Vallis, G., P. Zurita-Gotor, C. Cairns, and J. Kidston, 2014: Response of the large-scale structure of the atmosphere to global warming. *Quarterly Journal of the Royal Meteorological Society*, **(10.1002/qj.2456)**.

van der Ent, R. and H. Savenije, 2011: Length and times scales of atmospheric moisture recycling. *Atmospheric Chemistry and Pnysics*, **11**, 1853–1863.

Vecchi, G. and B. Soden, 2007: Global warming and the weakening of the tropical circulation. *Journal of Climate*, **20**, 4316–4340.

Vellinga, M. and P. Wu, 2004: Low-latitude freshwater influence on centennial variability of the atlantic thermohaline circulation. *Journal of Climate*, **17**, 4498–4511.

Walsh, K., I. Simmonds, and M. Collier, 2000: Sigma-coordinate calculation of topographically forced baroclinicity around Antarctica. *Dynamics of Atmospheres and Oceans*, **33**, 1–29.

Warren, B., 1983: Why is no deep water formed in the north pacific? *Journal of Marine Research*, **41**, 327–347.

Werner, M., M. Heimann, and G. Hoffmann, 2001: Isotopic composition and origin of polar precipitation in present and glacial climate simulations. *Tellus B*, **53 (1)**, 53–71.

Weyl, P., 1968: The role of the oceans in climate change; a theory of the ice ages. *Meteorological Monographs*, **8**, 37–62.

Willett, K., N. Gillett, P. Jones, and P. Thorne, 2007: Attribution of observed surface humidity changes to human influence. *Nature*, **449**, 710–712.

Xie, P. and P. Arkin, 1996: Analyses of global monthly precipitation using gauge observations, satellite estimates, and numerical model predictions. *Journal of Climate*, **9**, 840–858.

Yin, J., 2005: A consistent poleward shift of the storm tracks in simulations of 21st century climate. *Geophysical Research Letters*, **32 (L18701)**.

Yu, L., R. Weller, and B. Sun, 2004: Improving latent and sensible heat flux estimates for the atlantic ocean (1988-1999) by a synthesis approach. *Journal of Climate*, **17**, 373–393.

Zaucker, F. and W. Broecker, 1992: The influence of atmospheric moisture transport on the freshwater balance of the atlantic drainage basin: general circulation model simulations and observations. *Journal of Geophysical Research*, **97 (D3)**, 2765–2773.

Zhang, X., F. Zwiers, G. Hegerl, F. Lambert, N. Gillett, S. Solomon, P. Stott, and T. Nozawa, 2007: Detection of human influence on twentieth-century precipitation trends. *Nature*, **448**, 461–465.